Skeletal muscle: an exploration into an anti-metastatic niche and the molecular mechanisms that underlie it

Sarah B. Crist

A dissertation submitted in partial fulfillment of
the requirements for the degree of

Doctor of Philosophy

University of Washington
2021

Reading committee:
Cyrus Ghajar, Chair
Slobodan Beronja
Stephen Tapscott

Program authorized to offer degree:
Molecular and Cellular Biology

University of Washington

Abstract

Skeletal muscle: an exploration into an anti-metastatic niche and the molecular mechanisms that underlie it

Sarah B. Crist

Chair of the supervisory committee:
Professor Cyrus Ghajar
Department of Pharmacology

Over the past four decades, the cancer biology field has concentrated on defining the molecular basis of metastasis by characterizing changes to extracellular microenvironments of disseminated tumor cells that promote metastatic outgrowth in organs such as the lung, liver and bone. However, clinical reports highlight that patterns of metastatic dissemination are not random nor equal across all tissues in the body. If not all tissues are equally susceptible to metastatic colonization, what distinguishes a tissue that is resistant from another that is permissive? What constitutes an inhospitable microenvironment? My doctoral work aimed to address this gap in our knowledge by using skeletal muscle as a model for an anti-metastatic tissue. I employed mouse and organotypic culture models, along with metabolomics and proteomics, to identify i) a niche for disseminated tumor cells within skeletal muscle, ii) metabolic factors within this tissue microenvironment that inhibit outgrowth of breast and mammary cancer cells, and iii) a potential mechanism by which extracellular matrix remodeling breaks suppression. Together, these approaches identify sustained oxidative stress as a critical determinant of disseminated tumor cell suppression in skeletal muscle, and peritumoral collagen accumulation as a key promoter of disseminated tumor cell outgrowth.

Table of Contents

List of Figures

Chapter 1

Chapter 3

Chapter 4

Chapter 5

Acknowledgements.

I would like to thank my thesis committee – Dr. Cecilia Moens, Dr. Slobodan Beronja, Dr. Stephen Tapscott, Dr. Pete Nelson, and Dr. Cyrus Ghajar – for their constructive input and constant support. An additional thanks to Drs. Beronja, Tapscott and Ghajar for reading and providing critical feedback on this dissertation.

Huge thanks to Dr. Travis Nemkov and Megan Kufeld, who, as my primary research collaborators, made my job a whole lot easier. Working with you was always a pleasure. Recognition and gratitude are also needed for the Comparative Medicine staff and the CCEH core, especially Don Parilla, who have always taken such good care of my mice.

Thank you to the members of the Ghajar lab for making lab a home-away-from-home, for the meaningful conversation and for your selfless help. You collectively made the six years of the PhD worthwhile.

To Cyrus, thank you for being such a top-notch scientific role model. Your enthusiasm for and knowledge about all things DTC blows my mind every day. You never cease to amaze!

To my family, thank you for encouraging my interest in the natural world and your unwavering confidence in my abilities. You saw promise in me long before anyone else.

To my husband, words can't do this thank you justice. Your intellectual collaboration, love and optimism truly made my doctoral work the magnum opus it is today.

Dissertation Introduction.

"When a plant goes to seed, its seeds are carried in all directions.
But they can only live and grow if they fall on congenial soil.[1]"
Dr. Stephen Paget, 1889

Accounting for nearly 90% of all cancer related deaths, metastasis is arguably the most fearsome aspect of cancer[2]. Metastasis is the process by which tumor cell from a primary lesion leave this site, travel through the blood or lymphatics, root in secondary organs and again begin to grow. It was quickly evident to physicians that not all organs are equally susceptible to metastatic colonization, which prompted British surgeon Stephen Paget to be the first of many to tackle the question, "What is it that decides what organs shall suffer in a case of disseminated cancer?"[3]

Paget noticed a pattern when he was autopsied hundreds of breast cancer patients, whereby breast cancer demonstrated site preferences to organs like the brain, lung, bone and liver[1]. Paget likened the success of the tumor cell to a newly-sown seed (quote above) and concluded metastases formed only when the seed (disseminated tumor cell) and soil (secondary organ site) were compatible.

Over the past four decades, the cancer biology field has concentrated on defining the molecular basis of metastasis by defining changes to extracellular microenvironments of disseminated tumor cells that promote metastatic outgrowth in tissues such as the lung, liver and bone[4-6]. However, the opposite has gone ignored. What happens to those tumor seeds in the organs that are not hospitable? My doctoral work aimed to address this gap in our knowledge by determining, broadly: What constitutes an *inhospitable* microenvironment? To do so, I used skeletal muscle as a model tissue.

Skeletal muscle is a striking example of a tissue that resists metastasis: only 0.2% of malignant cancer cases involve skeletal muscle metastases[7]. Upon careful autopsy, however, microscopic lesions in skeletal muscle are detected almost 100-times more frequently[8]. Taken together, these data suggest that disseminated tumor cells (**DTCs**) successfully reach skeletal muscle and survive within this tissue, but rarely colonize it. Although skeletal muscle has been recognized as an inhospitable site for metastases for

decades, the anti-metastatic nature of skeletal muscle has eluded thorough molecular description.

To address this biological mystery, I employed mouse and organotypic culture models, along with metabolomics and proteomics, to identify i) a niche for disseminated tumor cells within skeletal muscle, ii) metabolic factors within this tissue microenvironment that inhibit outgrowth of breast and mammary cancer cells, and iii) a possible mechanism by which extracellular matrix remodeling breaks suppression. Together, these approaches identify sustained oxidative stress as a critical determinant of disseminated tumor cell suppression in skeletal muscle, and peritumoral collagen accumulation as a key promoter of disseminated tumor cell outgrowth.

Chapter 1 serves as an introduction to anti-metastatic niches and the mechanisms that underlie them, while Chapter 2 introduces the experimental methods employed in the following chapters. In Chapter 3, I show that unchecked oxidative stress is a key growth suppressor in skeletal muscle across several breast and mammary cancer cell lines in culture and *in vivo*. In Chapter 4, I describe how enhanced collagen deposition is sufficient to override the anti-metastatic cues in skeletal muscle, but how this phenomenon is not provoked by low-level myofiber injury, potentially explaining the rarity of skeletal muscle colonization despite the frequency of such injury. In Chapter 5, I propose complementary avenues of study based on preliminary data generated throughout the course of my doctoral training. Finally, in Chapter 6, I conclude this dissertation with a summary of my doctoral research and touch on several open questions that I believe the field must address in order to advance our understanding of how the tissue microenvironment regulates metastasis.

References

1. Paget S. The distribution of secondary growths in cancer of the breast. *Lancet* **133**(3421):571–32. (1889).

2. Chaffer, C. and Weinberg, R. A perspective on cancer cell metastasis. *Science.* **331**(6024):1559-64. (2011).

3. Fidler, IJ. The pathogenesis of cancer metastasis: The “seed and soil” hypothesis revisited. *Nat. Rev. Cancer* **3**:1–6. (2003).

4. Minn, AJ, Gupta, GP, Siegel, PM, Bos, PD, Shu, W, et al. Genes that mediate breast cancer metastasis to lung. *Nature* **436**(7050):518–24. (2005).

5. Costa-Silva, B, Aiello, NM, Ocean, AJ, Singh, S, Zhang H, et al. Pancreatic cancer exosomes initiate pre-metastatic niche formation in the liver. *Nat. Cell Biol.* **17**(6):816–26. (2015).

6. Kang, Y, Siegel, PM, Shu, W, Drobnjak, M, Kakonen, SM, et al. A multigenic program mediating breast cancer metastasis to bone. *Cancer Cell* **3**(6):537–49. (2003).

7. Disibio G, French SW. Metastatic Patterns of Cancers Results From a Large Autopsy Study. *Arch. Pathol. Lab. Med.* **132**:931–9. (2008).

8. Haygood, TM, Wong, J, Lin, JC, Li, S, Matamoros, A, et al. Skeletal muscle metastases: a three-part study of a not-so-rare entity. *Skeletal Radiol*. **41**(8):899–909 (2012).

Chapter 1. Introduction to Anti-Metastatic Niches

Chapter is adapted from a previously published review in Annual Reviews Pathology: Mechanisms of Disease, Crist and Ghajar 2021.

Over the last four decades, the cancer biology field has concentrated on cellular and microenvironmental drivers of metastasis. Despite this focus, mortality rates upon diagnosis of metastatic disease remain essentially unchanged. Would a small change in perspective help? Knowing what constitutes an inhospitable, rather than hospitable, microenvironment could provide the inspiration necessary to develop better therapies and preventative strategies. In this review, we canvas the literature for hints about what characteristics four common antimetastatic niches—skeletal muscle, spleen, thyroid, and yellow bone marrow— have in common. We posit that thorough molecular and mechanistic characterization of antimetastatic tissues may inspire reimagined therapies that inhibit metastatic development and/or progression in an enduring manner.

1. BACKGROUND

The pathogenesis of metastasis follows a series of interrelated steps dependent on both the intrinsic properties of tumor cells and the host organ microenvironment[1,2]. In 1889, Paget conducted 735 autopsies of metastatic breast cancer patients and discovered that breast cancer exhibits a predilection for metastasizing to specific visceral organs and to bones[3]. This led him to articulate his now famous seed and soil hypothesis, which states that tumor cells will metastasize to a site where the local microenvironment is favorable, just like a seed will grow only if it lands in fertile soil. He commented especially on the high incidence of metastasis in liver, ovary, and specific bones and the low incidence in the spleen—a clear discrepancy, in his opinion, between the relative blood supply and the frequency of metastasis to these sites. His observations brought two fundamental concepts to light that would rule the field for years to come: organotropism and the role of microenvironment.

Over the last four decades, the cancer biology field has concentrated on the molecular underpinnings of tumor cells and of organ microenvironments that promote metastatic outgrowth[4-11]. However, knowing the opposite could prove as useful, if not more, to prevent

or combat metastasis. That is, what constitutes an inhospitable microenvironment? The study of tissues where metastases rarely, if ever, emerge could ultimately inspire approaches to suppress metastasis throughout the body.

Here, I focus on tissue microenvironments that are inhospitable to disseminated tumor cells (**DTCs**). Taking a cue from Lyden and colleagues[6-7], I call these sites antimetastatic niches: tissues or tissue microenvironments that rarely succumb to metastatic colonization based ostensibly on features inherent to these sites. By definition, tumor cells disseminate to and may even persist within antimetastatic niches but cannot colonize them in a meaningful timeframe. Suppression of DTC outgrowth may occur in a variety of ways: (*a*) induction of DTC death via the proteinaceous and metabolic constituents within the niche; (*b*) avid recruitment of professional killer cells (e.g., macrophages or cytotoxic T cells) to rid the tissue of DTCs; (*c*) the induction of dormancy, a reversible growth-arrested state; or (*d*) the induction of senescence, a permanent exit from the cell cycle.

In this introduction, I survey the properties of four antimetastatic niches—skeletal muscle, spleen, thyroid, and yellow bone marrow—and emphasize the ongoing need for the identification of microenvironmental mechanisms by which these tissues suppress DTC colonization. The answers might inspire reimagined therapies that inhibit metastatic development and/or progression in both a systemic and enduring manner.

2. MECHANISMS BY WHICH DISSEMINATED TUMOR CELLS FIND A NEW HOME

The journey of a tumor cell to its second home (organ site) is not random. What are the factors that drive these deliberate patterns?

2.1. Ewing's Theory

Paget's original hypothesis placed the onus on the soil of the destination tissue[3]. But his hypothesis was upended nearly 40 years later when pathologist James Ewing[12] claimed that patterns of metastatic colonization by specific cancers could be explained simply by the anatomy of the local circulatory system (e.g., choriomas metastasize to lung; prostate

cancer and hypernephroma metastasize to bone marrow). He wrote that “the mechanism of the circulation will doubtless explain most of these peculiarities…[in the distribution of metastasis]…for there is as yet no evidence that any one parenchymatous organ is more adapted than others to the growth of embolic tumor cells”[12] (pp. 85–86). In other words, cancers preferentially metastasize to secondary sites that are easily accessible via the vasculature and downstream of blood flow. The importance of circulatory anatomy with respect to metastatic distribution in certain organs is beyond dispute. The anatomical route of vascular drainage from the primary tumor, vessel lumen diameter, blood flow and pressure, and the physical characteristics of the tumor cells all influence where tumor cells are likely to arrest as they transit through the vasculature[12-15] (**Figure 1.1**). In cases of carcinoma of the gastrointestinal tract, the preeminence of liver metastasis is due in large part to the hefty supply of tumor emboli in the portal venous blood[16-17]. Further, across

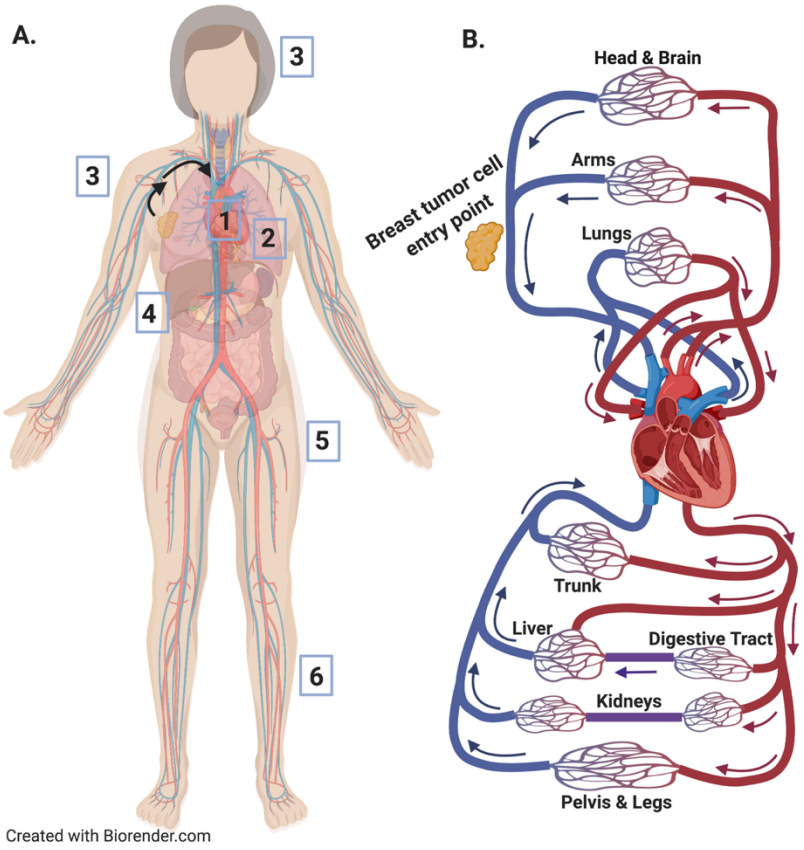

Figure 1.1 Vascular flow throughout the human body. Vascular routes enable tumor cells to traffic and lodge in all organs throughout the body. A) Breast tumor cells will enter the venous circulation and have the opportunity to travel systemically through the body via the arterial vasculature. As directed by arterial flow, breast tumor cell traffic should then occur in the order detailed numerically (#1 – 6). B) A close up of the venous (blue) and arterial (red) flow. The networks connecting the two are capillary beds.

cancers, the high frequency of metastatic tumors in the lungs may be attributed largely to the circumstance that the pulmonary capillary beds arrest emboli liberated from any part of the systemic venous blood stream[13,18].

Ewing's hemodynamic theory for metastatic colonization, though plausible, cannot be the sole explanation for metastatic seeding. For instance, hemodynamics alone cannot explain why metastases emerge often in organs distal to the initial organ encountered and downstream of the lung. Hemodynamics also cannot account for why metastases are not observed simply in the organs with the richest vascular supplies. A striking contradiction to Ewing's theory is skeletal muscle[3,19]. Although the muscles of the human body receive an enormous aggregate blood supply, blood-borne skeletal muscle metastases are very rare. The spleen, another richly vascular organ, is also among the least frequent sites of metastasis[3].

2.2. Paget's Theory

Despite such counterexamples, Ewing's hypothesis remained relatively unchallenged for 50 years. It wasn't until then that experiments were designed to pit Paget's and Ewing's hypotheses against one another. In one of the most convincing experiments, Hart & Fidler[4] sought to determine whether mechanical arrest of circulating emboli can explain patterns of metastasis, or whether the tissue microenvironment is dominant. When inoculated subcutaneously, B16-F10 melanomas metastasize to lung and ovary, but not kidney. What would happen once given equal opportunity to access all three sites? To address this question, the investigators grafted fragments of kidney, ovary, and lung under the skin or into the muscle of syngeneic mice and then intravenously injected B16-F10 cells labeled with [^{125}I]-5-iodo-2′-deoxyuridine (IdUrd). One day after inoculation, signal from radiolabeled cells was equivalent across sites. However, 3 weeks later, ≥70% of animals developed metastases in the grafted pulmonary or ovarian tissue, whereas only 4 of 28 animals developed tumors within transplanted kidney. Since renal grafts appeared to survive and vascularize as well as lung or ovarian grafts, the explanation for this selective pattern of tumor growth is more complex than simply granting equal access to a given organ.

Perhaps, though, vascular heterogeneity between organs (and not tissue microenvironments, per se) accounted for differences in tumor cell growth observed at ectopic sites. To address this possibility, Hart & Fidle[4] performed several experiments with parabiotically joined mice. No significant quantitative differences in radiolabeled tumor cell arrest were detected between graft bearer and control limbs, with the exception of the kidney implants where, at 24 h, more cells were held in the transplant-bearing limb than in the contralateral limb. Despite this, tumor growths did not develop in kidney implants. Instead, 4 weeks after tumor-free mice (guests) were joined parabiotically to tumor-bearing hosts, 6 of 15 (40%) guest mice had developed lung nodules[4]. This implies that there is indeed an organ specificity to metastasis.

Does the implanted lung tissue nonspecifically support growth of any injected tumor? A common denominator for the experiments above is the use of lung as a pro-metastatic tissue. To rule out the possibility that lung is a universally favorable site, Hart & Fidler used an M5076 granulosa cell tumor model. Here, the ovaries, liver, spleen, and kidneys—but not lung—are common sites of tumor growth. After intravenous delivery of M5076 tumor cells, only 1 of 10 animals developed M5076 tumors at the lung graft site, as compared with 7 of 10 animals receiving injection of the B16-F10 melanoma. However, 5 of 10 animals developed M5076 tumors at the site of ovary grafts, showing that the M5076 tumor line is capable of growth in ectopically maintained organs[4]. In sum, these experiments countered Ewing's theory and supported Paget's that there is a predilection for metastases to emerge in particular distant organs on the basis of both tumor cell properties and multiple host factors.

2.3. A Potential Marriage of the Two Theories

The conclusion of Hart & Fidler's study does not mean that Ewing's hypothesis remains without support. Indeed, the paradigm of the premetastatic niche[6] may unify Paget's and Ewing's theories. Pioneering experiments by Lyden and colleagues[5-8] demonstrated that highly metastatic tumor cells precondition distant sites to cultivate favorable soils prior to their arrival (**Figure 1.2**).

More recent evidence from Lyden's group[20] demonstrates that the premetastatic niche is effected by the following tumor-derived particles: Exosome-Small (**Exo-S**), Exosome-Large (**Exo-L**), and the exomere, a new nanoparticle that differs in size and content from all other reported nanoparticles. Each subtype of nanoparticle exhibits different organ biodistribution patterns, carries different cargo, and potentially readies the premetastatic niche through separate mechanisms. For example, Exo-L preferentially homes to lymph nodes, whereas exomeres and exosomes are internalized by hematopoietic organs, including the liver, spleen, and bone marrow. Interestingly, the higher uptake of exomeres by the liver and their enrichment in metabolism-associated protein cargo led the study authors to speculate that exomeres may specifically target the liver for metabolic reprogramming during tumor progression[20].

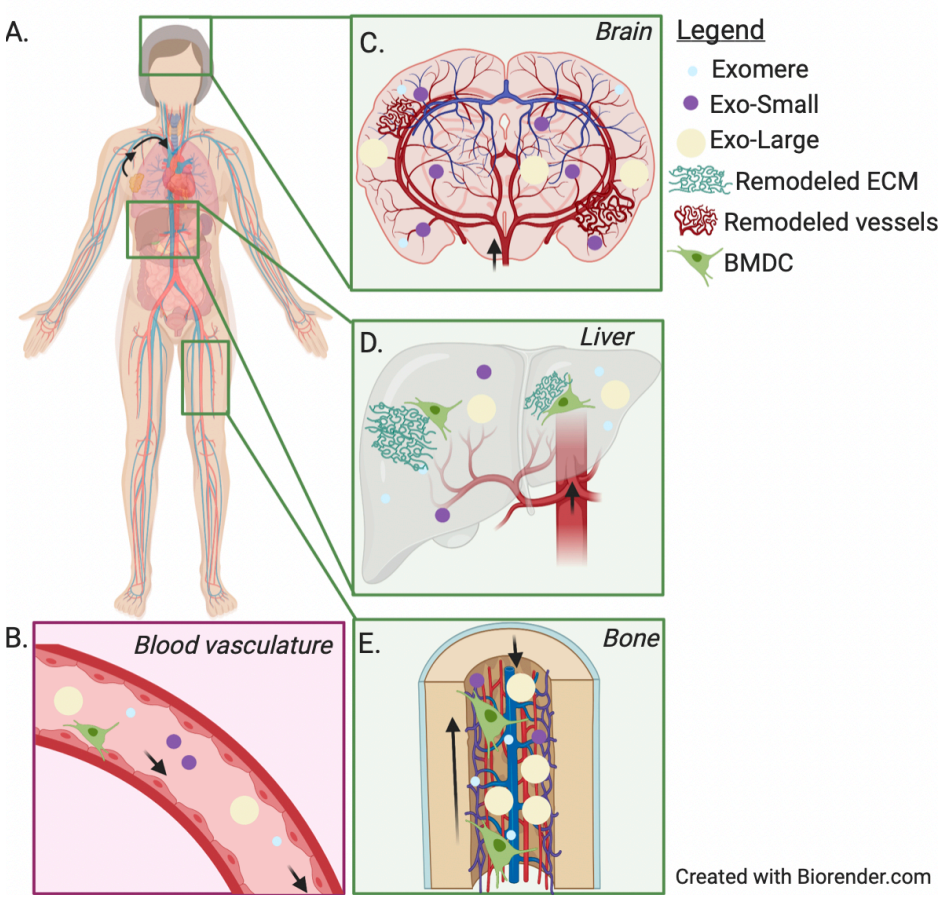

Figure 1.2. The concept of the premetastatic niche offers a union of Paget and Ewing's theories. Tumor-derived exosomes (Exo) and exomeres are found in transit through the vascular system (A,B) and in distant organs (C-E), readying the niche for tumor cell seeding through remodeling of vasculature and extracellular matrix (ECM) (C,D). Additionally, exosomes educate and mobilize non-tumor cells types such as bone marrow-derived cells (BMDCs) (E) to further the generation and maturation of the metastatic niche.

Tumor-derived exosomes play a leading role in drawing critical support cells into premetastatic organs. Peinado et al.[8] show that exosomal packaging of the receptor tyrosine kinase MET educates bone marrow–derived cells (**BMDCs**) into a provasculogenic phenotype and mobilizes them from the bone marrow. These myeloid cells then traffic to the premetastatic site, where they collaborate with local stromal and endothelial cells residing in the tissue parenchyma[21-22]. Together, BMDCs provide additional chemokines, growth factors, matrix-degrading enzymes, and adhesion molecules, thereby accelerating assembly of the metastatic site[23-24].

However, it is not only the cargoes of these nanoparticles that prepare the metastatic site. Elegant studies demonstrate that surface proteins of these nanoparticles also dictate the specific sites to which they transit. For example, exosomes expressing integrin αvβ5 specifically bind to Kupffer cells, mediating liver tropism, whereas exosomal integrin α6β4 and integrin α6β1 bind lung-resident fibroblasts and epithelial cells, governing lung tropism[5].

The ease with which these different particles transit through the blood are invariably linked to their size, bioelectrical properties, and the vascular route in which they traverse. Thus, the physical (and functional) diversity of nanoparticles secreted by tumor cells may help account for some of the blood flow–related differences in metastatic burden that are observed.

These foundational studies and others[25-28] unraveled the molecular constitution of fertile soil. But these studies have in effect addressed only half of Paget's hypothesis; inherent to Paget's theory is that certain soils are inhospitable to the seed of a tumor. What determines infertility of a given soil? Is it a lack of pro-metastatic factors? Or is it an abundant source of suppressive factors? In the sections below, we describe what is known about four inhospitable tissues and explore possible mechanisms that may drive their antimetastatic phenotype.

3. CLINICAL EVIDENCE FOR ANTIMETASTATIC NICHES

Clinical data spanning small case studies and metanalyses of autopsy series support the existence of both metastasis-prone and metastasis-resistant tissues. These data reveal an interesting paradox: Whereas certain tissues such as heart, spleen, kidney, intestine, and skeletal muscle collectively account for the majority of the arterial output of the heart, they are only sporadically colonized by DTCs[3,19,29]. Does this mean that these organs are somehow free of DTCs, or are these tissues abundant in niches that prevent metastatic outgrowth? Autopsy studies provide a clue.

Many studies have documented the metastatic patterns of various cancers in the clinical setting[29-33]. Fewer studies, however, provide quantitative analyses of such patterns arising from a broad range of cancers based primarily on postmortem tissue analyses. As an example, DiSibio & French[19] reviewed data from 3,827 autopsies performed between the years 1914 and 1943 on patients comprising 41 different primary cancers and 30 different metastatic sites. These findings provided a sensitive, quantitative baseline of metastatic patterns observed among the analyzed malignancies. Additionally, none of these patients included in the study received chemotherapy or radiation treatment. The findings, then, represent the unadulterated metastatic patterns of these cancers. Across all cancer types, local and regional lymph nodes were the most frequent metastatic targets (20.5% and 12.9%, respectively). Liver, lung, and bone were the next most common (11.1%, 10.7%, and 6.5%, respectively). The five least common metastatic sites across all primary cancers were stomach (0.6%), vagina (0.3%), prostate (0.3%), skeletal muscle (0.2%), and testes (0.1%).

The robustness with which breast cancer metastasized in this study is striking; it both represented a high proportion (11.3%) of all primary malignancies and contributed 23.6% of all metastases, the highest number among all cancer types analyzed. Despite the aggressiveness of this cancer, no patient with a breast cancer diagnosis presented with metastasis to skeletal muscle (0 of 432). The paucity of metastases to skeletal muscle demonstrates that certain tissues, seemingly against all odds, resist metastatic outgrowth.

An even closer look at metastasis-prone and metastasis-resistant tissues implies that there is more to an antimetastatic tissue than meets the eye. Advanced immunocytochemical and molecular techniques able to detect even single tumor cells have demonstrated that DTCs are frequently present long before clinical or histopathological metastasis[34]. Though the earliest examples of this come from bone marrow, a relatively accessible (and justifiable) site for biopsy, there is reason to believe that this is a systemic phenomenon. Elegant studies provide evidence that mouse mammary cancer cells migrate and disseminate from nonpalpable (early) lesions. Hosseini et al.[35] showed that 80% of metastases in BALB-NeuT mice, a Erb-B2 receptor tyrosine kinase 2 (**HER2$^+$**) mammary cancer model, were derived from early DTCs. Research by Harper et al.[36] used intravital imaging and organoid studies to support that HER2$^+$ mammary cancer cells invaded locally from early lesions, intravasated, and lodged in target organs like the lung. Several other studies have shown that this phenomenon is not HER2 specific; early dissemination is evident in mammary, pancreas, and melanoma cancer models and in patients[37-41].

If systemic dissemination happens early and often, then why do we not see even more metastases? Tumor cells may seed distant sites, but even if they survive, the dynamics of outgrowth vary considerably among cells, cancer types, and individual patients. In melanoma, breast, and prostate cancer, DTCs may enter into a quiescent state upon arrival at the secondary site only to awaken after years (or even decades) and form deadly metastases[42-45]. The findings that the earliest transformed cells are efficient disseminators emphasizes that cooperation from the microenvironment is required for metastatic colonization.

With the knowledge that colonization is not the guaranteed outcome of tumor cell dissemination, questions arise surrounding the induction of dormancy in DTCs and how this exit from the cell cycle is regulated by the surrounding microenvironment. And, clearly, this niche-based mechanism can be reversed or circumvented by DTCs in metastatic tissues over time[46].

How, then, can any tissue resist metastasis so consistently? What microenvironmental pressures are the early DTCs subjected to in antimetastatic tissues? Are there factors within distant sites that are sufficient to block the proliferation of DTCs long term? And, why do they never diminish? Mechanisms have been hypothesized, though many still require thorough exploration. Regardless, the fact remains that tissue environments like skeletal muscle, spleen, and thyroid seemingly have innate biological mechanisms that minimize the growth of DTCs. Below, we search for underlying commonalities between these sites that might negatively impact DTCs.

4. POTENTIAL ANTIMETASTATIC NICHES AND THEIR CONSTITUENTS

4.1. Skeletal Muscle

Skeletal muscle is the most striking example of an antimetastatic tissue[3,19,29]. It accounts for 40–50% of our body mass and is well vascularized. One could argue that it has more opportunities to harbor metastasis-initiating cells than any other organ. However, only 0.2% of malignant cases involve skeletal muscle metastases, making it the least likely site of metastasis shared by both sexes[19].

Nevertheless, a more thorough analysis of biospecimens detected microscopic lesions in skeletal muscle almost 100 times more frequently than reported clinically[32,33,47]. Though this may appear initially a stark contradiction, the disparity in the frequency of skeletal muscle metastases at clinical presentation versus upon exhaustive autopsy suggests that DTCs successfully reach skeletal muscle, survive, and persist there, but cannot colonize the tissue within a patient's lifetime. The molecular underpinnings of how skeletal muscle suppresses DTC outgrowth remain unknown.

Skeletal muscle is frequently invaded by tumors, e.g., the pectoral muscles by mammary cancer, and the muscles of the head and neck by oral and pharyngeal cancers[29]. However, blood-borne metastases are rare. In almost all cases of blood-borne muscle metastases that do occur, neoplasms are of rapid growing anaplastic character with numerous metastases in other tissues. Willis[29] conducted 500 necropsies and observed discrete metastases in skeletal muscles on only four occasions. In diSibio & French's[19] metanalysis,

only 16 skeletal muscle metastases were found in 3,827 cases. Why are these phenomena so infrequent?

The rarity of skeletal muscle metastases suggests that some aspect of the muscle environment prevents the progression of DTCs to metastatic lesions. The proposed mechanisms to date include anatomic barriers, mechanical activity, fusion of DTCs into existing myofibers, and tumor-suppressive secretory factors.

4.1.1. Anatomic barriers.

It was speculated that muscle vasculature exerts physiological or mechanical constraints that impede tumor cell extravasation into skeletal muscle[48,49], but there is no additional evidence to support this. On the contrary, both clinical data[29,32] and data from a study involving arterial injection of melanoma cells into mice[50] confirm that neoplastic cells cross vessel barriers within skeletal muscle.

4.1.2. Mechanical activity.

Studies[51,52] evaluating tumor cell survival in muscle showed greater survival in denervated skeletal muscle than in noncontracting muscle and the lowest survival rate in electrically stimulated muscle. This led the study authors to hypothesize that DTCs die rapidly within skeletal muscle because of its unique mechanical microenvironment. Three points of contention are that (*a*) these studies combined supraphysiological rates of skeletal muscle contraction with insensitive techniques to measure tumor cell burden, (*b*) DTCs survive and persist within skeletal muscle in autopsy-derived specimens[32], and (*c*) even normal stem cells (e.g., meso-angioblasts) transit to skeletal muscle via arterial vasculature and readily survive and propagate there[53,54].

4.1.3. Fusion of DTCs into existing myofibers.

Skeletal muscle myoblasts have the unique ability to form multinucleated structures with non-muscle cells (i.e., heterokaryons)[55]. Thus, the concept that DTCs could be shifted phenotypically by fusing with skeletal muscle myotubes is provocative. Using highly metastatic melanoma and lung carcinoma cells, Sassoon and colleagues[56] found that tumor

cells directly inoculated into skeletal muscle proliferated slowly. Further, the inoculated melanoma cells lost melanocyte features in part through downregulation of the lineage oncogene melanocyte inducing transcription factor (**MiTF**). Muscle-inoculated tumor cells phenotypically converted toward a myogenic program, even fusing with muscle fibers in certain instances. These observations resemble the pathology of invasion of an aggressive tumor into surrounding muscle. Willis[29] (pp. 284) described skeletal muscle invasion as occurring "…in two ways: (*a*) by invasion of the interstitial tissues and lymphatics between the muscle fibres, and (*b*) by invasion of the muscle fibres themselves and extension within the sarcolemmal sheaths.…The sarcolemma of the invaded fiber often persists as a distended investing sheath for the cylinder of growth which has destroyed the fiber substance." Thus, perhaps the appearance of fusion with muscle does not reflect tumor cell suppression but rather an aggressive/invasive cancer.

4.1.4. Adenosine and other undefined low-molecular-weight factors.

To date, the most advanced studies on the suppressive nature of skeletal muscle were conducted by Fishman and colleagues[57], who demonstrated that conditioned medium from muscle cells inhibits the growth of several different tumor cell types but promotes proliferation of normal cells—specifically those of hematopoietic lineages. Notably, intraperitoneal administration of skeletal muscle cell–conditioned medium suppressed tumor growth in mice. Through a series of biochemical studies, adenosine emerged as a factor capable of partially recapitulating the tumor suppressive effects of skeletal muscle cell–conditioned medium[58,59]. However, oral administration of adenosine itself was ineffective in halting tumor growth. Therefore, if skeletal muscle secretes a cocktail of suppressive factors, the precise composition remains a mystery.

4.1.5. Additional mechanisms.

Because none of these mechanisms fully accounts for the suppressive nature of skeletal muscle, we posit three additional factors that may contribute: stem cell niche factors, metabolic constraints, and composition of extracellular matrix (**ECM**).

4.1.5.1. Stem cell niche factors.

Satellite cells, the stem cells of skeletal muscle, are mitotically quiescent and enter the cell cycle in response to stress induced by weight bearing or by trauma such as injury[60]. Satellite cells are maintained by a niche[61]; their basal surface is enveloped within the basal lamina that coats the muscle fiber, whereas the apical surface juxtaposes the myofiber[62].

Upon division, the fate of the daughter cells is determined by their relative orientation within the satellite cell niche. In-plane or symmetric divisions result in both cells maintaining direct contact with the basal lamina and host myofiber, whereas asymmetric divisions result in an apical-basal orientation where one daughter cell is pushed toward the basal lamina and the other cell apically toward the host myofiber[63]. Those daughter cell(s) that remain in contact with both the myofiber and basal lamina reenter quiescence, repopulating the stem cell pool, whereas the daughter(s) that lose contact with basal lamina differentiate into a committed myogenic cell. Thus, contact with the satellite cell niche dictates cell-cycle fate of the cells that reside in it. DTCs in the skeletal muscle niche may respond to cell–cell contact signals in a similar fashion and, akin to satellite cells, become quiescent. Possible regulatory mechanisms include the following:

- **Notch.** Notch signaling is crucial for satellite cell homing, adhesion to the basal lamina-myofiber niche, and subsequent return to quiescence[64,65]. Initiated by ligation with Delta-like ligand (**DLL1**), Notch activation maintains a resident pool of myogenic progenitors by preventing their differentiation during muscle development[66,67]. While shed by the reserve pool of myogenic progenitors, DLL1 remains intact in differentiated myofibers. Two cells interacting via Notch–DLL1 signaling adopt different fates: sender (high ligand, low receptor) and receiver (low ligand, high receptor)[68]. This generates strongly biased signaling if a sender cell interacts with a receiver cell. It is possible that when DTCs traffic to the skeletal muscle, DTCs become receivers for the myofiber's DLL1 adhesion and quiescence signals.

Four Notch receptors (Notch1–4) and five Notch ligands (Delta-like 1, 3, and 4 and Jagged 1 and 2) have been identified in mammals[68]. Though Notch-DLL1 signaling is a major mechanism of satellite cell quiescence, enhanced Notch signaling is thought to be a key factor in the stem-like proliferation of cancer cells, thereby facilitating disease progression[69-71]. This begs questions: Are all Notch receptors and ligands created equal? Does the tissue source of the ligand matter? Could a mechanism that is pro-metastatic in lung be antimetastatic in skeletal muscle? Examples do exist of increased Notch expression driving tumor cell suppression. O'Neill et al.[72] demonstrated that activation of Notch2 within the human breast cancer cell line MDA-MB-231 inhibits xenograft outgrowth via G1 cell cycle inhibition. Similarly, Sriuranpong et al.[73] showed that Notch2 signaling leads to growth arrest of small cell lung cancer cells. These data and more imply that the microenvironmental and cellular context of Notch signaling is critical for tumorigenic outcome.

- **Cadherins.** Sustained adhesion to the myofiber is a key component of satellite cell regulation and fate choice. Goel et al.[74] identified M- and N-cadherin signaling between satellite cells and the apically oriented myofiber as a mechanism that regulates the transition from quiescence to activation. Active adhesion via M- and N-cadherins maintains the quiescent satellite cell state by providing structural integrity, mechanosensation, cell polarity, and juxtacrine signaling. Goel et al. argue that signals generated by cadherin-based adherens junctions are abrogated as part of the initial activation process. This, in turn, promotes an orderly entry into the proliferative state through the posttranscriptional production of myogenic factors myogenic differentiation 1 (**MYOD**) and myogenic factor 5 (**MYF5**) and liberation of β-catenin[74]. Localization of β-catenin in the nucleus provides one mechanism whereby the break in quiescence can be linked directly to the transition to activation.

A wealth of data suggest that metastatic cells transition from an epithelial to a mesenchymal phenotype to disseminate to secondary sites and, in doing so, commonly express N-cadherin[75]. Since cadherin ligation is critical for skeletal muscle to recognize and regulate its

progenitors, the expression of N-cadherin on mesenchymal-like DTCs could actually enable quiescence induction.

4.1.5.2. Metabolic constraints.

Skeletal muscle is unique in its metabolic plasticity, capable of pronounced energy adaptations in response to contractile activity[76]. During contraction, skeletal muscle myofibers deactivate reactive oxygen species (**ROS**) produced as a result of a concomitant shift from glycolysis to mitochondrial respiration [e.g., via oxidative phosphorylation and β-oxidation of fatty acids[76]]. Whereas moderate changes in the cellular reduction-oxidation (redox) state primarily exert regulatory properties, excessive ROS generation without adequate compensation results in damaging oxidative stress. Therefore, DTCs that reside in skeletal muscle may be incapable of meeting the cellular demands necessary to counterbalance the extreme levels of ROS present within the skeletal muscle microenvironment. Microdialysis studies reveal that the interstitial concentration of hydrogen peroxide (**H_2O_2**) within skeletal muscle ranges from 10 to 15 μM[77,78]. Non-muscle cells have been shown to respond to concentrations of H_2O_2 of this order (15 μM) with adaptive changes in redox-sensitive gene expression[79], whereas muscle fibers activate changes in redox-sensitive gene expression when exposed to much higher levels of extracellular H_2O_2 (25–100 μM)[80-82]. These data suggest that muscle fibers are able to generate higher levels of H_2O_2 than other tissues and have a higher tolerance for ROS. DTCs exposed to the muscle environment may respond to this increased H_2O_2 state by entering quiescence or senescence (if they survive at all).

In line with this hypothesis, recent evidence supports the notion that oxidative stress generally suppresses metastasis. Piskounova et al.[83] demonstrated that successfully metastasizing melanomas underwent reversible metabolic changes during metastasis that increased their capacity to withstand oxidative stress, including increased dependence on NADPH-generating enzymes in the folate pathway. Moreover, supplementation with antioxidants (to reduce oxidative stress) promoted distant melanoma metastasis in NSG mice. Similarly, Le Gal et al.[84] found that the administration of *N*-acetylcysteine, a synthetic glutathione precursor, increased lymph node metastases in a mouse model of malignant

melanoma but had no impact on the number and size of primary tumors. These results demonstrate that antioxidants and the glutathione system promote progression of melanoma. Research from the Tavazoie lab[85] extended this to colon cancer. Specifically, the research showed that liver and red blood cell (**RBC**) pyruvate kinase (**PKLR**) promotes colon cancer cell colonization of the liver, despite leaving proliferation unchanged in tissue culture. PKLR, they determined, was required to maintain levels of glutathione and support cancer cell survival, especially under conditions such as hypoxia and high cell density. Pharmacological targeting of this metabolic pathway reduced colonization in a patient-derived xenograft model.

In sum, these studies support a critical role for oxidative balance at secondary sites. The oxidative environment of skeletal muscle may present DTCs with an insurmountable challenge.

4.1.5.3. Extracellular matrix–mediated suppression.

Remodeling of the ECM is a critical step in tumorigenesis. Increased deposition of fibronectin, proteoglycans, and collagens type I and III promote tumor progression by destabilizing cell polarity and cell–cell adhesion and augmenting growth factor signaling via integrin clustering[86-91]. For example, multiple groups demonstrated that type I collagen enrichment at the metastatic site can trigger the dormant-to-proliferative switch through integrin β1 signaling and cytoskeletal reorganization in dormant tumor cells[89,92].

However, as long hypothesized, ECM contains elements both antagonistic and agonistic to the metastatic phenotype[93]. Therefore, the composition of skeletal muscle ECM may provide insight into its antimetastatic nature. Precise contact between epithelial cells and their underlying basement membrane, a specialized form of ECM, is crucial to the maintenance of tissue architecture and function[86].

Basement membrane, comprised mainly of laminins and type IV collagen, represents a large fraction of the total ECM of muscle[94]. Satellite cells localize between the basal lamina, a sublayer of the basement membrane, and the apical sarcolemma of myofibers, binding to

laminin and collagen type IV through integrin receptors[61]. Interaction with the basement membrane induces and maintains progenitor cell quiescence. If removed from this microenvironment, satellite cells quickly enter the cell cycle and lose their myogenic properties[62]. Thus, it is conceivable that the abundance of laminin in skeletal muscle steers resident DTCs into quiescence.

Laminin-111, an essential component of the basement membrane of many tissues, is heavily implicated in the regulation of tumor cell survival and quiescence[46, 86, 95-97]. Conversely, disruption of existing laminin scaffolds yields significant consequences; research by Albrengues et al.[98] revealed dormant tumor cells may awaken after the remodeling of laminin effected by neutrophil extracellular traps (**NETs**). NETs are DNA scaffolds with associated cytotoxic enzymes and proteases that are released by neutrophils into the extracellular space. NETs facilitate laminin cleavage via the concentration of neutrophil elastase and matrix metalloproteinase 9. This remodeling triggered integrin α3β1 activation and downstream protein tyrosine kinase 2 (**FAK**)/mitogen-activated protein kinase 1 (**ERK**)/myosin light chain kinase (**MLCK**)/Yes1 associated transcriptional regulator (**YAP**) signaling to promote the proliferation of dormant tumor cells.

We know that tumor progression, including metastatic colonization, is accompanied by disruption and proteolysis of the basement membrane and an increase in the deposition of the stromal ECM[89, 90, 92]. Thus, the composition of the ECM likely contributes not only to the antimetastatic bias of skeletal muscle but also to the inherent biases of all tissues.

Through case studies and autopsy analyses, it is clear that skeletal muscle harbors DTCs and micrometastases but prevents their progression to full-blown metastasis. Mechanisms by which skeletal muscle suppresses DTC growth have been speculated. To date, many microenvironmental components such as secretory molecules, biomechanics, and stromal interactions are implicated in driving this growth-restrictive phenotype. With the identification of putative skeletal-muscle-derived metastasis suppressors, we can then begin to functionally evaluate their utility. If one was to eliminate this element or elements within skeletal muscle, would metastases arise? Conversely, could ectopic expression of these

muscle-derived elements lessen or prevent metastases in organ sites where metastases commonly arise? For example, one might envision a scenario where the ectopic expression of a muscle-derived tumor suppressor is delivered in a spatially and temporally controlled manner to metastatic sites like the lung, thereby fashioning a suppressive niche. Alternatively, antimetastatic components might be supplied directly and/or systemically to educate the local environment, akin to the premetastatic niche, to prevent the colonization of DTCs. These experiments would provide proof of concept that antimetastatic factors exist and can be harnessed ectopically for therapeutic purposes.

4.2. Spleen

Spleen metastases of epithelial tumors are regarded as rare, with metastatic growths accounting for 1.1–4% of all fatal cases[3, 99-102]. Warren & Davis[103] discovered splenic metastases in 46 of 1,140 cases (4%), and in Willis's[29] 500 necropsies, he found discrete splenic metastases in only 14 (3%).

Is the spleen an antimetastatic niche? Playing devil's advocate, one may argue that splenic metastasis isn't rare at all. The average weights of liver, kidney, and spleen are 1,500, 250, and 125 grams, with a ratio of 12:2:1. If we look at Willis's[29] necropsy report, metastases to the three organs were present in 36%, 7.6%, and 3.0% of cases, respectively. These percentages mirror the weight ratios; thus, pound for pound, the spleen may be just as prone to metastasis as liver or kidney. Nevertheless, the supposed discrepancy between the abundant splenic blood supply and the low incidence of blood-borne embolic metastases in this tissue has led many to suppose that the spleen may possess anti-cancerous functions.

Hypotheses put forth in the past include that (*a*) the sharp angle made by the splenic artery makes it difficult for tumor emboli to enter the spleen[30], (*b*) the rhythmic contractile nature of the spleen squeezes out tumor emboli and prevents them from lodging[30, 104], and (*c*) the absence of afferent lymphatics prevents lymphatic dissemination to the spleen[103, 105]. However, the spleen expresses stromal cell–derived factor 1 (**SDF1/CXCL12**), the ligand for C-X-C motif chemokine receptor-4 (**CXCR4**)[99]. This lymphocyte homing signal also serves

as a strong homing signal for tumor cells in preferential sites of metastases like the bone marrow, lung, and lymph nodes[106]. This suggests that trafficking to the spleen may not be a barrier to metastasis after all.

It has also been proposed that (*d*) the spleen encourages phagocytosis and destruction via reticuloendothelial elements[107]. It must not be forgotten that other organs that possess abundant reticuloendothelium, such as the liver and the lymph node, are actually frequent sites of metastasis. Thus, the phagocytic cells that reside in the spleen may be only part of the mechanism by which the spleen resists metastatic outgrowth. Another mechanism hypothesized is that the spleen secretes diffusible cytotoxic substances such as cytolysins[29] and/or growth inhibitors like angiostatin[108, 109]. Last, the rich arterial oxygenation and sparse carbohydrate content of the spleen may provide an unfavorable environment for most solid tumor cells[29].

Interestingly, the arguably most obvious explanations for the antimetastatic nature of the spleen are not as commonly cited. Such hypotheses include:

1. The spleen is the largest organ of the lymphatic system, controlling circulation of the immune system. It contains two main regions of tissue called white pulp and red pulp. The white pulp mostly consists of T and B lymphocytes. In fact, approximately one-quarter of our lymphocytes are stored in the spleen at any one time. Monitoring of the spleen by the abundance of immune cells within it may explain the resistance to implantation and/or growth of DTCs. However, if this were the case, why wouldn't this apply to hematologic malignancies? Whereas both primary and metastatic malignancies to the spleen are uncommon, most hematological malignancies involve the spleen[110]. Do hematopoietic-derived cancers possess some inherent advantage that enables them to thrive in immune-rich niches?

2. The primary function of the spleen is to filter blood. It recognizes and removes old, malformed, or damaged RBCs. Splenic macrophages phagocytose senescent RBCs, which results in the degradation of heme and liberation of iron. Iron is

converted into ferritin or bilirubin and returned to the circulation. This focus for RBC breakdown may be central to DTC suppression. Free (nonprotein bound) heme is an abundant source of redox-active iron that can participate in the Fenton reaction to produce toxic free hydroxyl radicals[111, 112]. Hydroxyl radicals catalyze the oxidation and aggregation of protein, catalyze the formation of cytotoxic lipid peroxide, and damage DNA through oxidative stress. Due to its lipophilic properties, heme iron impairs lipid bilayers in organelles such as mitochondria and nuclei[113]. These properties of free heme can provoke a variety of cell types to under-go ferroptosis, a cell death program resulting from the accumulation of iron-dependent lipid modifications. DTCs residing in the spleen may therefore be exposed to unbound heme and/or iron, subjected to harmful oxidation, and driven to ferroptose.

While the above explanations are enticing, specific mechanisms driving the low frequency of metastases in spleen remain unknown and ripe for study.

4.3. Thyroid

Metastases to the thyroid gland occur in 1.4–3% of malignant solid tumors[114–117]. Given the extensive blood supply to the gland [(4–6 mL/(min·g)], the low incidence of metastases to the thyroid is surprising. However, postmortem examinations suggest that as many as 24% of patients who die of nonthyroid malignancies have small metastatic nodules and/or micrometastases within the thyroid[114, 118]. These data imply that a scenario akin to that of skeletal muscle may exist: Tumor cells may disseminate to and survive within the thyroid gland, but the thyroid microenvironment suppresses their growth, thus preventing clinical detection.

It is likely that specific mechanisms innate to the healthy thyroid gland create an environment inconducive to unchecked tumor cell growth. The association of metastatic lesions within areas of abnormal thyroid tissue is very striking, suggesting that the thyroid is far more resilient at homeostasis. Willis[29] observed that of 21 cases of thyroid metastases, 9 were accompanied by pronounced pathological changes like fibrosis, nodulation, and cyst

formation. In 7 additional cases, metastases were situated directly within adenomatoid deposits (benign, solid tumor masses of mesothelial origin) in the thyroid.

What, then, are the factors within a healthy thyroid that suppress metastatic outgrowth? Willis[29] ascribed the healthy thyroid's resistance to metastasis to its rich oxygenation and low concentration of carbohydrates, a combination that is typically unsuitable for tumor growth. He also remarked that the unique chemical composition of the thyroid, mainly its high iodine content, may play a part. Thus, retrograde changes that diminish arterial vascularity and the quantity or quality of parenchymatous elements of the tissue inevitably alter the metabolic characters that make a normal thyroid unfavorable to metastasis. We expand upon these hypotheses below:

1. A healthy adult body contains 15–20 mg of iodine, 70–80% of which is stored in the thyroid gland and regulates its function[119]. Iodine is a highly oxidizing element and, in isolation, has the power to induce extreme oxidative stress in cells[120–122]. Under basal conditions, iodine is processed by thyroid epithelial cells, producing moderate amounts of ROS that are physiologically required for thyroid hormone synthesis. ROS levels are continuously abated by either hormone synthesis or endogenous antioxidant systems. It has been proposed that iodine-induced toxicity in iodine-deficient thyrocytes occurs when endogenous antioxidant systems are overwhelmed by excess ROS, thereby leading to cellular destruction that in turn triggers inflammation[121]. Contempré et al.[123, 124] showed that combined iodine and selenium deficiencies make thyrocytes more sensitive to iodine and/or thiocyanate overloads because of altered antioxidant defenses. Poncin et al.[121] showed that iodide-treated hyperplastic thyrocytes were severely injured, as shown by the increased number of necrotic or apoptotic cells, presence of cellular debris, and massive inflammatory reaction. Tumor cells that have disseminated to this environment, which have no inherent affinity for iodine, may face fates similar to the iodine-deficient cells described above. The environment is too rich in oxidizing agents and oxidant products, and thus these DTCs are ill prepared to survive.

2. Immunosurveillance is a key mechanism of surveilling micrometastases and preventing metastatic outgrowth[125]. The thyroid gland produces and secretes three hormones vital to regulating the biochemical activity of most of the tissues of the body: triiodothyronine (**T3**), thyroxine (**T4**), and calcitonin[126, 127]. These thyroid hormones exert responses in various immune cells, in turn affecting many inflammation-related processes (e.g., chemotaxis, phagocytosis, ROS generation, and cytokine production)[128–131]. For example, high concentrations of T3 were linked with an increase in the amount of complement proteins, the number and phagocytic activity of monocytes, absolute counts of natural killer T cells, and the maturation of murine dendritic cells[132]. T3 was also associated with a lower incidence of early lymphocyte apoptosis, indicating that this thyroid hormone may facilitate maintenance of the lymphocyte population. T4 uniquely stimulated higher neutrophil counts and positively correlated with the percentage of total memory T, memory T helper, and memory cytotoxic T lymphocytes[133]. Taken together, these results suggest that higher concentrations of thyroid hormones could enhance innate and adaptive immunity via maintenance of lymphocyte subsets and increased responsiveness to immune stimuli. Thus, it is possible that the continuous generation and concentration of thyroid hormones stimulates hyperactive immunity that rids the thyroid of proliferating tumor cells.

4.4. Bone Marrow: Pro- or Antimetastatic Site?

Bone is one of the most preferential target sites for cancer metastases, particularly for primary tumors of the prostate, breast, and thyroid[3, 19, 134]. However, for bone metastases to occur, bone marrow must be seeded and eventually colonized by DTCs, which in turn spread to the firm bone matrix. Thus, interactions between DTCs and bone marrow cells are critical for establishment and development of bone metastases.

Conventional bone marrow biopsies indicate that approximately 30.6% of early stage breast cancer patients already have DTCs in their bone marrow at the time of primary tumor resection[135]. Approximately one-fourth of these patients go on to have metastases, and of this cohort, 80% progress within the first four years[135]. However, the occasional

incompatibility between seed and soil is clearly demonstrated by the inconsistency of metastasis formation throughout the skeleton. The axial skeleton represents a preferential target, whereas metastases rarely develop within the appendicular skeleton (e.g., hands and feet). If bone marrow is bone marrow, then how can discrepancies in metastatic colonization exist?

Bone marrow is found in the central cavities of axial and long bones and is one of the largest body organs, accounting for up to 4–5% of the total body weight in humans[136]. It is composed of a mixture of hematopoietic tissue islands and adipocytes, all surrounded by vascular sinuses. It is the major hematopoietic organ and a primary lymphoid tissue. Anatomically, breast cancer cells frequently metastasize to axial bones like the spine, ribs, girdles, and bony pelvis[137]. We offer three explanations for this pattern.

4.4.1. Bone marrow heterogeneity.

Bone marrow is not situated to universally accept metastasis. Again, Willis[29] (p. 240) noticed this, writing: “A notable feature of metastatic growths in bone is their almost inevitable situation in red bone marrow. In several cases in which widespread skeletal involvement was present I have examined the yellow marrow in the lower parts of the femur and humerus and in the tibia, fibula and tarsal bones, but I have not yet seen a metastatic growth situated in yellow marrow.” He asserted that in heathy adults, metastatic growths occurred only in the red marrow of the upper third of the humerus and femur, as the middle and lower thirds of these bones contain only fatty marrow.

Within bone marrow, adipocyte-poor and adipocyte-rich niches, called red and yellow marrow, respectively, are commonly described[136, 138]. Red bone marrow, named for its richness in hemoglobin and erythrocytes, is composed of both hematopoietic cells and adipocytes. It is typically composed of 40–60% lipids, 30–40% water, and 10–20% protein[136]. Red bone marrow is responsible for body blood cell production and has a rich vasculature containing a vast network of sinusoids that fuel cellular trafficking. Yellow bone marrow, named after the abundant carotenoid bodies in its adipocytes, is composed primarily of adipocytes, with a composition of 80% fat, 15% water, and 5% protein[136].

Yellow bone marrow is encountered primarily in the appendicular skeleton and is thought to negatively regulate hematopoiesis[139]. The mature or adult pattern of marrow is achieved with yellow marrow predominating throughout the appendicular skeleton, except for the proximal metaphyses of the femur and humerus. This is in contrast to the axial skeleton, including the spine, ribs, sternum, skull, and pelvis, which serves as a repository of red marrow throughout life. Here, yellow-to-red marrow conversion occurs much slower and to a lesser extent than in the appendicular skeleton. Does the abundance of yellow marrow explain why we don't see metastases in fingers and toes?

Cahu et al.[140] sought to understand if different bone marrow sites could differentially modulate the propagation of T cell acute lymphoblastic leukemia (**T-ALL**). They observed that mouse and human T-ALL develop slowly in the bone marrow of tail vertebrae, a site comprised entirely of adipocytes, compared with faster T-ALL development in the bone marrow of the thorax vertebrae, an adipocyte-poor (hematopoiesis-rich) niche. T-ALL cells infiltrated all bone marrow sites, but T-ALL expansion was strikingly delayed in the adipocyte-rich (hematopoiesis-poor) tail bone marrow compared with the other studied bone marrow sites, irrespective of the human or mouse T-ALL model. Taking a closer look into the cell cycle, Cahu et al. noted that the thorax-derived cells were actively proliferating, whereas tail-derived cells were more frequently in the G_0 state of the cell cycle. Further, microarrays highlighted an increase in apoptotic pathways in the tail-derived niche. Taken together, these data show that bone marrow niches can and do influence proliferation of leukemic cells.

Most adipocytes exist in discrete depots throughout the body, notably in well-defined white and brown adipose tissues[136, 138, 141]. However, adipocytes also reside within specialized niches, of which the most abundant is within bone marrow. It is important to note that bone marrow adipose tissue (**MAT**) is distinct from adipocytes in other depots, such as the white adipose tissue (**WAT**) found subcutaneously or the brown adipose tissue located in the neck. MAT shares many properties in common with WAT, but the distinct functions of MAT are reflected by its development, regulation, protein secretion, and lipid composition.

Very little is known about the full spectrum of marrow adipocyte function, though one could imagine that these tissue-specific adipocytes and the composition of red versus yellow marrow may underlie patterns of skeletal metastasis (in solid tumors). A 1976 study by Tavassoli[142] suggested that characteristics of red marrow adipocytes may differ from those of yellow marrow adipocytes. Recent research has confirmed that there are, in fact, region-specific differences in development, regulation, adipocyte size, lipid composition, and gene expression of marrow adipocytes[141]. Specifically, bone marrow adipocytes have been subdivided into two distinct groups: regulated MAT (**rMAT**) and constitutive MAT (**cMAT**)[138, 141]. rMAT are single adipocytes interspersed with active hematopoiesis, whereas cMAT has low hematopoiesis, contains larger adipocytes, and remains preserved upon systemic challenges. Scheller et al.[141] found that MAT forms in two distinct temporal waves that are spatially separated in mice and correspond histologically to rMAT in red marrow and cMAT in yellow marrow. While the microenvironment likely plays a major role in these site-specific responses, lipidomics and gene expression data have identified cell autonomous differences between the rMAT and the cMAT adipocytes that might also contribute to their distinct behaviors.

As others move forward with characterizing tumor cell-adipocyte interactions, it may be important to consider genetic and tissue-specific distinctions of bone marrow adipocytes. Do rMAT and cMAT contribute to the differential influence of red versus yellow marrow on DTC outgrowth? How? Identifying whether simply the absence of a hematopoietic niche or the presence of inhibitory and/or immunomodulatory adipokines underlies the metastasis suppressive capacity of yellow marrow would go a long way toward characterizing this antimetastatic niche.

4.4.2. Vascular heterogeneity.

The blood vasculature serves as the cellular highway for blood cells, leukocytes, and other cell types to traffic throughout the body. An easy explanation for the distribution of metastases across the skeleton could be inherent differences in vascular density and distance from the primary tumor between, e.g., the iliac crest and metatarsals. The more

distal the tissue, perhaps, the lesser chance that a tumor cell would arrest in its vascular bed.

A more convincing argument, however, is that the bone marrow vasculature itself is not homogenous. It includes arteries that penetrate compact bone at regular intervals, arborizing into capillaries that converge into a central sinus[143]. Molecular and structural differences distinguish arteries and distal arterioles in bone from sinusoidal capillaries. Sinusoidal capillaries form highly branched and irregular networks and are found primarily between hematopoietic cells within the marrow cavity[144]. Arteries contain comparably few side branches and preferentially enter long bone through the femoral or tibial head. Recent evidence from Itkin et al.[145] suggests that the specific subset of endothelial blood vessel dictates the phenotype of its local niche. Itkin et al. demonstrated that, relative to arteries, sinusoidal blood vessels display higher permeability and dramatically lower blood flow and shear rates. A functional consequence of high permeability of bone marrow sinusoids is that exposure to blood plasma increases bone marrow hemopoietic stem cell (**HSC**) ROS levels, promoting their mobilization while compromising their long-term repopulation and survival potential. Additionally, bone marrow oxygen tension is highest near arterial blood vessels, skewing arteries to the glycolytic pathway to avoid excessive ROS production. The spatial distribution of arteries and arteriole-capillary connections within the bone marrow determine regional differences in oxygenation, metabolic activity, HSC cell cycle status, and even HSC fate[145]. This heterogeneity may also underlie the patterns of metastases (or lack thereof) within specific bone marrow and across bone marrow sites within the body.

4.4.3. Evolution of the perivascular niche.

Another explanation for the disparities in skeletal metastasis patterns may be evolution of the perivascular niche. The perivascular niche refers to the immediate environment surrounding the vasculature, including the blood endothelial cells, pericytes, and deposited basement membrane. Growth-arrested DTCs persist on or very close to bone marrow microvasculature, and re-creating this niche in culture revealed that stable microvascular endothelium induces and sustains breast tumor cell quiescence[46,146]. Months or years later,

though, the quiescent cancer cells may grow into overt metastases. What causes the bone marrow to loosen its hold? And does this fail to occur in yellow marrow?

Bone marrow, as the primary site of hematopoiesis, needs to self-renew and self-amplify. As this vascular niche evolves (e.g., revascularizes) to meet the demands of the body, so too might the DTCs within the niche[46,147]. One mechanism of tumor cell emergence may be through sprouting endothelium and the secretion of pro-tumorigenic factors such as TGF-β1 and periostin[46]. Additional factors that influence the awakening of these dormant DTCs remain unclear, but a common denominator across studies involves loss of tissue homeostasis[92,148]. Because hematopoiesis occurs more frequently in the axial skeleton as compared to the appendicular regions, it is conceivable that the higher rates of metastases in the former may be related to the increased trafficking and constant tweaking of tissue homeostasis required to meet this demand.

Thus, while bone marrow is a common site for metastasis, when we look closer, one notices clear disparities across different bones in the human body. The composition of bone marrow differs from bone to bone and evolves throughout a lifetime. This likely plays a major (yet under-researched) role in directing the pattern of metastases observed clinically.

5. SUMMARY

Paget's seed and soil hypothesis introduced the concept that a permissive microenvironment is required for cancer cell colonization and metastasis formation. Now we are able to appreciate that this axiom relates also to the microenvironments of metastasis-free tissues. Understanding mechanisms by which antimetastatic microenvironments suppress tumor cell growth may inspire researchers to effect changes in metastasis-prone tissues that convert them to suppressive sites.

Above, we have described the discrepancies that exist in clinical presentation of solid tumors, the discovery of micrometastases and metastases in necropsy studies, and the biology that is likely somewhere between. We have surveyed three tissues (skeletal muscle,

spleen, and thyroid) long recognized as infrequent metastasis sites and highlighted that even within common metastatic sites, hot and cold spots invariably occur. For each of these tissues, we have examined the proposed mechanisms of suppression (**Figure 1.3**), ranging from vascular flow to immune composition, from secreted factors to incompatible metabolism. From this, one common theme emerges: redox homeostasis. Do antimetastatic niches cause constant, unchecked oxidative stress, whether via H_2O_2, iron, or iodine? Do more permissive tissues fail to induce or sustain this level of stress? And could this potentially be leveraged or transferred to other tissues without affecting their basic and critical physiologic functions? This all remains to be seen.

While we await answers, metastases continue to cause the vast majority of all cancer-related deaths. With a lack of breakthrough therapies on the horizon, perhaps the biochemical and physical definition of antimetastatic niches will provide the change in perspective necessary to fuel such needed advances.

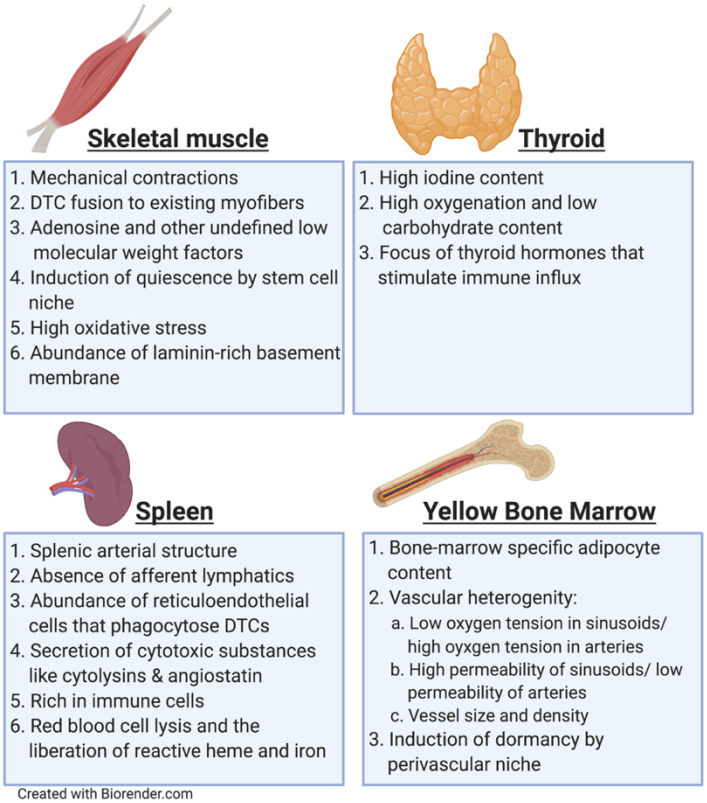

Figure 1.3. Summary of anti-metastatic tissues and possible mechanisms of microenvironmental tumor cell suppression.

Chapter 1 References

1. Poste G, Fidler IJ. 1980. The pathogenesis of cancer metastasis. *Nature* 283:139–46

2. Fidler IJ. 2003. The pathogenesis of cancer metastasis: The “seed and soil” hypothesis revisited. *Nat. Rev. Cancer* 3:1–6

3. Paget S. 1889. The distribution of secondary growths in cancer of the breast. *Lancet* 133(3421):571–3

4. Hart IR, Fidler IJ. 1980. Role of organ selectivity in the determination of metastatic patterns of b16 melanoma. Cancer Res. 40(7):2281–7

5. Hoshino A, Costa-Silva B, Shen TL, Rodrigues G, Hashimoto A, et al. 2015. Tumour exosome integrins determine organotropic metastasis. *Nature* 527(7578):329–35

6. Kaplan RN, Riba RD, Zacharoulis S, Bramley AH, Vincent L, et al. 2005. VEGFR1-positive haematopoietic bone marrow progenitors initiate the pre-metastatic niche. *Nature* 438(7069):820–7

7. Costa-Silva B, Aiello NM, Ocean AJ, Singh S, Zhang H, et al. 2015. Pancreatic cancer exosomes initiate pre-metastatic niche formation in the liver. *Nat. Cell Biol.* 17(6):816–26

8. Peinado H, Alečković M, Lavotshkin S, Matei I, Costa-Silva B, et al. 2012. Melanoma exosomes educate bone marrow progenitor cells toward a pro-metastatic phenotype through MET. *Nat. Med.* 18(6):883–91

9. Kang Y, Siegel PM, Shu W, Drobnjak M, Kakonen SM, et al. 2003. A multigenic program mediating breast cancer metastasis to bone. *Cancer Cell* 3(6):537–49

10. Bos PD, Zhang XHF, Nadal C, Shu W, Gomis RR, et al. 2009. Genes that mediate breast cancer metastasis to the brain. *Nature* 459(7249):1005–9

11. Minn AJ, Gupta GP, Siegel PM, Bos PD, Shu W, et al. 2005. Genes that mediate breast cancer metastasis to lung. *Nature* 436(7050):518–24

12. Ewing J. 1928. *Neoplastic Diseases: A Treatise on Tumours*. Vol. 16, British Journal of Surgery (Philadelphia and London). 76–88 pp.

13. Coman DR, DeLong RP. 1951. The role of the vertebral venous system in the metastasis of cancer to the spinal column: experiments with tumor-cell suspensions in rats and rabbits. *Cancer* 4(3):610–8

14. Weiss L, Bronk J, Pickren JW, Lane WW. 1981. Metastatic patterns and target organ arterial blood flow. *Invasion Metastasis* 1(2):126–35

15. Follain G, Osmani N, Azevedo AS, Allio G, Mercier L, et al. 2018. Hemodynamic Forces

Tune the Arrest, Adhesion, and Extravasation of Circulating Tumor Cells. *Dev. Cell* 45(1):33–52.e12
16. Riihimäki M, Hemminki A, Sundquist K, Sundquist J, Hemminki K. 2016. Metastatic spread in patients with gastric cancer. *Oncotarget* 7(32):52307–16
17. Weiss L, Grundmann E, Torhorst J, Hartveit F, Moberg I, et al. 1986. Haematogenous metastastic patterns in colonic carcinoma: An analysis of 1541 necropsies. *J. Pathol.* 150(3):195–203
18. Zeidman I, Buss J. 1952. Transpulmonary Passage of Tumor Cell Emboli. *Cancer Res*. 12:731–3
19. Disibio G, French SW. 2008. Metastatic Patterns of Cancers Results From a Large Autopsy Study. *Arch. Pathol. Lab. Med.* 132:931–9
20. Zhang H, Freitas D, Kim HS, Fabijanic K, Li Z, et al. 2018. Identification of distinct nanoparticles and subsets of extracellular vesicles by asymmetric flow field-flow fractionation. *Nat. Cell Biol.* 20(3):332–43
21. Wculek SK, Malanchi I. 2015. Neutrophils support lung colonization of metastasis-initiating breast cancer cells. *Nature* 528(7582):413–7
22. Duda DG, Duyverman AMMJ, Kohno M, Snuderl M, Steller EJA, et al. 2010. Malignant cells facilitate lung metastasis by bringing their own soil. *PNAS* 107(50):21677–82
23. Wortzel I, Dror S, Kenific CM, Lyden D. 2019. Exosome-Mediated Metastasis: Communication from a Distance. *Dev. Cell* 49(3):347–60
24. Psaila B, Lyden D. 2009. The metastatic niche: Adapting the foreign soil. *Nat. Rev. Cancer* 9:285–93
25. Oskarsson T, Acharyya S, Zhang XHF, Vanharanta S, Tavazoie SF, et al. 2011. Breast cancer cells produce tenascin C as a metastatic niche component to colonize the lungs. *Nat. Med.* 17(7):867–74
26. Kim S, Takahashi H, Lin WW, Descargues P, Grivennikov S, et al. 2009. Carcinoma-produced factors activate myeloid cells through TLR2 to stimulate metastasis. *Nature* 457(7225):102–6
27. Malanchi I, Santamaria-Martínez A, Susanto E, Peng H, Lehr HA, et al. 2012. Interactions between cancer stem cells and their niche govern metastatic colonization. *Nature* 481(7379):859-9.
28. O'Connell JT, Sugimoto H, Cooke VG, MacDonald BA, Mehta AI, et al. 2011. VEGF-A and Tenascin-C produced by S100A4 + stromal cells are important for metastatic colonization.

PNAS 108(38):16002–7
29. Willis RA. 1952. *The spread of tumours in the human body*. London, England: Butterworth & Co.; 148–300 pp.
30. Lam KY, Victor F. 2000. Metastatic Tumors to the Spleen A 25-Year Clinicopathologic Study. *Arch. Pathol. Lab. Med.* 124:526–30
31. Nixon IJ, Coca-Pelaz A, Kaleva AI, Triantafyllou A, Angelos P, et al. 2017. Metastasis to the Thyroid Gland: A Critical Review. *Ann. Surg. Oncol.* 24:1533–9
32. Surov A, Hainz M, Holzhausen H-J, Arnold D, Katzer M, et al. 2010. Skeletal muscle metastases: primary tumours, prevalence, and radiological features. *Eur. Radiol.* 20(3):649–58
33. Haygood TM, Wong J, Lin JC, Li S, Matamoros A, et al. 2012. Skeletal muscle metastases: a three-part study of a not-so-rare entity. *Skeletal Radiol*. 41(8):899–909
34. Klein CA. 2009. Parallel progression of primary tumours and metastases. *Nat. Rev. Cancer* 9:302–12
35. Hosseini H, Obradovic MMS, Hoffmann M, Harper KL, Sosa MS, et al. 2016. Early dissemination seeds metastasis in breast cancer. *Nature* 540(7634):552–8
36. Harper KL, Sosa MS, Entenberg D, Hosseini H, Cheung JF, et al. 2016. Mechanism of early dissemination and metastasis in Her2+ mammary cancer. *Nature* 540(7634):588–92
37. Hüsemann Y, Geigl JB, Schubert F, Musiani P, Meyer M, et al. 2008. Systemic Spread Is an Early Step in Breast Cancer. *Cancer Cell* 13(1):58–68
38. Rhim AD, Mirek ET, Aiello NM, Maitra A, Bailey JM, et al. 2012. EMT and dissemination precede pancreatic tumor formation. *Cell* 148(1–2):349–61
39. Eyles J, Puaux AL, Wang X, Toh B, Prakash C, et al. 2010. Tumor cells disseminate early, but immunosurveillance limits metastatic outgrowth, in a mouse model of melanoma. *J. Clin. Invest.* 120(6):2030–9
40. Rhim AD, Thege FI, Santana SM, Lannin TB, Saha TN, et al. 2014. Detection of circulating pancreas epithelial cells in patients with pancreatic cystic lesions. *Gastroenterology* 146(3):647–51
41. Schardt JA, Meyer M, Hartmann CH, Schubert F, Schmidt-Kittler O, et al. 2005. Genomic analysis of single cytokeratin-positive cells from bone marrow reveals early mutational events in breast cancer. *Cancer Cell* 8(3):227–39
42. Barnhill RL, Piepkorn MW, Cochran AJ, Flynn E, Karaoli T, Folkman J. 1998. Tumor vascularity, proliferation, and apoptosis in human melanoma micrometastases and macrometastases. *Arch. Dermatol.* 134(8):991–4

43. Meltzer A. 1990. Dormancy and breast cancer. *J. Surg. Oncol.* 43(3):181–8
44. Karrison TG, Ferguson DJ, Meier P. 1999. Dormancy of mammary carcinoma after mastectomy. *J. Natl. Cancer Inst.* 91(1):80-5
45. Rinker-Schaeffer CW, Welch DR, Sokoloff M. 2000. Defining the biologic role of genes that regulate prostate cancer metastasis. *Curr. Opin. Urol.* 10(5):397–401
46. Ghajar CM, Peinado H, Mori H, Matei IR, Evason KJ, et al. 2013. The perivascular niche regulates breast tumour dormancy. *Nat. Cell Biol.* 15(7):807–17
47. Seely S. 1980. Possible reasons for the high resistance of muscle to cancer. *Med. Hypotheses* 6(2):133–7
48. Weiss L, Orr FW, Honn KV. 1988. Interactions of cancer cells with the microvasculature during metastasis. *FASEB J.* 2(1):12–21
49. Weiss L. 1992. Comments on hematogenous metastatic patterns in humans as revealed by autopsy. *Clin. Exp. Metastasis* 10:191–9
50. Morris VL, MacDonald IC, Koop S, Schmidt EE, Chambers AF, Groom AC. 1993. Early interactions of cancer cells with the microvasculature in mouse liver and muscle during hematogenous metastasis: videomicroscopic analysis. *Clin. Exp. Metastasis* 11(5):377–90
51. Weiss L. 1989. Biomechanical destruction of cancer cells in skeletal muscle: a rate-regulator for hematogenous metastasis. *Clin. Exp. Metastasis* 7(5):483–91
52. Weiss L, Nannmark U, Johansson BR, Bagge U. 1992. Lethal deformation of cancer cells in the microcirculation: a potential rate regulator of hematogenous metastasis. *Int. J. Cancer* 50(1):103–7
53. Sancricca C. 2010. Vessel-associated stem cells from skeletal muscle: From biology to future uses in cell therapy. *World J. Stem. Cells* 2(3):39
54. Sampaolesi M, Blot S, D'Antona G, Granger N, Tonlorenzi R, et al. 2006. Mesoangioblast stem cells ameliorate muscle function in dystrophic dogs. *Nature* 444(7119):574–9
55. Blau HM, Pavlath GK, Hardeman EC, Chiu CP, Silberstein L, et al. 1985. Plasticity of the differentiated state. *Sciencence* 230(4727):758–66
56. Parlakian A, Gomaa I, Solly S, Arandel L, Mahale A, et al. 2010. Skeletal Muscle Phenotypically Converts and Selectively Inhibits Metastatic Cells in Mice. *PLOS ONE* 5(2):e9299
57. Djaldetti M, Sredni B, Zigelman R, Verber M, Fishman P. 1996. Muscle cells produce a low molecular weight factor with anti-cancer activity. *Clin. Exp. Metastasis* 14(3):189–96
58. Fishman P, Bar-Yehuda S, Vagman L. 1998. Adenosine and Other Low Molecular Weight

Factors Released by Muscle Cells Inhibit Tumor Cell Growth1. *Cancer Res*. 58:3181–7
59. Bar-Yehuda S, Barer F, Volfsson L, Fishman P. 2001. Resistance of muscle to tumor metastases: A role for A3 adenosine receptor agonists. *Neoplasia* 3(2):125–31
60. Dumont NA, Wang YX, Rudnicki MA. 2015. Intrinsic and extrinsic mechanisms regulating satellite cell function. *Co Biol*. 142:1572–81
61. Mauro A. 1961. Satellite Cell of Skeletal Muscle Fibers. *J. Cell Biol.* 9(2):493–5
62. Schultz E. 1996. Satellite cell proliferative compartments in growing skeletal muscles. *Dev. Biol.* 175(1):84–94
63. Kuang S, Kuroda K, Le Grand F, Rudnicki MA. 2007. Asymmetric Self-Renewal and Commitment of Satellite Stem Cells in Muscle. *Cell* 129(5):999–1010
64. Baghdadi MB, Castel D, Machado L, Fukada S-I, Birk DE, et al. 2018. Reciprocal signaling by Notch-Collagen V-CALCR retains muscle stem cells in their niche. *Nature* 557:714–8
65. Brö D, Vasyutina E, Czajkowski MT, Griger J, Rassek C, et al. 2012. Colonization of the Satellite Cell Niche by Skeletal Muscle Progenitor Cells Depends on Notch Signals. *Dev. Cell* 23:469–81
66. Kuroda K, Tani S, Tamura K, Minoguchi S, Kurooka H, Honjo T. 1999. Delta-induced Notch signaling mediated by RBP-J inhibits MyoD expression and myogenesis. *J. Biol. Chem.* 274(11):7238–44
67. Delfini MC, Hirsinger E, Pourquie O, Duprez D. 2000. Delta 1-activated Notch inhibits muscle differentiation without affecting Myf5 and Pax3 expression in chick limb myogenesis. *Development* 127(23):5213–24
68. Kopan R, Ilagan MXG. 2009. The Canonical Notch Signaling Pathway: Unfolding the Activation Mechanism. *Cell* 137:216–33
69. Danza G, Di Serio C, Ambrosio MR, Sturli N, Lonetto G, et al. 2013. Notch3 is activated by chronic hypoxia and contributes to the progression of human prostate cancer. *Int. J. Cancer* 133(11):2577–86
70. Hayashi T, Gust KM, Wyatt AW, Goriki A, Jäger W, et al. 2016. Not all NOTCH is created equal: The oncogenic role of NOTCH2 in bladder cancer and its implications for targeted therapy. *Clin. Cancer Res.* 22(12):2981–92
71. Ai Q, Ma X, Huang Q, Liu S, Shi T, et al. 2012. High-level expression of notch1 increased the risk of metastasis in T1 stage clear cell renal cell carcinoma. *PLOS ONE* 7(4):e35022
72. O'Neill CF, Urs S, Cinelli C, Lincoln A, Nadeau RJ, et al. 2007. Notch2 signaling induces apoptosis and inhibits human MDA-MB-231 xenograft growth. *Am. J. Pathol.* 171(3):1023–36

73. Sriuranpong V, Borges MW, Ravi RK, Arnold DR, Nelkin BD, et al. 2001. Notch signaling induces cell cycle arrest in small cell lung cancer cells. *Cancer Res*. 61(7):3200–5
74. Goel AJ, Rieder MK, Arnold HH, Radice GL, Krauss RS. 2017. Niche Cadherins Control the Quiescence-to-Activation Transition in Muscle Stem Cells. *Cell Rep*. 21(8):2236–50
75. Kalluri R, Weinberg RA. 2009. The basics of epithelial-mesenchymal transition. *J. Clin. Invest.* 119:1420–8
76. Niess AM. 2007. Response and adaptation of skeletal muscle to exercise - the role of reactive oxygen species. *Front. Biosci.* 12(12):4826
77. Reczek CR, Chandel NS. 2017. The Two Faces of Reactive Oxygen Species in Cancer. *Annu. Rev. Cancer Biol.* 1:1, 79-98.
78. Jackson MJ. 2011. Control of reactive oxygen species production in contracting skeletal muscle. Antioxidants and Redox Signaling. 15(9):2477–86
79. Powers SK, Li Ji L, Kavazis AN, Jackson MJ. 2011. Reactive Oxygen Species: Impact on Skeletal Muscle. *Compr. Physiol.* 1(2):941–69
80. Khassaf M, McArdle A, Esanu C, Vasilaki A, McArdle F, et al. 2003. Effect of vitamin C supplements on antioxidant defence and stress proteins in human lymphocytes and skeletal muscle. *J. Physiol.* 549(2):645–52
81. McClung JM, Judge AR, Talbert EE, Powers SK. 2009. Calpain-1 is required for hydrogen peroxide-induced myotube atrophy. *Am. J. Physiol. - Cell Physiol.* 296(2):C363
82. McArdle A, Pattwell D, Vasilaki A, Griffiths RD, Jackson MJ. 2001. Contractile activity-induced oxidative stress: Cellular origin and adaptive responses. *Am. J. Physiol. - Cell Physiol.* 280:621–27
83. McArdle F, Spiers S, Aldemir H, Vasilaki A, Beaver A, et al. 2004. Preconditioning of skeletal muscle against contraction-induced damage: The role of adaptations to oxidants in mice. *J. Physiol.* 561(1):233–44
84. Piskounova E, Agathocleous M, Murphy MM, Hu Z, Huddlestun SE, et al. 2015. Oxidative stress inhibits distant metastasis by human melanoma cells. *Nature* 527(7577):186–91
85. Gal K Le, Ibrahim MX, Wiel C, Sayin VI, Akula MK, et al. 2015. Antioxidants can increase melanoma metastasis in mice. *Sci. Transl. Med.* 7(308):308re8–308re8
86. Nguyen A, Loo JM, Mital R, Weinberg EM, Man FY, et al. 2016. PKLR promotes colorectal cancer liver colonization through induction of glutathione synthesis. *J. Clin. Invest.* 126(2):681–94
87. Petersen OW, Ronnov-Jessen L, Howlett AR, Bissell MJ. 1992. Interaction with basement

membrane serves to rapidly distinguish growth and differentiation pattern of normal and malignant human breast epithelial cells. *PNAS* 89(19):9064–8
88. Bissell MJ, Hall HG, Parry G. 1982. How does the extracellular matrix direct gene expression? *J. Theor. Biol.* 99(1):31–68
89. Paszek MJ, Zahir N, Johnson KR, Lakins JN, Rozenberg GI, et al. 2005. Tensional homeostasis and the malignant phenotype. *Cancer Cell* 8(3):241–54
90. Levental KR, Yu H, Kass L, Lakins JN, Egeblad M, et al. 2009. Matrix Crosslinking Forces Tumor Progression by Enhancing Integrin Signaling. *Cell* 139(5):891–906
91. Rizwan A, Bulte C, Kalaichelvan A, Cheng M, Krishnamachary B, et al. 2015. Metastatic breast cancer cells in lymph nodes increase nodal collagen density. *Sci. Rep.* 5(1):1–6
92. Provenzano PP, Eliceiri KW, Campbell JM, Inman DR, White JG, Keely PJ. 2006. Collagen reorganization at the tumor-stromal interface facilitates local invasion. *BMC Med*. 4(1):38
93. Barkan D, El Touny LH, Michalowski AM, Smith JA, Chu I, et al. 2010. Metastatic growth from dormant cells induced by a Col-I-enriched fibrotic environment. *Cancer Res*. 70(14):5706–16
94. Bissell MJ, Hall HG, Parry G. 1982. How does the extracellular matrix direct gene expression? *J. Theor. Biol.* 99(1):31–68
95. Sanes JR. 2003. The basement membrane/basal lamina of skeletal muscle. *J. Biol. Chem. Am. Soc. Biochem. Mol. Biol.* 278:12601–4
96. Boudreau N, Sympson CJ, Werb Z, Bissell MJ. 1995. Suppression of ICE and apoptosis in mammary epithelial cells by extracellular matrix. *Science* 267(5199):891–3
97. Spencer VA, Costes S, Inman JL, Xu R, Chen J, et al. 2011. Depletion of nuclear actin is a key mediator of quiescence in epithelial cells. *J. Cell Sci.* 124(1):123–32
98. Fiore APZP, Spencer VA, Mori H, Carvalho HF, Bissell MJ, Bruni-Cardoso A. 2017. Laminin-111 and the Level of Nuclear Actin Regulate Epithelial Quiescence via Exportin-6. *Cell Rep*. 19(10):2102–15
99. Albrengues J, Shields MA, Ng D, Park CG, Ambrico A, et al. 2018. Neutrophil extracellular traps produced during inflammation awaken dormant cancer cells in mice. *Science (80-)* 361(6409):1-13
100. Compérat E, Bardier-Dupas A, Camparo P, Capron F, Charlotte F. 2007. Splenic metastases: Clinicopathologic presentation, differential diagnosis, and pathogenesis. *Arch. Pathol. Lab. Med.* 131:965–9
101. Okuyama T. 2001. Isolated Splenic Metastasis of Sigmoid Colon Cancer: a Case Report.

Jpn. J. Clin. Oncol. 31(7):341–5
102. Genç V, Akbari M, Karaca AS, Çakmak A, Ekıncı C, Gürel M. 2010. Why is isolated spleen metastasis a rare entity? *Turk. J. Gastroenterol.* 21(4):452–3
103. Efared B, Mazti A, Atsame-Ebang G, Tahiri L, El Bouhaddouti H, et al. 2016. An unusual site of metastasis: splenic metastastasis from a colon cancer. *J. Surg. Case Rep.* 10:1–3
104. Warren S, Davis A. 1934. Studies on tumor metastasis. The metastasis of carcinoma to the spleen. *Am. J. Cancer* 21(3):517–33
105. Abi Saad GS, Hussein M, El-Saghir NS, Termos S, Sharara AI, Shamseddine A. 2011. Isolated splenic metastasis from colorectal cancer. *Int. J. Clin. Oncol.* 16;306–13
106. Berge T. 2009. Splenic Metastases. *Acta Pathol. Microbiol. Scand. Sect. A Pathol.* 82A(4):499–506
107. Müller A, Homey B, Soto H, Ge N, Catron D, et al. 2001. Involvement of chemokine receptors in breast cancer metastasis. *Nature* 410(6824):50–6
108. Miller JN, Milton GW. 1965. An experimental comparison between tumour growth in the spleen and liver. *J. Pathol. Bacteriol.* 90(2):515–21
109. Iype S, Akbar MA, Krishna G. 2002. Isolated splenic metastasis from carcinoma of the breast. *Postgr. Med. J.* 78:173–4
110. O'Reilly MS, Holmgren L, Shing Y, Chen C, Rosenthal RA, et al. 1994. Angiostatin: A novel angiogenesis inhibitor that mediates the suppression of metastases by a lewis lung carcinoma. *Cell* 79(2):315–28
111. Saboo SS, Krajewski KM, O'regan KN, Giardino A, Brown JR, et al. 2012. Spleen in haematological malignancies: spectrum of imaging findings. *Br. J. Radiol.* 85:81–92
112. Chiabrando D, Vinchi F, Fiorito V, Mercurio S, Tolosano E. 2014. Heme in pathophysiology: A matter of scavenging, metabolism and trafficking across cell membranes. *Front. Pharmacol.* 5:1–24
113. Kovtunovych G, Eckhaus MA, Ghosh MC, Ollivierre-Wilson H, Rouault TA. 2010. Dysfunction of the heme recycling system in heme oxygenase 1-deficient mice: Effects on macrophage viability and tissue iron distribution. *Blood* 116(26):6054–62
114. Everse J, Hsia N. 1997. The toxicities of native and modified hemoglobins. *Free Radic. Biol. Med.* 22(6):1075–99
115. Nixon IJ, Whitcher M, Glick J, Palmer FL, Shaha AR, et al. 2011. Surgical management of metastases to the thyroid gland. *Ann. Surg. Oncol.* 18(3):800–4
116. Plonczak AM, Dimarco AN, Dina R, Gujral DJ, Palazzo FF. 2017. Breast cancer

metastases to the thyroid gland - An uncommon sentinel for diffuse metastatic disease: A case report and review of the literature. *J. Med. Case Rep.* 11:269
117. Khalil J, Elomrani F, Benoulaid M, Elkacemi H, Kebdani T, et al. 2015. Isolated thyroid metastasis revealed an unknown lung adenocarcinoma: A case report. *J. Med. Case Rep.* 9(1):221
118. Chung AY, Tran TB, Brumund KT, Weisman RA, Bouvet M. 2012. Metastases to the Thyroid: A Review of the Literature from the Last Decade. *Thyroid* 22(3):258-68
119. Cordes M, Kuwert T. 2014. Metastases of non-thyroidal tumors to the thyroid gland: A regional survey in middle franconia. *Exp. Clin. Endocrinol. Diabetes* 122:273–6
120. Chung HR. 2014. Iodine and thyroid function. *Ann. Pediatr. Endocrinol. Metab.* 19(1):8
121. Schmitz G. 2001. The oxidation of iodine to iodate by hydrogen peroxide. *Phys. Chem. Chem. Phys.* 3(21):4741–6
122. Poncin S, Gérard A-C, Boucquey M, Senou M, Calderon PB, et al. 2008. Oxidative Stress in the Thyroid Gland: From Harmlessness to Hazard Depending on the Iodine Content. *Endocrinology* 149(1):424–33
123. Uyttersprot N, Pelgrims N, Carrasco N, Gervy C, Maenhaut C, et al. 1997. Moderate doses of iodide in vivo inhibit cell proliferation and the expression of thyroperoxidase and Na+/I-symporter mRNAs in dog thyroid. *Mol. Cell Endocrinol.* 131(2):195–203
124. Contempré B, De Escobar GM, Denef JF, Dumont JE, Many MC. 2004. Thiocyanate Induces Cell Necrosis and Fibrosis in Selenium- and Iodine-Deficient Rat Thyroids: A Potential Experimental Model for Myxedematous Endemic Cretinism in Central Africa. *Endocrinology* 145(2):994–1002
125. Contempre B, Denef JF, Dumont JE, Many MC. 1993. Selenium deficiency aggravates the necrotizing effects of a high iodide dose in iodine deficient rats. *Endocrinology* 132(4):1866–8
126. Goddard ET, Bozic I, Riddell SR, Ghajar CM. 2018. Dormant tumour cells, their niches and the influence of immunity. *Nat. Cell Biol.* 20(11):1240–9
127. Yamauchi K. 2016. Chapter 93 -Thyroid Hormones. In *Handbook of Hormones: Comparative Endocrinology for Basic and Clinical Research*. Academic Press (Oxford), pp. 493-e93–2
128. Nilsson M, Fagman H. 2017. Development of the thyroid gland. Development 144:2123–40
129. Montesinos M del M, Pellizas CG, Kong W, Wu L, Pellizas CG, Del M. 2019. Thyroid Hormone Action on Innate Immunity. Front. Endocrinol. 10:350
130. van der Spek AH, Fliers E, Boelen A. 2017. Thyroid hormone metabolism in innate immune

cells. J Endocrinol 232(2):R67-R81
131. del Mar Montesinos M, Pellizas C. 2019. Thyroid hormone action on innate immunity. *Front. Endocrinol. (Lausanne)* 10(JUN):350
132. Köhrle J. 2018. Thyroid hormones and derivatives: Endogenous thyroid hormones and their targets. In *Methods in Molecular Biology*. Humana Press Inc. (New York, NY), pp. 85–104
133. Mould RC, Vloten JP van, AuYeung AWK, Karimi K, Bridle BW. 2017. Immune responses in the thyroid cancer microenvironment: making immunotherapy a possible mission. *Endocr. Relat. Cancer* 24:T311–29
134. Mascanfroni I, Montesinos MDM, Susperreguy S, Cervi L, Ilarregui JM, et al. 2008. Control of dendritic cell maturation and function by triiodothyronine. *FASEB J.* 22(4):1032–42
135. Hodkinson CF, Simpson EEA, Beattie JH, O'Connor JM, Campbell DJ, et al. 2009. Preliminary evidence of immune function modulation by thyroid hormones in healthy men and women aged 55–70 years. *J. Endocrinol.* 202(1):55–63
136. Smid M, Wang Y, Zhang Y, Sieuwerts AM, Yu J, et al. 2008. Subtypes of breast cancer show preferential site of relapse. *Cancer Res.* 68(9):3108–14
137. Braun S, Vogl FD, Naume B, Janni W, Osborne MP, et al. 2005. A Pooled Analysis of Bone Marrow Micrometastasis in Breast Cancer. *N. Engl. J. Med.* 353(8):793–802
138. Karampinos DC, Ruschke S, Dieckmeyer M, Diefenbach M, Franz D, et al. 2018. Quantitative MRI and Spectroscopy of Bone Marrow. *J. Magn. Reson. Imaging* 47:332–53
139. Al-Muqbel KM. 2017. Bone Marrow Metastasis is an Early Stage of Bone Metastasis in Breast Cancer Detected Clinically by F18-FDG-PET/CT Imaging. *Biomed. Res. Int.* 2017:9852632
140. Horowitz MC, Berry R, Holtrup B, Sebo Z, Nelson T, et al. 2017. Bone marrow adipocytes. 6(3):193-204.
141. Naveiras O, Nardi V, Wenzel PL, Hauschka PV, Fahey F, Daley GQ. 2009. Bone-marrow adipocytes as negative regulators of the haematopoietic microenvironment. *Nature* 460(7252):259–63
142. Cahu X, Calvo J, Poglio S, Prade N, Colsch B, et al. 2017. Bone marrow sites differently imprint dormancy and chemoresistance to T-cell acute lymphoblastic leukemia. *Blood Adv.* 1(20):1760–72
143. Scheller EL, Doucette CR, Learman BS, Cawthorn WP, Khandaker S, et al. 2015. Region-specific variation in the properties of skeletal adipocytes reveals regulated and constitutive marrow adipose tissues. *Nat. Commun.* 6:7808

144. Tavassoli M. 1976. Marrow adipose cells. Histochemical identification of labile and stable components. *Arch. Pathol. Lab. Med.* 100(1):16–8
145. Ramasamy SK, Kusumbe AP, Itkin T, Gur-Cohen S, Lapidot T, Adams RH. 2016. Regulation of Hematopoiesis and Osteogenesis by Blood Vessel-Derived Signals. *Annu. Rev. Cell Dev. Biol.* 32(1):649–75
146. Kusumbe AP, Ramasamy SK, Adams RH. 2014. Coupling of angiogenesis and osteogenesis by a specific vessel subtype in bone. *Nature* 507(7492):323–8
147. Itkin T, Gur-Cohen S, Spencer JA, Schajnovitz A, Ramasamy SK, et al. 2016. Distinct bone marrow blood vessels differentially regulate haematopoiesis. *Nature* 532(7599):323–8
148. Aguirre-Ghiso JA. 2007. Models, mechanisms and clinical evidence for cancer dormancy. *Nat. Rev. Cancer* 7:834–46
149. Carlson P, Dasgupta A, Grzelak CA, Kim J, Barrett A, et al. 2019. Targeting the perivascular niche sensitizes disseminated tumour cells to chemotherapy. *Nat. Cell Biol.* 21(2):238–50
150. Mulcrone PL, Campbell JP, Clément-Demange L, Anbinder AL, Merkel AR, et al. 2017. Skeletal Colonization by Breast Cancer Cells Is Stimulated by an Osteoblast and β2AR-Dependent Neo-Angiogenic Switch. *J. Bone Miner. Res.* 32(7):1442–54

Chapter 2. Materials and Methods

Here I describe the experimental methodologies and reagents used to undertake the studies in the chapters that follow.

Human studies.

Specimen Collection. Human skeletal muscle biospecimens from metastatic breast cancer patients were obtained to confirm spontaneous tumour cell dissemination to skeletal muscle (IR # 10474). Patients were consented to donate tissue post-mortem and enrolled in The BROCADE rapid autopsy project. Upon rapid autopsy, skeletal muscle samples from the tibialis anterior, quadriceps and gastrocnemius were collected and placed in 10% neutral-buffered formalin (NBF). If unable to collect the above muscle sites, alternatives were selected as available. Formalin-fixed tissue was then paraffin-embedded following standard protocols. Healthy skeletal muscle was acquired as a FFPE block from Origene Technologies (PA154769F7), where pathology verification from H&E review were: 75% skeletal muscle and 25% interstitial tissue. Sample pathology was within normal limits. Two slides of 4 μm sections were stained as controls for pan-cytokerain (panCK), estrogen receptor (ER) and progesterone receptor (PR) antibody staining in skeletal muscle (see details below). The ER^+/PR^+ human breast tumour specimen was obtained from the Cancer Epidemiology Research Cooperative (CERC) at the Fred Hutchinson Cancer Research Centre and used as a positive staining control for our study. The pathology report confirmed that the tumour was ER^+/PR^+.

Multiplex Immunohistochemistry (mIHC). Pieces of tibialis anterior, quadriceps and gastrocnemius muscle were embedded in a single paraffin block. Serial sections at a thickness of 4 μm were cut and mounted onto positively charged slides. A total of 50 slides per patient were sectioned. Every 10th slide was stained with the mIHC panel. If cells of interest were identified, additional sections (4 slides preceding/4 slides proceeding) were stained with the mIHC panel or hematoxylin and eosin to confirm histology. Fully automated mIHC was performed on a DISCOVERY Ultra instrument (Ventana Medical Systems Inc. (VMSI)). Tissue sections were deparaffinized in DISCOVERY Wash buffer (VMSI, 950-510),

followed by heat-induced epitope retrieval in DISCOVERY CC1 solution (VMSI, 950-500). Multiplex IHC was performed sequentially, including wash steps with DISCOVERY Reaction Buffer (VMSI, 950-510) to removed unbound antibodies. First, the sections were incubated with a primary antibody cocktail containing Estrogen Receptor (ER; Genetex, 6F11) at 1:50 and Progesterone Receptor (PR; Genetex, 16) at 1:50 in Ventana Antibody Diluent with Casein (VMSI, 760-219). The biomarker cocktail was bound with DISCOVERY Anti-Mouse HQ (VMSI, catalog 760-4814), followed by DISCOVERY Anti-HQ HRP (VMSI, 760-4820) and visualized with the DISCOVERY Purple kit (VMSI, 760–229). Previously bound HRP was quenched with DISCOVERY Inhibitor (VMSI, 760-4840) prior to the application of the next biomarker in the sequence. The sections were incubated with pan Cytokeratin (pan-CKI Abcam, AE1/AE3+5D3) at 1:100, labelled with DISCOVERY Anti-Mouse NP Multimer (VMSI, 760-4816), followed by DISCOVERY Anti-NP AP Multimer (VMSI, 760-4827) and visualized with the DISCOVERY Yellow kit (VMSI, 760-229). Sections were counterstained with Hematoxylin II (VMSI, 790-2208) and Bluing Reagent (VMSI, 760-2037). Slides were dehydrated in a series of ethanol and xylene baths and mounted in Cytoseal XYL (Fisher Scientific, 22-050-262).

Imaging and Analysis. The slides were scanned at a magnification of 40X using the Aperio VERSA 200 scanner (Leica Biosystems) and evaluated with HALO (Indica Labs). Slides 1, 10, 20, 30, and 40 were reviewed and annotated. Cells of interest were identified on slide 20. Adjacent slides 16-19 and 21-24 were stained with the mIHC panel or hematoxylin and eosin. Serial registration of the sequential images was performed in HALO (Indica Labs). Cells that stained positively for the ER/PR cocktail and panCK were identified in the mIHC sections. Vascular tissue and skeletal muscle bundles were confirmed using the flanking hematoxylin and eosin sections. The findings were verified by a pathologist (L.T.).

Animal studies. All animal work was performed in accordance with institutional, IACUC (specifically, Fred Hutchinson Cancer Research Centre protocol 51075) and AAALAS guidelines and ethical regulations. NOD/SCID(NOD.CB17-Prkdcscid/J(NOD.SCID) (NOD-SCID, 394) and BALB/c (028) female mice were purchased from Charles River and enrolled

in study at six to eight weeks of age. C57BL/6NJ (005304) and B6.Cg-Tg(CAG-OTC/CAT)4033Prab/J ("mCAT", 016197) female mice were purchased from Jackson Laboratories and enrolled in study at six to ten weeks of age. In this manuscript, we use "MCAT" instead of "mCAT" to denote the B6.Cg-Tg(CAG-OTC/CAT)4033Prab/J mouse strain to distinguish from tumour cell line expression of catalase (denoted as "Tumour cell-mCAT"). Female NSG (NOD-SCID-Il2rg–/–) mice were obtained from the FHCRC CCEH core and enrolled in study at six weeks of age. Skeletal muscle specimens from female B6.Cg-Tg(CAG-OTC/CAT)4033Prab/J mice were also given as a gift from the Rabinovitch lab at the University of Washington.

Intracardiac injection. Anesthetized mice were positioned in dorsal recumbency on a VisualSonics Vevo 2100 Ultrasound Imaging System to guide injection of 2×10^5 MDA-MB-231 or 1×10^4 4T1-SkMx tumor cells in 100 µl PBS. Just prior to injection, tumour cell/PBS suspensions were pipetted repeatedly with a p1000 to ensure a well-mixed solution, and drawn into a 1 mL syringe mounted with a 22G needle for injections. Needle height and angle was adjusted on a stereotactic rig, and the needle was guided via ultrasound imaging into the left ventricle. Tumour burden was monitored over the subsequent weeks via bioluminescent imaging (BLI). In the event that metastases arose and 1) exceeded a BLI reading of $1x10^8$ p/sec/cm^3/sr, or 2) significantly impacted the health of the animal (e.g., changes in weight, abnormal resting posture, failure to groom, loss of mobility), the mouse was euthanized and organs of interest harvested.

Intramuscular injection. Anesthetized mice were positioned in dorsal recumbency, with the right hindlimb extended. EO771 murine mammary tumour cells expressing GFP-luciferase (1,000 cells) were injected i.m. (30 µl) into the tibialis anterior (TA) of six-to-eight-week-old female C57BL/6 mice. Similarly, MDA-MB-231 human breast cancer cells expressing GFP-luciferase (500 cells) were injected i.m. (30 µl) into the TA of six-to-eight-week-old female NOD-SCID mice. 4T1-mCherry tumour cells (100 cells) were injected i.m. (30 µl) into the tibialis anterior (TA) of six-to-eight-week-old female Balb/c mice. Tumour cell number has been titrated such that the tumour cells persist within the TA without colonization of the tissue nor local invasion. Tumour outgrowth was measured weekly via BLI. At the

established endpoint, mice were euthanized, and skeletal muscle harvested. In the event that tumours arose and 1) exceeded a BLI reading of $1x10^8$ p/sec/cm^3/sr, or 2) significantly impacted the health of the animal (e.g., loss of mobility), the mouse was euthanized.

Intravenous injection. In preparation of the injection, mice were physically restrained, and the animal's tail was heated with a heat lamp or warm water to increase vessel dilation. $5x10^5$ MDA-MB-231 or $1x10^6$ EO771 tumour cells (100 µl) were loaded into a 1mL syringe with a 27-gauge needle and administered into the tail vein of six-to-eight-week-old female NOD-SCID or C57BL/6 mice, respectively. Tumour colonization of lung was measured weekly via BLI. At the established endpoint, mice were euthanized and lungs harvested. In the event that tumours 1) exceeded a BLI reading of $1x10^8$ p/sec/cm^3/sr, or 2) significantly impacted the health of the animal (e.g., changes in weight, abnormal resting posture, failure to groom), the mouse was euthanized.

Orthotopic injection. To quantify the location of DTCs following spontaneous dissemination from orthotopic tumours, 1×10^6 ffluc-eGFP MDA-MB-231 cells were injected into the inguinal mammary gland of 6–8-week-old female NOD-SCID-Il2rg–/– (NSG) mice in 30 µl of a 1:1 solution of LrECM (Growth-factor reduced Cultrex; Trevigen): PBS. Tumours were resected at a final volume of ~250 mm^3 approximately 4 weeks later. Bioluminescent imaging (BLI) was performed on a IVIS Spectrum (Perkin Elmer) one-week post-resection following intraperitoneal delivery of 100 µl D-Luciferin (10 mg/mL, BioVision, Inc.) to confirm successful resection and weekly BLI was performed to track metastasis.

Barium chloride skeletal muscle injury study. Six-to-eight week old female C57BL/6 and Balb/c mice will be administered Buprenorphine SR and anesthetized with isoflurane prior to injury. To perform a full injury, 20–30 jabs will be applied over the entire area of the tibialis anterior muscle to allow for complete diffusion of the injected solution. Afterwards 50 µl 1.2% barium chloride ($BaCl_2$; Sigma SB8221) solution was injected over a total of five injection sites, again such that the entire muscle has been injured. Two days post-injury, $1x10^2$ 4T1-mCherry or $1x10^3$ EO771-ffluc-eGFP mammary cancer cells were injected into

the tibialis anterior. Prior to injection, mice were also anesthetized with isoflurane. Tumor cell outgrowth was be measured weekly via bioluminescent imaging (BLI).

Bioluminescence imaging (BLI). BLI of mice and organs of interest *ex vivo* was performed using an IVIS Spectrum (Perkin Elmer) with Living Image software. Mice were injected intraperitoneally with 100 µl of PBS containing D-luciferin sodium salt (10 mg/mL) (Biovision, 7902) five minutes before imaging, followed by general anaesthesia (2% isoflurane). The exposure time of images was determined by the signal intensity (auto exposure), ranging from 1 to 60 seconds. The bioluminescent signal was quantified with "region of interest" measurement tools in Living Image (Perkin Elmer) software. After *ex vivo* imaging of organs, samples were placed in 4% paraformaldehyde fixative for downstream processing.

Mammary tumour measurements. Mammary tumours were measured in vivo and ex vivo using digital calipers to measure the long (L) and short (w) axes of the tumour. Volume was calculated using the equation $V= 0.5Lw^2$.

Derivation of the 4T1-SkMx muscle-metastatic sublines. The 4T1-SkMx muscle-metastatic sublines were derived through serial intracardiac (i.c.) passaging. Initially, 4T1-parental-mCherry ($1x10^5$ cells) were i.c. injected into the left ventricle of six-to-eight week old female Balb/c mice. Metastases was monitored via bioluminescent imaging (BLI). Due to systemic metastasis, the mice required euthanasia within two weeks of injection. Several skeletal muscle sites (tibialis anterior, quadriceps, gastrocnemius and bulk upper limb muscles) were collected upon necropsy and imaged for $mCherry^+$ lesions (Zeiss AxioZoom). Once a $mCherry^+$ lesion was identified, the region was excised, minced and enzymatically digested. The skeletal muscle tissue digestion was based on a methods publication by Liu et al (Nature Protocols 2015.). 4T1-mCherry tumor cells (first passage termed 4T1-SkM1met if derived from multi-cellular lesion or 4T1-SkMmicro if derived from single cell/small cluster) were purified using puromycin selection, as the mCherry vector is puromycin-resistant. Puromycin was administered until no cell death was observed (~7 days). The 4T1-SkM1met cells ($1x10^4$) were then i.c. injected into the left ventricle of six-to-

eight-week-old female Balb/c mice and the steps above were repeated. The tumour cell line collected from this second passage was termed 4T1-SkM2met. The third and last passage through mice was termed 4T1-SkM3met.

AluYB8 qPCR.

Cell culture. Mouse OP-9 cells and human MDA-MB-231 cells were grown in culture until sufficient cell numbers were generated. Cell suspensions were generated, and densities counted using a haemocytometer. MDA-MB-231 cells were then mixed with OP-9 such that the following dilutions were made: $1x10^5$ MDA-MB-231 and $1x10^5$ OP-9 (1:1), $1x10^4$ MDA-MB-231 and $1x10^5$ OP-9 (1:10), $1x10^3$ MDA-MB-231 and $1x10^5$ OP-9 (1:100), $1x10^2$ MDA-MB-231 and $1x10^5$ OP-9 (1:1,000), $1x10^2$ MDA-MB-231 and $1x10^6$ OP-9 (1:10,000), $1x10^2$ MDA-MB-231 and $1x10^7$ OP-9 (1:100,000), $1x10^2$ MDA-MB-231 and $1x10^7$ OP-9 (1:1,000,000), and 50 MDA-MB-231 and $5x10^7$ OP-9 (1:10,000,000). Genomic DNA was then extracted using Qiagen's DNeasy Blood and Tissue Kit (69504). DNA was sheared into 500bp fragments using a Covaris S220 ultrasonicator. DNA concentrations were measured using a Nanodrop (ThermoFisher). PCR reactions were prepared using the sheared DNA samples, TaqMan Gene Expression Master Mix (4369016, ThermoFisher) and amplicon-specific primer/probe sets (human AluYB8 and mouse beta-actin). AluYB8 primers (Invitrogen) were based on a publication by Campbell et *al.*[39] Fw- YB8-ALU-S68: GTC AGG AGA TCG AGA CCA TCCT, Rv- YB8-ALU-AS244: AGT GGC GCA ATC TCG GC, Probe- YB8-ALU-167: 6-FAM-AGC TAC TCG GGA GGC TGA GGC AGG A-TAMRA. The mouse beta-actin primer/probe pair used was Mm02619580_g1 FAM (ThermoFisher). Samples were run in triplicate on a Bio-Rad CFX96 Real-Time System (C1000 Thermal Cycler) using the following cycling conditions: 1) UDG Incubation: 50°C for 2 minutes, 2) AmpliTaq Gold, UP Enzyme Activation: 95°C for 10 minutes, 3) Denaturation: 95°C for 15 seconds, followed by Annealing/Extension: 63°C for 1 minute, repeated for 39 more cycles, 4) Final extension: 63°C for 3 min. AluYB8 Cq values were normalized by B-actin Cq values. Additional details provided in Supplementary Table 4.

Mouse tissue. Upon necropsy, organs of interest (e.g., lung, brain, liver, bone, skeletal muscle) were immediately flash frozen (LN_2). Tissue samples were homogenized at 4ºC

using 2.8mm ceramic beads (19-628-3, OMNI) and optimized program settings for the OMNI Bead Ruptor 24. Most organs were processed using 5.65 m/s speed, for 3 cycles of 30 seconds (5 second dwell time). Genomic DNA was then extracted using Qiagen's DNeasy Blood and Tissue Kit (69504). DNA was sheared into 500bp fragments using a Covaris S220 ultrasonicator. DNA concentrations were measured using a Nanodrop (ThermoFisher). PCR reactions were prepared using the sheared DNA samples, TaqMan Gene Expression Master Mix (4369016, ThermoFisher) and amplicon-specific primer/probe sets (human AluYB8 and mouse beta-actin). AluYB8 primers are the same as described above. Mouse beta-actin primer/probe sets for Day 3 was Mm02619580_g1 VIC (ThermoFisher). For Week 7, Mm02619580_g1 FAM (ThermoFisher) was used. Samples were run in triplicate on a Bio-Rad CFX96 Real-Time System using the same cycling conditions described above. AluYB8 Cq values were normalized by B-actin Cq values, followed by normalization of tumour-bearing samples by uninoculated controls. Additional details provided in Supplementary Table 3.

Lung and skeletal muscle clearing via the Ce3D method and staining GFP$^+$ DTCs. Mice were euthanized and perfused with 25 mL ice cold PBS through the left ventricle. The left lobe of the lung and the left hindlimb skeletal muscles (tibialis anterior, gastrocnemius, quadriceps) were harvested and fixed in 1% PFA/PBS overnight, rocking at 4°C. Tissues were blocked in 1mL of 1% normal mouse serum (MP Biomedicals), 1% bovine serum albumin (Sigma), 0.3% Triton X-100 (Sigma) in PBS for eight hours at 37 °C in a shaking incubator. Primary antibodies were added to blocking solution and tissues were incubated in primary antibody solution for 72 hours while shaking at 37 °C. For lung, the primary antibodies used were chicken anti-GFP (Abcam ab13970, 1:500), while skeletal muscle samples were stained with both chicken anti-GFP and rabbit pan-laminin (Sigma L9393, 1:200). Tissues were washed for 24 hours in 0.2% Triton X-100 and 0.5% 1-thioglycerol (Sigma) in PBS while shaking at 37 °C. Lung and muscle were submerged in 1mL block solution containing goat anti-chicken 488 (1:250) and goat anti-rabbit 568 (1:250; for skeletal muscle only) and shaken for 48 hours at 37 °C. 4′,6-Diamidine-2′-phenylindole dihydrochloride (DAPI; 2 µg/mL) was used to label cellular nuclei. Afterwards, wash was repeated for another 24 hours.

After staining, tissues were cleared using Ce3D clearing solution (40% N-methylacetamide [Sigma] v/v, 86% w/v Histodenz [Sigma], 0.1% Triton X-100and 0.5% 1-thioglycerol in PBS). Lung and muscle were covered and incubated in 1 mL Ce3D clearing solution while shaking at 37 °C for 5 days. Cleared lung and muscle were stored in Ce3D clearing solution at 4 °C until imaged. Imaging to quantify DTCs was performed on a Zeiss LSM700 confocal microscope using a 0.3 NA 10x air objective. Z-stacks of lungs and muscles were tile-scanned at 10x, and structures of interest were confirmed to be cellular in nature at 20x. Cleared lung and muscle from three uninoculated mice were used as a control; these were used to subtract staining noise from our analyses.

Cell culture and reagents. Primary human skeletal muscle myoblasts (SkMc) were obtained commercially (Lonza) and propagated in SkGM or SkGM-2 growth media (CC-3160, CC-3245). Primary human lung fibroblasts (LF) were obtained commercially (Lonza) and propagated in high glucose DMEM (Gibco,11965-118) supplemented with 10% foetal bovine serum (FBS, Gibco 16140089) and 1% penicillin/streptomycin (P/S; Gibco 15140122). Murine skeletal muscle myoblasts derived from C57BL/6 wildtype or MCAT mice (SkMc-WT and SkMc-MCAT) were propagated in F10 (Gibco, 11550043) media supplemented with 20% FBS, 1% P/S and 10 ng/mL bFGF (PeproTech, AF-100-18B). Murine myoblasts are sub-cultured on 10% Matrigel-coated plates (Corning, 356234). All primary human and murine cells were used in experiments before passage 11. Differentiation media (2% horse serum (Gibco 26050070) in high glucose DMEM) was added to differentiate the SkMc and murine myoblasts. To minimize experimental variability, differentiation media was also added to LF cells at the same time.

Human breast cancer cell lines (MDA-MB-231, Hs578T, BT549, HCC70, MDA-MB-468) were purchased commercially (ATCC). High glucose DMEM supplemented with 10% FBS was used to culture the MDA-MB-231 and Hs578T lines. RPMI 1640 medium supplemented with 10% FBS was used to culture the BT549 and HCC70 lines. Leibovitz L-15 media (Gibco 11415064) supplemented with 10% FBS was used to culture the MDA-MB-468. Murine stromal cells (OP-9) were purchased commercially (ATCC). Mammary cancer cell line 4T1 was obtained from Karmanos Cancer Institute. EO771 were a gift from H.K. Lyerly

(Duke University). These three murine lines were cultured in high glucose DMEM supplemented with 10% FBS. All cells were maintained at 37°C, 5% CO_2 , with the exception the MDA-MB-468, which were grown in 0% CO_2 conditions. Additionally, all cell lines tested negative for mycoplasma.

Derivation of C57BL/6 WT and MCAT myoblasts. Female wild-type and MCAT C57BL/6 mice were obtained as a gift from Dr. Peter Rabinovitch at the University of Washington (aged 9 weeks). Several skeletal muscle sites (tibialis anterior, quadriceps, gastrocnemius) were collected upon necropsy, minced and enzymatically digested. The skeletal muscle tissue digestion was based on a methods publication by Liu et al.88. To obtain pure myoblast populations, we performed four pre-plating steps every two days preceding the initial myoblast isolation89. Pre-plating entailed i) creating a cellular suspension, ii) plating the suspension on tissue-culture treated dishes for 45 minutes, then iii) replating the suspension on 10% Matrigel-coated tissue culture dishes. The 45-minute incubation period allowed fibroblasts to adhere to the dish, whereas myoblasts remained in suspension. Myoblasts were cultured until sufficient cell numbers were generated and frozen back.

Skeletal muscle and lung niche co-cultures. SkMcs or LFs were seeded alone at a density of 8,333 cells/well (100 µl) in 96-well culture plates. Plates were then left undisturbed on a flat surface for 15 min to allow even cell seeding prior to incubation. Growth media (Lonza SkGM-2 for SkMc, 10% FBS in DMEM hi-glucose for LF) was changed every other day. After 4 days, differentiation media (2% horse serum in DMEM hi-glucose) was added to both SkMc and LF wells to initiate the maturation and fusion of the myocytes. To avoid experimental variability, media conditions for SkMc and LF niches were identical from the differentiation step onwards. Differentiation media was refreshed every other day. After an additional 4 days, YFP- or RFP-expressing tumour cells were suspended in supplement-free DMEM/F12 (Gibco, 11330-032). YFP or RFP tumour cells were seeded at a density of 100 cells/well in a total volume of 100 μl after washing cultures twice with PBS. Cells were allowed to settle for 15 min at room temperature, then a drip of reduced growth factor basement membrane extract (BME) PathClear Cultrex (Biotechne 3433-005-01) in DMEM/F12 was slowly added to each well (final concentration: 20%). The

BME Cultrex drip condensed for 10-15min at room temperature before polymerizing fully at 37ºC. If required, cultures were imaged immediately after seeding on a Zeiss LSM700 confocal microscope using a 0.3 NA 10x air objective. The objective was centred to each well before acquisition of 512x512 pixel, 6x6 tiles (zoom =0.7) that captured the near-entirety of each well. Cultures were maintained with media changes every 72 hours and imaged in two-five day intervals as required by the experiment.

Conditioned medium studies: SkMc and LF cells were grown up in a 96-well plate as established above. The number of wells seeded was proportionate to the experimental wells needed and doubled to account for the wells used for conditioned media. To differentiate cells, exosome-depleted differentiation media (2% horse serum in DMEM hi-glucose) was added. To remove exosomes, horse serum was centrifuged at 4ºC for 70 minutes at 100,000xg. Supernatant was filtered by pouring contents into vacuum-connected 0.22 µm filter on top of sterile bottle. As described above, SkMc and LF cultures were provided four days for differentiation, and media replenished at day two. $1x10^2$ MDA-MB-231 cells were then seeded on the experimental SkMC and LF wells (100 cell/µl, termed “SkMc+MDA” and “LF+MDA”). Media was removed from all wells, collecting only the media from the SkMc-only and LF-only wells (termed “SkMc-CM” and “LF-CM”, respectively). SkMc-CM was delivered to the SkMc+MDA and LF+MDA wells. As a control, LF-CM was added to SkMC+MDA and LF+MDA wells. Fresh differentiation media was added to the SkMC-only and LF-only wells. Collection and distribution steps were repeated daily or every 3rd day (depending on the experiment) during the ten-day outgrowth period. Imaging settings were the same as described in the paragraph above.

Extracellular vesicle studies: SkMc and LF cells were seeded in 96-well plates as established above, as well as an additional three 15 cm plates for extracellular vesicle (EV) collection. As described in the primary co-culture methods section, cells were propagated and differentiated over the course of eight days. Once differentiated, serum-free DME/F12 was added and allowed to incubate for three days before supernatant was collected for EVs using established methodologies[10]. EV-containing medium was transferred to a 50 mL conical and centrifuged at 4ºC for 10 minutes at 500xg. Supernatant was collected and

transferred to new a fresh conical tube. Samples were then centrifuged at 4ºC for 20 minutes at 20,000xg. Supernatant was transferred to 12mL tubes that were compatible with the ultracentrifuge's SW40-Ti rotor (Beckman Coulter). Samples were centrifuged at 4ºC for 70 minutes at 100,000xg. Supernatant was completely removed and pellets were resuspended 1mL 1x PBS. Samples were then centrifuged at 4ºC for 70 minutes at 100,000xg. Supernatant was removed and a small volume (20-100 µl) of 1x PBS was used to resuspend the pellet. Protein concentration of EVs was quantified using BioRad DC assay. Varying concentrations (5, 10, 20 µg/mL) of EVs were administered to the organotypic culture niches upon MDA-MB-231 seeding (day 0). Collection and distribution steps were repeated every third day during the 10-day MDA-MB-231 outgrowth period. Imaging settings were the same as described in the primary co-culture paragraph.

Decellularization studies: SkMc and LF niches were seeded as described above. 0.5% TritonX-100 (50 µl) was added to each well and incubated for approximately 5 minutes at room temperature. Cell lysis was monitored using an inverted microscope and allowed to continue until no intact cells were visible. Wells were then gently washed with 1x PBS (200 µl). ddH_20 was added to each well and incubated for ~3-5 min at room temperature. Wells were gently washed in 1xPBS (200 µl) 3-5 times. At this point, approximately $1.5x10^3$ tumour cells were seeded on top of the thin layer of ECM. Tumour cells were grown in DMEM-hi glucose with 1% FBS. No BME Cultrex was added to the decellularized wells. Tumour cells were cultured for the ten-day period and imaged at Day 0, 5 and 10.

SkMc–LF mixture studies: SkMc and LF cells were plated in admixture, with the ratio of SkMc to LF increasing sequentially. LF to SkMc ratios included 1:1, 1:10, 1:20, 1:50 and 1:100. The final cell seeding density of 8,333 per 96-well was maintained. Once both cell types were seeded, the procedure for differentiating the niches and seeding the tumour cells are the same as those described above. Imaging settings were the same as described in the primary co-culture paragraph.

H_2O_2 spike-in studies: SkMc and LF niches were seeded as described above. $1x10^2$ MDA231-roGFP2 cells were plated atop these niches, along with the BME Cultrex drip.

After allowing the tumour cells to fully settle into the niche, the culture medium was removed and DME/F12 containing 75 µM or 125 µM H_2O_2 was added to each well. The H_2O_2 solution was allowed to incubate in the wells for 2 hours and was then replaced with fresh serum-free DME-F12. This was repeated daily for the entirety of the ten-day experiment. Imaging settings were the same as described in the primary co-culture paragraph, as well as the Grx1-roGFP2 methods section.

Alanine studies: SkMc and LF niches were plated and cultured as described above. 1x102 MDA231-WT or MDA231-DAAO cells were seeded atop these niches, along with the BME Cultrex drip. After allowing the tumour cells to fully settle into the niche, the culture medium was removed and wells were treated with serum-free DME-F12 media containing 10 mM, 20 mM, or 100 mM D-alanine (A7377-100G, Sigma) or L-alanine (A7627-100G, Sigma). This was repeated daily for the entirety of the ten-day experiment. Imaging settings were the same as described in the primary co-culture paragraph. Additionally, 5x103 MDA231-WT or MDA231-DAAO cells were seeded on plastic and allowed to settle overnight. The next day, wells were treated with serum-free DME-F12 media containing 10 mM, 20 mM, 100 mM, or 500 mM D-alanine or L-alanine. Medium was collected at 1h, 4h, 8h, 24h and 48h timepoints and tested for H2O2 using the Amplex Red assay (A22188, Invitrogen), per manufacturer's instructions. Tumour area fraction (mCherry+) was measured at on a Zeiss CellDiscoverer7 microscope (10x magnification). For the 1h timepoint, wells were replenished with the various concentrations of D- or L-alanine in the serum-free medium. These wells were then used for the 24h and 48h timepoints. The wells used for the 4h and 8h timepoints were not used again. Tumour area fraction was also measured 72h post initial alanine treatment, though H2O2 concentrations were not measured due to the limited number of cells remaining at this timepoint.

LF-DAAO studies.

Generation and validation. To generate the LF-DAAO cell line, LF cells were infected with high-titre pLX311-HyPer3-DAAO lentivirus and selected with blasticidin (5 µg/mL) for a pure $DAAO^+$ population. Vector expression was confirmed through dose-dependent extracellular H2O2 generation (Amplex Red) upon alanine treatments. For this validation,

SkMc, LF and LF-DAAO niches were seeded at a density of 8,333 cells/well (100 µl) in 96-well culture plates. Growth media (Lonza SkGM-2 for SkMc, 10% FBS in DMEM hi-glucose for LF and LF-DAAO) was changed every other day. After 4 days, differentiation media (2% horse serum in DMEM hi-glucose) was added to both SkMc and LF wells to initiate the maturation and fusion of the myocytes. Differentiation media was refreshed every other day, for a total of 4 days. Wells were treated with serum-free DME-F12 media containing 10 mM, 20 mM, 30 mM, 40 mM, 50 mM, 70 mM or 100 mM. D-alanine or L-alanine. Medium was collected at 4h, 8h, 24h and 48h timepoints and tested for H_2O_2 using the Amplex Red assay (A22188, Invitrogen), per manufacturer's instructions. For the 4h timepoint, wells were replenished with the various concentrations of D- or L-alanine in the serum-free medium. These wells were then used for the 24h and 48h timepoints.

Co-culture. SkMc, LF and LF-DAAO niches were seeded alone at a density of 8,333 cells/well (100 µl) in 96-well culture plates. Plates were then left undisturbed on a flat surface for 15 min to allow even cell seeding prior to incubation. Growth media (Lonza SkGM-2 for SkMc, 10% FBS in DMEM hi-glucose for LF and LF-DAAO) was changed every other day. After 4 days, differentiation media was added to both SkMc and LF wells to initiate the maturation and fusion of the myocytes. Differentiation media was refreshed every other day. After an additional 4 days, mCherry-expressing tumour cells were suspended in supplement-free DMEM/F12. mCherry tumour cells were seeded at a density of 100 cells/well in a total volume of 100 μl after washing cultures twice with PBS. Cells were allowed to settle for 15 min at room temperature, then a drip of BME was added. After allowing the tumour cells to fully settle into the niche, the culture medium was removed and wells were treated with serum-free DME-F12 media containing 10 mM, 30 mM, or 50 mM D-alanine. This was repeated daily for the entirety of the five-day experiment. Tumour area fraction ($mCherry^+$) was measured at Day 0, Day 2.5 and Day 5 on a Zeiss CellDiscoverer7 microscope (10x magnification). Study endpoint was Day 5, instead of Day 10, because alanine treatment of the LF-DAAO cells caused niche rolling between Day 5 and Day 10, thus the data after this timepoint were unusable. Additionally, significant outgrowth differences were observed across the three niches within the 5-day culture window, so we could make the conclusions within this timeframe.

Collagen-I matrix studies. SkMcs or LFs were seeded alone at a density of 8,333 cells/well (100 µl) in 96-well culture plates. Plates were then left undisturbed on a flat surface for 15 min to allow even cell seeding prior to incubation. Growth media (Lonza SkGM-2 for SkMc, 10% FBS in DMEM hi-glucose for LF) was changed every other day. After 4 days, differentiation media (2% horse serum in DMEM hi-glucose) was added to both SkMc and LF wells to initiate the maturation and fusion of the myocytes. Differentiation media was refreshed every other day. After an additional 4 days, YFP- or RFP-expressing tumour cells were suspended in supplement-free DMEM/F12 (Gibco, 11330-032). YFP or RFP tumour cells were seeded at a density of 100 cells/well in a total volume of 100 μl after washing cultures twice with PBS. Cells were allowed to settle for 15 min at room temperature, then a layer of Collagen I matrix (R&D, 3447-020-01) in DMEM/F12 was slowly added to each well (final concentration: 3 mg/mL). The Collagen-I matrix condensed for 15min at room temperature before polymerizing fully at 37ºC. If required, cultures were imaged immediately after seeding on a Zeiss LSM700 confocal microscope using a 0.3 NA 10x air objective. The objective was centred to each well before acquisition of 512x512 pixel, 6x6 tiles (zoom =0.7) that captured the near-entirety of each well. Cultures were maintained with media changes every 72 hours and imaged in 2.5 day intervals.

Quantification of tumour cell outgrowth in organotypic niches. A macro was written using NIH ImageJ software to remove bias from data quantification. For the YFP channel (or RFP, depending on the cell's fluorescence), day 0 and 10 images were subjected to the following: contrast was enhanced such that 0.5% of pixels were saturated. The image was then sharpened, and a constant threshold was applied to all samples within a given experiment to eliminate variability. The total area fraction of the 6×6 tiled image occupied by YFP^+ cells was then calculated. For each image, the measured area fraction at day 10 was normalized by the corresponding day 0 value in order to account for any variations in seeding density from well-to-well. Values obtained for each condition were averaged, and these averages were subsequently normalized to the control where indicated.

Immunofluorescent staining.

Serial tissue sections (thickness: 30 *μ*m) of skeletal muscle, lungs, and brains were generated with a Leica Cryostat CM3050 S (Leica Microsystems). Sections were thawed, rehydrated in PBS and incubated in 0.1M Glycine/PBS for two hours to neutralize PFA activity. Tissues were then rinsed extensively with PBS and stained as described elsewhere. Tissue sections was incubated with the following: a rat monoclonal antibody targeting Cd49f (BD 555734, Clone GoH3, 1:250), a hamster monoclonal antibody targeting CD31 (Millipore MAB1398z, 1:300), a rabbit polyclonal to pan-laminin (Sigma L9393, 1:500), a mouse monoclonal antibody targeting laminin-2 alpha (Sigma L0663, Clone 4H8-2, 1:300), a chicken polyclonal antibody targeting GFP (Abcam ab13970, 1:1000), a rabbit polyclonal antibody targeting RFP (Rockland 600-401-379, 1:200). Proliferating cells were identified with a AlexaFluor647-conjugated monoclonal antibody targeting Ki67 (BD 561126, Clone B56, 1:100). 4′,6-Diamidine-2′-phenylindole dihydrochloride (DAPI; 2 μg/mL) was used to label cellular nuclei. Secondary antibodies used were goat anti-chicken 488, goat anti-rat 568 or 647, goat anti-rabbit 568 or 647, goat anti-mouse 647 (Invitrogen), all used at 1:500. Tissues were imaged on a Zeiss LSM 710 confocal microscope using either a 0.3 NA 10x air objective, a 0.55 NA 20x air objective or a 1.4NA 63x oil-immersion objective.

Organotypic cultures were stained after fixation (4% PFA for 15 minutes, room temperature) with AlexaFluor 568 Phalloidin (Invitrogen A12380, 1:200) to detect F-actin or with the following antibodies: rabbit polyclonal to pan-laminin (Sigma L9393, 1:500) and mouse monoclonal antibody to myosin (Sigma M4276, 1:400). Secondary antibodies used were goat anti-rabbit 488, 568 or 647 and goat anti-mouse 568 or 647 (Invitrogen), all at 1:500. DAPI (2 μg/mL) was used to label cellular nuclei. Stained organotypic cultures were imaged on a Zeiss LSM 710 confocal microscope using a 0.3 NA 10x air objective.

Bone marrow whole-mounting and immunofluorescent staining. Bone marrow wholemounts were generated as detailed by Carlson *et al*. OCT-embedded femurs were shaved at 50 μm intervals on a Leica Cryostat CM3050 S (Leica Microsystems) to expose bone marrow on one face, reversed, and sectioned to expose bone marrow on the opposite face. Sliced femurs were thawed from OCT, placed in a 1.5mL Eppendorf tube, washed

twice with PBS, and blocked overnight (4ºC) in a solution containing sterile-filtered (0.2 μm) 20% goat serum+0.5% Triton X-100 in PBS under constant, gentle agitation by circumferential rotation. Following blocking/permeabilization, bones were incubated for ~72 hours in 5% BSA containing a combination of chicken anti-GFP and rabbit anti-pan-laminin. Bones were washed the following day a minimum of 6 times in PBS before washing overnight at 4ºC. Femurs were then counterstained in 5% BSA containing DAPI (2 μg/mL) and the following secondary antibodies: donkey anti-chicken 488 (Biotium 20166, 1:400), donkey anti-rat 568 (Invitrogen, 1:400) and donkey anti-rabbit 647 (Life Tech A31573, 1:400). Femurs were washed again the following day in PBS and finally placed into a solution of PBS + 0.02% sodium azide to preserve the bone prior to imaging.

For imaging, whole-mounts were generated by gently placing femurs in aqueous mounting medium (Fluoromount-G, Southern Biotech) in a 3.5 cm plate containing a No 1.5 coverslip insert (MatTek Corporation P35G-1.5-20-C), and covering the femur with a 18x18 mm coverslip in order to press the marrow flush against the imaging window. Tile scans were generated by placing this culture dish on a Zeiss LSM700 and scanning the entire bone using four laser lines and a 0.3 NA 10x air objective to capture the entirety of the bone along with the entire imageable depth of the marrow (≤100 um). Images of individual DTCs were acquired using a 0.55 NA 20x air objective.

Lentiviral expression of eGFP, YFP, Luciferase, mCherry, Grx1-roGFP2, pLX311-HyPer3-DAAO, and TRE-MyoD/Empty vectors. 293T packaging cell line was transfected using FuGene6 (3:1 volume/weight, E2692 Promega) with 6.5 μg DNA containing the lentiviral construct of interest as well as DNA encoding the packaging proteins VSVG and pPAX2 (6.5 μg each). At the time of transfection, 293T cells were cultured in Opti-MEM media (51985034, Gibco). Media was removed 24hr after transfection and refreshed with hi-glucose DMEM with 10% FBS. Virus was harvested an additional 48–72 hrs after the media change. Lentiviral supernatant was 0.45um filtered and pelleted at 500x*g* for 10 minutes, followed by a 150x concentration step using Clontech's Lenti-X (631232, see manufacturer's protocol for details). Concentrated lentivirus was stored at -80ºC until use.

Mammalian cells were infected lentivirally by culturing in growth medium, 4 μg/mL polybrene, and concentrated lentivirus. Medium was changed the next day and then selection with antibiotic was conducted three days later. When infecting with virus encoding a construct that lacked antibiotic resistance, pure populations of fluorescent cells were flow sorted instead by gating on the 10% brightest cells.

Grx1-roGFP2 redox imaging and analysis. pEIGW Grx1-roGFP2 was a gift from Tobias Dick (Addgene plasmid # 64990; http://n2t.net/addgene:64990 ; RRID:Addgene 64990). Grx1-roGFP2 imaging settings and validation were followed in accordance with a previously published protocol by Morgan *et al*[60]. The Grx1-roGFP2 biosensor was excited using the 405 nm and 488 nm laser line and detected the emission through a 500–554 nm bandpass filter on a Zeiss LSM700 confocal microscope. Snaps of the region of interest were taken at 10x magnification (0.3 NA 10x air objective) and saved as .lsm files. Raw data were exported to ImageJ software as 16-bit .tif and converted for 32-bit images for analysis. The background was subtracted and a threshold set per channel to avoid analysis-created artifacts. Ratiometric images were created by dividing the 405nm (oxidized) channel by the 488 nm (reduced) channel, pixel by pixel. ImageJ LookUp Table 'Fire' was used to create false-coloured composite images. Numerical values were generated by plotting the Z-profile for each composite 405nm/488nm image. For Grx1-roGFP2 imaging of DTCs within lung and skeletal muscle, we followed published methods by Fujikawa *et al*.[61] for redox stabilization and tissue processing steps. Imaging settings were consistent with those described for cultured cells.

Amplex Red Extracellular H_2O_2 Assay. The manufacturer's protocol was followed for this assay (Invitrogen, A22188). 100 µl conditioned media was removed from the experimental 96-well plate and placed directly into a new 96-well plate. To maintain a 1:1 ratio, 100 µl of the Amplex Red reagent/HRP solution (100 µM Amplex Red reagent, 0.2U/mL HRP, 1x Reaction Buffer) was then added to each well. The reactions were incubated for 30 minutes at room temperature, protected from light. A serial dilution of H_2O_2 was included as a positive control and was used to generate a standard curve. For a negative control, 1X Reaction Buffer without H_2O_2 was included. A media-only control was also included to

account for baseline noise. Fluorescence was measured on a SpectraMax microplate reader, using an excitation of 530–560 nm and emission detection at ~590 nm. H_2O_2 measurements were generated based on standard curve and baseline subtraction of no-H_2O_2 media-only control.

CellROX Deep Red 647 ROS Assay. The manufacturer's protocol was followed for this assay (C10422, Molecular Probes by Fisher Scientific). 100 µl of 10 µM CellROX reagent was added to experimental wells in a 96-well plate containing the cells of interest covered by the ~100 µl BME Cultrex/media layer (final concentration of CellROX reagent ~5 µM). The wells were incubated for 1 hour at 37ºC to enable full penetration of the basement membrane layer and incorporation into the cells. After incubation, the media was removed, and wells washed thrice with 1x PBS. Wells were imaged immediately on a Zeiss LSM700 confocal microscope (0.3 NA 10x air objective). CellROX Deep Red has excitation/emission maxima at ~644/665 nm.

MitoTracker Green Mitochondrial Dye. The manufacturer's protocol was followed for this assay (M7514, Invitrogen). 100 µl of 200 nM MitoTracker reagent was added to experimental wells in a 96-well plate containing the cells of interest covered by the ~100 µl BME Cultrex/media layer (final concentration of MitoTracker reagent ~100 nM). The wells were incubated for 1 hour at 37ºC to enable full penetration of the basement membrane layer and incorporation into the cells. After incubation, the media was removed, and wells washed thrice with 1x PBS. Wells were imaged immediately on a Zeiss LSM700 confocal microscope (0.3 NA 10x air objective). MitoTracker Green has excitation/emission maxima at ~490/516 nm. When used in conjunction with CellROX DeepRed 647, both reagents are prepped as described above and added to each well together.

Quantification of CellROX intensity. Raw data exported as 8-bit or 12-bit .tif files were analysed using CellProfiler, an open-source software, to quantify: i) ROS intensity in tumour cells; ii) ROS intensity in muscle cells and iii) mitochondrial ROS intensity in tumour cells. (i) Tumour cells were identified as objects found within the immunofluorescent channel pertaining to the tumour cell's fluorescent marker (mCherry or GFP) and refined based on

shape, size and intensity of the objects. Tumoural ROS were identified by measuring the pixel intensity found in the ROS channel (CellROX647) within the confines of the objects identified as tumour cells. The ROS intensity values in the manuscript refer to the mean pixel intensity within each cell's area in the corresponding ROS channel image. (ii) Muscle cells were identified as objects found in the ROS channel (CellROX647) and refined based on shape, size and intensity. A mask was applied to exclude tumour cell populations in the muscle cell quantification. ROS intensity is reported as described above. Myotube intensity was found using ImageJ, an NIH open-source software. Myotubes were manually selected from the ROS channel images and their average pixel intensities were recorded. A second CellProfiler pipeline again quantified tumour and muscle cell ROS intensity, this time excluding the myotubes by masking out the selected regions to obtain separate data for myocytes and myotubes. (iii) To measure mitochondrial ROS, tumour cells were first identified as objects found within immunofluorescent channel pertaining to the tumour cell's fluorescent marker (mCherry, 568) and refined based on shape, size and intensity of the objects. Tumour cell mitochondria were defined as objects that existed in the 488 channel (MitoTracker Green 488 dye) and overlapped with objects in the primary tumour cell mask. Mitochondrial ROS in tumour cells were identified by measuring the pixel intensity found in the ROS channel (CellROX647) within the confines of the objects identified as mitochondria. ROS intensity values in the manuscript refer to the mean pixel intensity. With the exception of outlining myotube areas, this analysis was automated and did not require subjective user input.

Retroviral expression of pBMN-mCAT, pBMN-cCAT and pTS1-mCherry. Expression of mitochondrial catalase (pBMN-IRES-GFP-mCAT), cytosolic catalase (pBMN-IRES-GFP-cCAT), and empty vector control (pMBN-IRES-GFP, termed "Ctl") in MDA-MB-231 and EO771 was achieved through retroviral transfection. pTS1-mCherry expression in EO771 was also achieved through retroviral transfection. First, Phoenix Ampho packaging cell line were transfected using FuGene6 (3:1 v/w, E2692 Promega) with 12 μg DNA containing the retroviral expression vector of interest. At the time of transfection, Phoenix Ampho cells were cultured in Opti-MEM media (51985034, Gibco). Media was removed 24hr after transfection and refreshed with hi-glucose DMEM with 10% FBS. Virus was harvested an

additional 48–72 hrs after the media change. Retrovirus supernatant was 0.45μm filtered and pelleted at 500*g* for 10 minutes. The retrovirus was then 150x concentrated using Clontech Retro-X (631455, see manufacturer's protocol for details). Concentrated retrovirus was stored at -80ºC until use.

Mammalian cells were infected by culturing in hi-glucose DMEM with 10% FBS, 4 μg/mL polybrene, and concentrated retrovirus. Medium was changed the next day and after at least seven days of culture, pure populations of fluorescent cells were flow sorted by gating on the 10% brightest cells.

Western blotting. Tumour cells were lysed in 2% SDS/PBS containing cOmplete protease inhibitor cocktail (11697498001, Roche) and PhosSTOP phosphatase inhibitor cocktail (4906845001, Roche). Lysate (20-40 μg) was then separated on a Tris-Glycine 4-20% gel. Human and murine catalase were probed with a rabbit monoclonal antibody (Abcam ab16731, 1:2000). Loading of each lane was assayed by probing simultaneously for b-actin using a mouse polyclonal antibody (Sigma A5441, Clone AC-15, 1:7500). Blots were developed on a Li-Cor Odyssey. Densitometry was performed on Odyssey software v3.0.

Metabolomics.

Sample Collection: Lung and skeletal muscle (TA and bulk muscles from the upper arm) were collected upon necropsy and imaged for mCherry$^+$ 4T1-SkM lesions (Zeiss AxioZoom). Once a mCherry$^+$ lesion was identified, the region was excised, leaving as little tissue margins as possible. The sample was weighed and then flash frozen using LN_2. Healthy lung and skeletal muscle samples were collected through the same process, without the mCherry imaging step. 4T1-parental and 4T1-SkM cells were plated in 6-well plates at an initial density of 50,000 cells/well and collected 48h later (final density ~275,000 cells/well). Wells were washed twice with 1x PBS and cells were scraped into 1.5 mL microcentrifuge tubes and spun at 16,000 x g for 3 minutes. Samples were then flash frozen and stored at -80°C until ready to process.

Preparation: Prior to LC-MS analysis, tissue samples were weighed and resuspended in pre-chilled (-20°C) methanol:acetonitrile:water (5:3:2, v:v) to a final concentration of 30 mg/ml, cell samples were placed on ice and re-suspended with methanol:acetonitrile:water (5:3:2, v:v) at a concentration of $2x10^6$ cells/mL, and media samples were extracted with the same solution at a dilution of 1:25 (v/v). Suspensions were vortexed continuously for 30 min at 4°C. Insoluble material was removed by centrifugation at 18,000 g for 10 min at 4°C and supernatants were isolated for metabolomics analysis by UHPLC-MS. Analyses were performed as previously published. Injection volumes for tissue, cell, and media extracts were 2 μL, 10 μL, and 10μL, respectively. The analytical platform employs a Vanquish UHPLC system (ThermoFisher) coupled online to a Q Exactive mass spectrometer (ThermoFisher). Samples were resolved over a Kinetex C18 column, 2.1 x 150 mm, 1.7 μm particle size (Phenomenex, Torrance, CA) equipped with a guard column (SecurityGuard™ Ultracartridge – UHPLC C18 for 2.1 mm ID Columns – AJO-8782 – Phenomenex, Torrance, CA) using an aqueous phase (A) of water and 0.1% formic acid and a mobile phase (B) of acetonitrile and 0.1% formic acid for positive ion polarity mode, and an aqueous phase (A) of water:acetonitrile (95:5) with 1 mM ammonium acetate, and a mobile phase (B) of acetonitrile:water (95:5) with 1 mM ammonium acetate for negative ion polarity mode. Samples were eluted from the column using either an isocratic elution of 5% B flowed at 250 μL/min and 25°C or a gradient from 5% to 95% B over 1 min, followed by an isocratic hold at 95% B for 2 min, flowed at 400 μL/min and 45°C. The Q Exactive mass spectrometer (ThermoFisher) was operated independently in positive or negative ion mode, scanning in Full MS mode (2 μscans) from 60 to 900 m/z at 70,000 resolution, with 4 kV spray voltage, 45 sheath gas, 15 auxiliary gas. Calibration was performed prior to analysis using the Pierce™ Positive and Negative Ion Calibration Solutions (ThermoFisher). Acquired data was then converted from raw to mzXML file format using Mass Matrix (Cleveland, OH). Samples were analyzed in randomized order with a technical mixture injected periodically through analysis to qualify instrument performance. Metabolite assignments, isotopologue distributions, and correction for expected natural abundances of deuterium, ^{13}C, and ^{15}N isotopes were performed using MAVEN (Princeton, NJ).

Analysis: Comparisons (>2-fold increase or 50% decrease, $P<0.1$) were made for: 1) skeletal muscle metastasis versus healthy skeletal muscle, 2) lung metastasis versus healthy lung, and 3) Comparison (1) versus Comparison (2). MetaboAnalyst5.0 was used for MSEA, implementing KEGG's 'metabolism-related metabolite set' library. ORA was implemented using the hypergeometric test to evaluate whether a particular metabolite set is represented more than expected by chance within the given compound list. One-tailed *P* values are provided after adjusting for multiple testing. Fold-enrichment is calculated by dividing the observed number of hits by the expected number of hits ("Hits" / "Expect" columns of the ORA). Heatmaps were generated using the Broad Institute's Morpheus software: https://software.broadinstitute.org/morpheus.

Proteomic analysis of C57BL/6 injured skeletal muscle.

Sample Preparation. Tibialis anterior muscles were collected one-week post-$BaCl_2$ treatment and individually flash frozen on dry ice prior to storage at –80 °C until analysis. Prior to analysis, samples were thawed and homogenized in freshly prepared high-salt buffer (50 mM Tris-HCl, 3 M NaCl, 25 mM EDTA, 0.25% w/v CHAPS, pH 7.5) containing 1× protease inhibitor (Halt Protease Inhibitor, Thermo Scientific) at a concentration of 10 mg/mL. Homogenization took place in a bead beater (Bullet Blender Storm 24, Next Advance, 1 mm glass beads) for 3 min at 4 °C. Samples were then spun for 20 min @18,000g at 4 °C, and the supernatant removed and stored as Fraction 1. A fresh aliquot of high-salt buffer was added to the remaining pellet at 10 mg/mL of the starting weight, vortexed at 4 °C for 15 min, and spun for 15 min. The supernatant was removed and stored as Fraction 2. This high-salt extraction was repeated once more to generate Fraction 3, after which freshly prepared guanidine extraction buffer (6 M guanidinium chloride adjusted to pH 9.0 with NaOH) was added at 10 mg/mL and vortexed for 1 hour at room temperature. The samples were then spun for 15 min, the supernatant removed, and stored as Fraction 4 (sECM). Fractions 1, 2, & 3 (Cellular) were combined and all fractions were stored at –80 °C until further analysis.

Hydroxylamine (NH2OH) Digestion. The remaining pellets from each tissue, representing insoluble ECM proteins, were digested with hydroxylamine as previously

described69. Briefly, after chaotrope extraction pellets were treated with freshly prepared hydroxylamine buffer (1 M NH2OH-HCl, 4.5 M guanidine-HCl, 0.2 M K2CO3, pH adjusted to 9.0 with NaOH) at 10 mg/mL of the starting tissue weight. The samples were briefly vortexed, then incubated at 45 °C with vortexing for 16 hours. Following incubation, the samples were spun for 15 min at 18,000 × g, the supernatant removed, and stored as Fraction 5 (iECM) at –80 °C until further proteolytic digestion with trypsin. The final pellet was stored at –80 °C until further analysis.

Trypsin Digestion. For each sample, 200 µL of the Cellular fraction, and 100 µL of the sECM and iECM fractions, respectively, were subsequently subjected to reduction, alkylation, and enzymatic digestion with trypsin. A filter-aided sample preparation (FASP) approach, as well as C18 cleanup, was performed as previously described70.

LC-MS/MS Analysis. Samples were analyzed on an Q Exactive HF mass spectrometer (Thermo Fisher Scientific) coupled to an EASY-nanoLC 1000 system through a nanoelectrospray source. The analytical column (100 µm i.d. × 150 mm fused silica capillary) was packed in house with 2.7 µm 80 Å Cortex C18 resin (Phenomenex; Torrance, CA)). The flow rate was adjusted to 400 nL/min, and peptides were separated over a 120-min linear gradient of 4–28% ACN with 0.1% FA. Data acquisition was performed using the instrument supplied Xcalibur™ (version 2.1) software. The mass spectrometer was operated in positive ion mode. Full MS scans were acquired in the Orbitrap mass analyzer over the 300–2000 m/z range with 60,000 resolution. Automatic gain control (AGC) was set at 1.00E+06 and the fifteen most intense peaks from each full scan were fragmented via HCD with normalized collision energy of 28. MS2 spectra were acquired in the Orbitrap mass analyzer with 15,000 resolution with AGC set at 1.00E+05. All replicates of each tissue were run sequentially and pre-digested yeast alcohol dehydrogenase standard (nanoLCMS Solutions LLC, Rancho Cordova, CA) was run between sample groups to monitor drift in analytical performance.

Database Searching and Protein Identification. MS/MS spectra were extracted from raw data files and converted into .mgf files using Pava (UCSF). Peptide spectral matching was

performed with Mascot (Ver. 2.5) against the Uniprot mouse database (release 201701). Mass tolerances were +/– 10 ppm for parent ions, and +/– 0.2 Da for fragment ions. Trypsin specificity was used for cellular and sECM fractions, allowing for 1 missed cleavage. For iECM fraction, C-terminal N and trypsin were used, allowing for 1 missed cleavage. Met oxidation, Pro hydroxylation, protein N-terminal acetylation, and peptide N-terminal pyroglutamic acid formation were set as variable modifications with Cys carbamidomethylation set as a fixed modification. Scaffold (version 4.4.6, Proteome Software, Portland, OR, USA) was used to validate MS/MS based peptide and protein identifications. Peptide identifications were accepted if they could be established at greater than 95.0% probability as specified by the Mascot scoring algorithm. Protein identifications were accepted if they could be established at greater than 99.0% probability and contained at least two identified unique peptides. MetaboAnalyst was used for multivariate analysis of proteomic data.

pLX311-HyPer3-DAAO-NES Cloning. pAAV-HyPer-DAAO-NES was a gift from Thomas Michel (Addgene plasmid #119164 ; http://n2t.net/addgene:119164 ; RRID:Addgene 119164). The HyPer3-DAAO-NES sequence was cloned into lentiviral construct, pLX311-Luciferase (Addgene 11773), using an In-Fusion HD Cloning Plus Kit (638909, Takara Bio). The HyPer3-DAAO-NES sequence was excised from the pAAV vector at EcoRI and HindIII restriction sites. The luciferase sequence was removed from the pLX311 backbone at NheI and EcoRV restriction sites. The HyPer3-DAAO-NES sequence and pLX311 backbone was purified using a NucleoSpin Gel and PCR Clean-up kit (740609.10, Macherey-Nagel). Target fragments were amplified using CloneAmp HiFi PCR Premix (639298, Takara Bio) and gel electrophoresis run to extract the fragment of interest. Fragments were again purified. In-Fusion cloning reactions ligated the HyPer3-DAAO-NES sequence into the pLX311 backbone. The new pLX311-HyPer3-DAAO-NES vector was then transformed into Stellar competent cells (provided in the In-Fusion Cloning Plus kit) and grown up on ampicillin^{+} LB plates. DNA was isolated (GenElute Plasmid Miniprep Kit, PLN70-1KT) from single colonies and sequenced for correct insertion. Cloning primers: Fw - gtgtcgtgaggctagcgccaccatggagatggcaagc; Rv - gataggcttaccgatatcttacagggtcagccgctccag

Generation of the CRISPR knockout 4T1-SkM3met cell lines. To knock out our genes of interest, we utilized a lentiviral ZCLv2-CRISPR-hygromycin vector, where each lentivirus contained 4 pooled guides per gene. The original backbone, ZCLv2-CRISPR was purchased from Addgene (Plasmid #52961) and the Zhang Lentiviral CRISPRv2 (ZLCv2; Broad Institute) cloning protocol was used to assemble the ZLCv2-CRISPR. Single guide RNA (sgRNA) for the genes of interest was selected based on the Broad Brie Library. Non-targeting guides were used to control for viral transfection and introduction of the CRISPR/Cas9 system (controls: sgCTL1, -sgEGFP1, -sgEGFP2). After construction, final plasmids were sequenced from correct

To make the lentivirus, 293T packaging cell line was transfected using FuGene6 (3:1 volume/weight, E2692 Promega) with the transgene: viral packaging (psPAX2): viral envelope (pMD2G) constructs at a ratio of 6:4:1.5 DNA. At the time of transfection, 293T cells were cultured in Opti-MEM media (51985034, Gibco). Media was removed 24hr after transfection and refreshed with hi-glucose DMEM with 10% FBS. Virus was harvested an additional 48–72 hrs after the media change. Lentiviral supernatant was 0.45μm filtered and pelleted at 500g for 10 minutes, followed by a 150x concentration step using Clontech's Lenti-X (631232, see manufacturer's protocol for details). Concentrated lentivirus was stored at -80°C until use.

4T1-SkM3met cells were lentivirally infected by culturing in growth medium, 4 μg/mL polybrene, and the lentivirus described above. Medium was changed after 48 hours and then selection with hygromycin was conducted three days later.

Statistics and Reproducibility. Statistical analyses were conducted with GraphPad Prism 7 software. Data that were distributed normally were compared via unpaired, two-tailed t test (if only two conditions were tested) or via one- or two-way ANOVA (for experiments containing three or more conditions). A one-way ANOVA was used when the experiment contained only one independent variable, whereas a two-way ANOVA was used when the experiment contained two independent variables. Post-testing to correct for multiple comparisons was chosen based on whether a decision was made a priori to compare

conditions to untreated (Dunnett's), or to compare all treatment groups with each other (Tukey's). If multiple comparisons were made but tested independently of each other, Sidak's multiple comparisons test was used. Please refer to figure legends for individual n- and *P*- values, and the specific statistical test(s) employed. Unless noted otherwise, data are reported such that the centre line represents the mean, and error bars represent the s.e.m. Data depicted in the figures represent one experiment with multiple technical replicates, unless otherwise noted. Experiments were repeated independently with similar results. MSEA results were ranked using open-source MetabAnalyst5.0 software.

Chapter 3. Unchecked oxidative stress is an insurmountable barrier for tumour cells that disseminate to skeletal muscle

Chapter is adapted from a manuscript under revision by Crist et al., Nature Cell Biology

Abstract.

Skeletal muscle has long been recognized as an inhospitable site for disseminated tumour cells (**DTCs**), yet its antimetastatic nature has eluded a thorough mechanistic description. Here, we show that DTCs traffic to and persist within skeletal muscle in mice and in humans, raising the question as to how this tissue suppresses colonization. We employed mouse and organotypic culture models along with metabolomic profiling, which suggested that skeletal muscle imposes a sustained oxidative stress on DTCs to attenuate their proliferation. Functional studies demonstrated that disrupting redox homeostasis via chemogenetic induction of reactive oxygen species slowed proliferation in a more fertile site (the lung). Conversely, enhancing antioxidant potential of tumour cells via ectopic catalase overexpression allowed robust colonization of skeletal muscle. These findings reveal a profound metabolic bottleneck imposed on DTCs and sustained by skeletal muscle. Understanding this biology could reveal novel DTC vulnerabilities.

Introduction.

To successfully metastasize, a tumour cell must not only traffic to and survive within a distant tissue, but also colonize it. It is this proliferative phase of metastasis, and the accompanying destruction of the host organ's architecture and function, that accounts for the high incidence of cancer-related mortality.

Breast cancer exhibits a predilection for metastasizing to specific organs such as lung, liver, and bone. Stephen Paget's autopsy study laid a foundation for understanding the organotropic nature of tumour spread by hypothesizing that tumour "seeds" are capable of thriving in some but not all human "soils"[1]. Decades of work to mechanistically dissect this phenomenon of organotropism revealed a number of underlying mechanisms— including metabolic adaptation[2–7], stromal co-option[8–12], engagement with extracellular matrix (**ECM**)[13–21] and immune evasion[22–24] – that disseminated tumour cells (**DTCs**) employ to survive and thrive within foreign environments. Failure to acclimate often results in DTC

death or temporary or permanent exit from the cell cycle (quiescence and senescence, respectively[25,26]). Therefore, the ultimate success of DTCs is dictated by how extensively the host organ microenvironment can be corrupted. A number of studies have enumerated mechanisms by which primary tumours or various insults facilitate outgrowth of DTCs within distal sites that commonly succumb to metastasis, such as the lung[9–11,14,15,27]. Far less attention has been paid to why certain sites are inhospitable to DTCs, and cannot be subverted by common insults that disrupt tissue homeostasis. Such sites could reveal unique mechanisms of suppressing metastatic outgrowth.

Of these sites, one could argue that skeletal muscle represents the most metastasis suppressive tissue in our bodies. While it is frequently *invaded* by tumours[28] (e.g., the pectoral muscles by mammary cancer), blood-borne metastases are exceedingly rare. For example, in a metanalysis of autopsies from 3,827 individuals who succumbed to 41 different primary cancers, skeletal muscle metastases were identified in only 16 patients (0.4%)[29]. Considering the mass of skeletal muscle in the typical human far exceeds that of other tissues, a compelling question is why skeletal muscle is so rarely colonized by tumour cells.

Three other groups have asked this question, proposing tumour suppressive mechanisms related to skeletal muscle mechanics, lineage specification and soluble effectors[30–34]. Denervation studies showed that inoculated tumour cells readily proliferate within skeletal muscle when electrical or mechanical stimulation is absent, suggesting that skeletal muscle's distinctive contractile nature is the foundation of tumour suppression[30]. In a separate study, melanoma cells delivered to the tibialis anterior adopted a myogenic program, fusing with myofibers and downregulating lineage-specific factors[31]. More extensive studies on this subject demonstrated that skeletal muscle conditioned medium inhibits the growth of several different tumour cell types in culture[32]. Adenosine was identified as one of the factors in the conditioned medium that reprised tumour suppression in culture[33]; however, in pre-clinical models adenosine compounds were ineffective[34]. Therefore, convincing mechanisms underlying skeletal muscle-mediated metastasis suppression remain elusive. We hypothesized that careful examination of the interplay between the skeletal muscle microenvironment and DTCs that reside within might reveal

skeletal muscle-specific means of metastasis suppression and, in doing so, hint to universal vulnerabilities that may be exploited to prevent metastasis[35].

Here, we draw a contrast between the behaviour of DTCs in skeletal muscle, an inhospitable tissue, and lung, an organ prone to metastasis. We show definitively that tumour cells transit to skeletal muscle and survive there – in mice and in humans – but find no evidence of colonization at this site. To arrive at mechanisms underlying this profound suppression of DTCs, we employ mouse- and culture- models coupled with metabolomics and identify metabolic barriers that inhibit breast cancer cell outgrowth in the skeletal muscle microenvironment. Specifically, we find that that DTCs in the skeletal muscle niche are highly oxidized due to sustained environmental hydrogen peroxide (**H_2O_2**) exposure as well as endogenous induction of reactive oxygen species (**ROS**). Through a series of functional studies, we demonstrate that unchecked oxidative stress impedes DTC progression - even in a permissive niche like lung - and that enhancing antioxidant capacity permits colonization of skeletal muscle. These studies and analysis of compartment-specific ROS levels implicate mitochondrial ROS as particularly detrimental to DTC colonization of skeletal muscle. Together, these findings implicate oxidative stress as a barrier DTCs must overcome to colonize distant organs, and show that the ability of skeletal muscle to sustain this stress is at the heart of its antimetastatic nature.

Results.

Dissemination to skeletal muscle is not a rare event. To determine if breast cancer cells spontaneously disseminate to skeletal muscle, we interrogated skeletal muscle biospecimens from metastatic breast cancer patients for the presence of DTCs (**Fig. 3.1a**). Patients who consented to donate tissue post-mortem were enrolled in the BROCADE rapid autopsy project. Two donors had been diagnosed with estrogen receptor-positive (**ER^+**) and progesterone receptor-positive (**PR^+**) metastatic breast cancer, so we utilized these markers paired with pan-cytokeratin (**pan-CK**), an epithelial cell marker, in an attempt to identify breast tumour cells in the quadriceps, tibialis anterior (**TA**) or gastrocnemius. This antibody cocktail positively stained tumour cells within the breast (**Fig. 3.1b**, **Supplementary Fig. 3.1a**), but did not stain resident cells from donors with no documented history of cancer (**Supplementary Fig. 3.1b**). To our surprise, given the limited amount of tissue sampled

(approximately 200 μm of each muscle), we found multiple individual $ER^+/PR^+/panCK^+$ breast cancer cells located both in- and out-side of the microvasculature in the quadriceps muscle (**Fig. 3.1b, Supplementary Fig. 3.1c-f**). These data demonstrate that breast tumor cells spontaneously disseminate to the skeletal muscle of humans. Given the limited number of patients and tissues sampled, this may even be a common occurrence. But it is impractical to quantify the frequency of tumour dissemination to skeletal muscle in humans. So we next turned to mice, where we could apply higher throughput assays to assess the frequency of skeletal muscle dissemination.

To measure DTC burden in the skeletal muscles following spontaneous dissemination in mice, we orthotopically injected $1x10^6$ firefly luciferase-enhanced green fluorescent protein-expressing MDA-MB-231 cells (ffluc-eGFP-MDA-MB-231) into the inguinal mammary gland of female NSG mice (**Fig. 3.1c**). Primary tumours were surgically resected once they reached a volume of ~200mm^3. Three weeks post-resection, bioluminescence imaging (**BLI**) revealed that all mice had substantial metastatic burden in their lungs, warranting necropsy per our study design. We then compared DTC burden in lung and skeletal muscle via two parallel and complimentary assays: i) primate-specific Alu qPCR to measure the quantity of human AluYb8 DNA found in lung and in three skeletal muscle sites (TA, quadriceps and gastrocnemius), and ii) imaging of Ce3D-cleared[36] whole tissues to measure burden of GFP^+ human MDA-MB-231 breast cancer cells in paired, contralateral tissue.

Alu qPCR takes advantage of repetitive transposable elements that make up ~11% of the human genome[37] and are primate specific[38] to detect human breast cancer cells in mice[39–41]. Applying a modified version of this method to amplify AluYb8 repeats from MDA-MB-231 diluted serially (log-fold) in murine bone marrow cells (OP-9) demonstrated statistically reliable detection of one human cell in 10^6 murine cells, using pure OP-9 and water (no DNA template) as negative controls (**Fig. 3.1d-e**). With a method in hand that allowed sensitive identification of rare human cells in murine tissue, we proceeded to quantitatively assess DTC burden in of skeletal muscle.

AluYb8-qPCR revealed substantial metastatic burden in lung, consistent with observed BLI signal (**Fig. 3.1c,f**). When compared to uninoculated mice, we observed a 7.5-fold increase of human AluYb8 DNA in lung. We also observed an increase in AluYb8

signal from all skeletal muscle sites, ranging from a 3.5-fold increase in the quadriceps, a 2.6-fold increase in the gastrocnemius, and a 2.3-fold increase in the TA (**Fig. 3.1f**). Analysis of GFP burden in cleared tissues led to similar conclusions. GFP^+ tumour cells occupied a greater percentage of lung tissue (8.6%) than any of the three skeletal muscles assessed (1.2% of the TA, 0.16% of the quadriceps, or 0.08% of the gastrocnemius). But – GFP^+ tumour cells were identified in all three skeletal muscle sites (**Fig. 3.1g-h**).

These data substantiate our observations in human that spontaneous dissemination to skeletal muscle is not a rare event. We wished to go beyond this however to determine whether the differences observed at endpoint were a result of enhanced trafficking to lung, compared to TA, quadriceps or gastrocnemius. Spontaneous dissemination models like the one employed above result in a number of confounders from mouse to mouse (e.g., variations in rates of primary tumour growth and dissemination from mouse-to-mouse). Therefore, we employed an experimental model of metastasis, where injecting a prescribed number of cells directly into the left ventricle ensures equal input across mice, to address this question (**Supplementary Fig. 3.2a**). Quantification of the human AluYb8 DNA across brain, lung, liver, bone marrow, TA, quadriceps, and gastrocnemius three days post-intracardiac (**ic**) injection revealed that dissemination to muscle is not rate-limiting. Indeed, AluYb8 signal in TA was equivalent to that of lung at this early timepoint (**Supplementary Fig. 3.2b,** confirmed visually in a subset of tissues in **Supplementary Fig. 3.2c**). Analysis of the same set of tissues seven-weeks after ic injection let us confirm if suppression manifested even after equivalent cellular fractions reached the lung and TA. AluYb8-qPCR revealed that lung had the highest DTC burden across all animals (3-fold increase compared to control) at this timepoint (**Supplementary Fig. 3.2d**), consistent with the array of studies that utilize this model to study lung metastasis. Although dissemination to brain was high initially (**Supplementary Fig. 3.2b**), DTC persistence in brain was largely unsuccessful (**Supplementary Fig. 3.2d**). This is in line with intravital fate mapping studies conducted by our lab showing a large percentage of parental MDA-MB-231 cells reside within the vasculature three days following ic injection, and that the vast majority of these fail to survive[43]. More importantly, the assay revealed that: (i) despite trafficking to the TA and lung at equivalent levels, DTCs can emerge in lung fail to in TA, confirming that skeletal muscle is more resistant to metastasis in this model; (ii) DTCs persist for at least seven

weeks in multiple skeletal muscle sites at or above the frequency found in some bone marrow, liver and brain specimens, all of which are far more common sites of overt metastasis (**Supplementary Fig. 3.2d**); and (iii) persistence of DTCs in skeletal muscle was not rare, given the high penetrance observed in this model (**Supplementary Fig. 3.2d**). Examination of matched tissue samples via immunofluorescence confirmed the presence of DTCs within the TA (**Supplementary Fig. 3.2e**). Interestingly, when tumour cells were identified within skeletal muscle, they commonly resided on or near the basal lamina of a myofiber and were not proliferating (i.e., $Ki67^{-}$), in contrast to tumour cells found in other tissues (**Supplementary Fig. 3.2e-f**), suggesting that the niche surrounding skeletal muscle myofibers suppresses DTC outgrowth. Taken together, these data show that MDA-MB-231 breast tumour cells traffic to, extravasate into and persist within multiple skeletal muscles. They also draw attention to the myofiber niche as a potential source of DTC suppression.

Skeletal muscle myocytes suppress outgrowth of breast and mammary cancer cells in culture, but not through a transferrable factor. Using classic differentiation protocols[43], we observed that primary human skeletal muscle myocytes (**SkMc**) robustly generated myotubes, the multinucleated structures that approximate myofibers of the human and mouse tissue (**Fig. 2a-b**). Seeding breast tumour cells onto lung stroma (primary human lung fibroblasts, **LF**s) or SkMc-derived myotubes allowed us to compare breast tumour cell outgrowth between a permissive niche (lung) and one we suspected was suppressive **(Fig. 3.2a-b**).

Over a ten-day period, the SkMc niche significantly and substantially suppressed the growth of five highly metastatic breast cancer (MDA-MB-231, Hs578T, BT549, HCC70, MDA-MB-468) and two mammary cancer (4T1, EO771) cell lines when compared to outgrowth on LFs (**Fig. 3.2c-d**). On average, outgrowth on SkMcs was only 13%, 31%, 21%, 27%, and 23% of outgrowth measured on LFs for MDA-MB-231, HCC70, BT549, Hs578T, and MDA-MB-468, respectively. Average outgrowth on SkMc was only 6.9% and 2.3% of outgrowth measured on LFs for EO771 and 4T1, respectively.

How were myotubes so drastically suppressing tumour cell outgrowth? Our initial hypotheses were rooted in prior work defining soluble and insoluble microenvironmental factors that regulate DTC dormancy and outgrowth in organs that eventually succumb to

metastasis[10,11,17,44]. Mechanisms identified in these studies pointed to secretory molecules[8,45], vesicular cargo[10,16–18], and/or interaction with ECM[19,21,27] as metastasis mediators. To examine two of these potentially suppressive SkMc-derived fractions, SkMc-derived -conditioned medium (**CM**) and -extracellular vesicles (**EV**) were applied to LF and SkMc niches seeded with MDA-MB-231-YFP tumour cells. MDA-MB-231 outgrowth on LF and SkMc niches was unaltered by daily treatment with SkMc-CM (**Fig. 3.2e**). Suppression of tumour cell outgrowth was not observed when increasing doses of SkMc-EVs were added to MDA-MB-231 cells on LF, either, indicating that a suppressive factor is not delivered via SkMc-derived EVs (**Fig. 3.2f**). To test whether SkMc-derived ECM suppressed tumour cell outgrowth, MDA-MB-231-YFP cells were seeded onto decellularized LF or SkMc cultures. MDA-MB-231 cells proliferated 1.5-fold more on decellularized SkMc cultures (where ECM is the primary constituent left behind[46]) than decellularized ECM, casting doubt on the notion that SkMc-derived ECM suppresses breast tumour cell outgrowth (**Fig. 3.2g**). In fact, MDA-MB-231 outgrew to a substantially greater degree (four-times more) on decellularized SkMcs than they did on intact (live) SkMc niches, suggesting that live myotubes were critical for growth suppression. To test this hypothesis, we performed a SkMc-LF mixing experiment, where the ratio of SkMcs to lung fibroblasts was sequentially increased (LF to SkMc ratios of 1:1, 1:10, 1:20, 1:50 and 1:100). Tumour outgrowth inversely correlated with the percentage of SkMc myotubes present (**Fig. 3.2h**), confirming that live myotubes suppress tumour cell outgrowth.

The failure of SkMc-derived CM, EVs and ECM to recapitulate the suppressive effect that live, differentiated SkMcs have on breast and mammary cancer cell growth suggests that: i) competition for key nutrients by live SkMcs is a critical element of growth suppression, and/or ii) the suppressive component is transient and/or reactive. Both possibilities raised suspicion that skeletal muscle metabolism may underlie its metastasis-suppressive nature.

Metabolomics of skeletal muscle, lung and metastases within these organs suggest that glutathione metabolism plays a role in skeletal muscle-mediated metastasis suppression. Based on a growing body of evidence that metastases evolve towards the metabolism of their host tissue[4,47–49], we designed an experiment to define metabolic adaptations required

specifically for colonization of skeletal muscle. Our reasoning was that understanding these adaptations might reveal what the metabolic obstacles are in the first place, and thus explain why skeletal muscle colonization is such a rare event.

Though infrequent, we found that skeletal muscle metastases do occur occasionally when the highly metastatic mammary cancer line 4T1 is inoculated in a syngeneic (Balb/c) host. We leveraged this finding and, inspired by Fidler[50] and Massagué[44,51,52], serially passaged a 4T1 subline derived from a rare skeletal muscle metastasis through Balb/c mice to achieve a 4T1 derivative that effectively colonized skeletal muscle (termed "**4T1-SkM**", **Fig. 3.3a**). Ten thousand skeletal muscle-tropic 4T1-SkM cells were ic injected into Balb/c mice. Upon necropsy, metastatic lesions in lung and skeletal muscle were excised. Metabolomics was performed on the excised metastatic lesions to contrast with healthy tissues from uninoculated mice. Cultured 4T1-parental and 4T1-SkM cell lines collected from culture were run as controls.

First, we compared 4T1-parental cells with muscle-metastatic 4T1-SkM cells in culture against the tissue-based sample set (isolated muscle and lung metastases, healthy muscle and lung) to paint a more complete picture of how 4T1 cells adapt metabolically as they gain capacity to colonize skeletal muscle. Though the 4T1-parental and 4T1-SkM cell lines are metabolically distinct when compared to each other (**Supplementary Fig. 3.3a**), cultured 4T1-parental cells scored closer to lung tissue and lung metastases – which were statistically indistinct from one another – than 4T1-SkM cells (**Supplementary Fig. 3.3a**). On the other hand, 4T1-SkM cells shifted towards healthy skeletal muscle tissue. This shift was accentuated in vivo, as Principal Component Analysis placed skeletal muscle metastases in proximity of healthy muscle tissue (**Supplementary Fig. 3.3a**). These data hint that tumor cells that colonize skeletal muscle adapt to the new site and even become more muscle-like; but, they do not yet tell us what these adaptations entail.

Therefore, to understand metabolic adaptations required specifically for the colonization of skeletal muscle in vivo, metabolic profiles of tissues were analysed by: 1) normalizing measurements from skeletal muscle metastases to those from healthy skeletal muscle; 2) normalizing measurements derived from lung metastases to those of healthy lung; then 3) normalizing these respective values to each other (i.e., (1) normalized by (2)— **Fig. 3.3b**). Metabolite Set Enrichment Analysis (**MSEA**)[53] was performed on the most

divergent metabolites (≥2-fold increased or ≥ 50% decreased, P<0.1) arising from this final comparison (i.e., Comparison 3, **Fig. 3.3b**). The most enriched KEGG[54] pathways were purine metabolism and glutathione (**GSH**) metabolism (**Fig. 3.3c**). The level of enrichment measured for both sets was specific to this comparison; they were not observed when contrasting healthy skeletal muscle and lung tissue, for example (**Supplementary Fig. 3.3c,d**). Whereas purine metabolism may reflect the biosynthetic needs of proliferative metastases, GSH metabolism is invariably linked to ROS detoxification[55]. Maintenance of cellular reduction-oxidation (**redox**) homeostasis requires dynamic balance of ROS generation and capacity of the antioxidant system[56]. But, excessive ROS generation without adequate compensation results in damaging oxidative stress, leading to proliferative stasis or even cell death[56]. Therefore, GSH metabolism enrichment might reflect a particular evolution by skeletal muscle metastases to overcome a harsh microenvironment characterized by induction of oxidative stress. This hypothesis was particularly attractive because the volatile nature of ROS may explain why SkMc-derived CM could not suppress breast tumour cell outgrowth (**Fig. 3.2e**).

Examining raw metabolite values underlying MSEA revealed that skeletal muscle metastases and lung metastases modified their GSH programs in disparate ways (**Fig. 3.3d-e**). Of the metabolites that drive GSH enrichment, there were several GSH intermediates (S-glutathionyl-L-cysteine, 5-L-glutamyl-L-glutamine) enhanced specifically in skeletal muscle metastases compared to all other samples (**Fig. 3.3d-e**). We also observed trends towards increased glutamine and glutamate (a GSH precursor) in skeletal muscle metastases compared to both lung metastases and healthy lung. Cysteine (another GSH building block) was elevated in the skeletal muscle metastases compared to the healthy skeletal muscle. We observed a similarly strong increase in GSH metabolites like L-glutamine and L-glutamate in the skeletal muscle metastases compared to the 4T1-SkM cells in tissue culture, suggesting that utilization of these substrates occurs specifically and abundantly within the skeletal muscle niche (**Supplementary Fig. 3.3b**).

To gain insight into oxidative stress, we examined the ratio of reduced glutathione (**GSH**) to oxidized glutathione (**GSSG**)[57] (**Fig. 3.3f**). In a resting cell, the molar GSH:GSSG ratio exceeds 100:1, whereas in various models of oxidative stress, this ratio can decrease by one-to-two orders of magnitude[58,59]. Healthy skeletal muscle and skeletal muscle

metastases exhibited greater redox buffering capacity than lung or lung metastases (**Fig. 3.3g**). This trend did not hold true in culture, where one might have expected, 4T1-SkM to exhibit higher GSH:GSSG ratios than the parental line (**Supplementary Fig. 3.3e**). This may indicate that the metabolic programs that benefit the 4T1-SkM cells in skeletal muscle only become apparent and/or advantageous in vivo (**Supplementary Fig. 3.3e**).

Given their common tissue of origin and the likelihood that, due to hematogenous dissemination, the tumour cells that seed muscle and lung start at the same oxidized state, the substantially elevated GSH:GSSG of skeletal muscle metastases vs. lung metastases (**Fig. 3.3i**) could be interpreted in two mutually exclusive ways. The first is that tumour cells capable of colonizing skeletal muscle experience less ROS and therefore have less oxidation of GSH to GSSG. The second is that proliferating within skeletal muscle requires tolerating increased ROS, and thus only DTCs that have and can maintain a high GSH:GSSG ratio colonize skeletal muscle. A corollary is that the vast majority of DTCs residing within muscle cannot make this adaptation, fail to neutralize the tissue's higher ROS burden[56], and are effectively frozen in a single cell or micrometastatic state due to an unmanageable level of oxidative stress. Moving forward, we sought to determine which of these interpretations was more accurate.

Tumour cells exhibit signs of elevated oxidative stress within the muscle niche, corresponding with reduced outgrowth. To determine whether or not breast tumour cells in the skeletal muscle microenvironment exhibit symptoms of oxidative stress, particularly in the context of glutathione metabolism, we employed a glutaredoxin-redox sensitive-GFP2 (**Grx1-roGFP2**) biosensor[60,61] that allows dynamic and quantitative live imaging of GSH redox potential and, by association, a cell's oxidation state (**Fig. 3.4a**). To determine the sensitivity of the biosensor, we treated MDA-MB-231-Grx1-roGFP2 (MDA231-roGFP2) cells with 1 mM H_2O_2 (oxidizing agent) or 50 mM DTT (reducing agent) and tracked the GSH-specific redox flux (405 nm/488 nm ratio). The biosensor responded appropriately to the two agents: the 405/488 ratio - reflecting oxidation state - increased with H_2O_2 and dropped with DTT (data not shown here).

When plated in co-culture on differentiated SkMcs, MDA231-roGFP2 cells became highly oxidized (**Fig. 3.4b**). Of note, the oxidation state of the MDA231-roGFP2 cells on

SkMcs increased rapidly over the first several days and remained elevated throughout the course of study. Conversely, MDA231-roGFP2 cells grown in the LF niche experienced a modest increase in oxidation within the first three days, but returned eventually to baseline (**Fig. 3.4b**). This pattern of oxidation closely correlated with measured growth dynamics: rapid, sustained induction of oxidation and suppressed outgrowth on SkMc, versus transient and ultimately quenched oxidation and exponential growth on LF (**Fig. 3.4c**).

To confirm these findings, we employed a cell-permeable fluorescent dye (CellROX647) to more broadly quantify ROS abundance within MDA-MB-231 cells and the niches in which they reside. We consistently measured higher levels of ROS in tumour cells residing within the SkMc niche, compared to those within the LF niche (0.18 au v. 0.04 au; a 4.5-fold increase on SkMc niche; **Fig. 3.4d-e**). Fluorescent imaging of CellROX647 revealed that SkMc themselves exhibit elevated ROS levels. Quantification of CellROX mean intensity revealed the highest focus of ROS within myotubes (**Fig. 3.4e-f**). Myotubes had 6.7-fold the ROS levels measured in LF and 3.1-fold those measured in unfused myocytes (**Fig. 3.4e-f**).

Since H_2O_2 is arguably the longest-lived ROS and is reduced by GSH, we hypothesized that elevated levels of H_2O_2 present in the SkMc niche could account for the perturbed redox balance measured using the Grx1-roGFP2 biosensor. We measured the levels of extracellular H_2O_2 in SkMc and LF niches over 10-days of co-culture with MDA-MB-231 cells. SkMc niches contained 2-3 times higher H_2O_2 levels than lung-like niches over the course of the experiment (**Fig. 3.4g**). Whereas a maximum concentration of 0.42 μM H_2O_2 was achieved in the LF niche on day 7, the maximum H_2O_2 measured from SkMcs was nearly triple that (1.2 μM) and occurred early on. This was consistent with the early break in tumour cell oxidation state observed between LF and SkMc (**Fig. 3.4c**) and sustained throughout the ten-day timecourse (**Fig. 3.4b,g**). Admixing LF and SkMc at increasing SkMc:LF ratios demonstrated clearly that H_2O_2 level tracked with the quantity of myotubes in each well (**Fig. 3.4h**). These data demonstrate that ROS accumulates in SkMc niches in culture, disrupts redox balance of tumour cells within these niches, and that these factors are associated with tumour suppression. What remained unclear is whether any of these relationships were causative, and if any of this biology held true in vivo.

Disseminated MDA-MB-231 tumour cells exhibit oxidative stress in vivo. Using an established method[62], we employed the Grx1-roGFP2 sensor to measure oxidation state of MDA-MB-231 cells within lung and skeletal muscle in mice (**Fig. 3.4i**). MDA231-roGFP2 cells were ic injected into NOD-SCID mice, and lung and skeletal muscle were collected seven-weeks later upon necropsy. Consistent with our culture-based observations, DTCs within skeletal muscle were highly oxidized (**Fig. 3.4j-k**). To our surprise, single DTCs were oxidized to the same extent in lung (**Fig. 3.4j-k**). However, oxidation resolved over the course of metastatic progression in lung (**Fig. 3.4j-k**). This phenomenon did not occur in skeletal muscle. Here, micro and macro-metastases (clusters of 50+ cells) were significantly more reduced than single cells (**Fig. 3.4j-k**). These data lent further credence to the notion[63] that DTCs might start at similar oxidation states regardless of tissue, but must subsequently balance redox state to colonize a given site. This motivated functional studies to determine whether sustaining oxidative stress would prevent lung metastatic progression, and whether enhancing antioxidant reserves would enable tumour cells to restore redox balance and colonize skeletal muscle.

Increased oxidative stress suppresses MDA-MB-231 tumour cell outgrowth on a permissive niche. To determine if increased ROS attenuated outgrowth on permissive lung-like niches, we spiked sub-lethal doses of H_2O_2 (75 μM, 125 μM) into organotypic niches containing MDA231-roGFP2 tumour cells. The 75 μM H_2O_2 dose imposed a modest growth impediment to the MDA231-roGFP2 cells (**Fig. 3.5a**). The 125 μM dose, however, dramatically suppressed MDA231-roGFP2 outgrowth, mirroring outgrowth observed on untreated SkMCs (**Fig. 3.5a**). Tumoral oxidation state also rose significantly with the addition of 75 μM and 125 μM H_2O_2 (**Fig. 3.5b**). These data suggest that imposing oxidative stress is sufficient to suppress outgrowth within a permissive niche. But what troubled us about these data was that the dose of H_2O_2 required to achieve growth suppression was two orders of magnitude above the concentration measured in SkMc niches (**Fig. 3.4g**). We wondered if these measurements, the high concentrations of H_2O_2 required in these assays, and the inability of SkMc-derived CM to suppress outgrowth all reflected the volatile nature of H_2O_2.

Therefore, we asked whether lung colonization could be suppressed if DTCs were exposed to ROS at concentrations in line with those measured in the skeletal muscle niche. To reconstruct these conditions, we utilized a chemogenetic system (**DAAO**[64]) that enables sustained, on-demand generation of H_2O_2 in a cell type of interest. Based on the D-amino acid oxidase (**DAAO**) from R. gracilis, this vector produces H_2O_2 when DAAO converts D-amino acids (e.g., D-alanine) to their corresponding imino acids (**Fig. 3.5c**).

We first optimized DAAO in MDA-MB-231 cells on tissue culture plastic (**Supplementary Fig. 3.4a**) to establish the dynamics and scale of H_2O_2 accumulation that could be achieved. Though the DAAO vector is an intracellular H_2O_2 generator, H_2O_2 is freely diffusible and a fraction will diffuse into the culture media. Therefore, we measured extracellular H_2O_2 as a surrogate for overall H_2O_2. Serum-free culture media containing increased doses of D- or L-alanine (0 – 500 mM) was added to MDA231-DAAO or MDA231-WT cells and sampled 1-, 4-, 8-, 24- and 48-hours later. Extracellular concentrations of H_2O_2 increased initially to almost 300 nM over an 8-hour period across all conditions (**Supplementary Fig. 3.4b**), highlighting how sensitive these cells are to environmental stressors like serum starvation. By the 24-hour timepoint, MDA231-DAAO cells treated with 100 mM and 500 mM D-alanine accumulated significantly more H_2O_2 than all other conditions (**Supplementary Fig. 3.4b**).

Daily administration of 100 mM D-alanine significantly reduced the proliferation of the MDA231-DAAO cells (**Supplementary Fig. 3.4c**). An identical dose of L-alanine did not (**Supplementary Fig. 3.4c**). A very limited number of cells were alive by the study's endpoint (72h) in the D-alanine condition only. From this optimization study, we also learned that there is a cytotoxic limit to alanine dosage. Though 500 mM D-alanine generated the greatest amount of H_2O_2 in the MDA231-DAAO cells, it also outright killed all cells in a DAAO vector independent fashion (**Supplementary Fig. 3.4c**). Thus, the DAAO system was indeed able to stimulate a tuneable and sustainable H_2O_2 bolus, but had to be delivered in pure tumour cell cultures at 100 mM or less.

To determine whether chemogenetic induction of H_2O_2 impacted outgrowth on lung- and skeletal muscle-like niches, $1x10^2$ MDA231-DAAO or MDA231-WT cells were seeded on LF or SkMc and tracked over ten days (**Fig. 3.5d**). Immediately upon tumour cell seeding, we administered serum-free media containing 0 mM, 10 mM, 20 mM or 100 mM D-

or L-alanine. In these more nutrient limited conditions (sparse tumour cell density, serum-free media), dosing alanine at 100 mM compromised survival and outgrowth independent of the DAAO vector and thus was not suitable for comparison (**Fig. 3.5e, f**). However, MDA231-DAAO outgrowth in the LF niche was suppressed in the presence of 10 mM D-alanine (**Fig. 3.5e, f**). Importantly, outgrowth of controls (10 mM L-alanine, and D-alanine treated MDA231 cells lacking DAAO) were not impacted at these alanine concentrations (**Fig. 3.5e, f**). These data suggest that DTCs that experience a profound and sustained redox imbalance consistent with what is imposed by the SkMc niche are unable to take advantage of a growth-promoting environment.

Induction of tumoral H_2O_2 also impacted outgrowth on SkMc niches. Any outgrowth on SkMcs was diminished back to baseline in cultures seeded with MDA231-DAAO and treated with 10 mM and 20 mM D-alanine (**Fig. 3.5g-h**). This was consistent with elevated levels of H_2O_2 ultimately resulting in cell death in mono- (**Supplementary Fig. 2b-c**) and in co- cultures (**Fig. 3.5e**). Between the endogenous ROS produced by the microenvironment and those stimulated by the DAAO vector, there appeared to be sufficient H_2O_2 present by day 5 to provoke a switch from dampened proliferation to diminished survival (**Fig. 3.5e**). These data show that inducing and sustaining oxidative stress in tumour cells suppresses metastatic outgrowth in lung-like niches, and that this effect is nearly saturated in SkMc-comprised, H_2O_2-rich microenvironments. We next asked whether lung colonization could be suppressed if DTCs were exposed to a niche that produced ROS at concentrations in line with those measured in skeletal muscle. To answer this question, we introduced the DAAO system into LFs. Akin to MDA-MB-231s, LFs exhibited a dose response to D-alanine that allowed us to narrow in on a dose (30 mM) that did not compromise viability of LFs and stimulated H_2O_2 concentrations on par with those measured in SkMc cultures (**Supplementary Figure 3.4d,e**). Seeding wild-type MDA-MB-231 on these niches revealed that this level of H_2O_2 induction was sufficient to suppress MDA-MB-231 outgrowth to the degree observed on SkMc niches (**Fig. 3.5i-j**). Going beyond this (2.8 μM average peak H_2O_2 induced by 50 mM D-Alanine,) resulted in tumour cell death (**Fig. 3.5j**).

Enhancing antioxidant capacity enables skeletal muscle colonization in culture and in vivo. The data presented in Figure 5 demonstrate the consequence of transferring the phenotype

of sustained oxidative stress to a more permissive site. But the consequence of restoring redox balance by enhancing the antioxidant capacity of tumour cells delivered to skeletal muscle remained unknown. To address this question, we engineered MDA-MB-231 and EO771 cells to ectopically express catalase, a peroxisomal enzyme that rapidly converts H_2O_2 to H_2O and O_2, in their mitochondria (**mCAT**) or cytosol (**cCAT; Supplementary Fig. 3.5a**). Catalase acts in parallel to GSH to protect cells from ROS-inflicted oxidative damage[65,66]. Unlike GSH, catalase accomplishes detoxification without the need for cofactors or co-substrates, so it is a straightforward and potentially potent genetic manipulation.

To determine confidently whether ectopic expression of catalase neutralized ROS in MDA-MB-231 cells in co-culture, we stained for ROS in control- (empty vector), mCAT- and cCAT- MDA-MB-231 cells on skeletal muscle and lung niches using the CellROX647 dye. Expression of ectopic catalase significantly reduced ROS in MDA-MB-231, irrespective of niche (**Fig. 3.6a**). A difference between compartments was observed on SkMc; mCAT expression led to a 22% reduction in ROS intensity, whereas cytoplasmic expression resulted in a 52% reduction in ROS intensity.

Ectopic catalase expression promoted MDA-MB-231 outgrowth on SkMc in a manner commensurate with the level of ROS reduction achieved by each vector (mCAT: 3.6-fold increase; cCAT: 4.7-fold increase, **Fig. 3.6a-c**). Enhancing antioxidant capacity also promoted EO771 outgrowth on SkMcs; mCAT and cCAT vectors induced a 4.3-fold and 3.4-fold increase in EO771 outgrowth on SkMc, respectively, compared to control (**Fig. 3.6d-e**). Of note, this phenotype was not consistent across niches. Neither MDA231-mCAT nor MDA231-cCAT outgrew more than the MDA231-Ctl on LFs (**Supplementary Fig. 3.5b**). Indeed, ectopic catalase expression actually blunted outgrowth of EO771 on LF niches, compared to EO771-Ctl (**Supplementary Fig. 3.5b**). These data reveal that, in culture, levelling redox balance promotes outgrowth on SkMc niches. They suggest also a limit to the degree of ROS detoxification that enhances metastatic colonization potential.

To determine whether these general themes apply in vivo, we injected $1x10^3$ luciferase-expressing MDA231-Ctl, MDA231-mCAT, and MDA231-cCAT cells directly into the TA muscle of NOD-SCID hosts, and tracked outgrowth weekly by bioluminescence imaging (**BLI**; (**Fig. 3.6f**). Forty percent of mice in the MDA231-mCAT cohort developed

detectable BLI signal in their TA prior to the study endpoint (**Fig. 3.6g**). In contrast, neither the control nor cCAT cohorts developed a single skeletal muscle tumour (as assessed via BLI; **Fig. 3.6h**). Immunofluorescent quantification of DTCs within the TA revealed that both the MDA231-mCAT and MDA231-cCAT tumour cells have an enhanced ability to transition out of the single cell state (**Fig. 3.6i-l**). 86% of the MDA231-Ctl cells remaining in the TA after 16 weeks across four mice were single cells. In contrast, TAs inoculated with MDA231-mCAT and MDA231-cCAT housed tumour cell clusters ranging from doublets to clusters of ten or greater (**Fig. 3.6i**), including the only bona fide skeletal muscle tumour observed in this model (**Fig. 3.6k**). These data highlight and further substantiate the proliferative barrier DTCs encounter within skeletal muscle: oxidative stress/redox imbalance.

We utilized the syngeneic EO771–C57BL/6 mouse model to discern if these catalase findings - and thus their implications - translated to an immune-competent context. The TA muscle of C57BL/6 mice was inoculated with $1x10^3$ control- or mCAT-expressing EO771-mCherry-luciferase cells (**EO771-Ctl** or **EO771-mCAT**) (**Fig. 3.6m**). Tumour cell colonization was tracked weekly by BLI over a six-week period. There was a robust increase in EO771-mCAT tumour burden in skeletal muscle by three weeks, with 5 of 14 mice (36%) having full-blown skeletal muscle lesions (**Fig. 3.6n-o**). In contrast, only 1 of 14 mice (7%) in the EO771-Ctl cohort developed BLI signal, and this emerged later than tumours in the mCAT cohort (**Fig. 3.6n**). These data show that restoring redox balance within breast and mammary tumour cells overcomes proliferative barriers imposed by the skeletal muscle microenvironment, substantially enough in some cases to facilitate full-blown colonization of the tissue.

MDA-MB-231 and EO771 tumour cells do not benefit from enhanced redox capacity in lung. Based on these results, one might expect that increasing tumoral catalase would lead to increased metastatic potential irrespective of organ site. Yet, outgrowth of ectopic catalase variants on LFs suggested otherwise (**Supplementary Fig. 3.5b**). To test the impact of ectopic catalase expression on lung colonization in vivo, $5x10^5$ ffluc-eGFP-expressing MDA231-Ctl, MDA231-mCAT, and MDA231-cCAT cells were injected intravenously (**iv**) and tracked weekly by BLI (**Supplementary Fig. 3.5c**). The MDA231-mCAT and MDA231-cCAT cells did not increase tumour burden in lung compared to control. At endpoint (six-

weeks), lung bioluminescence from intact mice (**Supplementary Fig. 3.5d**) and from dissected lung (**Supplementary Fig. 3.5e**) was significantly diminished in MDA231-mCAT and -CAT, compared to control. The number and size of lung metastases visualized by eGFP fluorescence on the surface of the lung supported this conclusion (an average 51 Ctl lesions, v. 11.6 mCAT lesions v. 1.6 cCAT lesions; **Supplementary Fig. 3.5f**). The failure of ectopic catalase expression to promote lung colonization perpetuated in immune-competent settings. C57BL/6 mice inoculated with $5x10^5$ EO771-mCAT cells via iv injection (**Supplementary Fig. 3.5g**) also exhibited lower BLI in intact mice (**Supplementary Fig. 3.5h**) and in explanted lungs (**Supplementary Fig. 3.5i**) compared to EO771-control at study endpoint (two-weeks). Immunofluorescent imaging of lungs upon necropsy revealed that the number of foci in the EO771-Ctl inoculated animals was significantly greater in number than the number of foci counted in mice iv inoculated with EO771-mCAT (an average 119.6 Ctl lesions v. mCAT 71.8 lesions; **Supplementary Fig. 3.5j**). These data highlight how redox interactions between a DTC and its microenvironment are not equal across tissues, and that disrupting this balance too far in either direction can substantially impact colonization.

Reduction of environmental mitochondrial ROS stimulates skeletal muscle – but not lung – colonization. We took advantage of the MCAT transgenic mouse model to test if ectopic expression of mitochondrial catalase in the skeletal muscle niche would recapitulate the pro-growth phenotype we observed when catalase was expressed intra-tumourally. The MCAT mouse, first described by Schriner et al.[66], expresses mitochondrial-targeted catalase (akin to our system) to reduce H_2O_2 generation and is expressed in all organs surveyed, with highest expression measured in cardiac and skeletal muscle[66]. The TA muscle of C57BL/6 wildtype (**WT**) and MCAT mice was inoculated with $1x10^3$ EO771-Ctl or EO771-mCAT (**Fig. 3.7a**). Tumour cell colonization was tracked weekly by BLI over a six-week period and, upon necropsy, measured in skeletal muscle ex vivo (**Fig. 3.7b**). Only 1 of 19 WT mice (5%, **Fig. 3.7c**) in the EO771-Ctl cohort developed BLI signal, whereas 6 of 19 WT mice (32%, **Fig. 3.7d**) in the EO771-mCAT cohort developed stable tumour burden over the course of the study. Interestingly, 3 of 9 MCAT mice (33%, **Fig. 3.7e**) developed stable

tumour burden when inoculated with EO771-Ctl cells and 3 of 9 MCAT mice (33%, **Fig. 3.7f**) when inoculated with EO771-mCAT cells.

These data reveal that enhanced capacity to neutralize mitochondrial ROS in the skeletal muscles of the mCAT host facilitates colonization to the level observed when tumoral mitochondrial ROS is reduced via ectopic catalase expression, suggesting the contribution of ROS from the environment is as important as the ROS generated intratumorally in response to (or transmitted by) an oxidative environment. Resolving either stressor is sufficient for DTCs to progress within skeletal muscle. To our surprise, however, we did not see an additive effect of tumoural and microenvironmental ROS suppression (EO771-mCAT cells in MCAT mice; **Fig. 3.7f**). Based on BLI kinetics, proliferation is enhanced early on in a larger fraction of the cohort (55%), but two lesions regressed. This might suggest that there is a fine-tuned range for DTCs in skeletal muscle where redox state must fall in order to stimulate outgrowth. This observation nicely ties into our observations in lung, where tumoral mCAT expression hinders metastatic colonization rather than promoting it (**Fig. 3.7g-l**). Here, however expression of mCAT in the host did not promote or inhibit metastasis when the total number of metastatic lesions were quantified (**Fig. 3.7k**). These data confirm that enhanced capacity to neutralize oxidative stress in the tumor or its surrounding tissue promotes colonization of muscle in a tissue-specific manner, since these manipulations fail to promote lung metastasis. These data also implicate the mitochondria as a relevant compartment where ROS orchestrates metastasis suppressive functions in the skeletal muscle.

MDA-MB-231 and EO771 tumour cells have a higher mitochondrial ROS burden when cultured in the skeletal muscle niche. The potency of mCAT in stimulating skeletal muscle colonization suggested that the mitochondria of cells residing within skeletal muscle were a relevant site of oxidative stress. Therefore to determine if the amount of mitochondrial ROS differed between MDA-MB-231 on skeletal muscle and lung niches, we combined a live cell mitochondrial dye (MitoTracker Green) with CellROX DeepRed to measure the level of ROS that localize in the mitochondria. In line with cellular ROS measurements presented in **Figure 3.4**, the mitochondrial ROS burden for MDA-MB-231-Ctl cells on SkMcs was 4.7-times higher than what was measured on LF (**Fig. 3.8a-b**). Introduction of the mCAT vector

into MDA-MB-231 cells significantly reduced the mitochondrial ROS on SkMcs to 50.6% of what was measured with wild-type cells on LFs (**Fig. 3.8a-b**). This coincided with a level of outgrowth that eclipsed what was measured on LFs seeded with either wild-type or mCAT MDA-MB-231 (**Fig. 3.8c**). Measuring mitochondrial ROS in EO771 cells on LFs and SkMcs revealed similar levels of induction of mitochondrial ROS on SkMcs, which was alleviated by mCAT and resulted in outgrowth that approached what occurred on LFs (**Fig. 3.8d-f**). These data highlight the close relationship between mitochondrial stress and outgrowth on the SkMc niche.

In light of our data revealing that reducing host mitochondrial ROS promoted colonization of skeletal muscle in vivo, we probed whether culturing E0771 on syngeneic SkMcs established from mCAT mice resulted in reduced levels of tumoral mitochondrial ROS versus wild-type littermates/controls. We established two unique myoblast cultures (MCAT-1 and -2) from the gastrocnemius of MCAT mice and a single myoblast culture from the gastrocnemius of a wild-type littermate. Consistent with our observations in mCAT hosts (**Fig. 3.7e**), outgrowth was significantly enhanced when EO771-Ctl were cultured on either the MCAT-1 or MCAT-2 niche as opposed to the wild-type myoblast niche (**Fig. 3.8g**). Measuring the amount of mitochondrial ROS in the EO771 cells across the three niches revealed that tumoral mitochondrial ROS was decreased by 88.2% and 91.8% on mCAT-1 and -2 SkMcs versus wild-type SkMcs (**Fig. 3.8h-i**), perhaps indicating that the skeletal muscle microenvironment imparts mitochondrial redox stress on the tumour cell, and that this is a source of metastasis/colonization suppression within this tissue.

These data, along with the EO771-mCAT mouse studies in **Figure 3.6 and 3.7,** demonstrate that mitochondrial ROS burden in muscle DTCs is greater than that of lung DTCs, and suggest a direct role for mitochondrial ROS in moderating tumor cell outgrowth. More specifically, the data point to increased mitochondrial ROS in DTCs that reside in skeletal muscle due to both internal and environmental stressors.

In sum, we believe that sustained oxidative stress and reduced antioxidant capacity drive a profound redox imbalance in skeletal muscle that poses a unique problem to DTCs. Restoring this balance via ectopic catalase expression in tumour cell or in the host tissue mitochondria enhances metastatic potential within skeletal muscle, specifically. To our

knowledge, this is the first demonstration that colonization of an antimetastatic niche can be achieved by tuning a cell's antioxidant capacity.

Discussion.

In this manuscript, we interrogated the molecular basis of what we argue is the most anti-metastatic tissue in our body: skeletal muscle. We provide evidence of DTC persistence within the quadriceps muscle of a stage IV breast cancer patient, and applied a quantitative PCR assay, paired with immunofluorescent microscopy of optically cleared whole tissue, to show that DTC trafficking and persistence within multiple skeletal muscles occurs with similar frequency to more common sites of metastasis. We performed a combination of mouse studies and organotypic culture studies to show that skeletal muscle consistently suppresses breast and mammary cancer outgrowth. Metabolomic analysis of skeletal muscle tissue and organotypic cultures prompted us to probe the role of oxidative stress on DTC outgrowth and tissue colonization. We utilized a GSH-specific redox biosensor, Grx1-roGFP2, and saw that DTCs in skeletal muscle are under sustained and elevated levels of oxidative stress in culture and *in vivo*. Studies where the antioxidant catalase was ectopically expressed in breast and mammary cancer cells demonstrated that DTCs with enhanced antioxidant pools could bypass this oxidative bottleneck and proliferate within skeletal muscle. Complementary studies where catalase was ectopically expressed in skeletal muscle highlighted that microenvironmental ROS significantly contributes to tumoural redox state, and suggested that there is a fine-tuned range where redox state must fall in order for DTCs to remain capable of outgrowth. In line with this, leveraging oxidative stress through the on-demand generation of H_2O_2 (DAAO) slowed – and even halted - progression of MDA-MB-231 cells in a lung-like niche. Further, rewiring the lung-like niche to secrete H_2O_2 to the same extent as the SkMc niche (LF-DAAO) dramatically impeded MDA-MB-231 cell outgrowth, in line with our findings that high levels of environmental ROS are sufficient to arrest DTC growth. In sum, we have demonstrated that unchecked oxidative stress and the consequent disruption in redox homeostasis is key to skeletal muscle-mediated metastasis suppression.

The role of ROS has been controversial in the cancer research field because of their dichotomous ability to promote or suppress tumour development depending on

context. ROS-induced oxidative stress can lead to enhanced mutation rates and genomic instability, promoting transformation of a normal cell into a tumour cell. Thus, it was believed originally that the delivery of antioxidants to quench ROS would emerge as a preventive anti-cancer therapy[67–70]. However, antioxidant regimens not only failed to benefit patients, but were associated with a significant increase in the incidence of lung, breast and prostate cancer[71–76] . Subsequent studies in mice confirmed the pro-tumorigenic effects of antioxidant supplementation[70,77,78]. Sayin *et al*.[78], for example, showed that the GSH precursor *N*-acetylcysteine (**NAC**) and the antioxidant vitamin E markedly increased tumour progression and reduced survival in *Braf*- and *Kras*-induced lung cancer models.

Recently, the pro-tumorigenic role of ROS has been re-evaluated at metastatic sites. For example, Piskounova *et al*. demonstrated that xenografted melanoma cells derived from patients displayed higher levels of cytoplasmic and mitochondrial ROS in blood and in liver than cells implanted subcutaneously[79]. Treatment with NAC increased the presence of circulating cancer cells and metastatic burden in this model[79]. Administration of NAC potentiated lung and lymph node metastasis in additional melanoma models, as well[80]. These papers indicate that cellular oxidative stress limits metastasis in multiple organs *in vivo*. But what is the source of oxidative stress? Recent work from the Morrison laboratory implicates free iron within blood, suggesting tumour cells circulating through the bloodstream encounter oxidative stress by default[63].

In the full context of the literature, data within this manuscript suggest a general framework where successful recurrences are comprised of cells that have undergone metabolic changes at the primary site, in blood, and/or in other organs that allow residual tumour cells to better withstand oxidative stress [63,79,81,82]. Our study applies skeletal muscle as a filter and shows that this is not coincidental; DTCs within an antimetastatic site cannot achieve redox balance and never progress as a result, suggesting that sustained oxidative stress might prevent colonization of other organs, also. Indeed, one might also characterize tissues such as the spleen and thyroid gland as antimetastatic[83]. While the basis for these phenotypes remains unstudied, the levels of free heme in the spleen and iodine within the thyroid gland suggests that a role for sustained oxidative stress is plausible in these organs, as well[83]. The question is whether this biology is transferrable to more permissive sites like the lung, thereby forming the foundation for antimetastatic therapies.

In this work, we did not uncover transferrable mediators of tumour suppression derived from skeletal muscle at homeostasis. Nonetheless, our work does add to mounting evidence[63,83] that sustained oxidative stress should be considered a DTC hallmark. The fact that single DTCs experience high oxidative stress suggests that this state might be exploited for a selective approach to target DTCs. Identification of unique dependencies required to survive this metabolic constraint may provide molecular targets that enable elimination of metastasis-initiating populations.

Our study also reveals that profound elevation of antioxidant capacity enables colonization of skeletal muscle. But it does not uncover why this so rarely takes place. For instance, mutations and/or amplifications to enzymes that promote antioxidant capacity would be expected to result in skeletal muscle metastasis, at least occasionally. Yet metastases at these sites are observed so rarely. Is this because such mutations are proportionally rare? Because the level of antioxidant capacity required is never achieved? Or, is it because the microenvironment must also be complicit? Skeletal muscle homeostasis is consistently disrupted by exercise[84]. These disruptions are sufficient to trigger emergence of quiescent satellite cells[84], but clearly insufficient to promote DTC outgrowth in cancer survivors[85]. Mechanistic differences underlying the response of satellite cells and DTCs to disruption of tissue homeostasis may provide further insight into DTC-specific growth suppressive stresses that can be leveraged therapeutically.

Our work provides evidence that trafficking to skeletal muscle and DTC survival within this environment is not the major bottleneck to colonizing this tissue. Instead, a hostile microenvironment characterized by elevated levels of ROS and manifesting in sustained oxidative stress – with the mitochondria as a key potential battleground – is the core mechanism by which skeletal muscle so suppresses DTC outgrowth. Critically, we provide evidence that if this phenomenon could be perpetuated in lung, it would restrict metastasis there, also. This presents a challenge to uncover means by which oxidative stress can be prolonged and/or ultimately leveraged to compromise DTC survival, thereby effectively converting permissive niches into antimetastatic sites.

This chapter was made possible with help from the following: Travis Nemkov, Jinxiang Dai, Ruth F. Dumpit, Lawrence D. True, Stephen J. Tapscott, Lucas B. Sullivan, Peter S. Nelson, Alexander Swarbrick, Kirk C. Hansen, and Cyrus M. Ghajar. We would also like to acknowledge the BROCADE rapid autopsy team for their hard work and the women with metastatic breast cancer who selflessly donated to this study.

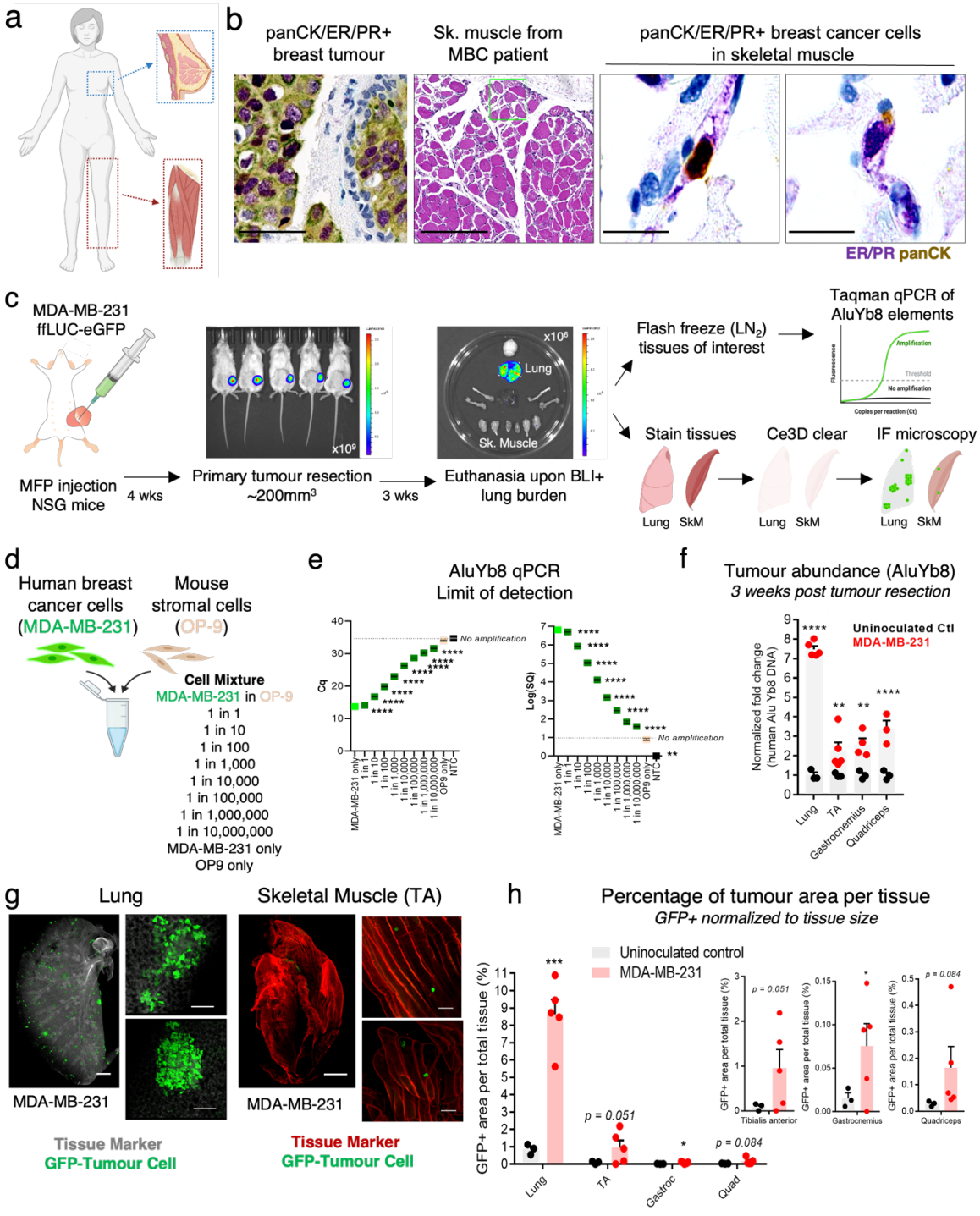

Figure 3.1. Breast cancer cells traffic to and persist within skeletal muscle. a) Schematic of the locations surveyed for the identification of human breast cancer cells in skeletal muscle from metastatic breast cancer (**MBC**) patients. b) Multiplex IHC panel of a primary breast tumour and skeletal muscle with disseminated breast cancer cells from an MBC patient. Estrogen receptor and progesterone receptor (**ER** and **PR**, respectively; breast cell markers) are depicted in purple and pan-cytokeratin (**panCK**, epithelial cell marker) in yellow. Hematoxylin & eosin (**H&E**) stained skeletal muscle in centre panel. Scale bar, 50 μm primary tumour, 500 μm skeletal muscle H&E and 20 μm tumour cells in skeletal muscle. c) Schematic of the orthotopic mouse

study to determine if disseminated tumour cells spontaneously traffic to skeletal muscle. d) Schematic of experiment to determine detection sensitivity of AluYb8-qPCR method. e) AluYB8-qPCR detects 1 human MDA-MB-231 cell in 10^6 OP-9 mouse cells, as reflected by cycle of quantification (**Cq**) and log of the starting quantity (**SQ**). n = 3 technical replicates, run three times. Statistical significance was determined using an ordinary one-way analysis of variance (ANOVA), followed by an uncorrected Fisher's least significant difference (LSD) method to analyse each comparison individually. All comparisons were against the OP-9 only (no human DNA) negative control. **** $P < 0.0001$ for all comparisons, except OP-9 only v. NTC. f) AluYB8 amplification 3 weeks post-tumour resection, normalized by internal control (b-actin) and graphed as fold change above uninoculated control. n = 5 inoculated and 3 uninoculated mice. Two-way ANOVA was performed, followed by an uncorrected Fisher's LSD, where ****$P < 0.0001$ for lung and quadriceps when comparing tumour-bearing tissue against uninoculated controls. **$P = 0.007$ for tumour-bearing TA v. uninoculated TA and **$P = 0.002$ for tumour-bearing gastrocnemius v. uninoculated control. n = 5 inoculated and 3 uninoculated mice. g) Representative images for Ce3D-cleared lung and skeletal muscle (TA) of MDA-MB-231-bearing mice. Insets are magnifications of GFP^+ tumours cells in lung and skeletal muscle. Scale bar 1 mm whole tissue, Inset 100 μm. h) Percentage of GFP^+ tumour area normalized by total tissue area for lung, TA, gastrocnemius and quadriceps. Unpaired t-tests, with Welch's correction, were performed for comparison of GFP area in tumour-bearing tissue over uninoculated controls, where **$P = 0.0003$ for lung, $P = 0.051$ for TA, *$P = 0.039$ for gastrocnemius and $P = 0.084$ for quad. n = 5 inoculated and 3 uninoculated mice. For e-f, h, centre line represents the mean, and error bars the standard error of the mean (s.e.m.).

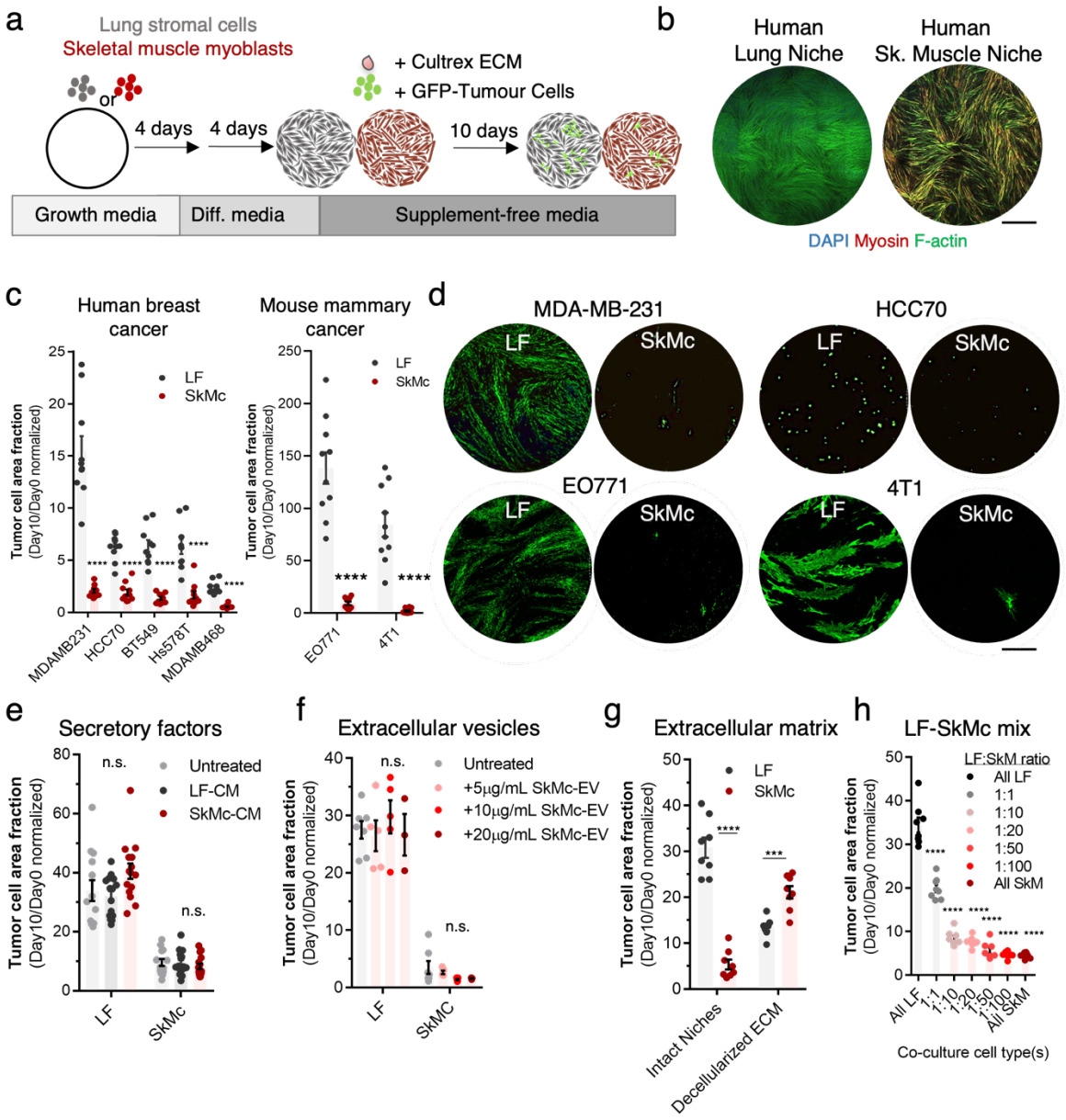

Figure 3.2. Skeletal muscle myocytes suppress outgrowth of breast and mammary cancer cells in culture, but not through a secreted or deposited factor. a) Schematic of experiment to determine if 3D organotypic culture models of skeletal muscle suppress breast and mammary cancer cell outgrowth. b) Representative images of 3D organotypic niches of human lung and skeletal muscle (SkMc). Scale bar, 10 mm. c) Outgrowth (YFP area fraction, A.F.) of a panel of breast and mammary cancer cell lines on the SkMc and lung niche after ten days. n = 8-10 technical replicates, repeated in triplicate. Multiple t-tests were performed to determine statistical significance between outgrowth on LF versus SkMc per cell line, ****P<0.0001 for all comparisons. d) Representative images of breast cancer (MDA-MB-231, HCC70) and mammary cancer (EO771, 4T1) outgrowth on the SkMc niche. Scale bar, 10 mm. e) Outgrowth (YFP A.F.) of MDA-MB-231 cells on LF and SkMc niche that were treated daily with conditioned medium (CM) from LF or SkMc monoculture. n = 10-15 technical replicates, performed in triplicate. One-way ANOVA was performed, followed by Dunnett's multiple comparisons test, to find that neither LF-CM nor SkMc-CM significantly altered outgrowth compared to the untreated control per niche (P>0.05). f) Outgrowth (YFP A.F.) of MDA-MB-231 cells on LF and SkMc that were treated daily with extracellular vesicles (EV; 5, 10 and 20 μg/mL) collected from SkMc monoculture. n = 7 technical replicates, performed in duplicate. Compared against untreated condition

per niche, no comparison was statistically significant *(P*>0.1 for all) when one-way ANOVA, followed by Dunnett's multiple comparisons test, was performed. g) Outgrowth (YFP A.F.) of MDA-MB-231 cells on decellularized lung or SkMc niches, compared with outgrowth on intact LF and SkMc niches. n = 5-8 technical replicates, performed in triplicate. ****P<0.0001 for the following comparisons: intact LF v intact SkMc, intact LF v. decellularized LF, intact SkMc v. decellularized SkMc when a two-way ANOVA, followed by Sidak's multiple comparisons test, was performed. P=0.0004 for intact LF v. decellularized SkMc, P=0.005 for intact SkMc v. decellularized LF, P=0.0088 for decellularized LF v. decellularized SkMc. ***P=0.0005 for decellularized LF v. decellularized SkMc and ****P<0.0001 for intact LF v. intact SkMc via unpaired two-tailed t-tests were performed to find that. h) Outgrowth (YFP A.F.) of MDA-MB-231 cells in co-culture with a mixture of LF and SkMc cells, LF-only or SkMc-only. n = 5-8 technical replicates, performed in triplicate. **** P<0.0001 when all conditions were compared against LF-only wells using one-way ANOVA, followed by Dunnett's multiple comparisons test. For c, e-h, centre line represents the mean, and error bars the s.e.m.

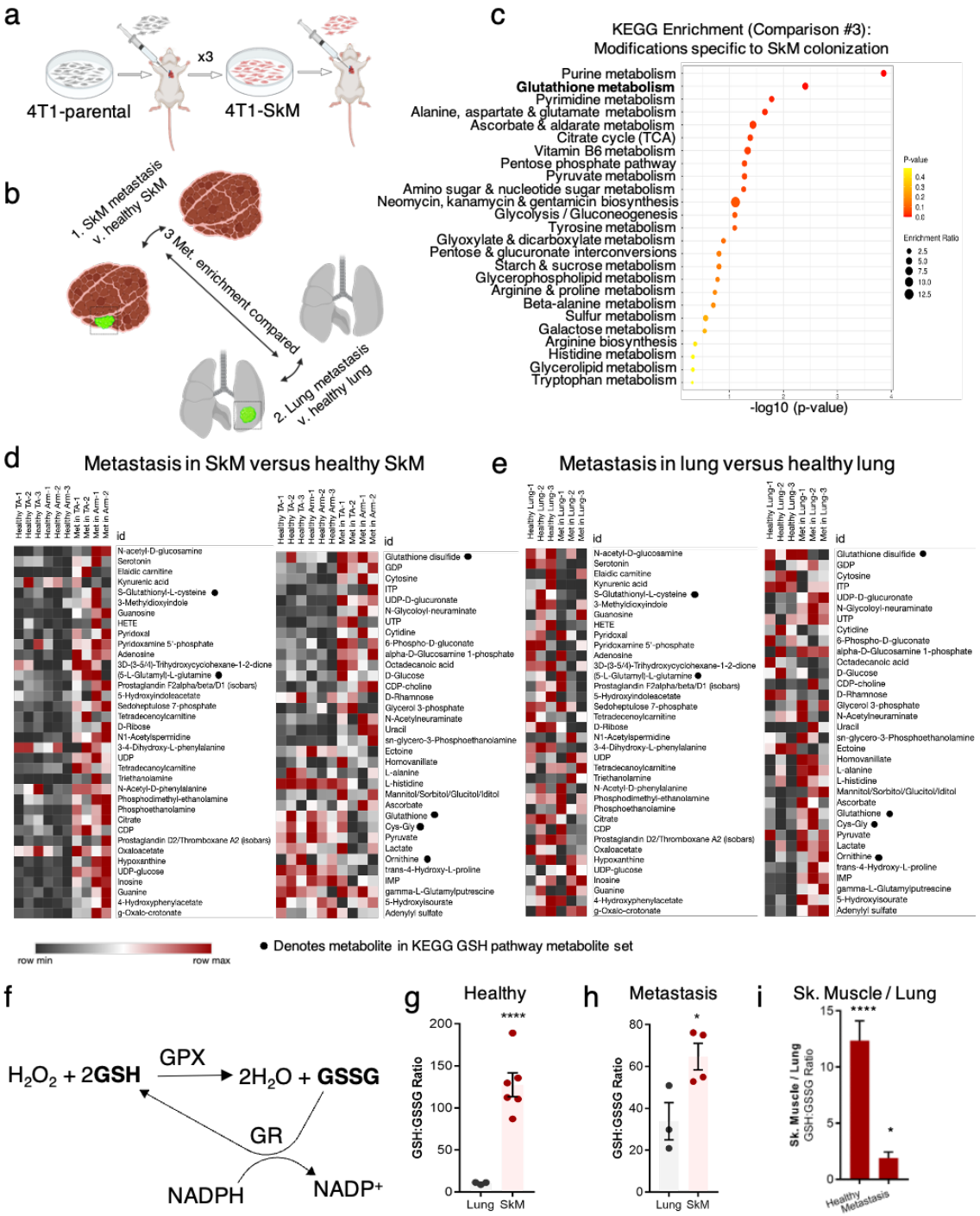

Figure 3.3. Glutathione metabolism is significantly altered between skeletal muscle and lung metastases. a) Schematic of the derivation of a skeletal muscle-metastatic 4T1 subline ("**4T1-SkM**"). b) Schematic of the tissue samples collected and comparisons made for metabolomic analysis. c) KEGG Metabolite Set Enrichment Analysis (**MSEA**) of (SkM metastasis / healthy SkM) / (lung metastasis / healthy lung) - referred to as Comparison #3. Over Representation Analysis (ORA) used the hypergeometric test; one-tailed *P*-values were provided after adjusting for multiple testing. d) Heatmap displaying the row min-max for the raw values of the healthy SkM and SkM metastasis (**met**) samples. Metabolites presented in this heatmap represent those that were at least 2-fold increased or 50% decreased in Comparison #3, *P*<0.1. Black circles

denote metabolites that are included within KEGG's "glutathione metabolism metabolite" set. e) Heatmap displaying the row min-max for the raw values of the healthy lung and lung met samples. Metabolites presented in this heatmap represent those that were at least 2-fold increased or 50% decreased in Comparison #3, $P<0.1$. Black circles denote metabolites that are included within KEGG's "glutathione metabolism metabolite" set. f) Schematic of chemical reaction for glutathione-mediated H_2O_2 detoxification. g) Dot-plot of the ratio of reduced to oxidized glutathione (GSH:GSSG) for healthy skeletal muscle and lung. n = 6 healthy SkM and 3 healthy lung. Unpaired t-test was performed, where ****$P<0.0001$ for healthy lung v. healthy SkM. h) Dot-plot of GSH:GSSG ratio for skeletal muscle metastases and lung metastases. n = 4 skeletal muscle- and 3 lung-metastases. Metastasis samples were collected from seven separate mice. Unpaired t-test was performed, where *$P=0.038$ for lung metastases v. muscle metastases. i) Bar graph comparison of skeletal muscle's GSH:GSSG ratio compared with lung's GSH:GSSG, for both healthy and metastasis samples. Multiple t-tests, followed by the Holm-Sidak method, were run for comparison of muscle to lung GSH:GSSG ratios, where ****$P<0.0001$ for healthy and *$P=0.01$ for metastasis. n = 3 per condition. For **e-h**, centre line represents the mean, and error bars the s.e.m.

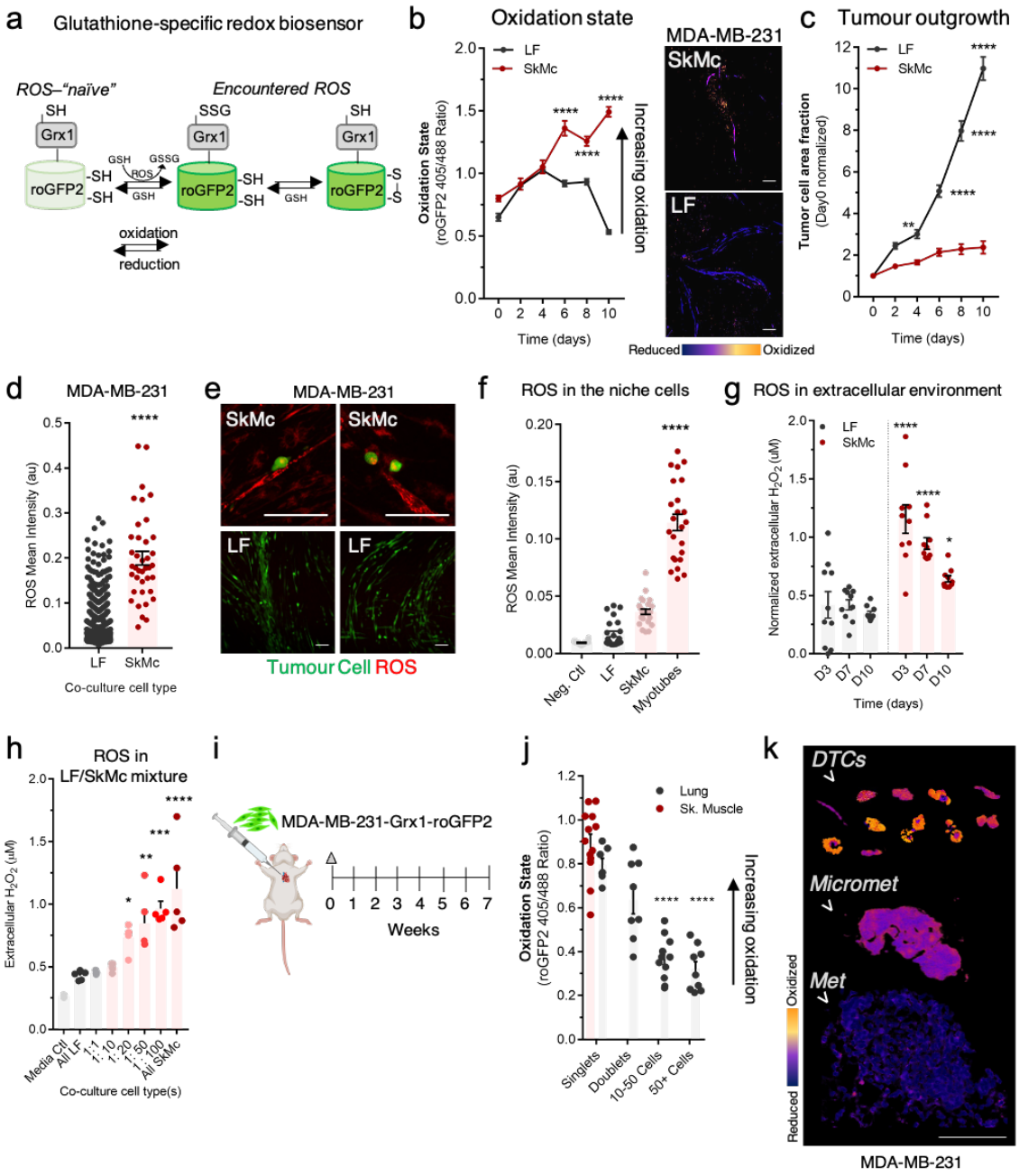

Figure 3.4. The skeletal muscle myocyte niche causes unchecked oxidative stress in DTCs. a) Schematic of the Grx1-roGFP2 redox biosensor used to measure GSH-specific oxidative stress. b) Dot-plot depicting the oxidation state of MDA231-roGFP2 cells seeded in the LF and SkMc niches over ten days. n = 8 technical replicates, performed in triplicate. Two-way ANOVA, followed by Sidak's multiple comparisons test, was performed. Outgrowth on LF v. SkMc per timepoint: * P=0.036 for 4d and **** P<0.0001 for 6d, 8d, and 10d. P=0.07 for the 2d timepoint. *Right panels*: Representative images of MDA231-roGFP2 cells on SkMc (oxidized) and LF (reduced). Scale bar: 100 μm. c) MDA231-roGFP2 outgrowth (mCherry A.F.) on the LF and SkMc niches over ten days. n = 8-12 technical replicates, performed in triplicate. Two-way ANOVA, followed by Sidak's multiple comparisons test, was performed. Oxidation on LF v. oxidation on SkMc per timepoint: *P=0.02 for 0d and **** P<0.0001 for 6d, 8d, and 10d. Comparisons at 2d and 4d yielded P>0.05. d) ROS mean intensity of MDA-MB-231 cells on LF and SkMc niche (CellROX647). n = 852 cells in LF, 39 cells in SkMc from n = 3-5 wells per condition across two independent experiments. An unpaired t-test resulted in a two-tailed ****P value < 0.0001. e) Representative images of MDA-MB-231 cells stained with CellROX647 on

SkMc and LF. Scale bar: 50 μm for SkMc images and 100 μm for LF images. f) ROS mean intensity (CellROX647) measurements per well for LF, SkMc, and the myotube subset of SkMc. n = 24 negative control wells, 23 LF wells, 24 SkMc wells (412 individual myotubes; average plotted per well). One-way ANOVA, followed by uncorrected Fisher's LSD test: ****P<0.0001 for negative control v. myotubes, LF v. myotubes and SkMc v. myotubes. All other comparisons yielded * P>0.05. g) Extracellular H_2O_2 measured within the LF and SkMc niches over a 10-day period via Amplex Red assay. n = 8 technical replicates, repeated in triplicate. Two-way ANOVA, followed by Tukey's multiple comparisons test: at 3d and 7d, **** P<0.0001 for LF v. SkMc. At 10d, *P=0.011 for LF v. SkMc h) Extracellular H_2O_2 detected in the following niches: LF-only, SkMc-only or LF/SkMc mixture (Amplex Red). n = 5 technical replicates. The mean of each condition was compared against the mean of LF-only: * P=0.049 for 1:20, * P=0.04 for 1:50, ** P=0.0002 for 1:100, *** P=0.0001 for All SkMc. All other comparisons yielded P>0.05. i) Schematic of mouse study to determine if DTCs are oxidized in skeletal muscle and lung. j) Dot-plot of the oxidation state of MDA231-roGFP2 cells found in skeletal muscle and lung. n = 5 mice, where 13 cells were found in skeletal muscle and 35 cells or lesions were detected in lung. Skeletal muscle and lung were sampled equally. One-way ANOVA was used test for statistical significance, followed by Dunnett's multiple comparisons test. Oxidation state was compared against the mean for single DTCs per organ site: for lung, P= 0.053 for doublets, ***P=0.0001 for clusters of 3-10 and 11+ cells. k) Visual representation of metastases and DTCs found in lung and SkM. Dark colours (purple) denote reduction and hot colours (orange) denote oxidization. Scale bar, 50 μm. For **c-d, f-g, h,** and **j**, centre line represents the mean, and error bars the s.e.m.

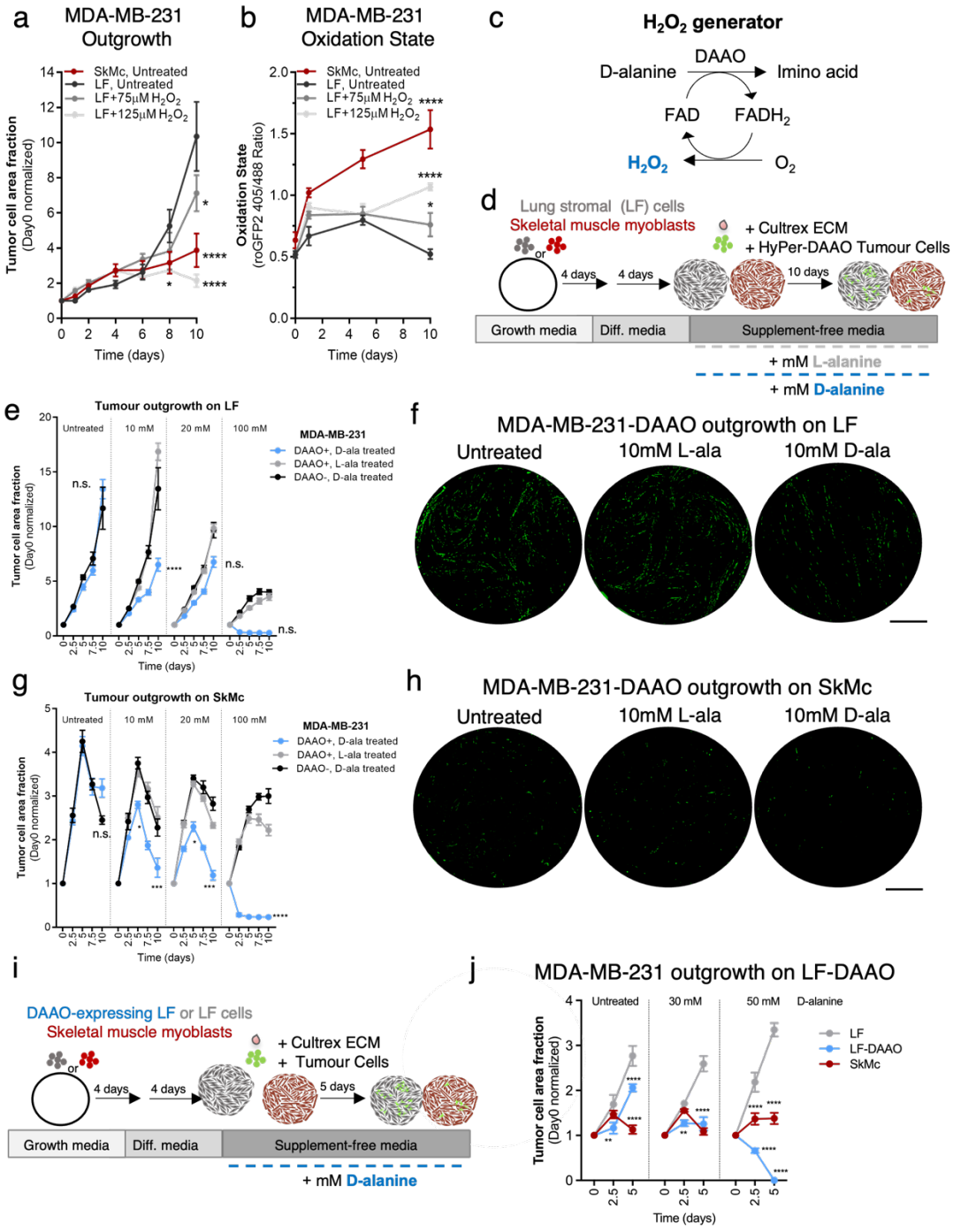

Figure 3.5. Sustained oxidative stress prevents DTC outgrowth independent of organ site. a) MDA231-roGFP2 outgrowth on LF when treated with 75 μM and 125 μM H_2O_2, as compared to outgrowth on SkMc. n = 6 technical replicates, repeated in triplicate. Two-way ANOVA was performed, followed by Dunnett's multiple comparison test. Compared against untreated LF, * P=0.029 for SkMc and * P=0.032 for 125 μM H_2O_2 at 8d. *** P =0.0001 for SkMc, * P=0.033 for 75 μM H_2O_2, and *** P=0.0001 for 125 μM H_2O_2 at 10d. b) Oxidation state of MDA231-roGFP2 on LF when treated with 75 μM and 125 μM H_2O_2, compared to oxidation state when on SkMc. n = 3-6 technical replicates, repeated in duplicate. Two-way ANOVA was performed, followed by an uncorrected Fisher's LSD test. Compared against the untreated LF cohort, **** P<0.0001 for SkMc at 1d, 5d, and 10d. * P=0.011 for 125 μM H_2O_2 at 1d. **P=0.0096 for 75 μM H_2O_2 and **** P<0.0001 for 125 μM H_2O_2 at

10d. c) Schematic showing biochemistry of the chemogenetic H_2O_2 generator called DAAO. d) Schematic depicting the experiment to test if increased tumoral H_2O_2 production would stunt outgrowth on LF and SkMc niches. e) MDA231-DAAO or MDA231-WT outgrowth on LF following daily treatment of 10 mM, 20 mM and 100 mM L-alanine or D-alanine. n = 4-5 technical replicates, repeated in triplicate. One-way ANOVA was performed, followed by Tukey's multiple comparisons test. At Day 10, all D-alanine doses significantly reduced outgrowth on LF when compared to untreated $DAAO^+$ cells (**** P<0.0001). However, only the 10 mM D-ala dose suppressed growth when compared to 10 mM L-ala ($DAAO^+$) and 10 mM D-ala (WT) controls. 10 mM D-ala v. 10 mM L-ala, ****P<0.0001. 10 mM D-ala in the DAAO versus WT, **** P<0.0001. All others yielded P>0.05. f) Representative IF images of MDA231-DAAO outgrowth on LF. Scale bar, 10 mm. g) MDA231-DAAO or MDA231-WT outgrowth on SkMc following daily treatment with 10 mM, 20 mM and 100 mM L-alanine or D-alanine. n = 4-5 technical replicates, repeated in triplicate. One-way ANOVA was performed, followed by Tukey's multiple comparisons test. At Day 5, all D-alanine doses significantly reduced outgrowth on SkMc when compared to untreated $DAAO^+$ cells (**** P<0.0001). 10 mM D-ala in the DAAO v. WT, ***P=0.0004; 10 mM D-ala v. 10 mM L-ala, * P=0.012. At Day 10, all D-alanine doses significantly reduced outgrowth on SkMc when compared to the untreated $DAAO^+$ cells (**** P<0.0001). 10 mM D-ala in the DAAO v. WT, * P=0.01; 10 mM D-ala v. 10 mM L-ala, ** P=0.0006. 20 mM D-ala in the DAAO v. WT, **** P<0.0001; 20 mM D-ala v. 20 mM L-ala, ** P=0.0007. 100 mM D-ala in the DAAO v. WT, **** P<0.0001; 100 mM D-ala v. 100 mM L-ala, **** P<0.0001. h) Representative IF images of MDA231-DAAO outgrowth on SkMc. Scale bar, 10 mm. i) Schematic depicting the experiment to test if increased H_2O_2 production in the LF niche would stunt tumour cell outgrowth. j) MDA231-WT outgrowth on LF, LF-DAAO or SkMc following daily treatment of 30 mM and 50 mM D-alanine. n = 3 technical replicates, repeated in triplicate. Two-way ANOVA, followed by uncorrected Fisher's LSD, was performed. At Day 2.5, ** P = 0.0013 for LF-DAAO untreated v. LF untreated, P = 0.06 for LF-DAAO untreated v. SkM untreated, ** P = 0.007 for LF-DAAO 30 mM v. LF 30 mM, **** P < 0.0001 for LF-DAAO 50 mM v. LF 50 mM. At Day 5, **** P < 0.0001 for LF-DAAO untreated v. LF untreated, LF-DAAO untreated v. SkM untreated, LF-DAAO 30 mM v. LF 30 mM, and LF-DAAO 50 mM v. LF 50 mM. For **a-b, e, g and j**, centre line represents the mean, and error bars the s.e.m.

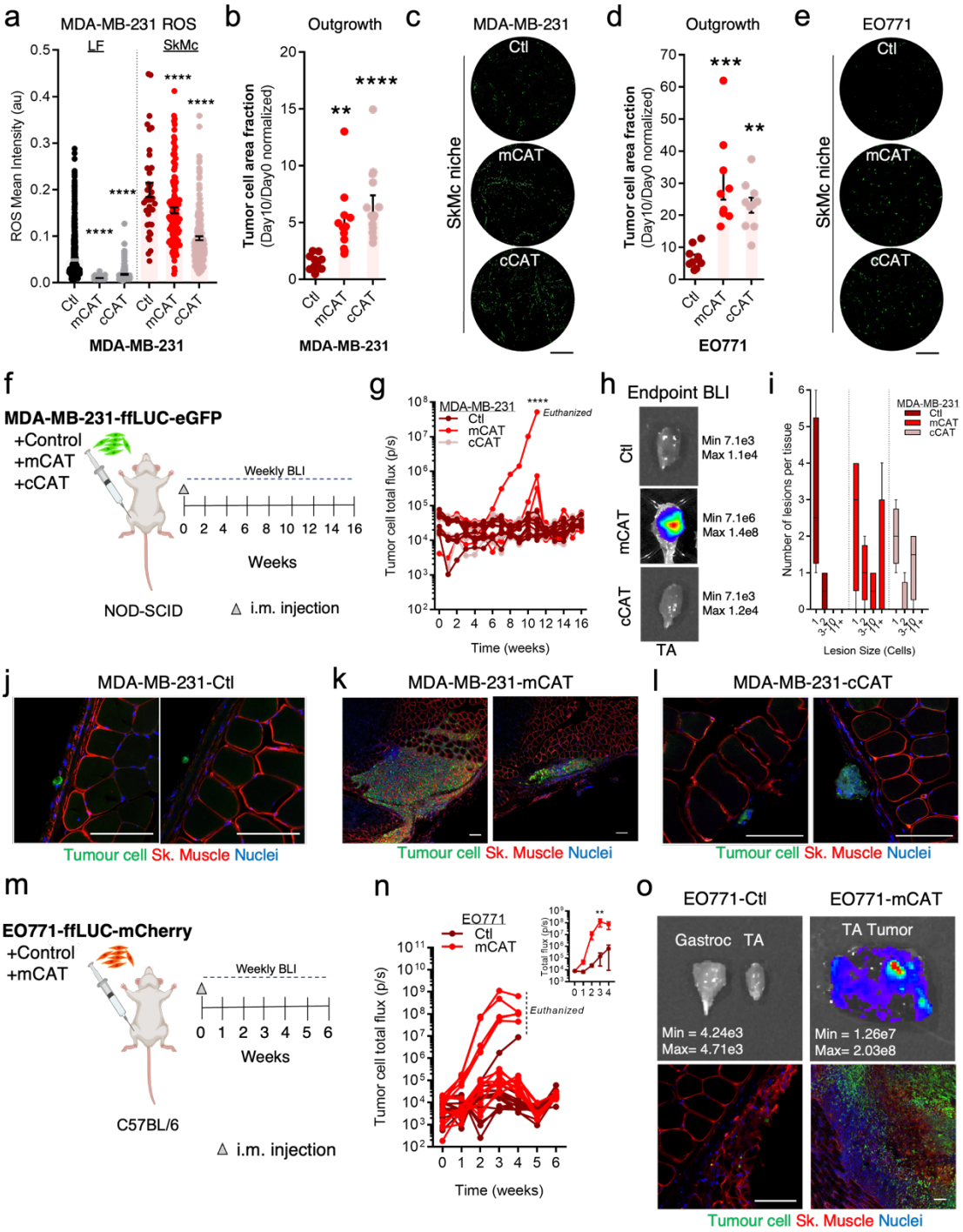

Figure 3.6. Enhancing antioxidant capacity enables skeletal muscle colonization in culture and *in vivo*. a) ROS mean intensity (CellRox647) of MDA231-Ctl, -mCAT or -cCAT seeded in co-culture with LF or SkMc. n = 39 cells for SkM – Ctl, 137 cells for mCAT, 199 cells for cCAT, 851 cells for LF – Ctl, 200 cells for mCAT, 233 cells for cCAT. Datapoints were collected from 8 wells across two independent experiments. One-way ANOVA was used, followed by Tukey's multiple comparisons test: all comparisons ****P<0.0001 except LF mCAT v. LF cCAT, p=0.53. b) Dot-plot of MDA231-Ctl, -mCAT or -cCAT outgrowth (GFP A.F.) on the SkMc niche. n = 10 technical replicates, repeated in triplicate. One-way ANOVA, followed by Dunnett's multiple comparisons test, was performed. The mean of each condition was compared against the mean of MDA231-Ctl: Ctl v mCAT (** *P*

=0.009) and Ctl v cCAT (** *P* =0.0001). c) Representative IF images of MDA231-Ctl, -mCAT or -cCAT outgrowth (green) on SkMc. Scale bar, 20 mm. d) EO771-Ctl, -mCAT or -cCAT outgrowth (GFP A.F.) on the SkMc niche. n = 10 technical replicates, repeated in triplicate. One-way ANOVA, followed by Dunnett's multiple comparisons test, was performed. Ctl v mCAT, *** *P* = 0.0001. Ctl v cCAT, ** *P* =0.001. e) Representative IF images of EO771-Ctl, -mCAT or -cCAT outgrowth (green) on SkMc. Scale bar, 20 mm. f) Schematic of NOD-SCID mouse study to examine if ectopic catalase expression promotes skeletal muscle colonization *in vivo*. g) BLI measurements total flux (photon/second) for MDA231-Ctl, -mCAT and -cCAT over 16 weeks. n = 10 mice per cohort. Two-way ANOVA, followed by Dunnett's multiple comparisons test, was performed. At Week 11, **** *P*<0.0001 for Ctl v. mCAT. All others yielded *P*>0.05. h) MDA231 total flux (photons/second) of *ex vivo* TA at Week 11 for mCAT and Week 16 for Ctl and cCAT cohorts. i) IF quantification (number of lesions per TA versus size of the lesion) of MDA231 cells that persist in the TA after 16 weeks. n = 4 tissues per cohort analysed. Chi-square test for trend was performed, Ctl v. CAT (both ectopic expression constructs grouped together), *P* =0.016. j) Representative immunofluorescence images of (j) MDA231-Ctl, (k) MDA231-mCAT, and (l) MDA231-cCAT DTCs/lesions in skeletal muscle. Scale bar: 100 μm. m) Schematic of C57BL/6 mouse study to examine if ectopic catalase expression promotes colonization of skeletal muscle. n) BLI (total flux, p/s) for EO771-Ctl and -mCAT over 6 weeks. n = 14 mice per cohort. Two-way ANOVA, followed by uncorrected Fisher's LSD, was performed, where ** *P* =0.0032 at Week 3; *P* =0.09 at Week 4. Comparisons yielded *P*>0.8 for all other timepoints. o) Representative BLI (total flux, p/s) and IF images for EO771-Ctl and mCAT cohorts. Scale bar, 100 μm. For **a-b** and **d**, centre line represents the mean, and error bars the s.e.m. For **i**, centre line represents the median, and the whiskers the smallest and largest values.

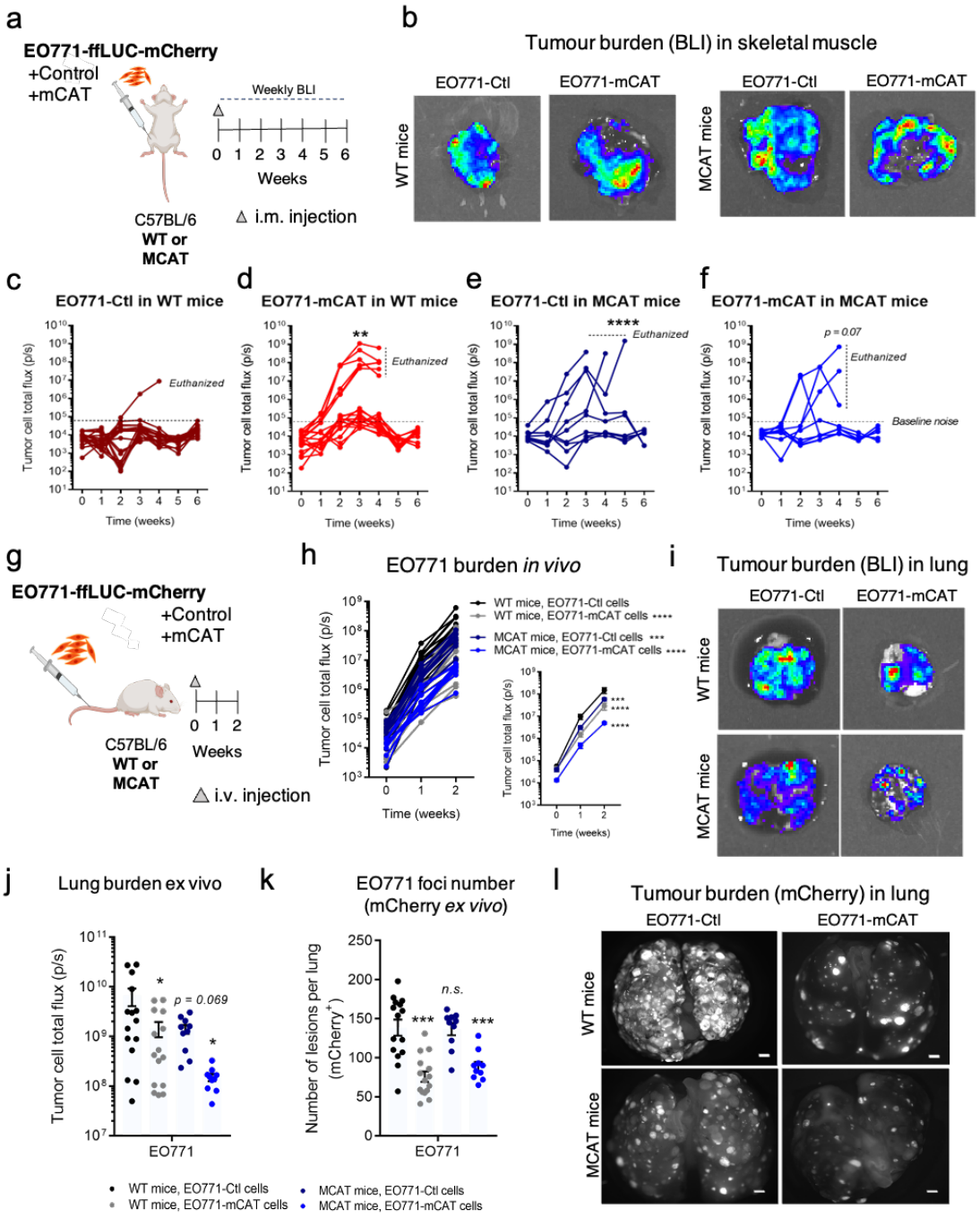

Figure 3.7. Reduction of tumoural or environmental mtROS stimulates skeletal muscle colonization but hinders lung colonization. a) Schematic of C57BL/6 mouse study to examine if ectopic catalase expression in the tissue environment promotes skeletal muscle colonization. b) Representative BLI (total flux, p/s) images for EO771-Ctl and mCAT cells in wildtype (**WT**) and MCAT mice. c-f) BLI (total flux, p/s) for EO771-Ctl and -mCAT cell i.m. injected into WT or MCAT mice over 6 weeks. n = 19 mice per WT cohort, 9 mice per MCAT cohort. Two-way ANOVA, followed by uncorrected Fisher's LSD, was performed, where ** $P = 0.0065$ at Week 3 for EO771-Ctl v. EO771-mCAT in WT mice and $P = 0.07$ at Week 4 for EO771-Ctl in WT mice v. EO771-mCAT in MCAT mice. **** $P < 0.0001$ at Week 5 for EO771-Ctl in WT mice v. EO771-Ctl in MCAT mice. All other comparisons against EO771-Ctl in WT mice are $P > 0.15$ for all timepoints. g) Schematic of C57BL/6 mouse study to examine if ectopic catalase expression in the tissue environment promotes lung colonization. h)

BLI (total flux, p/s) for EO771-Ctl and -mCAT cell iv injected into WT or MCAT mice over 2 weeks. n = 15 WT and 10 MCAT mice per cohort. Two-way ANOVA, followed by Dunnett's multiple comparison test, was performed, where at Week 2, ** $P = 0.0003$ for EO771-Ctl in WT v. MCAT mice and *** $P = 0.0001$ for both EO771-Ctl v. EO771-mCAT in WT mice and EO771-Ctl in WT mice v. EO771-mCAT in MCAT mice. There were not significant differences at earlier timepoints. i) Representative BLI (total flux, p/s) images for EO771-Ctl and mCAT cells in WT and MCAT mice. j) BLI (total flux, p/s) of lung *ex vivo* from WT and MCAT mice iv injected with EO771-Ctl and -mCAT cells. One-way ANOVA, followed by Dunnett's multiple comparison test, was performed where * $P = 0.038$ for EO771-Ctl v. EO771-mCAT in WT mice and * $P = 0.018$ for EO771-Ctl in WT mice v. EO771-mCAT in MCAT mice. $P = 0.069$ for EO771-Ctl in WT v. MCAT mice. k) Quantification of EO771-Ctl and -mCAT lesions in WT or MCAT lungs. One-way ANOVA, followed by Dunnet's multiple comparison test, was performed where *** $P = 0.0001$ for EO771-Ctl v. EO771-mCAT in WT mice and ** $P = 0.005$ for EO771-Ctl in WT mice v. EO771-mCAT in MCAT mice. $P = 0.996$ for EO771-Ctl in WT v. MCAT mice. l) Representative fluorescent (mCherry) images of lung *ex vivo* from WT and MCAT mice iv injected with EO771-Ctl and -mCAT cells. Scale bar, 1 mm. For **c-f, h and j-k**, centre line represents the mean, and error bars the s.e.m.

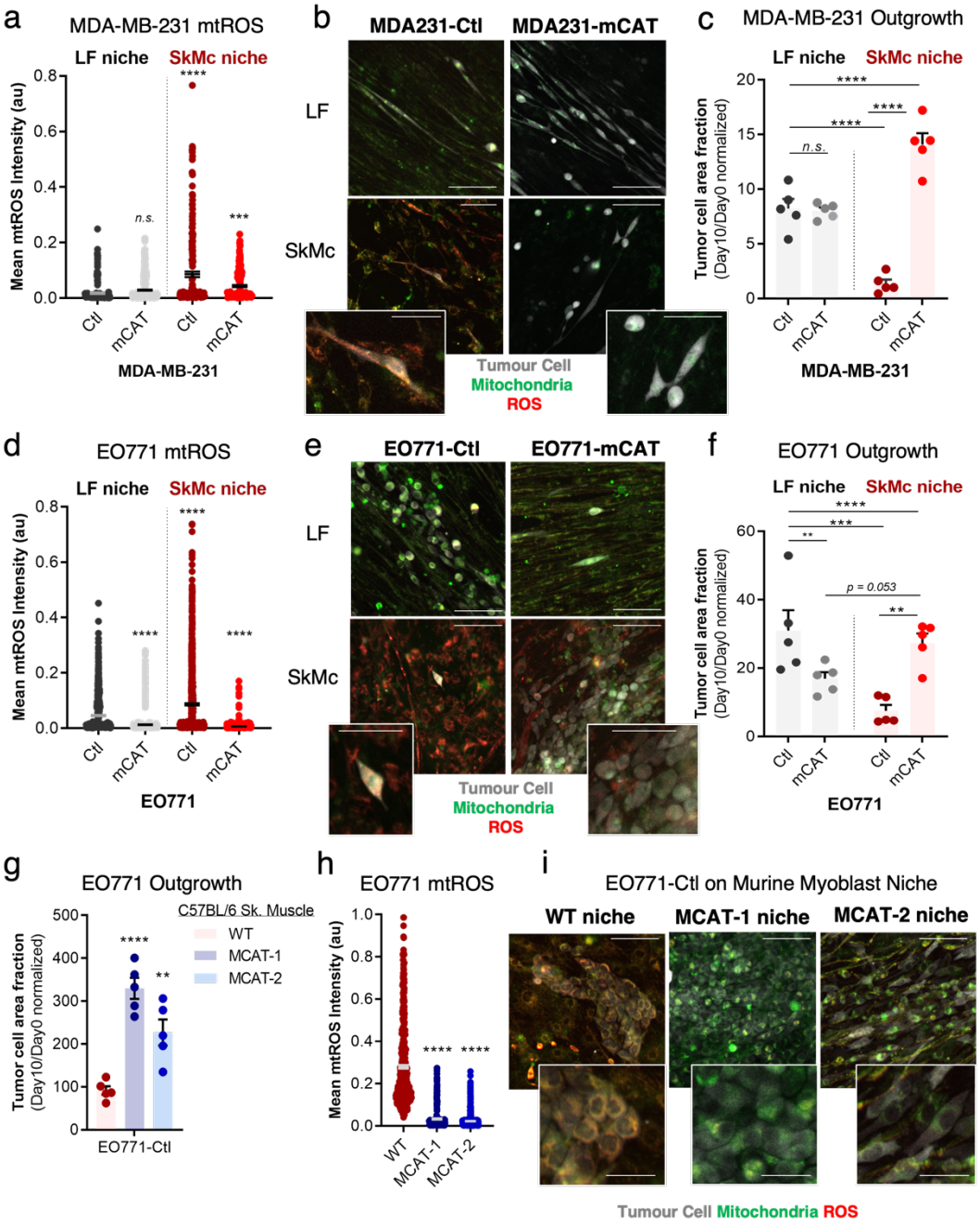

Figure 3.8. Mitochondrial ROS burden in tumour cells induced by the skeletal muscle niche resolves with mitochondrial catalase expression in tumour cells or in myocytes. a) Dot-plot of mean mitochondrial ROS intensity (a.u.) for MDA231-Ctl or -mCAT tumour cells on the LF or SkM niche. n = 208 MDA231-Ctl cells on LF, 662 MDA231-mCAT cells on LF, 202 MDA231-Ctl cells on SkMc, and 229 MDA231-mCAT cells on SkMc. Analysed cells came from 3 experimental replicates, where each contained 5 technical replicates. One-way ANOVA, followed by Tukey's multiple comparisons test, was performed where **** $P < 0.0001$ for MDA231-Ctl on LF *v.* MDA231-Ctl on SkMc and MDA231-Ctl on LF v. MDA231-mCAT on SkMc. $P = 0.17$ for MDA231-Ctl *v.* MDA231-mCAT on LF. b) Representative IF images of mitochondrial ROS in MDA231 cells. Scale bar, 100 μm; Inset scale bar, 50 μm. c) Dot-plot of the MDA231 outgrowth on LF or SkMc niche, paired with the mitochondrial ROS data in (a). n = 5 wells per cohort, repeated in triplicate. One-way ANOVA, followed by uncorrected Fisher's LSD, was performed where **** $P < 0.0001$ for all comparisons except MDA231-Ctl v.

MDA231-mCAT on LF, where $P = 0.84$. d) Dot-plot of mean mitochondrial ROS intensity (a.u.) for EO771-Ctl or -mCAT tumour cells on the LF or SkM niche. n = 1129 EO771-Ctl cells on LF, 980 EO771-mCAT cells on LF, 1080 EO771-Ctl cells on SkMc, and 1133 EO771-mCAT cells on SkMc. Analysed cells came from 3 experimental replicates, where each contained 5 technical replicates. One-way ANOVA, followed by Tukey's multiple comparisons test, was performed where **** $P < 0.0001$ for MDA231-Ctl *v.* MDA231-mCAT on LF, MDA231-Ctl on LF *v.* MDA231-Ctl on SkMc, and MDA231-Ctl on LF v. MDA231-mCAT on SkMc. **** $P < 0.0001$ for MDA231-Ctl v. MDA231-mCAT on SkMc. e) Representative IF images of mitochondrial ROS in EO771 cells. Scale bar, 100 μm; Inset scale bar, 50 μm. f) Dot-plot of the EO771 outgrowth on LF or SkMc niche, paired with the mitochondrial ROS data in (d). n = 5 wells per cohort, repeated in triplicate. One-way ANOVA, followed by uncorrected Fisher's LSD, was performed where $P = 0.13$ for EO771-Ctl v EO771-mCAT on LF, ** $P = 0.0002$ for MDA231-Ctl on LF *v.* SkMc, ** $P = 0.0011$ for EO771-Ctl *v.* EO771-mCAT on SkMc. $P = 0.053$ for EO771-mCAT on LF *v.* SkMc, $P = 0.78$ for EO771-mCAT on LF *v.* EO771-Ctl on SkMc, and $P = 0.48$ for EO771-Ctl on LF *v.* EO771-mCAT on SkMc. g) Dot-plot of the EO771-Ctl outgrowth on wildtype (WT), MCAT-1 or MCAT-2 murine myoblast niches. n = 5 wells per cohort, repeated twice. One-way ANOVA, followed by Dunnett's multiple comparisons test, was performed where **** $P < 0.0001$ for WT *v.* MCAT-1 and ** $P = 0.0027$ for WT *v.* MCAT-2. h) Dot-plot of mean mitochondrial ROS intensity (a.u.) for EO771-Ctl cells on WT, MCAT-1 and MCAT-2 myoblast niches, paired with the outgrowth data in (g). n = 540 EO771-Ctl cells on WT, 346 EO771-Ctl cells on MCAT-1 and 750 EO771-Ctl cells on MCAT-2. Analysed cells came from 2 experimental replicates, where each contained 5 technical replicates. One-way ANOVA, followed by Tukey's multiple comparisons test, was performed where **** $P < 0.0001$ for WT *v.* MCAT-1 and WT *v.* MCAT-2. $P = 0.37$ for MCAT-1 *v.* MCAT-2. i) Representative IF images of mitochondrial ROS in EO771 cells on WT, MCAT-1 or MCAT-2 myoblast niches. Scale bar, 100 μm; Inset scale bar, 50 μm. For **a, c-d, f-h**, centre line represents the mean, and error bars the s.e.m.

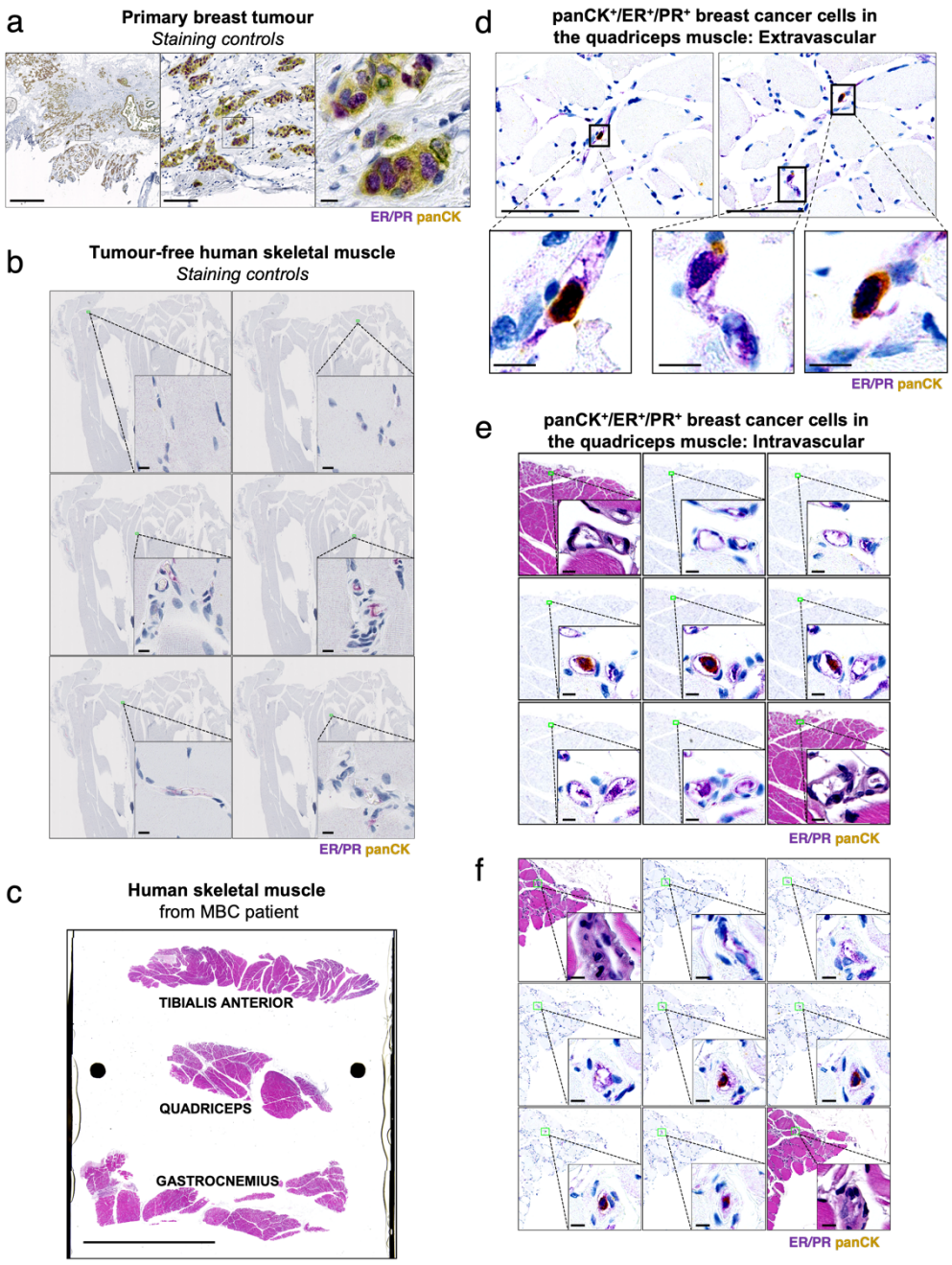

Supplementary Figure 3.1. Human skeletal muscle from a metastatic breast cancer patient harbours panCK$^+$/ER$^+$/PR$^+$ breast cancer cells. a) Representative multiplex IHC images from an ER$^+$/PR$^+$ primary breast tumour specimen, used as a positive staining control. ER/PR (breast cell marker) staining in purple, pan-cytokeratin (**panCK,** epithelial cell marker) staining in yellow. Scale bar: 1 mm (left), 100 μm (centre) and 10 μm (right). b) Representative multiplex IHC images from human skeletal muscle, used as a negative staining control. ER/PR staining in purple, panCK staining in yellow. Scale bar, 10 μm. c) Representative IHC image of the three human skeletal muscle sites sampled (tibialis anterior, quadriceps and gastrocnemius) from a patient with metastatic breast cancer (MBC). Scale bar, 1 cm. d) Multiplex IHC panels of three panCK$^+$/ER$^+$/PR$^+$ cells located inside the quadriceps muscle. ER/PR staining in purple, pan-cytokeratin staining in yellow. Scale bar 100 μm, Inset 10 μm. e-f) Two micropictographs of serial sections (4 μm) of FFPE skeletal muscle tissue from an individual with metastatic breast cancer. The slides were stained with hematoxylin and eosin or sequentially stained with a multiplex IHC panel consisting of ER/PR (purple) and panCK (yellow). Two ER$^+$/PR$^{+/}$panCK$^+$ breast cancer cells were identified in a vessel located within the quadriceps muscle. Scale bar, 10 μm.

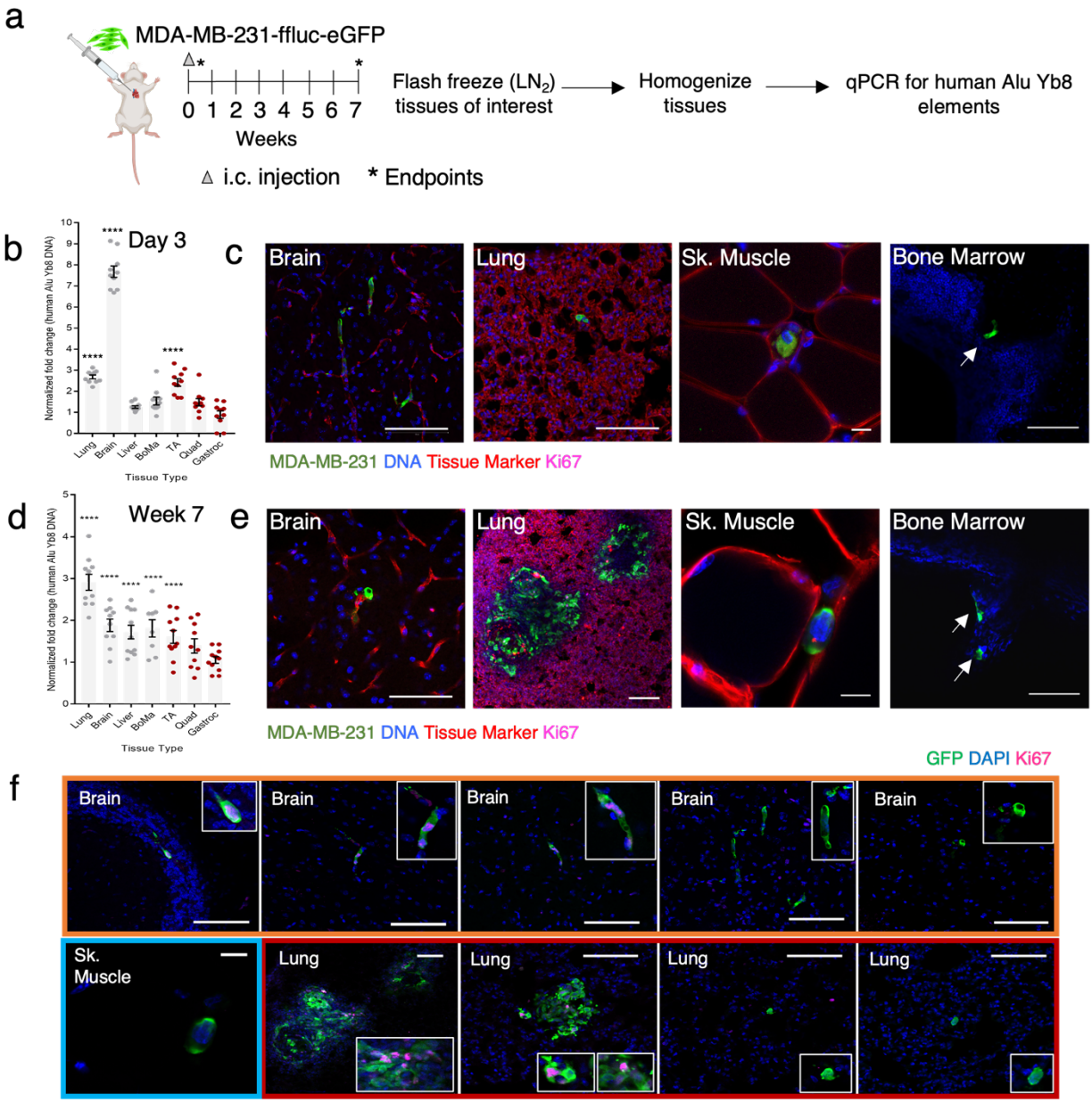

Supplementary Figure 3.2. AluYb8 qPCR reveals that DTCs travel to and persist within mouse skeletal muscle following intracardiac injection of breast cancer cells. a) Schematic of the mouse study to examine frequency of DTCs across organ site at early and late timepoints. b) AluYb8 amplification at Day 3 post ic injection, normalized by internal control (B-actin) and graphed as fold change above uninoculated control. Data collected from n = 11 inoculated and n=3 uninoculated mice. Lung, brain and TA, ****P<0.0001 when t-tests, followed by the Holm-Sidak method, were run for comparison of tumour-bearing tissues to uninoculated controls. c) Representative immunofluorescence images of matched brain, lung, skeletal muscle and bone marrow (BoMa) with DTCs in these tissue sites at the early timepoint. Scale bar: 100 μm for lung, brain and BoMa. Scale bar: 10 μm for skeletal muscle. d) AluYb8 amplification at Week 7 normalized by internal control (b-actin) and graphed as fold change above uninoculated control. Data collected from n = 11 inoculated and n = 3 uninoculated mice. Lung, brain, liver, BoMa and TA, **** P<0.0001 when multiple t-tests, followed by Holm-Sidak method, were run for comparison of tumour-bearing tissues to uninoculated controls.

Supplementary Figure 3.2. AluYb8 qPCR reveals that DTCs travel to and persist within mouse skeletal muscle following intracardiac injection of breast cancer cells. e) Representative immunofluorescence images of matched brain, lung, skeletal muscle and BoMa with DTCs in these tissue sites at the late timepoint. Scale bar: 100 μm for lung, brain and BoMa; 10 μm for skeletal muscle. f) Representative IF images of DTCs or clusters of tumour cells in the brain, lung or skeletal muscle. $Ki67^+$ marks proliferating cells. Scale bar: 100 μm for lung, brain and BoMa; 10 μm for skeletal muscle. For c, e and g, centre line represents the mean, and error bars the standard error of the mean (s.e.m.).

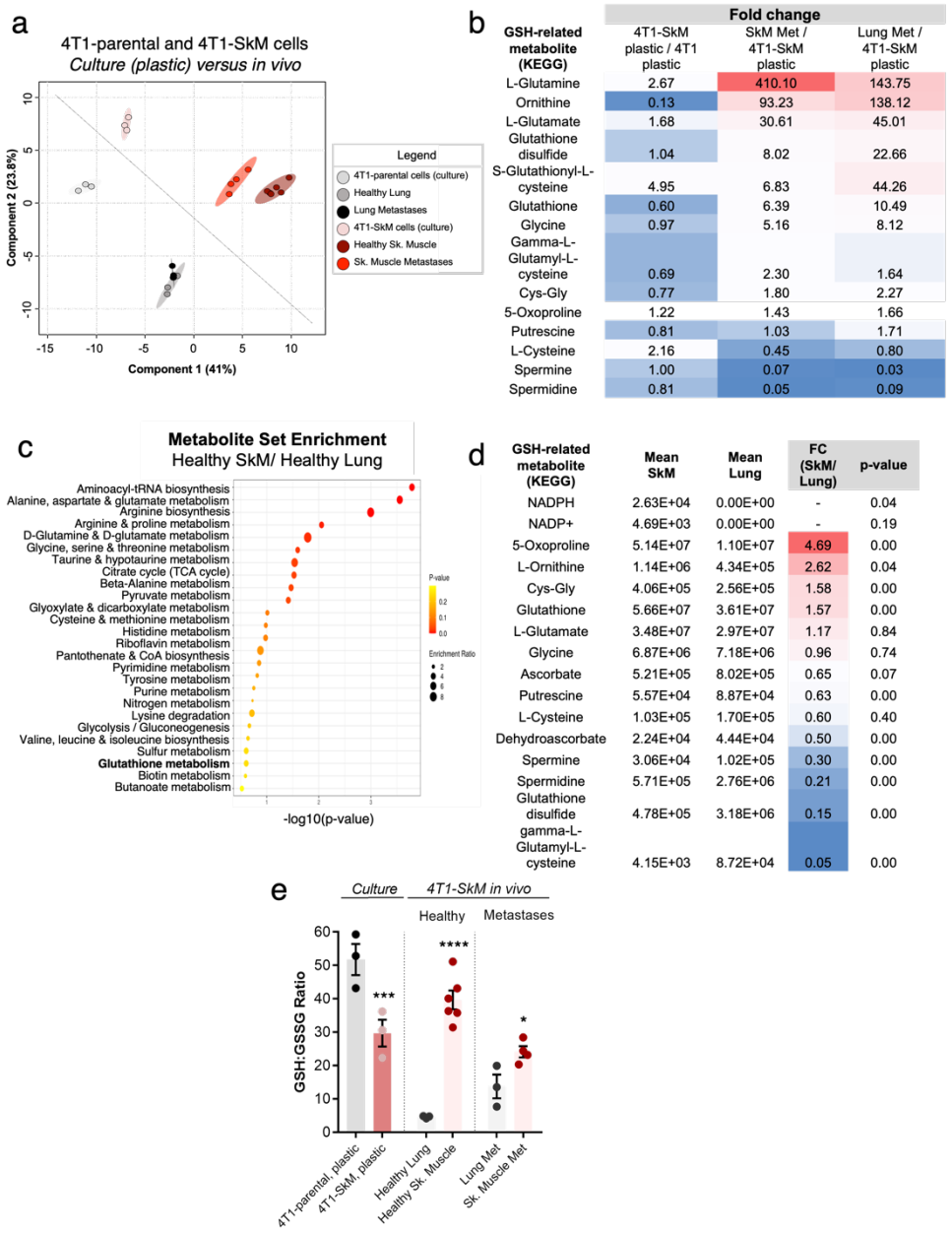

Supplementary Figure 3.3. Metabolic comparison of skeletal muscle-metastatic 4T1 cells pre- and post-injection reveal that 4T1-SkM adapt to skeletal muscle. a) PLS-DA score plot comparing 4T1-parental and 4T1-SkM cells in tissue culture against 4T1-SkM skeletal muscle metastases, 4T1-SkM lung metastases, healthy skeletal muscle and healthy lung. b) Fold change enrichment of GSH-related metabolites (as defined by KEGG's GSH metabolism set) for 4T1-SkM v. 4T1-parental in culture, skeletal muscle metastases v. 4T1-SkM in culture, and lung metastases v. 4T1-SkM in culture. c) Metabolite Set Enrichment of the metabolites that were 2-fold enriched in healthy skeletal muscle versus healthy lung. Over Representation Analysis used the hypergeometric test; one-tailed P-values were provided after adjusting for multiple testing. d) Table displaying the mean values for the GSH-related metabolites in healthy skeletal muscle and healthy lung, followed by the fold-change difference between the two. e) Dot-plot of the ratio of reduced to oxidized glutathione (GSH:GSSG) for 4T1-SkM and 4T1-parental in culture, healthy skeletal muscle and healthy lung, and skeletal muscle and lung metastases. n = 3 replicate for 4T1-parental and 4T1-SkM culture samples. n = 4 muscle- and 3 lung- metastases, 6 healthy muscle and 3 healthy lung. An one-way ANOVA, followed by uncorrected Fisher's LSD, was performed where *** $P = 0.0004$ for 4T1-parental v 4T1-SkM, **** $P < 0.0001$ for healthy skeletal muscle v. lung, * $P = 0.037$ for skeletal muscle met v. lung met.

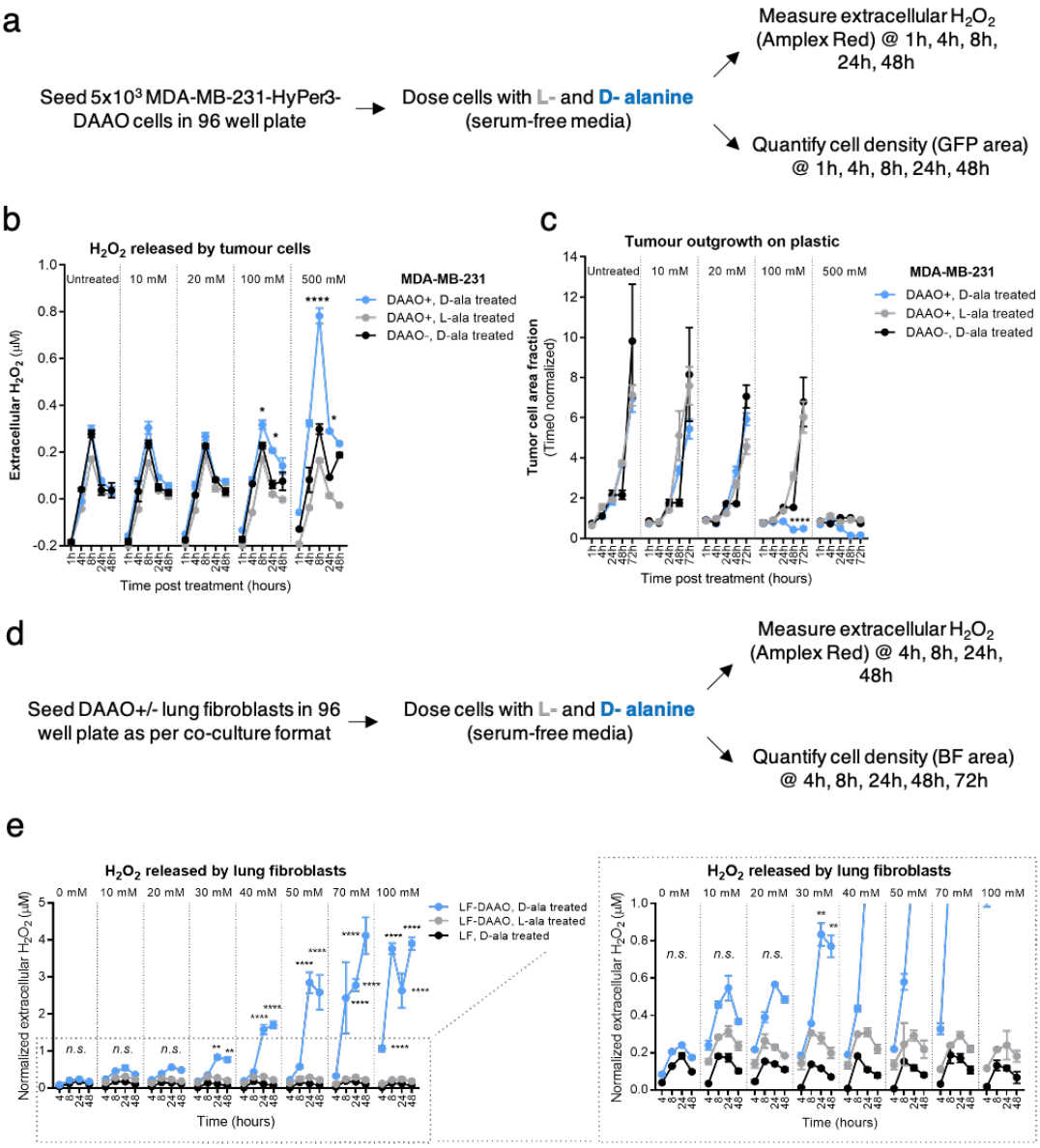

Supplementary Figure 3.4. H_2O_2 is robustly generated upon D-alanine treatment in DAAO-expressing tumour cells and lung fibroblasts. a) Schematic showing the experimental workflow to test if D-alanine and L-alanine stimulates H_2O_2 production from MDA231-WT and MDA231-DAAO cells, and the effect of these treatments on tumour cell outgrowth. b) Extracellular H_2O_2 measurements of MDA231-WT and MDA231-DAAO cells treated with 10, 20, 100 or 500 mM of D- or L-alanine. Samples collected at 1h, 4h, 8h, 24h and 48h. n = 3 technical replicates. Two-way ANOVA was used, followed by Dunnett's multiple comparisons test. The mean of each condition was compared against the mean of the untreated MDA231-DAAO datapoints. At 1h, * P= 0.028 for 100 mM D-ala. At 4h, *** P= 0.0001 for 100 mM D-ala, ** P= 0.0017 20 mM D-ala, and ** P= 0.0019 for 100 mM D-ala MDA231-WT cells. At 8h, *** P= 0.0001 for 100 mM L-ala and 20 mM L-ala. * P= 0.023 for 100 mM D-ala MDA231-WT cells and * P= 0.018 for 20 mM D-ala MDA231-WT cells. At 24h, *** P= 0.0001 for 100 mM D-ala and * P= 0.011 for 100 mM L-ala. At 48h, *** P= 0.0001 for 100 mM D-ala. All other comparisons yielded P>0.05.

Supplementary Figure 3.4. H_2O_2 is robustly generated upon D-alanine treatment in DAAO-expressing tumour cells and lung fibroblasts. c) Outgrowth (A.F.) of MDA231-WT and MDA231-DAAO cells treated with 10, 20, 100 or 500 mM of D- or L-alanine. Samples collected at 0h, 1h, 4h, 24h, 48h and 72h. n = 3 technical replicates. Two-way ANOVA was used, followed by Dunnett's multiple comparisons test. The mean of each condition was compared against the mean of untreated MDA231-DAAO. At 48h, *** P=0.0001 for 100 mM D-ala, ** P=0.0011 for 100 mM D-ala MDA231-WT cells, P=0.0036 for 20 mM D-ala MDA231-WT cells, and * P=0.04 for untreated MDA231-WT cells. At 72h, *** P=0.0001 for 100 mM D-ala, untreated MDA231-WT cells, and 20 mM L-ala MDA231-WT cells. All other comparisons yielded P>0.05. d) Schematic showing the experimental workflow to test if D-alanine and L-alanine stimulates H_2O_2 production in LF-DAAO or LF cells. e) Extracellular H_2O_2 measurements of LF-DAAO or LF cells treated with 0, 10, 20, 30, 40-, 50-, 70- or 100-mM D- or L-alanine. Samples collected at 4h, 8h, 24h and 48h. n = 3 technical replicates per condition. Two-way ANOVA, followed by an uncorrected Fisher's LSD, were performed where P< 0.0001 for LF-DAAO 100 mM D-ala *v.* LF 100 mM D-ala and LF-DAAO 100 mM D-ala *v.* LF-DAAO 100 mM L-ala at 4h. At 8h: P = 0.03 for LF-DAAO 50 mM D-ala *v.* LF 50 mM D-ala. **** P < 0.0001 for the 70- and 100-mM D-ala comparison between LF-DAAO and LF cells At 24h: * P = 0.033 for LF-DAAO 20 mM D-ala v. LF 20 mM D-ala, ** P = 0.004 for LF-DAAO 30 mM D-ala v. LF 30 mM D-ala. **** P< 0.0001 for the 40-, 50-, 70- and 100-mM D-ala comparison between LF-DAAO and LF cells. At 48h: *** P = 0.0006 for LF-DAAO 30 mM D-ala *v.* LF 30 mM D-ala. **** P< 0.0001 for the 40-, 50-, 70- and 100-mM D-ala comparison between LF-DAAO and LF cells. All other comparisons between LF-DAAO and LF upon D-ala treatment are n.s. For **b-c** and **e**, error bars represent the s.e.m.

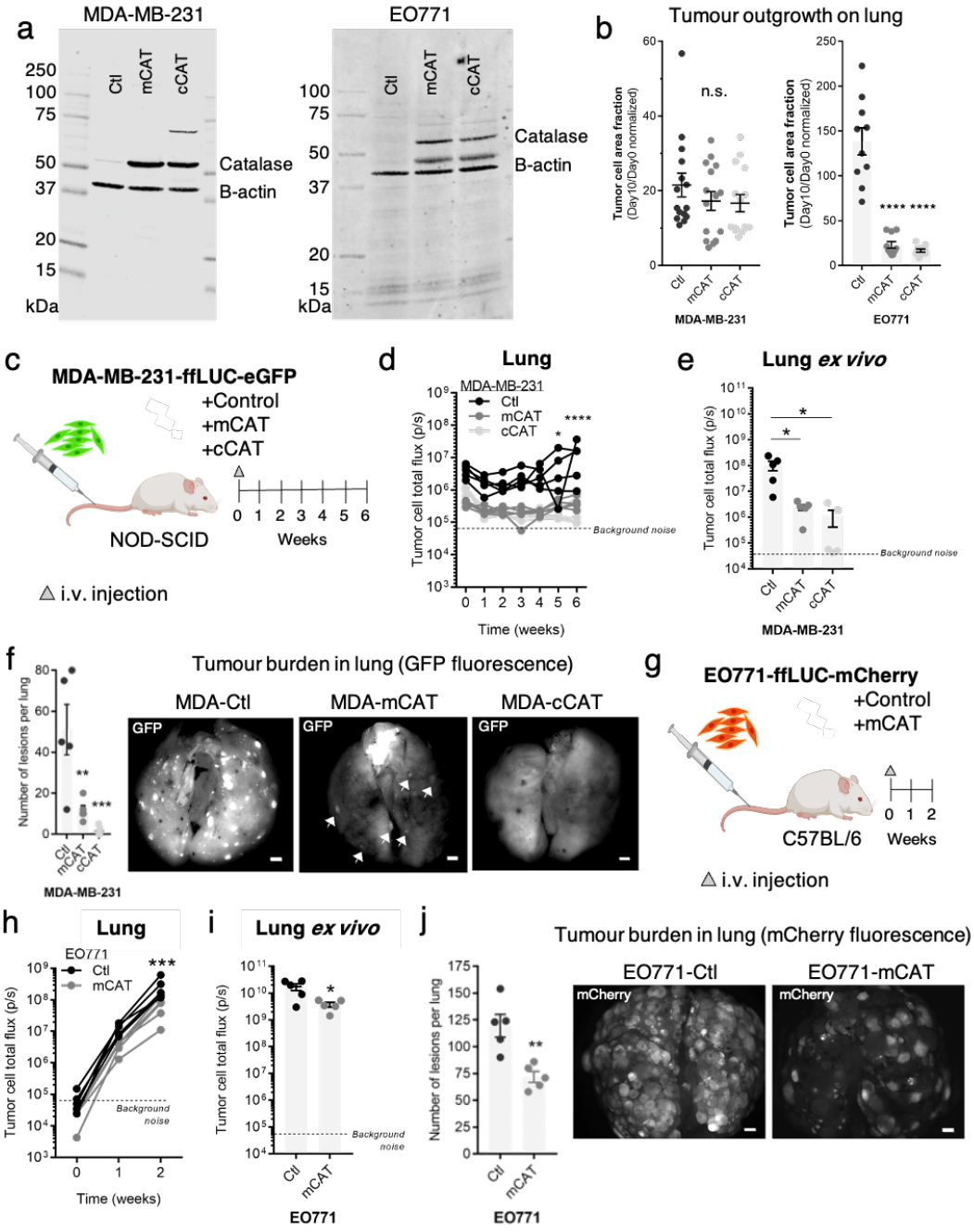

Supplementary Figure 3.5. Targeting catalase to the mitochondria of the tumour cell does not promote lung colonization. a) Representative Western blots of MDA231-Ctl, -mCAT and -cCAT protein lysates. Catalase runs at approximately 60 kDa. B-actin at 42 kDa. b) Dot-plots of MDA231-Ctl, -mCAT or -cCAT and EO771-Ctl, -mCAT and -cCAT outgrowth (GFP A.F.) on the LF niche. n =10-15 technical replicates, performed in triplicate. One-way ANOVA, followed by Dunnett's multiple comparisons test, was performed. The mean of each condition was compared against the mean for Ctl: MDA231- Ctl v mCAT, *P* =0.43 and Ctl v cCAT, *P* =0.35; EO771- both Ctl v mCAT and Ctl v ccAT, **** *P*< 0.0001. c) Schematic of NOD-SCID mouse study to examine if ectopic catalase expression promoted lung colonization *in vivo*. d) BLI measurements (total flux, photon/second) for MDA231-Ctl, -mCAT and -cCAT over six weeks. n = 5 mice per cohort. Two-way ANOVA, followed by Tukey's multiple comparisons test, was performed. At Week 5, Ctl v mCAT, * *P*=0.032 and Ctl v cCAT, * *P* =0.027. At Week 6, both Ctl v. mCAT and Ctl v. cCAT, **** *P*<0.0001.

Supplementary Figure 3.5. Targeting catalase to the mitochondria of the tumour cell does not promote lung colonization. e) BLI measurements (total flux, photon/second) for MDA231-Ctl, -mCAT and -cCAT in the lung *ex vivo*. n = 5 mice per cohort. One-way ANOVA, followed by Tukey's multiple comparisons test, was performed: Ctl v mCAT, * *P*=0.028 and Ctl v cCAT, * *P* =0.026. f) Quantification of MDA231-Ctl, -mCAT and -cCAT lesions in lung, accompanied by representative images of tumour burden (endogenous GFP). Arrows point to small GFP^+ lesions. Scale bar, 1 mm. One-way ANOVA was performed, followed by Dunnett's multiple comparisons test, to determine ***P*=0.0044 for Ctl v. mCAT, ****P*=0.0008 for Ctl v. cCAT. g) Schematic of C57BL/6 mouse study to examine if ectopic catalase expression promotes lung colonization *in vivo*. d) BLI quantification (total flux, photon/second) for EO771-Ctl and EO771-mCAT over two weeks. n = 5 mice per cohort. Two-way ANOVA, followed by Sidak's multiple comparisons test, was performed. At Week 2, Ctl v mCAT, * *P* =0.039. e) BLI quantification (total flux, photon/second) for EO771-Ctl and EO771-mCAT tumours in the lung *ex vivo*. n = 5 mice per cohort. Unpaired t-test was performed to determine statistical significance. Ctl v mCAT, * *P* =0.026. f) Quantification of EO771-Ctl and -mCAT lesions in lung, accompanied by representative images of tumour burden (endogenous mCherry). Scale bar, 1 mm. Unpaired two-tailed t-test was performed to find that ***P*=0.0036. For b, e-f and i-j, centre line represents the mean, and error bars the s.e.m.

Chapter 3 References

1. Paget, S. The distribution of secondary growths in cancer of the breast. *The Lancet* **133**, 571–573 (1889).
2. Elia, I. *et al.* Breast cancer cells rely on environmental pyruvate to shape the metastatic niche. *Nature* **568**, 117–121 (2019).
3. Elia, I. *et al.* Proline metabolism supports metastasis formation and could be inhibited to selectively target metastasizing cancer cells. *Nature Communications* **8**, (2017).
4. Dupuy, F. *et al.* PDK1-dependent metabolic reprogramming dictates metastatic potential in breast cancer. *Cell Metabolism* **22**, 577–589 (2015).
5. Tasdogan, A. *et al.* Metabolic heterogeneity confers differences in melanoma metastatic potential. *Nature* **577**, 115–120 (2020).
6. Sullivan, M. R. *et al.* Increased Serine Synthesis Provides an Advantage for Tumors Arising in Tissues Where Serine Levels Are Limiting. *Cell Metabolism* **29**, 1410-1421.e4 (2019).
7. Knott, S. R. V. *et al.* Asparagine bioavailability governs metastasis in a model of breast cancer. *Nature* **554**, 378–381 (2018).
8. Ghajar, C. M. *et al.* The perivascular niche regulates breast tumour dormancy. *Nature Cell Biology* **15**, 807–817 (2013).
9. Gupta, G. P. *et al.* Mediators of vascular remodelling co-opted for sequential steps in lung metastasis. *Nature* **446**, 765–770 (2007).
10. Peinado, H. *et al.* Melanoma exosomes educate bone marrow progenitor cells toward a pro-metastatic phenotype through MET. *Nature Medicine* **18**, 883–891 (2012).
11. Kaplan, R. N. *et al.* VEGFR1-positive haematopoietic bone marrow progenitors initiate the pre-metastatic niche. *Nature* **438**, 820–827 (2005).
12. Hiratsuka, S., Watanabe, A., Aburatani, H. & Maru, Y. Tumour-mediated upregulation of chemoattractants and recruitment of myeloid cells predetermines lung metastasis. *Nature Cell Biology* **8**, 1369–1375 (2006).
13. Kim, S. *et al.* Carcinoma-produced factors activate myeloid cells through TLR2 to stimulate metastasis. *Nature* **457**, 102–106 (2009).
14. Oskarsson, T. *et al.* Breast cancer cells produce tenascin C as a metastatic niche component to colonize the lungs. *Nature Medicine* **17**, 867–874 (2011).
15. Wculek, S. K. & Malanchi, I. Neutrophils support lung colonization of metastasis-initiating breast cancer cells. *Nature* **528**, 413–417 (2015).

16. Costa-Silva, B. *et al.* Pancreatic cancer exosomes initiate pre-metastatic niche formation in the liver. *Nature Cell Biology* **17**, 816–826 (2015).
17. Hoshino, A. *et al.* Tumour exosome integrins determine organotropic metastasis. *Nature* **527**, 329–335 (2015).
18. Zhang, H. *et al.* Identification of distinct nanoparticles and subsets of extracellular vesicles by asymmetric flow field-flow fractionation. *Nature Cell Biology* **20**, 332–343 (2018).
19. Barkan, D. *et al.* Metastatic growth from dormant cells induced by a Col-I-enriched fibrotic environment. *Cancer Research* **70**, 5706–5716 (2010).
20. Boudreau, N., Sympson, C. J., Werb, Z. & Bissell, M. J. Suppression of ICE and apoptosis in mammary epithelial cells by extracellular matrix. *Science (New York, N.Y.)* **267**, 891–3 (1995).
21. Petersen, O. W., Ronnov-Jessen, L., Howlett, A. R. & Bissell, M. J. Interaction with basement membrane serves to rapidly distinguish growth and differentiation pattern of normal and malignant human breast epithelial cells. *Proceedings of the National Academy of Sciences of the United States of America* **89**, 9064–9068 (1992).
22. Pommier, A. *et al.* Unresolved endoplasmic reticulum stress engenders immune-resistant, latent pancreatic cancer metastases. *Science* **360**, aao4908 (2018).
23. Pantel, K. *et al.* Frequent Down-Regulation of Major Histocompatibility Class I Antigen Expression on Individual Micrometastatic Carcinoma Cells. *Cancer Research* **51**, (1991).
24. Malladi, S. *et al.* Metastatic Latency and Immune Evasion through Autocrine Inhibition of WNT. *Cell* **165**, 45–60 (2016).
25. Coller, H. A. Cell biology: The essence of quiescence. *Science* vol. 334 1074–1075 (2011).
26. Kuilman, T., Michaloglou, C., Mooi, W. J. & Peeper, D. S. The essence of senescence. *Genes and Development* vol. 24 2463–2479 (2010).
27. Albrengues, J. *et al.* Neutrophil extracellular traps produced during inflammation awaken dormant cancer cells in mice. *Science* **361**, (2018).
28. Willis, R. A. *The spread of tumours in the human body*. (Butterworth & Co., 1952).
29. Disibio, G. & French, S. W. Metastatic Patterns of Cancers Results From a Large Autopsy Study. *Arch Pathol Lab Med* **132**, 931–939 (2008).
30. Weiss, L. Biomechanical destruction of cancer cells in skeletal muscle: a rate-regulator for hematogenous metastasis. *Clinical & Experimental Metastasis* **7**, 483–91 (1989).
31. Parlakian, A. *et al.* Skeletal Muscle Phenotypically Converts and Selectively Inhibits Metastatic Cells in Mice. *PLoS ONE* **5**, e9299 (2010).

32. Djaldetti, M., Sredni, B., Zigelman, R., Verber, M. & Fishman, P. Muscle cells produce a low molecular weight factor with anti-cancer activity. *Clinical and Experimental Metastasis* **14**, 189–196 (1996).
33. Fishman, P., Bar-Yehuda, S. & Vagman, L. Adenosine and Other Low Molecular Weight Factors Released by Muscle Cells Inhibit Tumor Cell Growth1. *Cancer Research* **58**, 3181–3187 (1998).
34. Bar-Yehuda, S., Barer, F., Volfsson, L. & Fishman, P. Resistance of muscle to tumor metastases: A role for A3 adenosine receptor agonists. *Neoplasia* **3**, 125–131 (2001).
35. Ghajar, C. M. Metastasis prevention by targeting the dormant niche. *Nature Reviews Cancer* vol. 15 238–247 (2015).
36. Li, W., Germain, R. N. & Gerner, M. Y. Multiplex, quantitative cellular analysis in large tissue volumes with clearing-enhanced 3D microscopy (Ce3D). *Proceedings of the National Academy of Sciences* **114**, E7321–E7330 (2017).
37. Lander, E. S. *et al.* Initial sequencing and analysis of the human genome. *Nature* **409**, 860–921 (2001).
38. Batzer, M. A. & Deininger, P. L. Alu repeats and human genomic diversity. *Nature Reviews Genetics* vol. 3 370–379 (2002).
39. Schneider, T., Osl, F., Friess, T., Stockinger, H. & Scheuer, W. v. Quantification of human Alu sequences by real-time PCR - An improved method to measure therapeutic efficacy of anti-metastatic drugs in human xenotransplants. *Clinical and Experimental Metastasis* **19**, 571–582 (2002).
40. Walker, J. A. *et al.* Human DNA quantitation using Alu element-based polymerase chain reaction. *Analytical Biochemistry* **315**, 122–128 (2003).
41. Campbell, J. P. *et al.* TRIzol and Alu qPCR-based quantification of metastatic seeding within the skeleton. *Scientific Reports* **5**, (2015).
42. Dai, J. *et al.* Astrocytic laminin-211 drives disseminated breast tumour cell dormancy in brain. *Nature Cancer, In Press*.
43. Blau, H. M. *et al.* Plasticity of the differentiated state. *Science* **230**, 758–766 (1985).
44. Kang, Y. *et al.* A multigenic program mediating breast cancer metastasis to bone. *Cancer Cell* **3**, 537–549 (2003).
45. Bragado, P. *et al.* TGF-β2 dictates disseminated tumour cell fate in target organs through TGF-β-RIII and p38α/β signalling. *Nature Cell Biology* **15**, 1351–1361 (2013).

46. Franco-Barraza, J., Beacham, D. A., Amatangelo, M. D. & Cukierman, E. Preparation of extracellular matrices produced by cultured and primary fibroblasts. *Current Protocols in Cell Biology* **2016**, 10.9.1-10.9.34. (2016).
47. Schild, T., Low, V., Blenis, J. & Gomes, A. P. Unique Metabolic Adaptations Dictate Distal Organ-Specific Metastatic Colonization. *Cancer Cell* vol. 33 347–354 (2018).
48. Sullivan, M. R. & vander Heiden, M. G. Determinants of nutrient limitation in cancer. *Critical Reviews in Biochemistry and Molecular Biology* vol. 54 193–207 (2019).
49. Muir, A., Danai, L. v. & vander Heiden, M. G. Microenvironmental regulation of cancer cell metabolism: Implications for experimental design and translational studies. *Disease Models and Mechanisms* vol. 11 (2018).
50. Fidler, I. J. Biological Behavior of Malignant Melanoma Cells Correlated to Their Survival in Vivo. *Cancer Research* **35**, (1975).
51. Minn, A. J. *et al.* Genes that mediate breast cancer metastasis to lung. *Nature* **436**, 518–524 (2005).
52. Bos, P. D. *et al.* Genes that mediate breast cancer metastasis to the brain. *Nature* **459**, 1005–1009 (2009).
53. Chong, J., Wishart, D. S. & Xia, J. Using MetaboAnalyst 4.0 for Comprehensive and Integrative Metabolomics Data Analysis. *Current Protocols in Bioinformatics* **68**, e86 (2019).
54. Kanehisa, M. & Goto, S. KEGG: Kyoto Encyclopedia of Genes and Genomes. *Nucleic Acids Research* vol. 28 27–30 (2000).
55. Bansal, A. & Celeste Simon, M. Glutathione metabolism in cancer progression and treatment resistance. *Journal of Cell Biology* vol. 217 2291–2298 (2018).
56. Powers, S. K., Li Ji, L., Kavazis, A. N. & Jackson, M. J. Reactive Oxygen Species: Impact on Skeletal Muscle. *Compr Physiol* **1**, 941–969 (2011).
57. Townsend, D. M. S-Glutathionylation: Indicator of Cell Stress and Regulator of the Unfolded Protein Response. *Molecular interventions* **7**, 313 (2007).
58. Zitka, O. *et al.* Redox status expressed as GSH:GSSG ratio as a marker for oxidative stress in paediatric tumour patients. *Oncology Letters* **4**, 1247–1253 (2012).
59. Chai, Y. C., Ashraf, S. S., Rokutan, K., Johnston, R. B. & Thomas, J. A. S-thiolation of individual human neutrophil proteins including actin by stimulation of the respiratory burst: Evidence against a role for glutathione disulfide. *Archives of Biochemistry and Biophysics* **310**, 273–281 (1994).

60. Gutscher, M. *et al.* Real-time imaging of the intracellular glutathione redox potential. *Nature Methods* **5**, 553–559 (2008).
61. Morgan, B., Sobotta, M. C. & Dick, T. P. Measuring EGSH and H2O2 with roGFP2-based redox probes. *Free Radical Biology and Medicine* vol. 51 1943–1951 (2011).
62. Fujikawa, Y. *et al.* Mouse redox histology using genetically encoded probes. *Science Signaling* **9**, rs1–rs1 (2016).
63. Ubellacker, J. M. *et al.* Lymph protects metastasizing melanoma cells from ferroptosis. *Nature* **585**, 113–118 (2020).
64. Steinhorn, B. *et al.* Chemogenetic generation of hydrogen peroxide in the heart induces severe cardiac dysfunction. *Nature Communications* **9**, 1–10 (2018).
65. Glorieux, C. & Calderon, P. B. Catalase, a remarkable enzyme: Targeting the oldest antioxidant enzyme to find a new cancer treatment approach. *Biological Chemistry* vol. 398 1095–1108 (2017).
66. Schriner, S. E. *et al.* Extension of murine life span by overexpression of catalase targeted to mitochondria. *Science* **308**, 1909–1911 (2005).
67. Chandel, N. S. & Tuveson, D. A. The Promise and Perils of Antioxidants for Cancer Patients. *New England Journal of Medicine* **371**, 177–178 (2014).
68. Yun, J. *et al.* Vitamin C selectively kills KRAS and BRAF mutant colorectal cancer cells by targeting GAPDH. *Science* **350**, 1391–1396 (2015).
69. Diehn, M. *et al.* Association of reactive oxygen species levels and radioresistance in cancer stem cells. *Nature* **458**, 780–783 (2009).
70. Gorrini, C., Harris, I. S. & Mak, T. W. Modulation of oxidative stress as an anticancer strategy. *Nature Reviews Drug Discovery* vol. 12 931–947 (2013).
71. The Alpha-Tocopherol Beta Carotene Cancer Prevention Study. The Effect of Vitamin E and Beta Carotene on the Incidence of Lung Cancer and Other Cancers in Male Smokers. *New England Journal of Medicine* **330**, 1029–1035 (1994).
72. Goodman, G. E. *et al.* The Beta-Carotene and Retinol Efficacy Trial: Incidence of lung cancer and cardiovascular disease mortality during 6-year follow-up after stopping β-carotene and retinol supplements. *Journal of the National Cancer Institute* **96**, 1743–1750 (2004).
73. Klein, E. A. *et al.* Vitamin E and the risk of prostate cancer: The selenium and vitamin E cancer prevention trial (SELECT). *JAMA* **306**, 1549–1556 (2011).
74. Gaziano, J. M. *et al.* Vitamins E and C in the prevention of prostate and total cancer in men: The physicians' health study II randomized controlled trial. *JAMA* **301**, 52–62 (2009).

75. Ambrosone, C. B. *et al.* Dietary supplement use during chemotherapy and survival outcomes of patients with breast cancer enrolled in a cooperative group clinical trial (SWOG S0221). *Journal of Clinical Oncology* **38**, 804–814 (2020).
76. Omenn, G. S. *et al.* Effects of a Combination of Beta Carotene and Vitamin A on Lung Cancer and Cardiovascular Disease. *New England Journal of Medicine* **334**, 1150–1155 (1996).
77. Harris, I. S. *et al.* Glutathione and Thioredoxin Antioxidant Pathways Synergize to Drive Cancer Initiation and Progression. *Cancer Cell* **27**, 211–222 (2015).
78. Sayin, V. I. *et al.* Cancer: Antioxidants accelerate lung cancer progression in mice. *Science Translational Medicine* **6**, 221ra15 (2014).
79. Piskounova, E. *et al.* Oxidative stress inhibits distant metastasis by human melanoma cells. *Nature* **527**, 186–191 (2015).
80. le Gal, K. *et al.* Antioxidants can increase melanoma metastasis in mice. *Science Translational Medicine* **7**, 308re8 (2015).
81. Nguyen, A. *et al.* PKLR promotes colorectal cancer liver colonization through induction of glutathione synthesis. *Journal of Clinical Investigation* **126**, 681–694 (2016).
82. Fox, D. B. *et al.* NRF2 activation promotes the recurrence of dormant tumor cells through regulation of glutathione and nucleotide synthesis pathways. *Nature Metabolism* **2**, 318–334 (2020).
83. Crist, S. B. & Ghajar, C. M. When a House Is Not a Home: A Survey of Antimetastatic Niches and Potential Mechanisms of Disseminated Tumor Cell Suppression. *Annual Review of Pathology: Mechanisms of Disease* **16**, 409–432 (2021).
84. Snijders, T. *et al.* Satellite cells in human skeletal muscle plasticity. *Frontiers in Physiology* vol. 6 283 (2015).
85. Hojman, P., Gehl, J., Christensen, J. F. & Pedersen, B. K. Cell Metabolism Perspective Molecular Mechanisms Linking Exercise to Cancer Prevention and Treatment. *Cell Metabolism* **27**, 10–21 (2018).
86. Liu, L., Cheung, T., Charville, G. & Rando, T. Isolation of skeletal muscle stem cells by fluorescence-activated cell sorting. *Nature protocols* **10**, 1612–1624 (2015).
87. Hindi, L., McMillan, J., Afroze, D., Hindi, S. & Kumar, A. Isolation, Culturing, and Differentiation of Primary Myoblasts from Skeletal Muscle of Adult Mice. *Bio-protocol* **7**, (2017).
88. Carlson, P. *et al.* Targeting the perivascular niche sensitizes disseminated tumour cells to chemotherapy. *Nature Cell Biology* **21**, 238–250 (2019).

89. Nemkov, T., Hansen, K. C. & D'Alessandro, A. A three-minute method for high-throughput quantitative metabolomics and quantitative tracing experiments of central carbon and nitrogen pathways. *Rapid Communications in Mass Spectrometry* **31**, 663–673 (2017).
90. Nemkov, T., Reisz, J. A., Gehrke, S., Hansen, K. C. & D'Alessandro, A. High-throughput metabolomics: Isocratic and gradient mass spectrometry-based methods. in *Methods in Molecular Biology* vol. 1978 13–26 (Humana Press Inc., 2019).
91. Clasquin, M. F., Melamud, E. & Rabinowitz, J. D. LC-MS data processing with MAVEN: A metabolomic analysis and visualization engine. *Current Protocols in Bioinformatics* **14**, (2012).

Chapter 4. Enhanced collagen deposition overrides the metastasis-suppressive nature of skeletal muscle.

Introduction.

Molecular characterization of organ microenvironments has gained real traction in the metastasis research field, as it is now clear that the eventual success of the metastatic lesion lies in a disseminated cell's ability to interact and adapt to the organ in which it resides. Chapter 3 characterized the skeletal muscle niche as a metastasis-suppressive site, and suggested that further experimental study would provide valuable insight into the environmental constraints placed on disseminated tumor cells **(DTCs)**[1].

Whereas skeletal muscle metastasis is a rare event, it does occur occasionally in clinical settings[2-4]. This begs the questions: How does the tumor cell adapt to such an inhospitable environment? We posit that a complementary approach to discovering how the skeletal muscle microenvironment suppresses tumor cell outgrowth is to probe the mechanism by which tumor cells overcome this suppression. Defining the molecular adaptations that enable a DTC to colonize skeletal muscle may provide insight into the intrinsic properties exhibited by anti-metastatic tissues.

Transcriptomic analysis of mammary cancer cells that successfully metastasize to skeletal muscle revealed enrichments in collagen trimerization and extracellular matrix (**ECM**) remodeling. ECM forms up to 10% of healthy skeletal muscle's mass and plays a principal role in force transmission, maintenance and repair of muscle fibers following injury[5-6]. In fact, ECM remodeling is an essential and tightly regulated physiological process in development and wound repair in all organs[6-7]. Therefore, it is not surprising that cells dysregulate this process in pathologic conditions such as inflammatory diseases, tissue fibrosis, and cancer/metastasis. Tumoral collagen deposits not only supply cells with an anchoring dock that contributes to tissue mechanostructure maintenance but also, by engaging with corresponding receptors, ultimately triggers signaling pathways that elicit important cancer- and stromal- cell functions[7]. As increased collagen deposition is regarded as pro-tumorigenic in most cancer contexts[8-11], we hypothesized that DTCs that successfully develop into metastatic lesions within skeletal muscle either possess or gain the molecular machinery needed to remodel peri-tumoral ECM.

Results.

Generation of skeletal muscle-metastatic 4T1 sublines shows enhanced capacity to colonize skeletal muscle. In order to examine how mammary cancer cells might adapt to grow within the skeletal muscle environment, we derived skeletal muscle-metastatic mammary cancer cell line through serial intracardiac (**i.c.**) injection of the highly-metastatic murine line, 4T1-mCherry ($1x10^5$ for the initial injection and $1x10^4$ for all subsequent injections; **Fig. 4.1a**). At endpoint, dissected fore- and hindlimb skeletal muscle were examined for mCherry fluorescence using an IVIS Spectrum, 4T1 lesions were isolated, enzymatically digested and grown in standard culture conditions. With the first two passages through mouse, 4T1-mCherry cells gained increased capacity to colonize skeletal muscle. Skeletal muscle involvement in the muscle-metastatic sublines increased by 250%, 360% and 320% for the first ("**4T1-SkM1met**"), second ("**4T1-SkM2met**"), and third ("**4T1-SkM3met**") passages through mouse, respectively, compared to the parental line (**Fig. 4.1b-c, Supplementary Fig. 4.a**). Though metastasis to skeletal muscle significantly increased with each daughter line, metastasis abundance to other secondary sites (e.g. lung, ovaries, adrenal glands) were unchanged (**Suppl. Fig4.1b**). A micro-metastatic subline "**4T1-SkMmicro**" was also generated from a small cluster of cells (~ <10 cells) that had successfully trafficked to skeletal muscle but was not able to grow out. The 4T1-SkMmicro cells did not generate a great number of skeletal muscle metastases than the parental 4T1.

Culture upon organotypic skeletal muscle niches mirrored the in vivo phenotype. To recreate the myofiber niche in organotypic culture, skeletal muscle myocytes (**SkMc**) were plated in a 96-well format, cultured in differentiation medium and seeded with $1x10^2$ of each 4T1-SkMx subline per well (**Fig. 4.1d**). Measuring tumor cell outgrowth through the area occupied by mCherry+ tumor cells at Day 10 normalized by Day 0, we observed that 4T1-parental and 4T1-SkMmicro cell lines were largely restricted in growth, whereas the 4T1-SkM1met, 4T1-SkM2met and 4T1-SkM3met lines colonized the SkMc niche with increased efficacy compared to the parental control (**Fig. 4.1e-f**). In parallel, we modeled a lung-like niche using lung fibroblasts (**LF**) to serve as an environmental comparison/ contrast point,

as lung is a common site for breast cancer metastasis. Here we saw little change in tumor cell outgrowth across the cell lines (**Fig. 4.1e, Supplementary Fig 4.1d)**. Thus, culture upon organotypic skeletal muscle and lung-like niches mirrored the phenotype observed *in vivo*, offering a readily accessible platform to screen for drivers of skeletal muscle colonization. Accordingly, these sublines presented a unique opportunity to study transcriptomic changes that coincide with the ability to successfully colonize skeletal muscle.

Transcriptomics of muscle-metastatic 4T1 sublines implicate ECM remodeling as key to colonizing the muscle niche. RNA was isolated from parental 4T1 and its SkMx variants, libraries were prepared, and cDNA was sequenced. Gene Set Enrichment comparing the 4T1-SkM3met (the most muscle-metastatic) and the 4T1-parental found that "collagen trimerization", "banded collagen fibril and "extracellular matrix" were among the top pathways enriched in the muscle-colonizing line, hinting towards a role for collagen remodeling in skeletal muscle metastasis (**Fig. 4.1e-g**). However, to more strategically test for genes and/or molecular pathways that enable DTCs to adapt and overcome skeletal muscle, we selected 43 of the most differentially expressed genes as potential "colonization-promoters" based on their $\log_2$-fold stepwise increase in 4T1-SkM3met compared against 4T1-parental, 4T1-SkM1met and 4T1-SkM2met (**Fig. 4.2a**). Other inclusion criteria included p-value less than 0.05, False Discovery Rate less than 0.05, and raw counts greater than 150. Interestingly, the collagen signature was retained in this narrowed candidate list as the top GOTERMS included "extracellular region", "proteinaceous extracellular matrix", "extracellular matrix" and "collagen trimer".

CRISPR knockout screen reveals collagen genes as mediators of skeletal muscle colonization. To examine if any of the 43 candidate genes played a direct role in promoting tumor cell outgrowth in skeletal muscle, the candidate genes were knocked out in the 4T1-SkM3met line using CRISPR/Cas9 technology (**Supplementary Fig. 4.2a**). High-titer lentivirus from sgRNA libraries were generated and transduced cells were selected with hygromycin. SkMc were plated in a 96-well format, cultured in differentiation medium and seeded with the knockout versions of the 4T1-SkM3met tumor cells ($1x10^2$ cell/well, **Fig.**

4.2b). After the ten-day culture period, tumor cell outgrowth was measured through the area fraction of mCherry cells present at Day 10 normalized by the seeding density at Day 0. The culture-based screen resulted in the identification of 17 pooled guides that block colonization of SkMc by 4T1-SkM3met cells (**Fig. 4.2c**). Five of these were genes that participate in collagen trimerization and extracellular matrix organization: collagen 1a2 (**Col1a2**), collagen 5a2 (**Col5a2**), collagen 1a1 (**Col1a1**), collagen 6a1 (**Col6a1**) and lysyl oxidase (**Lox**) (**Fig. 4.2c, Supplementary Fig. 4.b-c**). These data suggest that the remodeling of skeletal muscle into a collagen-rich environment may be critical for tumor cell colonization within this tissue (and that absence of such collagen components contributes to lack of outgrowth). The ability of a DTC to surround itself in a substrate-rich matrix is useful in most organs[10-12], and this cloaking may be especially critical within skeletal muscle.

Collagen deposition also aids tumor colonization in lung. To determine if the pro-metastatic effect of increased collagen deposition was skeletal muscle-specific or provided a proliferative advantage across organs, we examined the lung-like niche in parallel. LF were plated in a 96-well format and seeded with CRISPR-targeted 4T1-SkM3met tumor cells (**Fig. 4.2b**). After the ten-day culture period, tumor cell outgrowth was measured through the area fraction of mCherry cells present at Day 10 normalized by the seeding density at Day 0. Here, knockdown of only 8 of 43 genes significantly reduced tumor cell growth in LF, perhaps implicating a requirement for tumor cell colonization (**Supplementary Fig. 4.3a**). Similar to the SkMc hits, 4 of the 8 genes that significantly facilitate tumor cell outgrowth in the LF niche participate in collagen trimerization and extracellular matrix organization (Col1a2, Col5a2, Col1a1 and Lox; **Supplementary Fig. 4.3b-c)**. Thus, collagen deposition appears equally advantageous in the lung setting. Though the growth advantage bestowed by collagen is not skeletal muscle-specific, it is possible that this type of ECM remodeling is more indispensable in the muscle setting than other organs.

Collagens of interest are enhanced in the tumor-bearing regions of skeletal muscle. During the 4T1-SkMx derivation process, we banked several sets of skeletal muscle containing 4T1-SkM3met lesions for immunofluorescence (**IF**) staining. With a shortened candidate list of genes that facilitate colonization of skeletal muscle, we tested 4T1-SkM3met- containing

muscle for increased collagen expression. In the skeletal muscle that contained metastatic lesions, we were able to observe a significant increase in accumulation of types I, V and VI collagen, compared to healthy skeletal muscle (**Fig. 4.2d)**. Therefore, we believe that Col1a1, Col1a2, Col5a2 and Col6a1 (the top candidates in our CRISPR screen) singly or in concert may be important in overcoming the proliferative hurdles imposed by skeletal muscle.

Application of a collagen matrix facilitates tumor cell outgrowth on skeletal muscle. To determine if collagen deposition was sufficient to enhance tumor cell growth on skeletal muscle, a 3 mg/mL type I collagen layer was applied to 4T1-parental and EO771-seeded SkMc niches ($1x10^2$ cells/well, **Fig. 4.3a**). Addition of purified type I collagen to the organotypic co-culture model permits 4T1-parental cell outgrowth, which typically do not colonize SkMc (**Fig. 4.3b)**. In fact, 4T1-parental cells grew twice as well compared to the control in the presence of type I collagen (**Fig. 4.3b)**. EO771 outgrowth with collagen trended towards a significant increase but was inconsistent across replicates (**Fig. 4.3c**). Addition of a 3 mg/mL type I collagen layer also improved outgrowth of 4T1 and EO771 tumor cells when cultured in the LF niche (**Supplementary Fig. 4.3d-e)**.

Overexpression of collagen and Lox together may stimulate tumor cell outgrowth on the skeletal muscle niche. To assess if Col1a1, Col1a2, Col5a2, Col6a1 or Lox could elicit tumor growth in skeletal muscle, we designed overexpression constructs, made high-titer lentivirus and transduced 4T1-parental and EO771 cells with said virus. Cell lines were placed under blasticidin selection (10 μg/mL) to create a pure population of ORF-expressing cells and Western blot confirmed the integration of all single inserts. We also asked if perhaps overexpression of both a collagen gene and Lox would be necessary, as Lox is critical for covalently crosslinking collagen fibrils (which is essential for correct collagen fiber assembly and increases tensile strength and stiffness). In this case, we infected 4T1 and EO771 cells with both lentiviruses simultaneously and selected for the vectors using blasticidin (as the antibiotic resistance gene is the same for both). Not all lines expressed both collagen and Lox at sufficiently high levels (**Supplementary Fig. 4.4a-b**). One reason

might be that Lox and collagen ORFS were introduced simultaneously and selected using the same antibiotic.

After a ten-day co-culture period on SkMc (**Fig. 4.3d**), 4T1-parental cells that expressed Col1a2+Lox and Col6a1+Lox grew significantly more than the non-targeting eGFP control line on the SkMc niche (**Fig. 4.3e**). This experiment was repeated once, with 5 wells per replicate, and yielded different hits across both. Thus, additional replicates are necessary to really untangle if Col1a2+Lox and Col6a1+Lox are sufficient to enhance growth on skeletal muscle.

It is tempting to speculate that enhancement of collagen *and* Lox is necessary for the 4T1s to naturally overcome the growth constraints in skeletal muscle, as all three hits at present include both one of two collagens and Lox. Future optimization includes using two different backbones, with separate selectable markers, to ensure that both collagen and Lox expression is enhanced and the impact of each can be parsed apart.

Looking at the EO771 model, we find that tumor cell outgrowth is enhanced when EO771 cells express either Col1a2, Col5a2, Lox, or Col1a1+Lox (**Fig. 4.3f**). Again, these data represent two technical replicates, with 5 wells per condition, and the hits from each replicate are not consistent. The results of this EO771-based study do not overlap with those in the previous 4T1 study. There might be several explanations for this: i) functional redundancy in collagen's pro-tumorigenic behavior, ii) various collagen genes work within the same pathway to enable growth in muscle, or iii) variation in ORF expression per cell in the 4T1 and EO771 lines that appear between experimental replicates.

Overexpression of collagen and Lox together potentially promote skeletal muscle colonization in vivo. The obvious next steps in the pursuit to validate collagen's pro-metastatic role is to test collagen overexpression vectors *in vivo*. Do tumor cells that overexpress Col1a1, Col1a2, Col5a2, Col6a1 or Lox gain the ability to form tumors in skeletal muscle? Findings in culture suggest that a combination of Lox and collagen may be necessary to reproduce the level of outgrowth achieved by the 4T1-SkM3met muscle-metastatic line. This study will be performed once the new overexpression vectors have been made and tested in the co-culture setting. The three candidates that most significantly increase outgrowth in the SkMc co-culture setting will progress to studies *in vivo*.

Barium chloride, a chemical method of myofiber injury, promotes skeletal muscle regeneration. To examine how the active regeneration of skeletal muscle post-injury influences its anti-metastatic capabilities, we administered a multi-focal chemical injury to the tibialis anterior of female NOD-SCID mice (20 jabs, followed by 50 μl of barium chloride **$BaCl_2$** over 5 sites[11-13]). Upon injury, quiescent satellite cells activate and provoke a series of regeneration steps: i) satellite cells proliferate and differentiate to form new myotubes, and ii) released growth factors and chemokines stimulate fibroblasts to produce of new ECM and endothelial cells to create new blood vessels and nerves[5-6, 11-12]. Myotubes mature into myofibers and ECM undergoes further remodeling[5-6, 11-12]. The regenerated muscle in normal conditions resembles undamaged muscle in morphological, as well as, functional states[11-12]. Before introducing tumor cells, we first confirmed that our injury method could sufficiently damage the niche and that we could capture active regeneration. Muscle was collected one week post-injury and stained for markers of myofiber regeneration. At this timepoint, we confirmed centrally-located nuclei in myofibers and increased accumulation of ECM (**Supplementary Fig. 4.5a**), both signs of active regeneration.

Barium chloride injury does not provoke tumor colonization of the tibialis anterior. In a second study, barium chloride injuries were performed on the tibialis anterior (**TA**) muscle of C57BL/6 or Balb/c female mice as described above. Two days following barium chloride injections, $1x10^3$ EO771-ffluc-eGFP or $1x10^2$ 4T1-parental-mCherry mammary cancer cells were injected into the regenerating TA (**Fig. 4.4a,d**). Tumor outgrowth was measured over a period of six-weeks by either bioluminescence imaging (**BLI**, for EO771-ffluc-eGFP cells) or tumor volume measurements (4T1-parental-mCherry). Counter to our hypothesis, neither the EO771 nor 4T1 cell lines were better able to colonize skeletal muscle upon $BaCl_2$ injury. EO771 cells outgrew into stable tumors in 2 of 17 mice (11.8%) in the injured cohort, whereas EO771 cells formed stable tumors in 1 of 17 mice in the control cohort (5.9%) (**Fig. 4.4b-c**). Though the injured condition did foster more EO771 outgrowth, the increase was not statistically significant. In the Balb/c setting, 3 of 8 mice (37.5%) developed palpable 4T1 tumors in the uninjured controls whereas 0 of 9 mice (0%) developed muscle tumors in

the $BaCl_2$-treated cohort. In conclusion, $BaCl_2$ injury did not provoke tumor colonization in muscle in either C57BL/6 or Balb/c models (**Fig. 4.4e-f**).

Barium chloride injury does not induce pro-metastatic collagen deposition in skeletal muscle. We wondered why $BaCl_2$ injury was not sufficient to promote tumor colonization of skeletal muscle**.** We knew that regeneration was occurring in this model, so we postulated that perhaps the constituents that comprised this response were not pro-metastatic in the skeletal muscle setting. Further, though ECM accumulation has been reported in nearly all models of muscle injury, the accumulation is transient in some injury models and the mechanisms of rebuilding may vary. To determine if $BaCl_2$ injury induced ECM remodeling and gain insight into the other mechanisms enriched in our model, we performed proteomics on uninjured and $BaCl_2$ –injured TA muscle collected one week after injury (**Fig. 4.5a-b, Supplementary Fig. 4.5b**). DAVID Pathway Analysis was then performed to determine what the most significant changes were that occurred upon $BaCl_2$ injury. Extracellular exosomes, cell-cell adherens junctions and cytosolic proteins scored the highest in cellular component enrichment (**Fig. 4.5c**). Extracellular matrix proteins, though significantly represented, were not as abundant (**Fig. 4.5d**). Looking at the changes that occurred in collagen deposition upon injury, we documented a significant increase in Col14a1, Col12a1 and Col11a2 (**Fig. 4.5e**). These collagen isotypes, of course, are not those that we identified as being pro-muscle metastatic. Interestingly, Col14a1 and Col12a1 are both members of the FACIT (fibril-associated collagens with interrupted triple helices) collagen family[15] and only a handful of studies have implicated their involvement in metastasis[16-17]. Col14a1 and Col12a1 are more often described for their importance in the structural integrity of regions with high mechanism stress like the myocardium and tendons, respectively[18-19]. Col11a2, a minor fibrillar collagen, is part of a heterotrimer that has little known connection to cancer or metastasis[20-21].

Thus, we hypothesize we were unable to break skeletal muscle's suppressive hold on 4T1 or EO771 cells despite active remodeling of the niche due to the lack of pro-metastatic collagens. Our belief remains that DTCs that successfully develop into metastatic lesions within skeletal muscle either possess or gain the molecular machinery to remodel peri-tumoral ECM.

Discussion.

What molecular adaptations must occur for metastatic colonization of an anti-metastatic niche? In this Chapter, we begin to understand how DTCs that reside in skeletal evolve to overcome proliferative bottlenecks. Modeling of the skeletal muscle niche through 3D organotypic co-culture and derivation of muscle-metastatic mammary cancer cells, paired with CRISPR/Cas9 technology, enabled us to learn that increased peri-tumoral collagen deposition facilitated skeletal muscle metastasis. Though not a mechanism unique to skeletal muscle metastases, it appears that the ability to deposit growth-promoting collagen is especially beneficial to DTCs in skeletal muscle.

We next turned to skeletal muscle injury with the hopes that forced tissue remodeling would simultaneously increase collagen content and tumor take. Trauma and wounding have long been reported to support tumor outgrowth[22-26]. Clinical reports describe skeletal muscle metastasis development at documented sites of previous trauma, implying that breakdown of the skeletal muscle microenvironment, then, seemingly is required to give tumor cells the growth advantage they need[27]. However, our data imply that not all skeletal muscle remodeling is sufficient to overcome the stronghold that the environment has over DTC proliferation. Proteomic analysis of $BaCl_2$-injury muscle revealed that though we achieved active regeneration, the collagen subsets that historically have been classified as pro-tumorigenic were not present. These data are congruous with (or at least not counter to) our identification of Col1a1, Col1a2, Col5a2, Col6a1 and Lox as mediators of skeletal muscle metastasis. Our $BaCl_2$ model of injury did not provoke enhanced deposit of any of these genes, and thus we theorize that this was the reason for the lack of tissue colonization. To test this hypothesis, alternative injury methods that better provoke collagen deposition (surgically induced trauma like laceration or denervation) or mouse models of skeletal muscle fibrosis (e.g. *mdx* muscular dystrophy) might be implemented.

As evidenced by its rarity, skeletal muscle metastasis is the result of adaptation to significant environmental constraints. Our data suggests that peri-tumoral collagens are sufficient for metastatic colonization of skeletal muscle. However, we have not yet addressed *how* peri-tumoral collagen alters either environmental or tumoral programs to facilitate proliferation. Does collagen act as an amino acid or growth-factor repository,

where an environmental-deprived DTC may siphon extra reserves? Could collagen rewire the metabolic state (e.g. redox state) of a DTC to avoid oxidative strain? Or does collagen simply interact with surface receptors on a DTC to stimulate pro-growth programs? Several groups have begun to ask the same questions[29-31], but we as a field have a lot to learn.

Another implication of this work also includes that the absence of specific collagen constituents in the skeletal muscle niche contributes to a DTC's inability to outgrow in this site. It is also reasonable to postulate that the composition of healthy skeletal muscle may inherently be metastasis suppressive. Continued study of skeletal muscle ECM is necessary to untangle if it is the *presence* of growth-restricting ECM constituents or rather the *absence* of growth-promoting ECM constituents that underlie skeletal muscle's inhospitable nature. Making this distinction may better refine our definition of an anti-metastatic tissue and what molecular constituents comprise it. Equally, identification of specific pathways that are necessary for DTCs to overcome the environmental obstacles may reveal targetable vulnerabilities that might be used for metastasis prevention.

With this Chapter, we aimed to determine what genes could promote metastatic colonization of skeletal muscle and address the question of why we don't see metastatic outgrowth in skeletal muscle more frequently. With this insight, we take another step in defining the molecular mechanisms that underlie skeletal muscle's suppressive nature.

This chapter was made possible with help from the following: Ilsa Coleman, Megan Kufeld, Mark Malasanka, Slobodan Beronja, Kirk C. Hansen, Patrick Paddison, Peter S. Nelson, and Cyrus M. Ghajar.

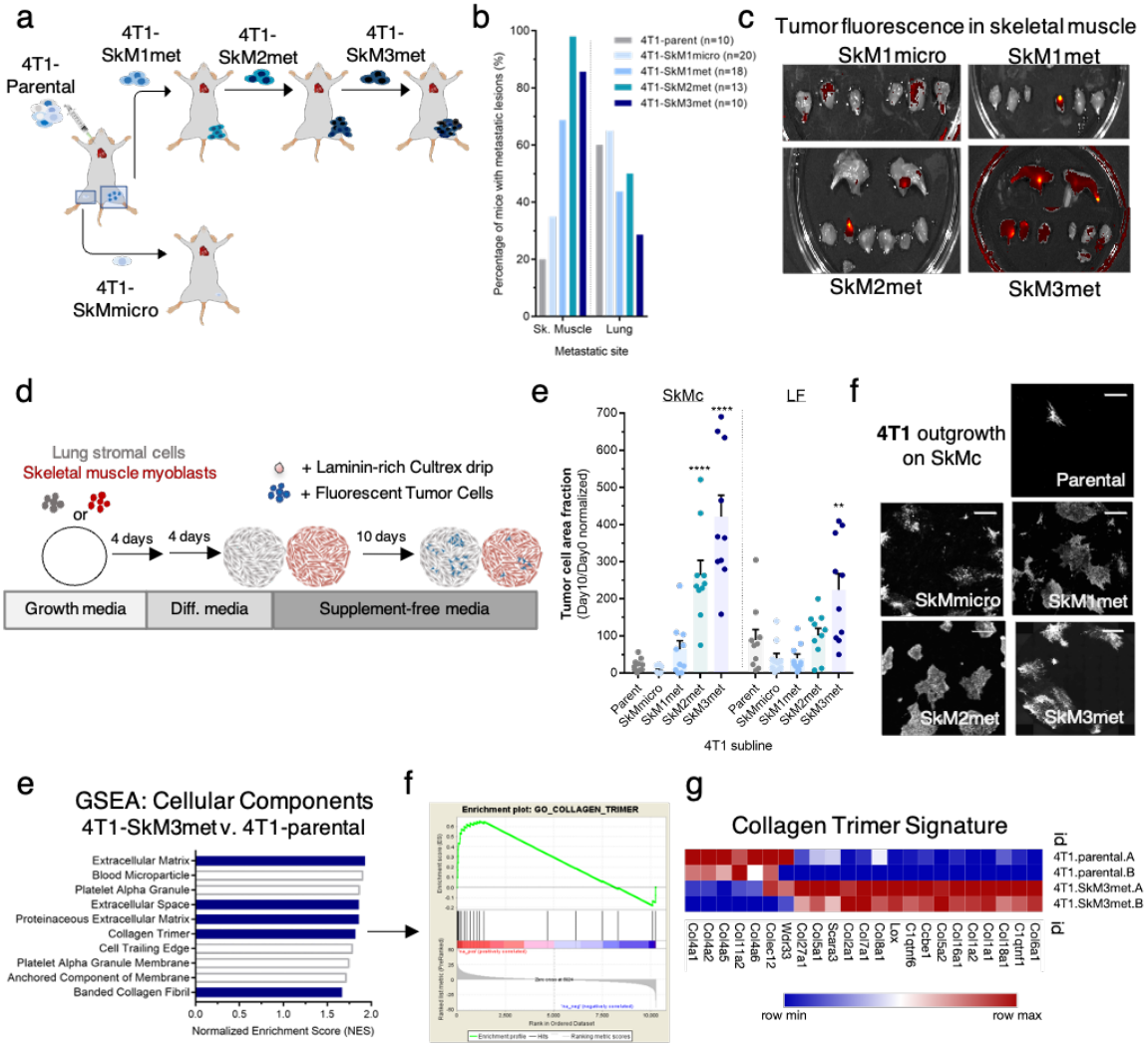

Figure 4.1. 4T1-SkMx sublines increase in skeletal muscle-specific metastatic capability and implicate ECM remodeling as key to growing in the muscle niche. a) Schema for 4T1 SkMx-metastatic subline generation. b) Percentage of mice with metastases to skeletal muscle or lung. 4T1-SkM1met, 4T1-SkM2met and 4T1-SkM3met lineages significantly increase in metastatic capability within SkM while remaining constant in lung colonization. c) Representative fluorescent (mCherry) images of skeletal muscle metastases upon *ex vivo* IVIS imaging of 4T1-SkMx sublines. d) Schematic of the experiment to determine if the 4T1-SkMx sublines could outgrow in a 3D organotypic culture model of skeletal muscle. e) 4T1 sublines maintain SkMc colonization phenotype in culture. Proliferation of 4T1 lines increases in SkMc with each daughter line, whereas outgrowth of all remain similar or diminish within LF niche. Two-way ANOVA, followed by uncorrected Fisher's LSD, was performed where $P < 0.0001$ for 4T1-parental v. SkM2met and 4T1-parental v. SkM3met on SkMc. All other comparisons on SkMc are n.s. f) Representative images of 4T1-SkMx outgrowth on SkMc. e) GSEA (Cellular Components) of 4T1-SkM3met compared to parental. f) Enrichment plot for collagen trimer gene signature comparing 4T1-SkM3met v. 4T1-parental. g) Heatmap displaying the raw counts for the genes found in the "Collagen Trimer" set, for 4T1-parental and 4T1-SkM3met sublines. $P < 0.05$, $^{**}P < 0.05$, $^{***}P < 0.005$, $^{****}P < 0.0005$.

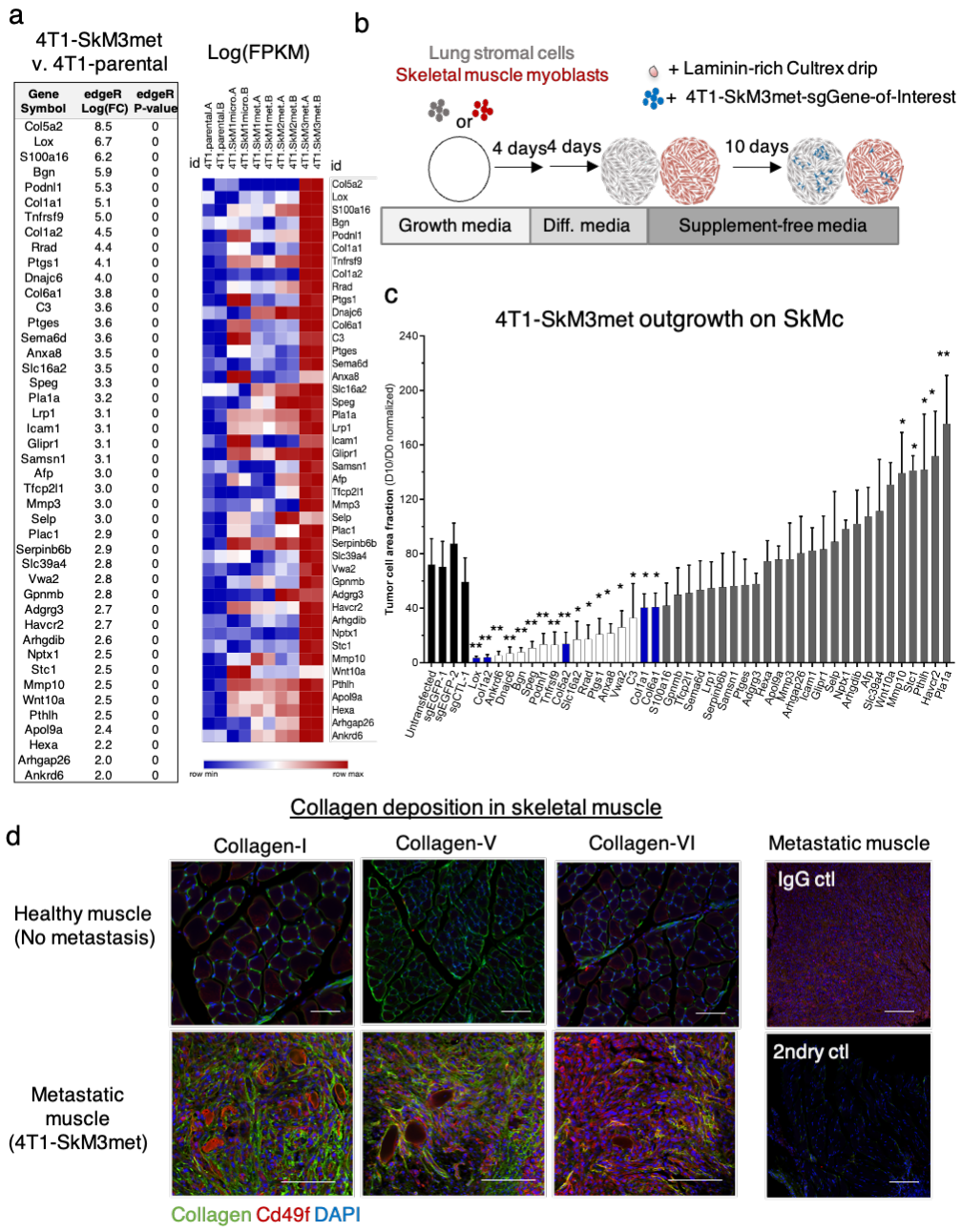

Gene Symbol	edgeR Log(FC)	edgeR P-value
Col5a2	8.5	0
Lox	6.7	0
S100a16	6.2	0
Bgn	5.9	0
Podnl1	5.3	0
Col1a1	5.1	0
Tnfrsf9	5.0	0
Col1a2	4.5	0
Rrad	4.4	0
Ptgs1	4.1	0
Dnajc6	4.0	0
Col6a1	3.8	0
C3	3.6	0
Ptges	3.6	0
Sema6d	3.6	0
Anxa8	3.5	0
Slc16a2	3.5	0
Speg	3.3	0
Pla1a	3.2	0
Lrp1	3.1	0
Icam1	3.1	0
Glipr1	3.1	0
Samsn1	3.1	0
Afp	3.0	0
Tfcp2l1	3.0	0
Mmp3	3.0	0
Selp	3.0	0
Plac1	2.9	0
Serpinb6b	2.9	0
Slc39a4	2.8	0
Vwa2	2.8	0
Gpnmb	2.8	0
Adgrg3	2.7	0
Havcr2	2.7	0
Arhgdib	2.6	0
Nptx1	2.5	0
Stc1	2.5	0
Mmp10	2.5	0
Wnt10a	2.5	0
Pthlh	2.5	0
Apol9a	2.4	0
Hexa	2.2	0
Arhgap26	2.0	0
Ankrd6	2.0	0

Figure 4.2. CRISPR knockout screen reveals collagens as highly influential in skeletal muscle colonization. a) Top 43 genes with most differential gene expression between 4T1-SkM3met and 4T1-parental, as identified through RNA-sequencing. Data displayed as log(fold change) and log(FPKM). b) Schematic of the 3D co-culture system to determine if the CRISPR knockouts could reduce 4T1-SkM3met outgrowth on SkMc. One-way ANOVA, followed by Fisher's LSD, was performed where comparisons were made against the sgEGFP-2 control. c) 3D coculture of 4T1-SkM3met with the 55 genes knockouts (CRISPR) reveals 17 genes that significantly reduce growth on SkMc. Two-way ANOVA d) IF staining of healthy and tumor-bearing skeletal muscle shows collagen deposition of collagen-1,5 and 6 in the metastatic setting. Scale bar = 100 μm. P <0.05, **P<0.005, ***P<0.0005, ****P<0.0001.

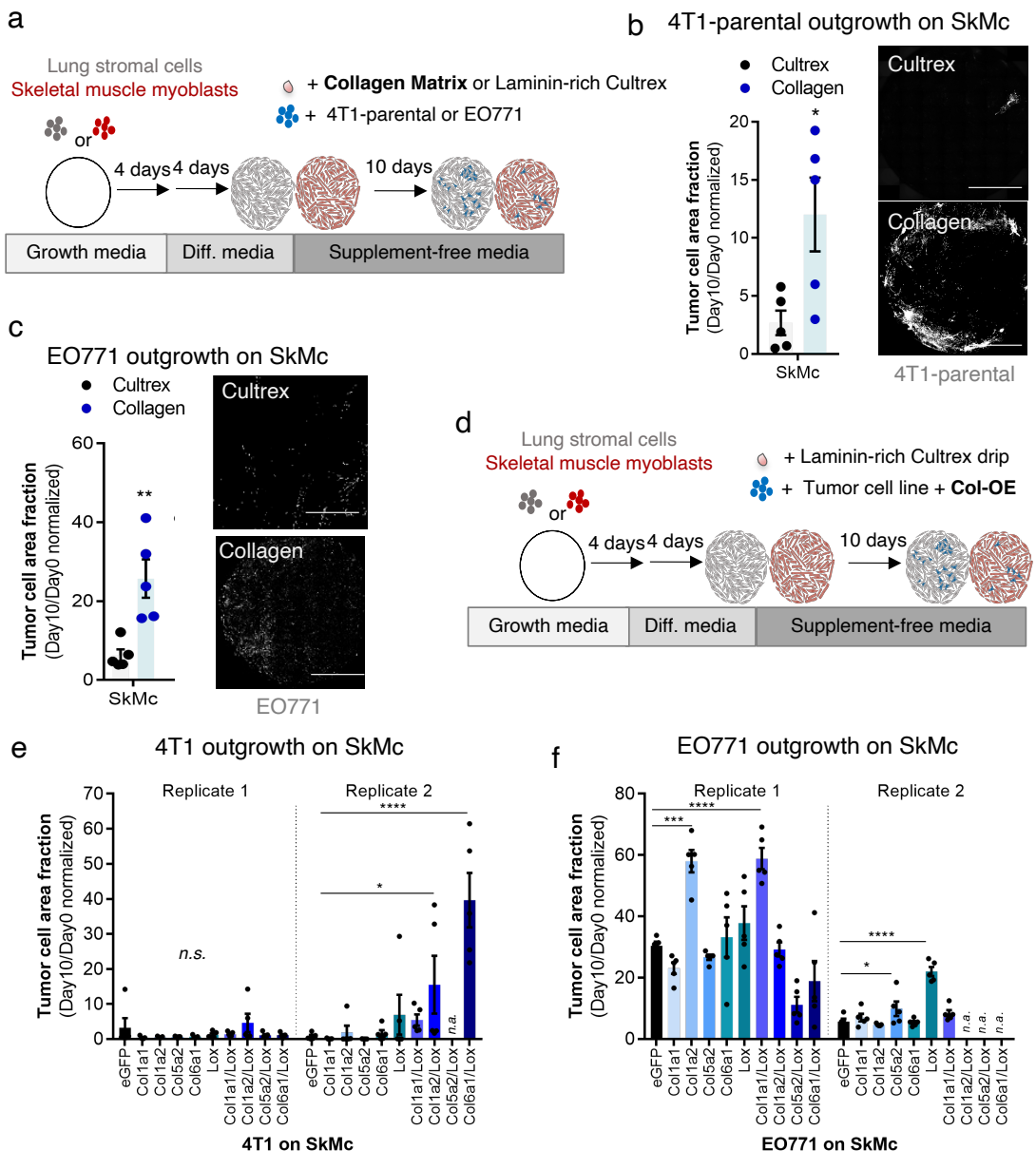

Figure 4.3. Deposition of collagen matrix facilitates tumor cell outgrowth in skeletal muscle. a) Schematic of the 3D coculture system to examine if addition of a collagen-I layer could increase tumor cell outgrowth on SkMc. b) Collagen increases 4T1-parental outgrowth on SkMc, compared to culture on Cultrex. Unpaired t-test was performed where $P = 0.02$. Scale bar = 1 mm. c) Collagen increases EO771 outgrowth on SkMc, compared to growth in Cultrex. Unpaired t-test was performed where $P = 0.006$. Scale bar = 1 mm. d) Schematic of the 3D coculture system to examine if addition of tumoral collagen overexpression could increase tumor cell outgrowth on SkMc. e) Collagen-expressing 4T1 cells grow significantly better if Lox is co-expressed with Col1a2 or Col6a1. These data are inconsistent across replicates, though. Two-way ANOVA, followed by Fisher's LSD, was performed where all comparisons were against the eGFP control. One-way ANOVA, followed by Fisher's LSD, was performed where all comparisons were against the eGFP control. $P < 0.0002$ for Col6a1/Lox, and $P = 0.02$ for Col1a1/Lox. f) Collagen-expressing EO771 cells grow significantly better if Lox is co-expressed with Col1a1, or if Col1a2, Col5a2 or Lox are singly expressed. Again, these data are inconsistent across replicates, though. Two-way ANOVA, followed by Fisher's LSD, was performed where all comparisons were against the eGFP control. $P < 0.0002$ for Col1a2 and Col1a1/Lox, and $P = 0.0001$ for Lox. $^{*}P<0.05$, $^{**}P<0.005$, $^{***}P<0.0005$, $^{****}P<0.0001$.

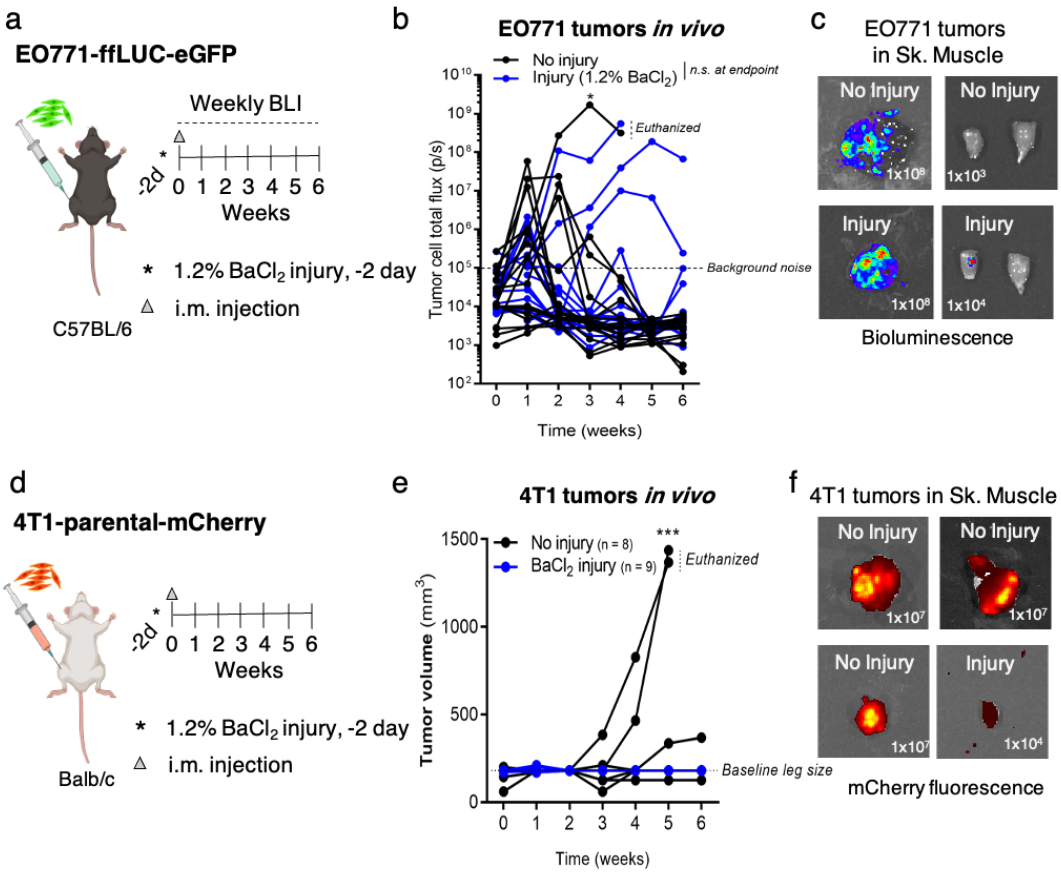

Figure 4.4. A chemical model of skeletal muscle injury does not provoke tumor colonization. a) Schematic of the C57BL/6 mouse study to examine if 1.2% barium chloride ($BaCl_2$) injury could promote skeletal muscle colonization *in vivo*. b) Bioluminescence imaging (BLI) measurements total flux (photon/second) for EO771-ffluc-eGFP cells delivered to uninjured (n= 17) or injured (n = 17) cohorts. Two-way ANOVA, followed by Fisher's LSD, was performed where $P = 0.02$ at Week 3. All other timepoints were n.s. c) Representative BLI images of skeletal muscle tumors in the injured and uninjured cohorts upon necropsy. d) Schematic of the Balb/c mouse study to examine if 1.2% $BaCl_2$ injury could promote skeletal muscle colonization *in vivo*. e) Fluorescent measurements (mCherry radiance/second) for 4T1-parental-mCherry cells delivered to uninjured (n= 8) or injured (n = 9) cohorts. Two-way ANOVA, followed by Fisher's LSD, was performed where $P = 0.0001$ at Week 5. All other timepoints were n.s. f) Representative fluorescent images (mCherry, IVIS) of skeletal muscle tumors in the injured and uninjured cohorts upon necropsy. *P <0.05, **P<0.005, ***P<0.0005, ****P<0.0001.

.

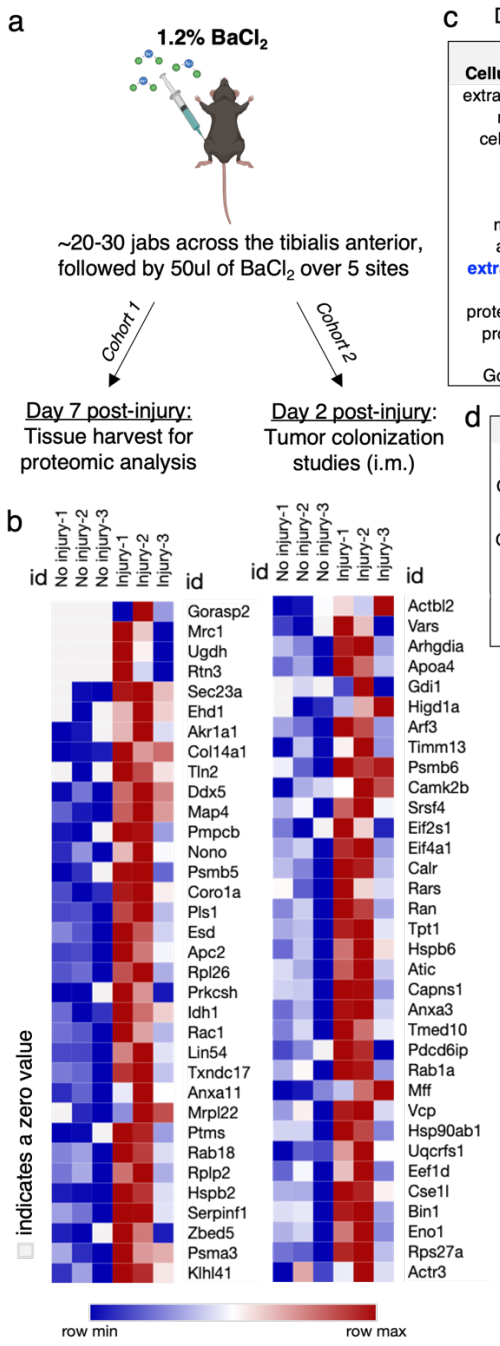

c DAVID Pathway Analysis: Enrichment in injured muscle

GOTERMS Cellular Component	Count	Percentage (%)	P-value	Benjamini (FDR)
extracellular exosome	41	62.1	3E-19	5.9E-17
melanosome	8	12.1	4.2E-08	0.0000041
cell-cell adherens junction	10	15.2	0.00000093	0.000061
cytosol	20	30.3	0.000003	0.00015
cytoplasm	39	59.1	0.000037	0.0013
myelin sheath	7	10.6	0.000041	0.0013
actin filament	5	7.6	0.000076	0.0021
extracellular matrix	7	10.6	0.00042	0.01
membrane	37	56.1	0.00086	0.019
proteasome complex	4	6.1	0.0014	0.027
proteasome core complex	3	4.5	0.002	0.035
Golgi membrane	7	10.6	0.0021	0.035

d

Extracellular Matrix Proteins	
Q5U222	DEAD (Asp-Glu-Ala-Asp) box polypeptide 5(Ddx5)
Q3ULW0	RAN, member RAS oncogene family(Ran)
Q9D859	RAS-related C3 botulinum substrate 1(Rac1)
Q3UWP8	calreticulin(Calr)
Q80X19	collagen, type XIV, alpha 1(Col14a1)
P60843	eukaryotic translation initiation factor 4A1(Eif4a1)
P97298	serine (or cysteine) peptidase inhibitor, clade F, member 1(Serpinf1)

e Collagen changes upon injury (1 week)

Gene Symbol	Fold Change (Injury / No injury)	P-value
Col18a1	17.14	0.157
Col14a1	**11.19**	**0.014**
Col12a1	**2.92**	**0.073**
Col16a1	1.98	0.259
Col6a3	1.83	0.137
Col15a1	1.46	0.127
Col6a1	1.45	0.282
Col6a2	1.41	0.351
Col11a1	1.38	0.289
Col11a2	**1.33**	**0.080**
Col5a1	1.25	0.510
Col4a2	1.25	0.555
Col5a2	1.20	0.553
Col2a1	1.14	0.776
Col4a1	1.08	0.732
Col1a2	1.06	0.839
Col1a1	1.06	0.846
Col6a6	1.01	0.950
Col5a3	0.97	0.675
Col17a1	0.96	0.945
Col3a1	0.94	0.824
Col4a3	0.53	0.319
Col8a1	0.47	0.247
Col6a5	0.34	0.329

Figure 4.5. Barium chloride injury does not induce pro-metastatic collagen deposition in skeletal muscle. a) Workflow for the barium chloride ($BaCl_2$) injury study and downstream tissue processing. b) Heatmap displaying the raw count values for the top genes enriched in the injured tibialis anterior, compared against uninjured muscle. c) DAVID pathway analysis of the Cellular Component GOTERMS for pathways enriched in injured v. uninjured muscle. d) List of the genes that comprise the "extracellular matrix proteins "set that are enriched in injured muscle. e) List of the fold-change for all collagen genes found in the proteomic data, comparing injured v. uninjured muscle. Arrows denote the collagen hits identified in the CRISPR knockout screen.

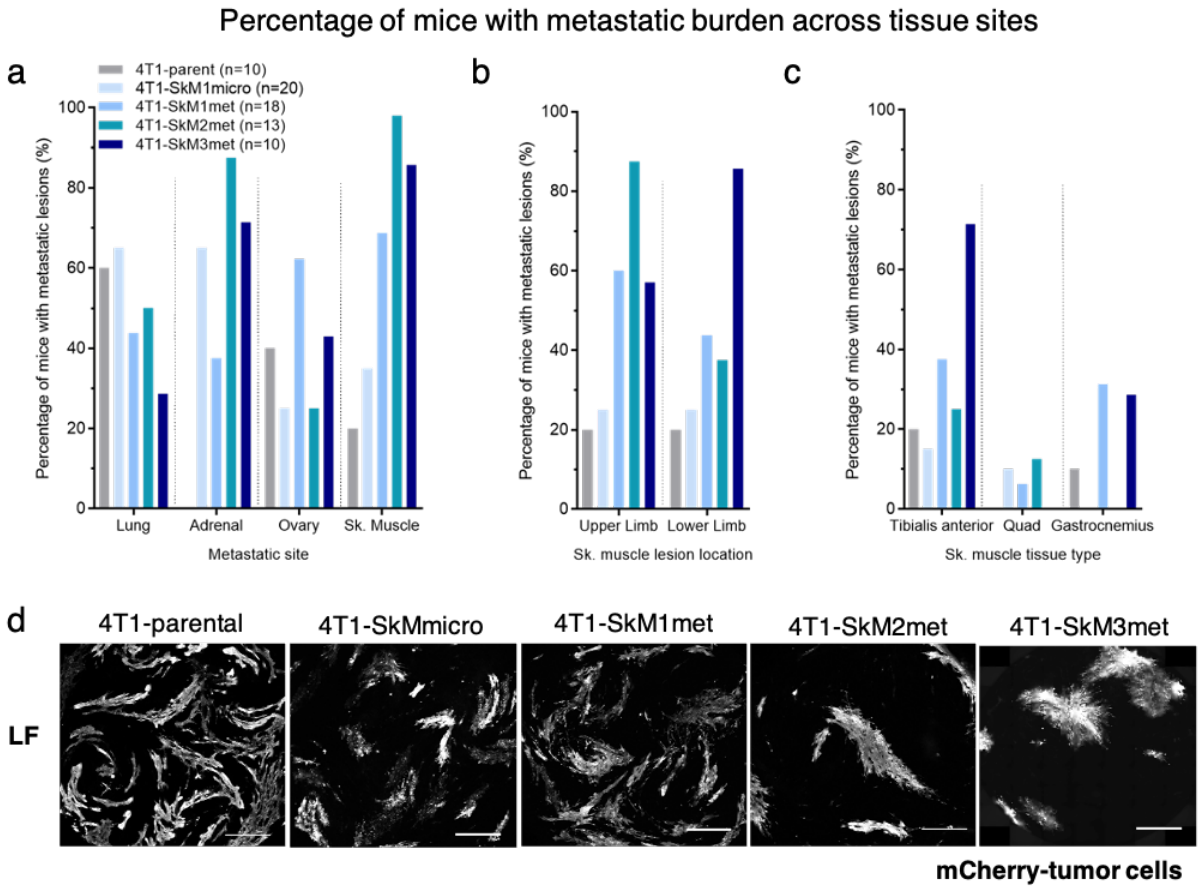

Supplementary Figure 4.1 4T1-SkMx subline colonize skeletal muscle, but do not show enhanced outgrowth in other metastatic organs. a. Percentage of mice with metastases to lung, adrenal glands, ovary or skeletal muscle. 4T1-SkM1met, 4T1-SkM2met and 4T1-SkM3met lineages significantly increase in metastatic capability within skeletal muscle while remaining relatively constant in all other organs. b) Percentage of mice with skeletal muscle metastases found in the upper limb (arm) or lower limb. c) Percentage of mice with skeletal muscle metastases found in the lower limb grouped by specific site: tibialis anterior, quadriceps or gastrocnemius. d. Representative images of 4T1-SkMx subline outgrowth on LF. Proliferation of 4T1 lines increases in SkMc with each daughter line, whereas outgrowth of all remain similar or diminish within LF niche. Scale bar = 1 mm.

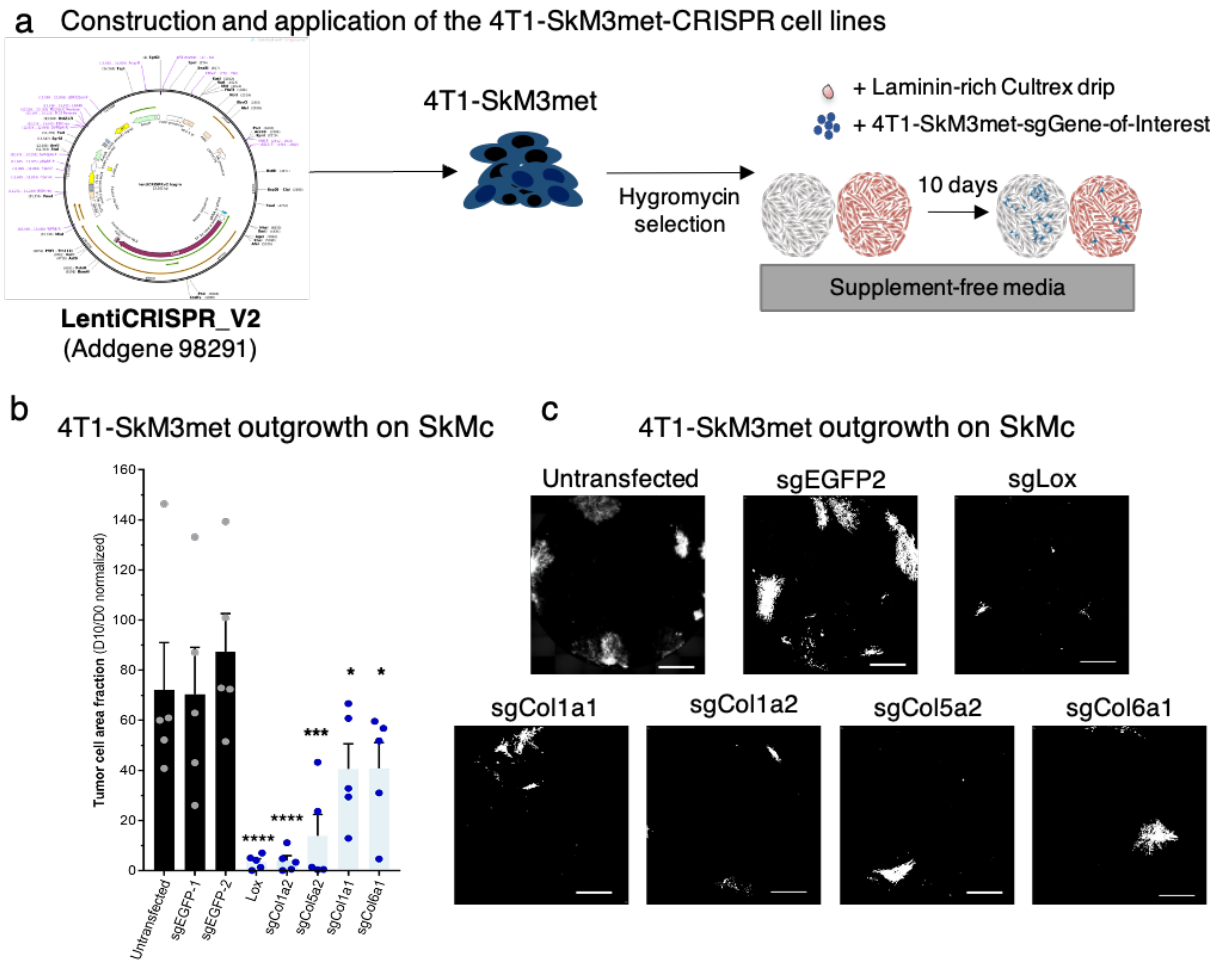

Supplementary Figure 4.2. CRISPR knockout screen reveals that collagen knockout prevents skeletal muscle metastasis of 4T1-SkM3met cells. a) Schematic of the construction and co-culture application of the 4T1-SkM3met-CRISPR cell lines. b) 4T1-SkM3met outgrowth is restricted when collagens Col1a2, Col5a2 and Lox are knocked out. One-way ANOVA, followed by Fisher's LSD, was performed, where comparisons were made against the sgEGFP-2 control. c) Representative images of 4T1-SkM3 outgrowth on SkMc. Scale bar = 1 mm. **P* <0.05, ***P*<0.005, ****P*<0.0005, *****P*<0.0001.

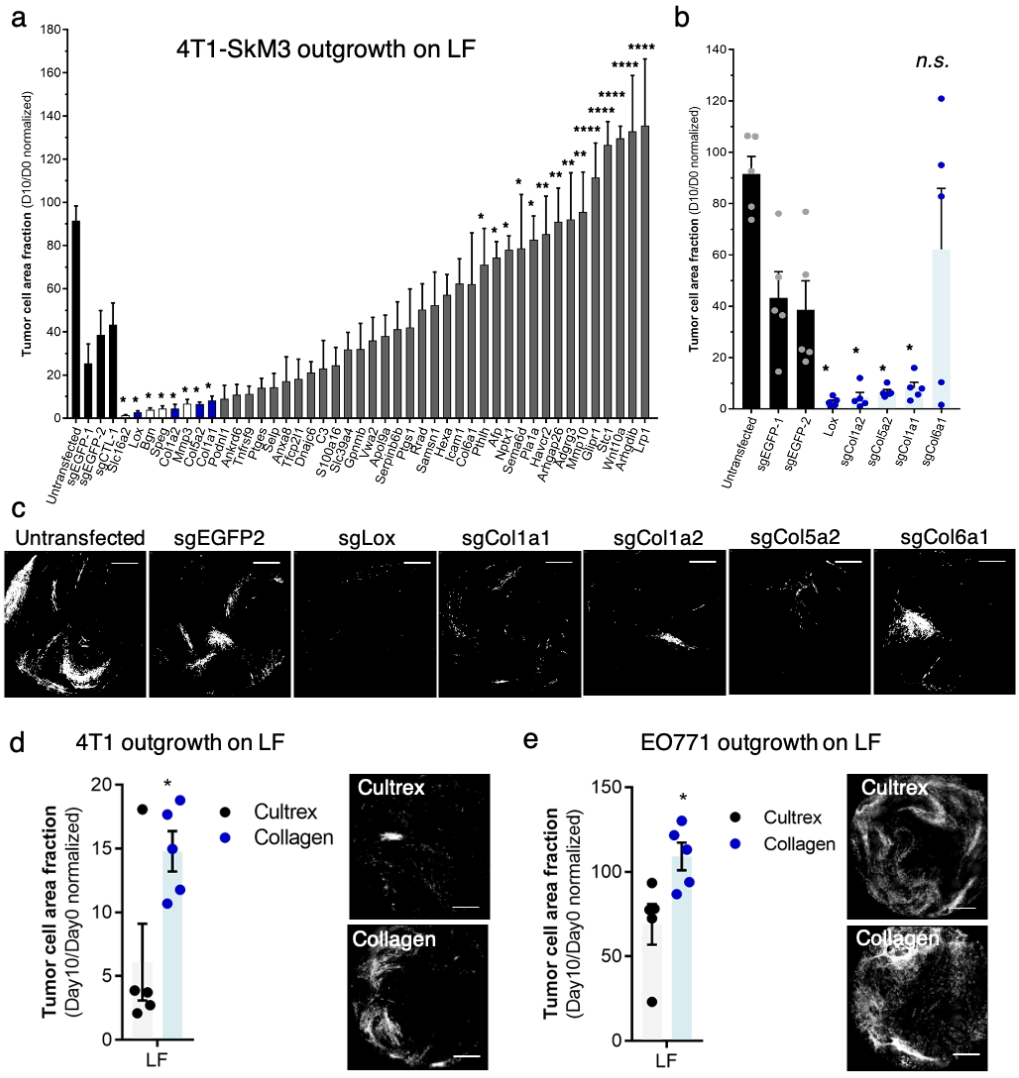

Supplementary Figure 4.3. Deposition of collagen also enhances tumor cell outgrowth on lung-like niche. a) 3D coculture of 4T1-SkM3met with the 55 genes knockouts (CRISPR) reveals 8 genes that significantly reduce growth on LF. Five of the eight genes are collagen-related. One-way ANOVA, followed by Fisher's LSD, was performed where comparisons were made against the sgEGFP-2 control. b) Close-up of the 4T1-SkM3met tumor cell outgrowth on LF niche pertaining to the collagen genes. One-way ANOVA, followed by Fisher's LSD, was performed where comparisons were made against the sgEGFP-2 control. c) Representative images of the outgrowth 4T1-SkM3met cells with the Lox or collagen knockouts on the LF niche. Scale bar = 1 mm. d) 4T1-parental outgrowth on LF niche when grown in either Cultrex or a collagen-I matrix layer. Unpaired t-test was performed, where $P < 0.022$. Scale bar = 1 mm. e) EO771 outgrowth on LF niche when grown in either Cultrex or a collagen-I matrix layer. Unpaired t-test was performed, where $P < 0.03$. Scale bar = 1 mm. *P <0.05, **P<0.005, ***P<0.0005, ****P<0.0001.

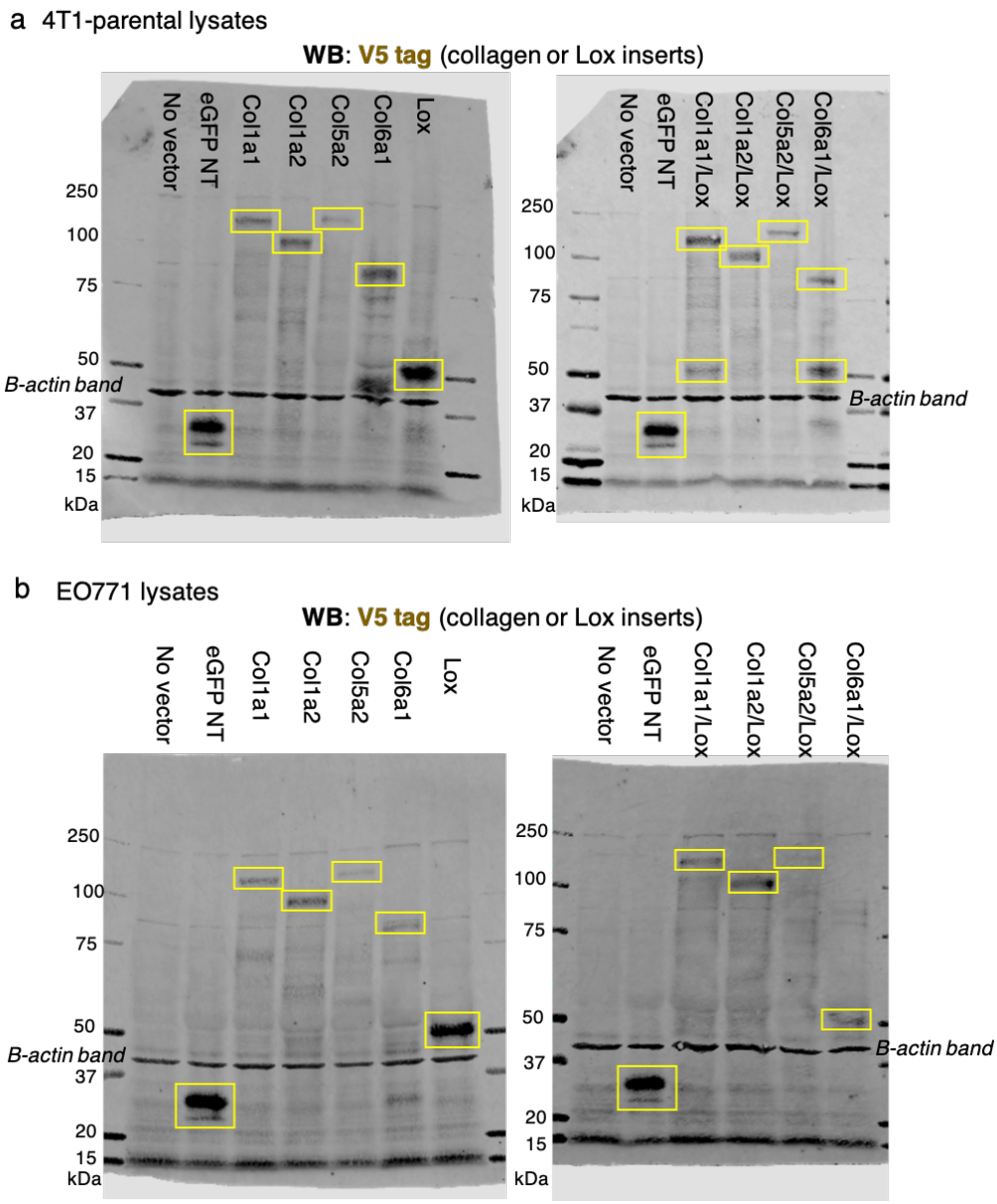

Supplementary Figure 4.4. Collagen genes are overexpressed in 4T1 and EO771 cell lines. a) Western blot showing the overexpression of collagen and lox genes in the 4T1 parental cell line. Genes were probed for using V5 antibody. B-actin served as a loading control. b) Western blot showing the overexpression of collagen and lox genes in the EO771 parental cell line. Genes were probed for using V5 antibody. B-actin served as a loading control.

a C57BL/6 model – Validation of injury (1 week post)

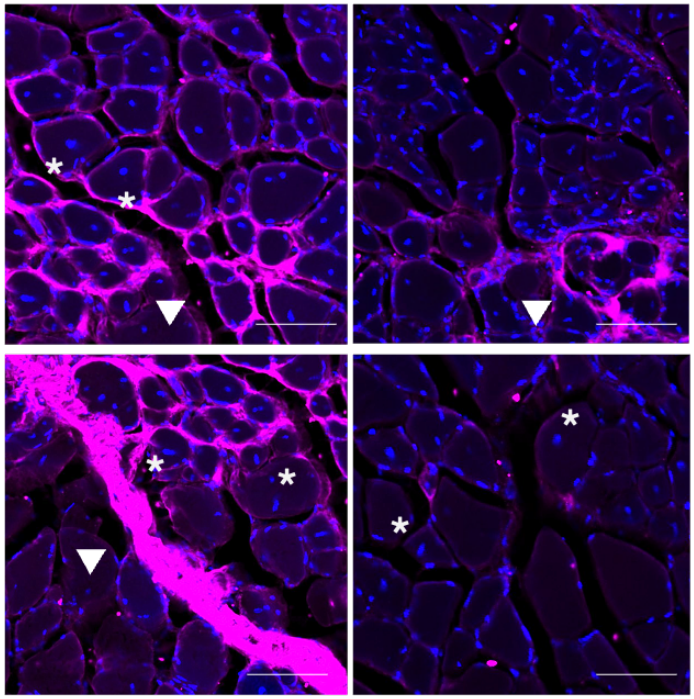

Nuclei New ECM deposits

b Proteomics – 1 week post $BaCl_2$

Gene Symbol	Fold Change (Inj/No inj)	T-test P-value
Gorasp2	Injury Only	0.033
Mrc1	Injury Only	0.032
Ugdh	Injury Only	0.015
Rtn3	Injury Only	0.029
Sec23a	14.88	0.021
Ehd1	11.76	0.002
Akr1a1	11.38	0.034
Col14a1	11.19	0.014
Tln2	10.29	0.021
Ddx5	6.33	0.000
Map4	5.72	0.015
Pmpcb	5.43	0.025
Nono	4.79	0.013
Psmb5	4.72	0.039
Coro1a	4.40	0.043
Pls1	4.09	0.047
Esd	4.04	0.027
Apc2	3.96	0.029
Rpl26	3.80	0.047
Prkcsh	3.71	0.047
Idh1	3.56	0.019
Rac1	3.47	0.046
Lin54	3.47	0.035
Txndc17	3.41	0.038
Anxa11	3.38	0.050
Mrpl22	3.34	0.002
Ptms	3.33	0.001
Rab18	3.28	0.023
Rplp2	3.23	0.033
Hspb2	3.17	0.043
Serpinf1	3.10	0.024
Zbed5	3.08	0.019
Psma3	3.07	0.000
Klhl41	3.06	0.024
Actbl2	3.03	0.017
Vars	3.01	0.042
Arhgdia	2.99	0.048
Apoa4	2.98	0.047
Gdi1	2.91	0.016
Higd1a	2.80	0.016
Arf3	2.76	0.047
Timm13	2.76	0.041
Psmb6	2.74	0.028
Camk2b	2.66	0.015
Srsf4	2.64	0.001
Eif2s1	2.63	0.013
Eif4a1	2.62	0.036
Calr	2.58	0.031
Rars	2.55	0.003
Ran	2.53	0.050
Tpt1	2.52	0.011
Hspb6	2.50	0.001
Atic	2.47	0.033
Capns1	2.42	0.038
Anxa3	2.36	0.030
Tmed10	2.35	0.046
Pdcd6ip	2.29	0.010
Rab1a	2.29	0.047
Mff	2.20	0.036
Vcp	2.18	0.019
Hsp90ab1	2.18	0.044
Uqcrfs1	2.16	0.044
Eef1d	2.12	0.038
Cse1l	2.08	0.004
Bin1	2.06	0.027
Eno1	2.05	0.044
Rps27a	2.05	0.043
Actr3	2.02	0.020

Supplementary Figure 4.5. Barium chloride injury promotes remodeling of skeletal muscle. a) IF staining of skeletal muscle injured by 1.2% barium chloride, harvest 1 week post-injury. Stars denote examples of centrally-nucleated myofibers, whereas triangles highlight areas of increased ECM deposition. Scale bar = 200 μm. b) Table displaying all of the genes with >2 fold change (with p-value <0.05) in injured tibialis anterior versus uninjured tibialis anterior skeletal muscle.

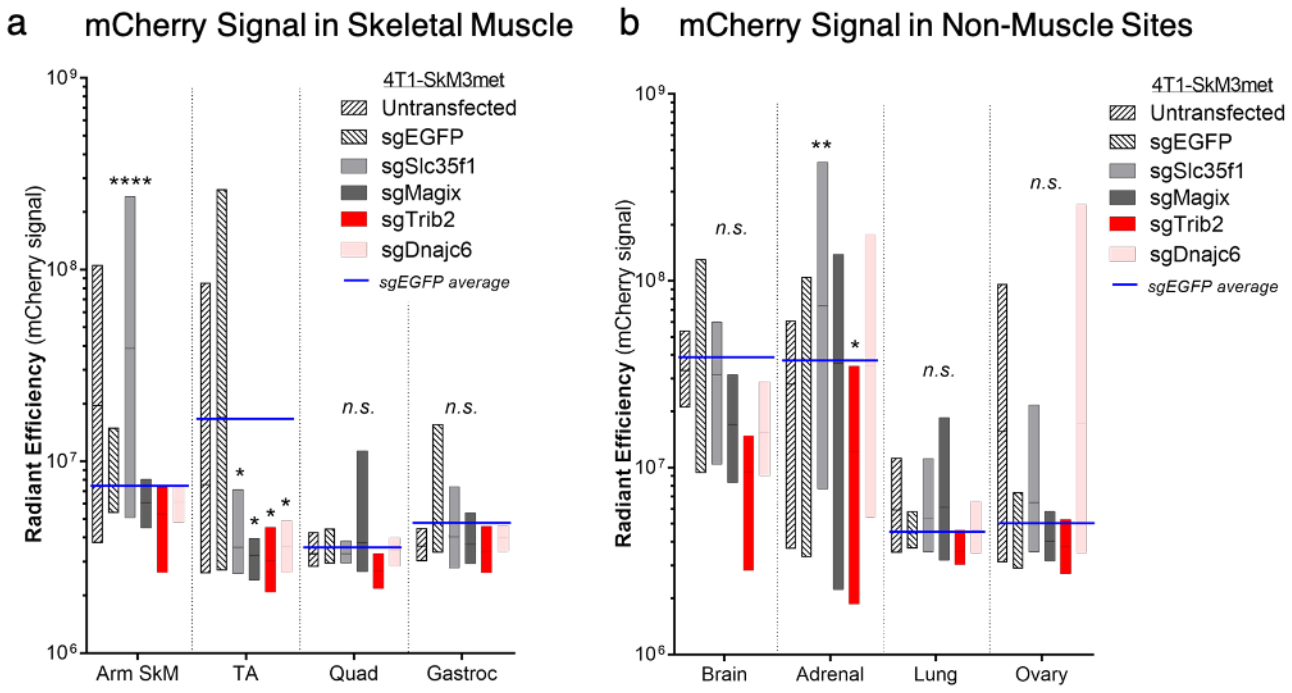

Supplementary Figure 5.3. Average mCherry tumor signal is reduced in the tibialis anterior of all CRISPR knockout lines. a) 4T1-SkM3 tumor cell fluorescence (mCherry, radiant efficiency, IVIS) in skeletal muscle sites. Two-way ANOVA, followed by uncorrected Fisher's LSD, was performed where $P<$ 0.0001 for sgEGFP v. sgSlc35f1 in arm SkMc. $P < 0.05$ for sgEGFP and the following in the TA: sgTrib2, sgDnajc6, sgMagix and sgSlc35f1. All other comparisons against sgEGFP are n.s. b) 4T1-SkM3 tumor cell fluorescence (mCherry, radiant efficiency, IVIS) in non-muscle sites (brain, adrenal gland, lung and ovary). Two-way ANOVA, followed by uncorrected Fisher's LSD, was performed where $P = 0.02$ in sgEGFP v. sgTrib2 in the adrenal gland and $P = 0.0015$ in sgEGFP v. sgSlc35f1 in the adrenal gland. All other comparisons against sgEGFP are n.s. *P <0.05, **P<0.005, ***P<0.0005, ****P<0.0001.

Chapter 4 References

1. Crist SB et al. Unchecked oxidative stress is an insurmountable barrier for tumour cells that disseminate to skeletal muscle. *Nature Cell Biology (In Revision).*

2. Disibio, G., French, S.W. Metastatic patterns of cancers: results from a large autopsy study. *Archives of Pathology & Laboratory Medicine* **132**(931). (2008).

3. Surov A. et al., Skeletal muscle metastases: primary tumors, prevalence and radiological features. *Eur Radiol*, **20**:649-658. (2010).

4. Surov A. et al, Muscle metastases: comparison of features of different primary tumors. *Cancer Imaging,* **14**:21 (2014).

5. Gillies A.R and Lieber R. Structure and Function of the Skeletal Muscle Extracellular Matrix. *Muscle Nerve* **44**(3): 318-331. (2011).

6. Csapo R, Gumpenberger M and Wessner B. Skeletal Muscle Extracellular Matrix – What Do We Know About Its Composition, Regulation, and Physiological Roles? A Narrative Review. *Front. Physiol.* (2020).

7. Winkler J, Abisoye-Ogunniyan A, Metcalf K and Werb Z. Concepts of extracellular matrix remodelling in tumour progression and metastasis. *Nature Communications*. 11(5120). 2020

8. Fang M., Yuan J., Peng C., Li Y. Collagen as a double-edged sword in tumor progression. *Tumor Biology* **35**(4):2871-2882. (2014).

9. Y-C Lee et al. Collagen-rich airway smooth muscle cells are a metastatic niche for tumor colonization in the lung. *Nature Communications* **10**:2131. (2019).

10. Kai, F., Drain, A.P., Weaver, V.M. The extracellular matrix modulates the metastatic journey. *Dev Cell* **49**(3):332-346. (2019).

11. Pickup, M.W., Mouw, J.K., Weaver, V.M. The extracellular matrix modulates the hallmarks of cancer. *EMBO Rep* **15**(12):1243-53. (2014).

12. Erler, J.T., V.M. Weaver, V.M. Three-dimensional context regulation of metastasis. *Clinical & Experimental Metastasis* **26(**1):35-49. (2009).

13. D. Hardy et al, Comparative study of injury models for studying muscle regeneration in mice. *PLoS One* **11**(1): e0147198. (2016).

14. Tierney MT and Sacco A. Inducing and Evaluating Skeletal Muscle Injury by Notexin and Barium Chloride. *Methods Mol. Biol*. **1460**:53-60 (2016).

15. Morton AB. et al. Barium chloride injures myofibers through calcium-induced proteolysis with fragmentation of motor nerves and microvessels. *Skeletal Muscle*. **9**(27). (2019).
16. Gordon MK et al. Cloning of a cDNA for a new member of the class of fibril-associated collagens with interrupted triple helices. *European Journal of Biochemistry*. **201**(2):333-38. (1991).
17. Ruijiao K et a;. Col14a1 promotes self-renewal of human liver cancer stem cells through activation of ERK signaling. *Journal of Bio-X Research.* **4**(1):10-17. (2021).
18. Xiang Z. et al. A positive feedback between IDO1 metabolite and Col12a1 via MAPK pathway to promote gastric cancer metastasis. *Journal of Experimental and Clinical Cancer Research.* **38**(314). (2019).
19. Tao G. et al. Collagen XIV is important for growth and structural integrity of the myocardium. *Journal of Molecular and Cellular Cardiology.* **53**(5):626-638. (2012).
20. Izu et al. Collagen XII mediated cellular and extracellular mechanisms regulate establishment of tendon structure and function. *Matrix Biology*. **95**:52-67. (2021).
21. Collagen Type XI Alpha 2 Chain. Gene ID: 1302. NCBI. Updated 2021. https://www.ncbi.nlm.nih.gov/gene/1302
22. Roos L. et al. Integrative DNA methylome analysis of pan-cancer biomarkers in cancer discordant monozygotic twin-pairs. *Clinical Epigenetics*. **8**(7). (2016).
23. Sieweke, M.H., Thompson, N.L., Sporn, M.B., Bissell M.J. Mediation of wound-related Rous sarcoma virus tumorigenesis by TGF-beta. *Science.* **248**(4963):1656–1660 (1990).
24. Fisher, B., Fisher, E., Feduska, N. Trauma and the localization of tumor cells. *Cancer* **20**:23-30 (1967).
25. El Saghir, N. et al., Trauma-associated growth of suspected dormant micrometastasis. *BMC Cancer.* **5**:95 (2005).
26. Dvorak H. Tumors: wounds that do not heal. Similarities between tumor stroma generation and wound healing. *N Engl J Med* **315**(26):1650-9 (1986).
27. Schafer and Werner. Cancer as an overhealing wound: an old hypothesis revisited. *Nature Reviews: Mol. Cell Biol* **9**:628-638 (2008).
28. Magee, T., H. Rosenthal, H., Skeletal muscle metastases at sites of documented trauma. *American Journal of Roentgenology* **178**(985). (2002).
29. Barcus, C.E., et al. Elevated collagen-I augments tumor progressive signals, intravasation and metastasis of prolactin-induced estrogen receptor alpha positive mammary tumor cells. *Breast Cancer Research.* **19**(1):9. (2017).

30. Rainero E., et al. Extracellular matrix internalization links nutrient signaling to invasive migration. *International Journal of Experimental Pathology*. **99**:4–9. (2018).
31. Mah, E.J., Lefebvre, A.E., McGahey, G.E., Yee, A.F., Digman, M.A. Collagen density modulates triple-negative breast cancer cell metabolism through adhesion-mediated contractility. *Scientific Reports.* **8**(1). (2018).

Chapter 5. Future Directions

1. Do ECM composition and redox metabolism synergize to suppress DTC outgrowth in skeletal muscle?

Introduction.

The data in Chapter 3 imply that skeletal muscle creates a harsh metabolic environment through the generation of high levels of ROS. The balancing of DTC redox state in skeletal muscle positions tumor cells to transition from the single cell state, but does not guarantee long-term success. Perhaps DTCs in skeletal muscle benefit from an additional "grow" cue. Hernandez-Munoz and colleagues found a striking correlation of collagen synthesis and breakdown with cytosolic and mitochondrial redox potential[1-3]. More specifically, they describe that an attenuation of NAD/NADH (a measurement of oxidation) in cytosol and mitochondria is related to an increase in collagen synthesis[1-3]. A continuous feedforward loop consisting of high oxidation and limited collagenous substrate in skeletal muscle, therefore, may be the cause of persistent DTC arrest. Based on the findings described in Chapter 4, I hypothesized that extracellular matrix (**ECM**) composition of healthy skeletal muscle may complement this tissue's metabolic state to prevent metastatic outgrowth. In this subsection, we performed experiments to determine if altered ECM composition (e.g. enhanced collagen) could pair with redox stabilizers to foster tumor cell outgrowth in the skeletal muscle niche.

Preliminary Results.

mCAT-expressing breast tumor cells are capable of greater outgrowth when paired with a collagen-rich environment. We showed previously that tumor cell outgrowth could be stimulated in a collagen-rich skeletal muscle environment, independent of other perturbations (Chapter 4). To evaluate a possible metabolic component to collagen's pro-growth signaling, I examined the outgrowth of cytosolic catalase- (**cCAT**) or mitochondrial catalase (**mCAT**)-expressing breast cancer cell lines in the context of a collagen-rich microenvironment. If collagen drives tumor cell proliferation via heightened metabolic activity (e.g. enhanced biosynthesis of macromolecules, ATP generation[4]), perhaps cCAT and mCAT could mitigate toxic byproducts generated during this activated state, further enhancing tumor cell outgrowth in the skeletal muscle niche.

Seeding breast cancer cells onto human skeletal muscle-derived myotubes allowed us to recreate the myofiber niche in organotypic culture, and compare subsequent breast tumour cell outgrowth to growth on a more permissive niche comprised of lung stroma (primary human lung fibroblasts, **LF**s). To do this, skeletal muscle myocytes (**SkMc**) and LF cells were plated in a 96-well plate, differentiated to form myotubes, and seeded with $1x10^2$ GFP-MDA-MB-231 human breast cancer cells. To better understand the role of ECM composition on tumor outgrowth in these niches, organotypic cultures were topped with either a laminin-rich basement membrane extract (Cultrex) or a type I collagen extract ("**collagen**"). Tumor cell outgrowth was measured over the course of ten days by quantification of the GFP^+ area occupied at Day 10 normalized by Day 0. From this study, we found that MDA-MB-231 cells expressing mCAT in a collagen matrix grow four times as well on SkMc compared to control (Cultrex, no catalase vector) (**Fig. 5.1a**). MDA-MB-231-

mCAT cells grown in collagen on SkMc trended towards increased outgrowth when compared against MDA-MB-231-mCAT cells in Cultrex or MDA-MB-231-Ctl cells in collagen (**Fig. 5.1a**). We also noted that ectopic catalase expression paired with collagen deposition also facilitates better tumor cell outgrowth in the lung-like environment in this study (**Fig. 5.1b**). Unlike the SkMc study, outgrowth of MDA-MB-231-mCAT cells cultured in collagen on LF was significantly increased outgrowth when compared against MDA-MB-231-mCAT cells in Cultrex or MDA-MB-231-Ctl cells in collagen (**Fig. 5.1b**). From these findings, we estimated that the absence of a collagen-rich ECM and effective ROS management may together shape SkM into a hostile microenvironment. This made us wonder about the mechanism underlying collagen's pro-growth phenotype. As our interest lies in metabolism, we were particularly intrigued by the question: Does collagen deposition remodel the redox environment of the skeletal muscle niche? This might explain why collagen synergizes best with the mitochondrial form of catalase, where both major sources of ROS impacting tumor cell growth (e.g. the mitochondria and the extracellular environment) are neutralized.

Collagen deposition correlates with reduced tumor cell oxidation in the SkMc niche. To determine whether collagen reduces the amount of oxidative stress experienced by breast tumour cells in the skeletal muscle microenvironment we employed a glutaredoxin-redox sensitive-GFP2 (**Grx1-roGFP2**) biosensor[5-6] that allows dynamic and quantitative live imaging of GSH redox potential and a cell's oxidation state. Over a ten-day period, the SkMc niche significantly and substantially suppressed the growth of the MDA231-roGFP2 cells when compared to outgrowth on LFs as expected (**Fig. 5.1c-d**, left panel). When plated in co-culture on SkMcs with Cultrex, MDA-MB-231-Grx1-roGFP2 ("**MDA231-**

roGFP2") cells became highly oxidized by Day 5 and stayed oxidized for the duration of the study (**Fig. 5.1c-d**, right panel). MDA231-roGFP2 cells on the LF niche with Cultrex did not show the same oxidation (**Fig. 5.1c-d**, right panel)**.** When MDA231-roGFP2 cells were cultured on the SkMc and LF niches with collagen, we not only observe significant improvement in tumor cell outgrowth by Day 10 on the skeletal muscle niche (**Fig. 5.1c-d**, left panel), but also a significant reduction in oxidation (**Fig. 5.1c-d**, right panel). Therefore, there is a correlation between collagen deposition and reduced oxidation in tumor cells on the SkMc niche.

Collagen facilitates redox stabilization prior to tumor cell growth in SkMc. To parse apart if collagen has a direct role on reducing tumor cell oxidation or if redox homeostasis is achieved as a product of proliferation, we looked closer at the growth and oxidation kinetics. For the first experimental replicate (**Fig. 5.1c**), collagen causes a significant increase in MDA231-roGFP2 cell outgrowth on SkMc on Day 6. In the same experiment, collagen significantly reduced MDA231-roGFP2 oxidation on SkMc on Day 5 (**Fig. 5.1c**). These data suggest that collagen might directly aid the tumor cell response to balance oxidative stress, which enables concurrent or subsequent proliferation. In a second study (**Fig. 5.1d**), collagen caused a significant increase in MDA231-roGFP2 cell outgrowth on SkMc on Day 9. In the same experiment, collagen significantly reduced MDA231-roGFP2 oxidation on SkMc temporarily at Day 1 and consistently from Day 5 onwards (**Fig. 5.1d**). This further supports the idea that collagen acts on the metabolic state of the tumor cell. Left to be discovered are the mechanisms by which collagen acts to alter the redox balance of the tumor cell as well as the environment where these cells reside.

Discussion.

In sum, we have learned that ectopic catalase expression (mCAT, especially) and the addition of a collagen type I matrix facilitate better tumor cell outgrowth in the skeletal muscle niche. We have also demonstrated, here and in Chapter 3, that both strategies center around lowering tumoral oxidative stress. Moving forward, it will be necessary to uncover several other key pieces of information: Does increased collagen deposition alter the redox state of DTCs in skeletal muscle *in vivo?* Is collagen sufficient to promote tumor burden in skeletal muscle? If enhanced collagen content in skeletal muscle's extracellular matrix *is* sufficient to foster tumor cell proliferation, why do we not observe more skeletal muscle metastases? Understanding the composition and impact of ECM on metastasis growth dynamics is critical. Therefore, we believe that these early findings may open new lines of inquiry for the study of metabolic modulators of ECM - and ECM on metabolism - on DTC outgrowth in anti-metastatic and metastatic tissues alike.

2. Does the master regulator MyoD drive suppression via a metabolic or ECM-based route?

Introduction.

Myogenic differentiation 1 (**MyoD**) is a master regulator that has long been recognized for its crucial role in skeletal muscle specification and differentiation[6]. As a transcriptional activator of at least 1,000 genes[7,8], signal transduction downstream of MyoD may underlie the anti-metastatic phenotype observed within skeletal muscle. We know that

MyoD can remove muscle cells from the cell cycle (halt proliferation for terminal cell cycle arrest in differentiated myocytes) by enhancing the transcription of p21 and myogenin[9]. As sustained MyoD expression is necessary for retaining the expression of SkM-related genes, its constant expression may also be key to the sustained growth arrest of DTCs in this niche. We hypothesized that MyoD might drive the transcriptional program that underlies the anti-metastatic microenvironment at skeletal muscle, as documented thoroughly in Chapters 3-4.

Preliminary Results.

Ectopic expression of MyoD reduces tumor cell growth on lung fibroblast niches. Tapscott and others have demonstrated that ectopic expression of MyoD is sufficient to convert a number of cell types (e.g. fibroblasts, adipocytes, chondrocytes) into skeletal muscle through a myogenic program[7-8,10]. We found this to be true in our hands, as well. Inducible MyoD expression within lung fibroblasts ("**LF-MyoD**") using a doxycycline-inducible lentiviral system (LV-TRE-MyoD) led to fibroblast fusion and differentiation into myotubes (**Fig. 5.2a**). Introduction of a lentiviral vector to the LF cells was controlled for by using an empty-vector control ("**LF-Empty**"). We wondered if transdifferentiating lung fibroblasts, through ectopic MyoD expression, would be sufficient to reduce tumor cell outgrowth in an otherwise highly permissive niche (the lung-like niche). If true, this would imply that MyoD and its associated programs, unique to skeletal muscle, are central to the metastasis suppressive phenotype.

To examine if ectopic expression of MyoD could reduce tumor cell outgrowth on the lung-like niche (LF or LF-MyoD) to the extent observed in the myocyte niche, we utilized a

3D organotypic culture model. Skeletal muscle myocytes (**SkMc**), LF, LF-MyoD and LF-Empty cells were plated in a 96-well format, cultured in differentiation medium and seeded with $1x10^2$ YFP-MDA-MB-231 human breast cancer cells. Doxycycline (3 μg/mL) was added to the LF-MyoD wells to begin transdifferentiation 24 hours post-initial seeding. To make consistent conclusions across the conditions, doxycycline was applied to all niches 24h post-seeding. Tumor cell outgrowth was measured over the course of ten days by quantification of the YFP^+ area occupied at Day 10 normalized by Day 0. Tumor cell outgrowth on the LF-MyoD niche was suppressed to levels approaching those observed on SkMc, and substantially less than observed on uninduced control LFs (**Fig. 5.2b**). Tumor cells grown on lung-like niches comprised of empty vector controls (LF-Empty) or on the LF-MyoD in the absence of doxycycline show no significant reduction in outgrowth (**Fig. 5.2b**).

Doxycycline removal at early timepoints demonstrates that the first several days within the SkMc niche is critical to tumor cell suppression. To examine the permanence of MyoD's effect, doxycycline was withdrawn from the co-cultures at various timepoints prior to and during the duration of the ten-day growth period. These experiments aimed to determine if the component responsible for this reduction of MDA-MB-231 outgrowth is fixed, or instead relies upon persistent MyoD induction. If the suppressive factor was stable post-MyoD induction, tumor cell outgrowth should remain restricted. However, if the suppressive factor is more plastic/transitory in nature, removal of doxycycline from the co-cultures would result in restoration of tumor cell outgrowth on the lung-like niche.

We observed that, as before, treatment with doxycycline throughout the duration of the ten-day study resulted in reduced MDA-MB-231 outgrowth on the LF-MyoD compared against untreated LF-MyoD and treated LF-Empty conditions (**Fig. 5.2c**). However, tumor

cell outgrowth on the doxycycline-treated LF-MyoD still did not match the reduced level on the SkMc niche, possibly suggesting that though MyoD does enforce suppression, there is an additional element missing. When doxycycline was withdrawn mid-way through the study (at Day 5), we make the same observations. MDA-MB-231 outgrowth is reduced on the LF-MyoD compared to untreated LF-MyoD and treated LF-Empty conditions (**Fig. 5.2d).** This suggests that either i) the MyoD program that drives tumor cell suppression is stable after transdifferentiation, or ii) that suppressive mechanisms occur (or are most influential) within the first five days of culture. When doxycycline was removed at the time of tumor cell seeding (Day 0), we observed something interesting: MDA-MB-231 cells outgrew significantly better on LF-MyoD niches than LF-Empty or untreated LF-MyoD when doxycycline was present at the time of tumor cell seeding (**Fig. 5.2e**). This study implied that the myogenic mechanism that suppresses tumor cell outgrowth is not stable/permanent post-transdifferentiation but rather the critical window for suppression is in the first several days of culture on a muscle-like niche. Though the increase in MDA-MB-231 growth does not outmatch the other conditions until the final Day 10 timepoint, the findings from the doxycycline withdrawl studies, as a whole, imply that the impact of the skeletal muscle is felt early on.

MyoD knockdown in skeletal muscle does not lead to increased tumor cell outgrowth. To test whether the suppressive SkMc program relies on MyoD, we generated high-titer lentivirus from shRNA libraries targeting MyoD and non-targeting (**NT**) control. Loss of MyoD expression (as well as ectopic MyoD expression in the LF-MyoD) was confirmed using PCR methodologies (**Fig. 5.2f-g**). Only one of three shMyoD clones (**"shMyoD38"**) demonstrated significantly MyoD reduction, so this was the knockdown

chosen for subsequent studies. Transfected shMyoD-myoblasts were plated in 96-well format, cultured in differentiation medium and seeded with $1x10^2$ YFP-MDA-MB-231 breast tumor cells. While we hypothesized that the MyoD-depleted SkMc niche would have increased tumor cell outgrowth compared to control cultures, based on the LF data, we did not observe this to be the case. Knockdown of MyoD in skeletal muscle had no impact on tumor cell outgrowth over the ten-day study (**Fig. 5.2h**). Therefore, we concluded that MyoD is not the sole mediator of tumor cell suppression in the skeletal muscle niche. Though upstream of many critical signaling nodes, MyoD does not independently control all of these programs. Perhaps with MyoD downregulated, other regulators compensate to enforce the mechanisms that underlie tumor cell suppression in our culture models. This will be the focus of future study.

Discussion.

Here we discuss the possibility that MyoD, a master regulator for skeletal muscle myogenesis, is the basis for skeletal muscle's anti-metastatic behaviors. Transdifferentation of lung fibroblasts to ectopically enforce the myogenic program confirmed our suspicions that making a niche "more muscle-like" might recapitulate the growth suppression. In our models, MDA-MB-231 human breast cancer cells grow poorly on MyoD-expressing lung niches compared to unmanipulated controls. However, when we conversely tried to promote tumor proliferation on the skeletal muscle niche by MyoD knockdown, tumor outgrowth was unchanged. Reduced or absent MyoD expression was not sufficient to overcome the other suppressive barriers found in the skeletal muscle niche. We reasoned that perhaps redundant transcription factors acted to compensate in the pathways/nodes most relevant

for tumor cell suppression. Therefore, our findings do not rule out the possibility that myogenic factors like MyoD underlie the tumor suppressive nature of skeletal muscle. More targeted study will be required to understand if muscle-specific programs dictate the interactions between the environment and tumor cell that result in growth arrest.

MyoD plays critical roles in embryonic skeletal muscle development and injury repair of postnatal muscle[11-13]. However, whether this transcription factor also regulates skeletal muscle metabolism is only beginning to be explored. Despite the integral role of energy metabolism in muscle function[14], myogenic transcription factors such as MyoD have not been directly identified to regulate mitochondrial biogenesis until recently. Shintaku *et al*. discovered that MyoD is a major regulator of skeletal muscle oxidative metabolism, where MyoD and RelB cooperatively bind enhancers along the PGC-1β gene to regulate its transcription[15]. As a member of the PPARγ coactivator-1 (PGC-1) family, PGC-1β interacts with and stimulates the transactivation functions of NRF-1, NRF-2, PPARα, PPARδ, and ERRα to enhance mitochondrial content and the oxidative capacity of muscle[16]. Given our lab's burgeoning interest in oxidative metabolism and the impact redox balance has on disseminated tumor cell outgrowth, we argue that inquiry into the PGC-1β/RelB signaling axis might be a good place to continue our initial studies. Knowing that MyoD plays a direct role in maintaining the oxidative metabolic capacity of homeostatic adult skeletal muscle[15], we wonder if MyoD then is equally behind the metabolic constraints imposed on DTCs in this tissue.

3. Are there molecular mechanisms that facilitate DTC colonization uniquely in skeletal muscle?

Introduction.

Whereas skeletal muscle metastasis is a rare event, it does occur occasionally in animal models. Therefore, there must be biological mechanisms that enable DTCs to overcome the skeletal muscle bottlenecks, given the right circumstances. Here we explored the notion that there may be genes that better assist metastasis to skeletal muscle than other secondary sites.

Preliminary Results.

Several genes enhance tumor cell outgrowth exclusively within skeletal muscle. As shown in Chapter 3 and 4, we created a skeletal muscle-metastatic progression series and conducted whole transcriptome sequencing via RNAseq. Based on analysis of the resulting data, we generated a list of candidate genes that potentially promote outgrowth of 4T1-SkM3met (3rd generation skeletal muscle metastatic cells). A total of 43 genes were chosen to screen based on their log-fold increase in the most muscle-metastatic subline compared to non-muscle-metastatic subline, as well as those that trend consistently (increase as the sublines become more metastatic). Candidate genes were knocked out and screened for their necessity for skeletal muscle colonization in organotypic culture using the CRISPR/Cas9 system (previously shown in Chapter 4). To identify genes that were required to mediate tumor cell outgrowth specifically in skeletal muscle (v. lung), we normalized the amount of 4T1-SkM3met outgrowth in the SkMc niche to the amount of 4T1-SkM3met

outgrowth in the LF niche. Therefore, those hits that have the greatest values after this normalization step will be the genes that have the greatest specificity for skeletal muscle. The data suggest that four genes - Magix, Dnajc6, Trib2 and Slc35f1 – significantly enhance tumor cell outgrowth *exclusively* within skeletal muscle compared to lung. Presently these genes are ill-defined at large.

Dnajc6 and Trib2 knockout significantly reduce skeletal muscle metastases. We tested the impact of these four candidate genes on skeletal muscle colonization *in vivo*. Ten thousand mutant 4T1-SkM3met cells were i.c. injected into 6-8-week-old Balb/c mice and sacrificed three weeks later. We hypothesized that the mice inoculated with the CRISPR-edited 4T1-SkM3met would have reduced skeletal muscle metastases. Fluorescent imaging (mCherry) of the tissues of interest *ex vivo*, we observed that the knockout of two of the four genes, Dnajc6 and Trib2, resulted in significantly reduced skeletal muscle metastases, as compared to a non-targeting control (eGFP). Only metastasis to skeletal muscle decreased without Dnajc6 and Trib2 expression, as compared to the other organs surveyed (brain, lung, ovary and adrenal), strengthening the earlier hypothesis that the identified genes confer a specific advantage for colonization of skeletal muscle.

Only Trib2 is both sufficient and necessary for colonization of skeletal muscle in culture. We then examined if enhanced Dnajc6 and Trib2 expression was sufficient for skeletal muscle colonization. The 4T1-parental (non-muscle metastatic) and 4T1-SkMmicro (travels to muscle but does not colonize it) cell lines were transfected with Dnajc6 and Trib2 overexpression vectors. These cells were then screened in co-culture and tumor growth quantified over a period of ten days. Only one candidate, Trib2, was necessary and sufficient to support tumor cell colonization of skeletal muscle in the culture setting. Of even

more interest, Trib2 expression is only sufficient in the 4T1-SkMmicro cell line. As we already know, metastasis is a multi-step process that requires a cell to be competent to travel to, survive within and grow successfully in the secondary environment. The 4T1-parental cells seem to lack the ability to proliferate within muscle and Trib2 expression is not enough to rescue this. The 4T1-SkMmicro cell line, on the other hand, has generally adapted to the survival constraints. Trib2 expression, then, appears to aid in the colonization stage of the metastatic cascade.

Future studies are needed to determine if Trib2 expression is sufficient to promote tumor colonization in skeletal muscle *in vivo*. Further, to round out the above experiments, it would be ideal to generate rescue constructs (codon-optimized overexpression vectors) for the CRISPR-edited 4T1-SkM3 cells to further confirm the role of Trib2 in skeletal muscle colonization.

Literature suggests that expression of Trib2 dramatically blocks cellular senescence of colorectal cancer cells by negatively regulating p21 promoter activities[17]. Knowing this, we are interested in identifying the mechanism at play in the skeletal muscle setting. Is Trib2 involved in blocking of skeletal muscle-induced cellular senescence of DTCs? Trib2 expression as a means to prevent senescence is an attractive hypothesis: Tumor cells, new to the muscle environment, upregulate Trib2 in order to resist oxidative stress-induced cell cycle arrest. Those cells, having escaped the microenvironmental pressures, may go on to evolve within the niche and colonize the tissue.

This chapter was made possible with help from the following: Ilsa Coleman, Megan Kufeld, Stephen Tapscott, Slobodan Beronja, Kirk C. Hansen, Patrick Paddison, Peter S. Nelson, and Cyrus M. Ghajar.

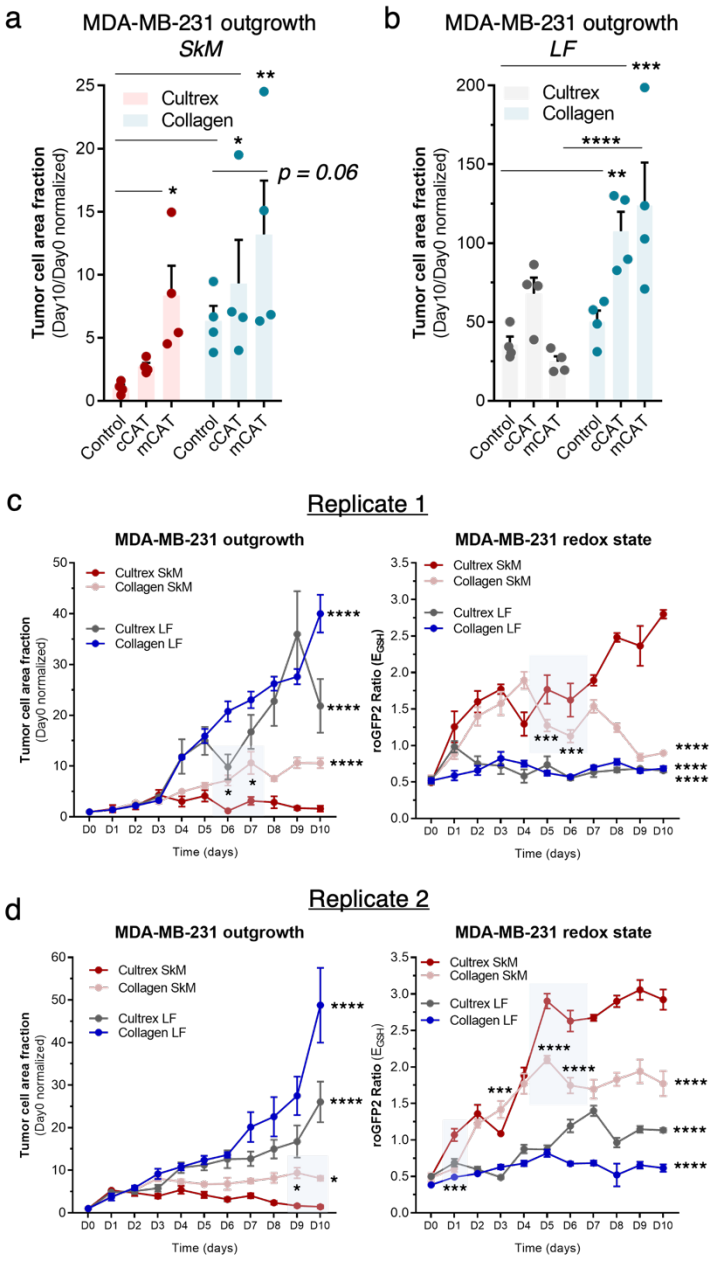

Figure 5.1. Ectopic catalase expression and collagen deposition both facilitate redox stabilization prior to tumor cell growth in SkMc. a) MDA-MB-231- control, -mCAT or -cCAT cells are cultured on SkMc in the context of a Cultrex or collagen-rich layer. Outgrowth is only significantly increased when the mCAT vector is present, collagen is present or both the mCAT vectors and collagen matrix are present. One-way ANOVA, followed by Fisher's LSD, was performed where comparisons were made against the "Cultrex MDA-control" condition. **b**) MDA-MB-231- control, -mCAT or -cCAT cells are cultured on the LF niche in the context of a Cultrex or collagen-rich layer. Here, outgrowth is only significantly increased when the mCAT vector is present in the context of a collagen-rich environment. **c-d**) MDA-MB-231-Grx1-roGFP2 cells are co-cultured in the SkMc and LF niches in the presence of either a Cultrex or collagen-I layer. Tumor cell outgrowth (left) and redox state (right) are measured in two experimental replicates (c-d). For (c-d), two-way ANOVA, followed by Fisher's LSD, was performed where comparisons again "Cultrex SkM" are denoted on graph above. **P* <0.05, ***P*<0.005, ****P*<0.0005, *****P*<0.0001.

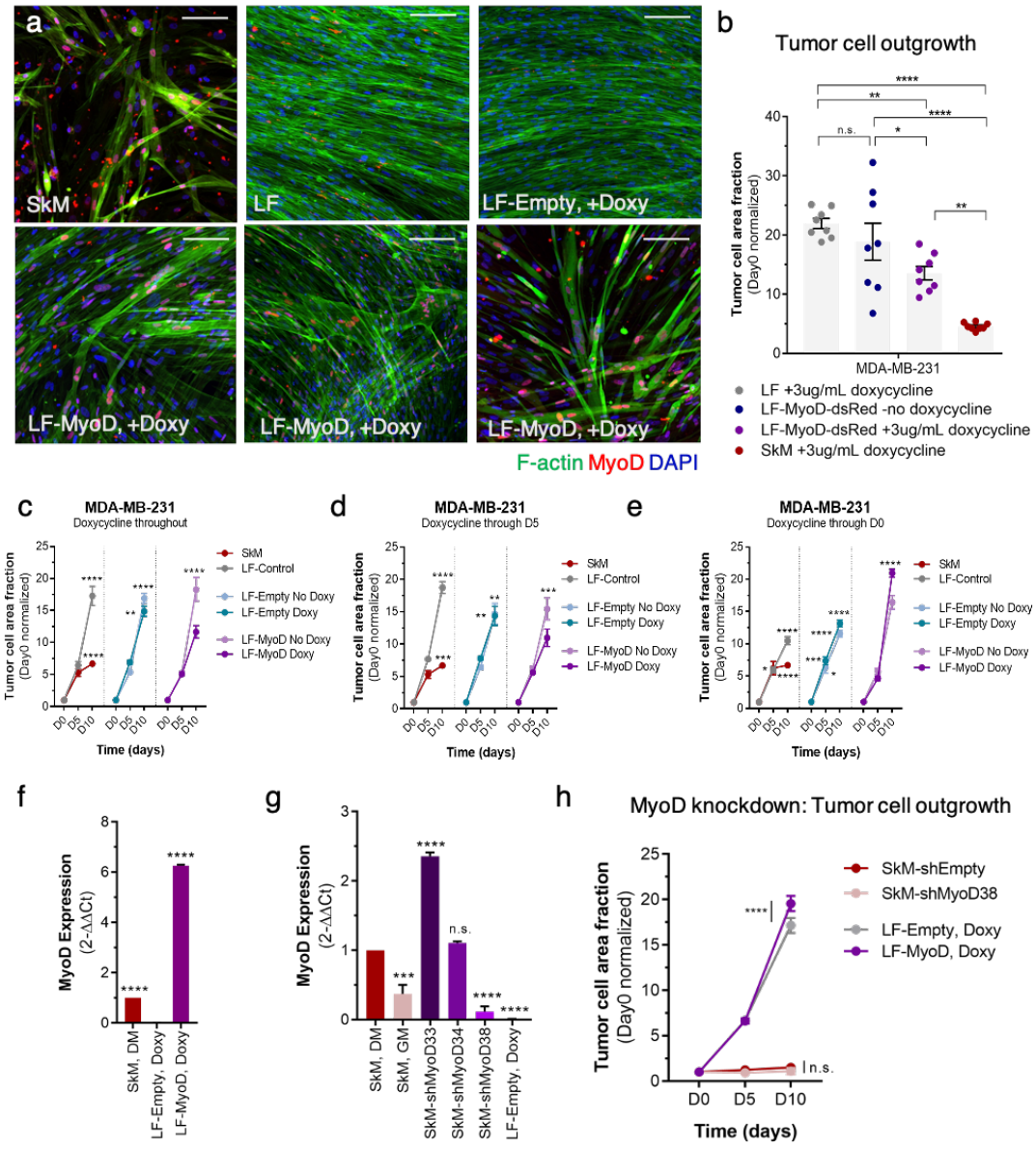

Figure 5.2. Introduction of MyoD in lung fibroblasts can reduce tumor cell outgrowth, but knockdown of MyoD in skeletal muscle has no effect on tumor cell outgrowth. a) Representative images of SkMc, LF (untransfected), LF-Empty and LF-MyoD cell lines. Upon doxycycline treatment, MyoD is induced in LF-MyoD cells. Scale bar = 1 mm. b) MDA-MB-231 outgrowth on SkMc, LF-Empty and LF-MyoD cell lines. Outgrowth is reduced when LF cells express MyoD, compared to controls. c-e) MDA-MB-231 tumor cell outgrowth is tracked over 10-days, with doxycycline being removed at various timepoints (throughout, at D5, at D0 tumor cell seeding). For (c-e), one-way ANOVA was performed, followed by Fisher's LSD, where comparisons were made against the LF-MyoD +doxycycline condition. f) MyoD expression in SkMc, LF-Empty and LF-MyoD niches. g) MyoD expression in SkMc, MyoD-knockout SkM, and LF-Empty niches. h) MDA-MB-231 outgrowth on SkMc and SkMc-shMyoD, along with LF-Empty and LF-MyoD cell lines. Here, outgrowth is not effected by either induction or knockout of MyoD. Two-way ANOVA was performed, followed by Fisher's LSD, and highlighted comparisons are graphed based on niche type (SkM v. SkM-shMyoD, LF v LF-MyoD). *P <0.05, **P<0.005, ***P<0.0005, ****P<0.0001.

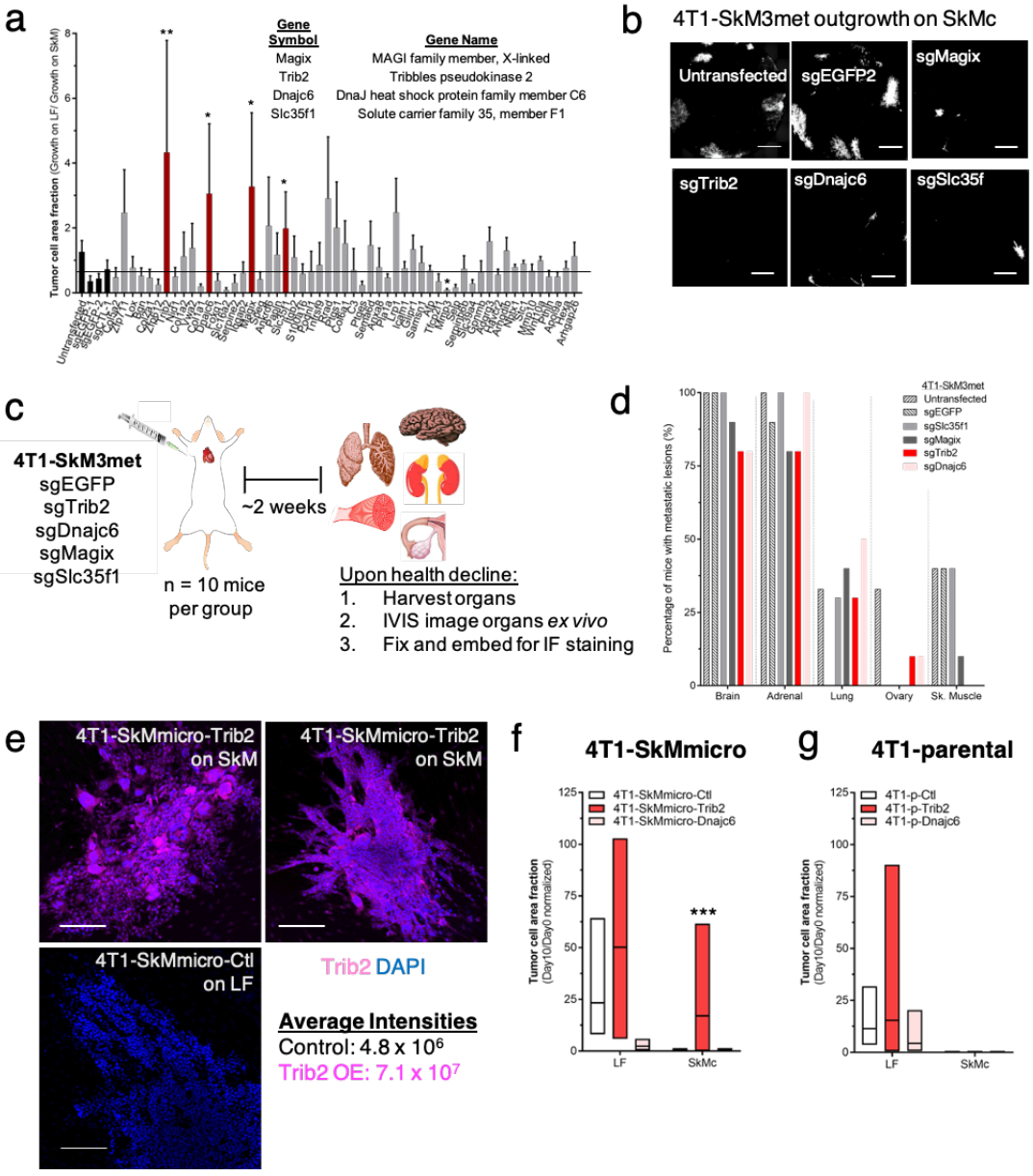

Figure 5.3. Dnajc6 and Trib2 knockout significantly reduce skeletal muscle metastases, but only Trib2 is both sufficient and necessary for colonization of skeletal muscle in culture. a) 4T1-SkM3met outgrowth on LF niche normalized to outgrowth on the SkMc niche, to determine what genes were uniquely detrimental to outgrowth on SkMc. Four candidates were significantly biased towards the SkMc versus LF niche. One-way ANOVA, followed by Fisher's LSD, was performed where comparisons were made against the sgEGFP2 control. b) Representative 4T1-SkM3met images for the outgrowth four candidate genes and two control conditions on SkMc. Scale bar = 1 mm. c) Schematic for the mouse study to determine if the knockout of Trib2, Dnajc6, Magix or Slc35f would prevent 4T1-SkM3 skeletal muscle metastasis *in vivo*. d) Percentage of mice with metastases to brain, adrenal glands, lung, ovary or skeletal muscle. e) Representative images of Trib2 staining of 4T1-SkMmicro cell lines, confirming positive expression in culture. Scale bar = 1 mm. f) Tumor cell outgrowth of 4T1-micro-sgTrib2 or -sgDnajc6 on SkMc and LF niches. f) Tumor cell outgrowth of 4T1-parental-sgTrib2 or -sgDnajc6 on SkMc and LF niches. **P* <0.05, ***P*<0.005, ****P*<0.0005, *****P*<0.0001.

Chapter 5 References

1. Hernandez-Munoz, R., Diaz-Munoz, M., Chagoya de Sanchez, V. Possible role of cell redox state on collagen metabolism in carbon tetrachloride-induced cirrhosis as evidenced by adenosine administration to rats. *Biochimica et Biophysica Acta* 1200:93-94. (1994).

2. Hernandez-Munoz, R., Diaz-Munoz, M., Chagoya de Sanchez, V. Adenosine partially prevents cirrhosis induced by carbon tetrachloride in rats. *Hepatology* 12(2):242-8. (1990).

3. Chagoya de Sanchez, V., Hernandez-Munoz, R., Yanez L., Vidrio S., Diaz-Munoz M.. Possible mechanism of adenosine protection in carbon tetrachloride acute hepatoxicity. Role of adenosine by-products ad glutathione peroxidase. *J Biochem Toxicol.* 10(1):41-50. (1999).

4. Fang, M., Yuan, J., Peng, C., Li Y.. Collagen as a double-edged sword in tumor progression. *Tumor Biology* 35(4):2871-2882. (2014).

5. Gutscher, M. *et al.* Real-time imaging of the intracellular glutathione redox potential. *Nature Methods* **5**, 553–559 (2008).

6. Morgan, B., Sobotta, M. C. & Dick, T. P. Measuring EGSH and H2O2 with roGFP2-based redox probes. *Free Radical Biology and Medicine* vol. 51 1943–1951 (2011).

7. Tapscott, S. The circuitry of a master switch: Myod and the regulation of skeletal muscle gene transcription. D*evelopment* 132: 2685-269. (2005).

8. Fong A. and S. Tapscott, S.. Skeletal muscle programming and re-programming. *Curr Opin Genet Dev*. 23(5):568-573. (2014).

9. Rudnicki R. and Jaenisch R. The MyoD family of transcription factors and skeletal myogenesis. *Bioessays.* 17(3):203-9. (1995).

10. Hollenberg, S., Cheng, R., and Weintraub, H. Use of a conditional MyoD transcription factor in studies of MyoD trans-activation and muscle determination. *Proc Natl Acad Sci* 90(17):8028-32. (1993).

11. Rudnicki, M., Schnegelsberg, P., Stead, R., Braun, T., Arnold, H., Jaenisch, R. MyoD or Myf-5 is required for the formation of skeletal muscle. Cell. 75(7):1351-9. (1993).

12. Megeney, L., Kablar, B., Garrett, K., Anderson, J., Rudnicki, M. MyoD is required for myogenic stem cell function in adult skeletal muscle. Genes Dev. 10(10):1173-83. (1996).

13. Cornelison, D., Olwin, B., Rudnicki, M., Wold, B. MyoD(-/-) satellite cells in single-fiber culture are differentiation defective and MRF4 deficient. *Dev Biol.* 224(2):122-37. (2000).

14. Kraft, C., LeMoine, C., Lyons, C., Michaud, D., Mueller, C., Moyes, C. Control of mitochondrial biogenesis during myogenesis. *Am J Physiol Cell Physiol.* 290(4):C1119-27. (2006).
15. Shuntaku, J. Peterson, J. Talbert, E. Gu, JM., Ladner, K., Williams, D., Mousavi, K., Wang, R., Sartorelli, V., Guttridge, D. MyoD Regulates Skeletal Muscle Oxidative Metabolism Cooperatively with Alternative NF-κ B. *Cell Reports.* 17(2):514-526. (2016).
16. Arany Z. PGC-1 coactivators and skeletal muscle adaptations in health and disease. *Curr Opin Genet Dev.* 18(5):426-34. (2008).
17. Zhenlin, H. Kaixuan, G. Sun, X., Fuqing, H., Chen, Q., Luo, X., Wang, G., Hu, J., Sun L. TRIB2 functions as novel oncogene in colorectal cancer by blocking cellular senescence through AP4/p21 signaling. *Molecular Cancer.* 17(172). 2018.

Chapter 6. Perspectives and Concluding Remarks

Dissertation Summary

In my thesis, I showed that the skeletal muscle microenvironment is profoundly suppressive of disseminated tumor cell colonization. I was able to locate breast or mammary DTCs in human and mouse skeletal muscle and showed that these cells are able to persist over long periods of time, but demonstrate little signs of proliferating past a single cell stage. We were able to model the skeletal muscle niche in culture through the use of a 3D organotypic system, where we were able to recapitulate the suppressive phenotype that we and others have reported in physiological systems. Using mouse and organotypic culture models, along with metabolomics, we identified metabolic factors within the skeletal muscle microenvironment that inhibit outgrowth of breast and mammary cancer cells. We found that redox metabolism – and unchecked oxidative stress - is key in the suppression of DTCs in skeletal muscle.

The generation and transcriptional analyses of skeletal muscle-metastatic mammary cancer sublines enabled our identification of genes that confer skeletal muscle-metastatic capacity and implicate molecular pathways involved for skeletal muscle-driven suppression. Candidate genes were functionally screened for their necessity for skeletal muscle colonization using the CRISPR/Cas9 system in both the organotypic co-culture and *in vivo*. A large portion of the candidates that significantly promote tumor cell outgrowth in skeletal muscle are required for collagen trimerization and extracellular matrix organization. Thus, the data suggest that the remodeling of skeletal muscle into a collagen-rich environment may be critical for tumor cell colonization within this tissue.

I concluded my dissertation with a survey of potential avenues of study based on preliminary data generated over the course of my doctoral training. We have reason to believe that the muscle-specific transcription factor MyoD might regulate skeletal muscle's suppression of tumor outgrowth. But does MyoD do it through either the metabolic or extracellular matrix routes described in Chapters 3 or 4? Additionally, our 4T1-SkM3met CRISPR screen yielded several candidates for metastasis-enhancers unique to skeletal muscle. Trib2, the top candidate, requires further follow-up to determine the mechanism of action.

Though my doctoral work has provided great insight into the molecular mechanisms that underlie the suppressive nature of skeletal muscle, it has also opened the door to so many additional questions. To conclude, I ask the reader to consider the following:

Viewing oxidative stress and redox balance as a therapeutic vulnerability

Our findings demonstrate that sustained oxidative stress drives a profound redox imbalance in skeletal muscle that poses a unique problem to DTCs. This adds to mounting evidence that sustained oxidative stress should be considered a DTC hallmark and that this state might be exploited for metastasis prevention. It has become clear that antioxidant activities are essential for tumorigenesis and that the timing of antioxidant/oxidant bursts throughout the metastatic cascade can dictate the fate of the tumor cell[1-6]. Increased intracellular levels of glutathione are required for the initiation and progression of various types of cancer and inhibitors of glutathione reductase behave as anticancer drugs[5], while treatments based on depletion of glutathione (e.g. isothiocyanates) or blocking the uptake of rate-limiting precursors (e.g. the cysteine/glutamate antiporter xCT) greatly reduce cancer cell survival[6,7].

The complex interconnection between ROS levels and metastasis is largely based on precise fine-tuning between ROS production and scavenging. The early stages of the tumorigenesis leverage slight increases in ROS levels. Consequently, cancer cells thrive on levels of ROS that are moderately higher than those in their normal counterparts. We believe that this feature renders cancer cells more sensitive to external stimuli that further increase the production of ROS. How do we leverage the knowledge that residence in certain microenvironments further elevate tumoral ROS and/or deprive a tumor cell of antioxidant synthesis? Could environmental strategies to drive tumoral ROS push the cell past its survival limits? Our work here implies that this is a very real possibility.

The impact of microenvironmental metabolism on ECM and metastatic outgrowth

The transition from a single DTC to an overt metastasis requires not only internal tumor cell adaptation, but also a permissive external microenvironment. Most approach the concept of metabolic adaptation from the perspective of the tumor cell – what reprogramming occurs to overcome harsh new environments? However, we posit that a

greater understanding of how the metabolic microenvironment, *with* ECM, alters DTC proliferation will lead to the discovery of targetable vulnerabilities of DTCs.

Historically, researchers have viewed cellular metabolism and ECM remodeling as independent entities that drive tumorigenesis and metastasis[8-11]. For example, we know that neighboring cells provide DTCs with essential nutrients to further biomass synthesis; cancer cells switch to a more glycolytic phenotype to make ATP more quickly[10-11]. We also accept that excess ECM deposition and cross-linking promotes loss of polarity and a more invasive phenotype[11-12]. While interest is growing to understand the impact of ECM remodeling on cancer cell metabolism, there have been no comprehensive investigations into how changes in a microenvironment's metabolism remodels ECM in a way that encourages - or discourages – DTC outgrowth. Thus, we think it critical to investigate how alterations to a niche's metabolic demands remodel its ECM composition and architecture to prevent or promote metastatic outgrowth.

Further characterization of injury as a modulator of tumor cell colonization

Trauma and wounding have long been reported to support tumor outgrowth[13-17]. Skeletal muscle is no exception. Clinical reports describe skeletal muscle-metastasis development at documented sites of previous trauma[18], implying that breakdown of the skeletal muscle microenvironment, then, seemingly is required to give tumor cells the growth advantage they need. Interestingly, while acute wounding (ischemia, crush injury, contusion, laceration[13-17]) has been reported to enhanced tumor growth, exercise – a mild form of muscular injury – is described by many to directly suppress tumor growth[19]. While skeletal muscle recovery and tissue regeneration are tightly-regulated programs, there are mechanistic differences that occur based on the severity of insult[20-23]. These variant molecular responses to injury may be key to understanding how low-grade chronic skeletal muscle injury is tumor-suppressive whereas high-grade skeletal muscle injury is tumor-promoting.

For example, the influence of exercise as an external modulator of tissue microenvironments still necessitates extensive study. Epidemiological studies demonstrate that leisure-time physical activity reduces the risk of at least 13 different cancer types and provides evidence for an exercise-dependent reduction in the risk of recurrence for breast,

colon and prostate cancer[24-26]. Exercise is an energy-consuming activity that induces marked changes in whole body and intracellular metabolism[27-28]. What are the mechanisms by which metabolic adaptations to exercise protect tissue microenvironments from metastatic outgrowth? Future experiments would enable elucidation of specific metabolic adaptations within the tissue microenvironment that actively contribute to growth suppression of DTCs that reside in or traffic to that niche. Moreover, these data would indicate *why* the initiation of specific exercise practices are effective as an adjunct therapeutic aid when combating metastatic breast cancer.

Exercise-related studies, like my doctoral research, would provide much-needed insight into the distinguishing characteristics of metastasis-resistant tissues. Based on the emerging data, pharmaceutical and/or lifestyle interventions may be more rationally constructed to extend metastasis-free survival of cancer patients.

Concluding remarks

Despite considerable effort by physicians and researchers alike, metastasis still remains lethal. With insight into the biology of skeletal muscle-mediated suppression, I hope that researchers may one day be able to convert fertile tissues into resistant ones. Given all that we know about the role of the microenvironment, strategies to “change the soil” may be as effective as those that attempt to outright kill the seed. I hope that this dissertation will inspire such approaches to alter the course of metastasis therapies in the future.

Chapter 6 References

1. Menegon, S., Columbano, A. & Giordano, S. The dual roles of NRF2 in cancer. *Trends Mol. Med.* **22**, 578–593 (2016).

2. Lignitto, L. et al. Nrf2 activation promotes lung cancer metastasis by inhibiting the degradation of Bach1. *Cell* **178**, 316–329 (2019).

3. Bae, I. et al. BRCA1 induces antioxidant gene expression and resistance to oxidative stress. *Cancer Res.* **64**, 7893–7909 (2004).

4. Gorrini, C. et al. BRCA1 interacts with Nrf2 to regulate antioxidant signaling and cell survival. *J., Exp. Med.* **210**, 1529–1544 (2013).

5. Harris, I. S. et al. Glutathione and thioredoxin antioxidant pathways synergize to drive cancer initiation and progression. *Cancer Cell* **27**, 211–222 (2015).

6. Sayin, V. I. et al. Antioxidants accelerate lung cancer progression in mice. *Sci. Transl. Med.* **6**, 221ra215 (2014).

7. Lo, M., Wang, Y. Z. & Gout, P. W. The x(c)-cystine/glutamate antiporter: a potential target for therapy of cancer and other diseases. *J. Cell Physiol.* **215**, 593–602 (2008).

8. D. Anastasiou. Tumour microenvironment factors shaping cancer metabolism landscape. British Journal of Cancer. 116:277-286. (2017)

9. G. Pascual, D. Domingez, S. Benitah. The contributions of cancer cell metabolism to metastasis. Dis- ease Models and Mechanisms 11: dmm032920. (2018)

10 R. DeBerardinis, J. Lum, G. Hatzivassiliou, C. Thompson. The biology of cancer: Metabolic reprogramming fuels cell growth and proliferation. Cell Metabolism 7(1):11-20 (2008)

11 J. Erler and V. Weaver. Three-dimensional context regulation of metastasis. Clin Exp. Metastasis 26(1):35-49. (2009).

12. E. Rainero. Extracellular matrix internalization links nutrient signaling to invasive migration. International Journal of Experimental Pathology. doi:10.1111/iep.12265 (2018).

13. MH. Sieweke, NL Thompson, MB Sporn, MJ Bissell. Mediation of wound-related Rous sarcoma virus tumorigenesis by TGF-beta. Science. 248(4963):1656–1660 (1990).

14. B. Fisher, E. Fisher, N. Feduska. Trauma and the localization of tumor cells. Cancer 20:23-30 (1967).

15. N. El Saghir et al., Trauma-associated growth of suspected dormant micrometastasis. BMC Cancer. 5:95 (2005).

16. H. Dvorak. Tumors: wounds that do not heal. Similarities between tumor stroma generation and wound healing. N Engl J Med 315(26):1650-9 (1986).
17. Schafer and Werner. Cancer as an overhealing wound: an old hypothesis revisited. Nature reviews: mol. cell bio 9:628-638 (2008).
18. T. Magee, H. Rosenthal, Skeletal muscle metastases at sites of documented trauma. American journal of roentgenology 178, 985 (2002).
19. J. Goh et al., Exercise training in transgenic mice is associated with attenuation of early breast cancer growth in a dose-dependent manner. PLoS ONE 8(11):e80123. (2013
20. C. Lepper, T. Partridge, CM Fan, An absolute requirement for Pax7-positive satellite cells in acute injury-induced skeletal muscle regeneration. Development. 138(17): 3639-3646 (2011).
21. Z. Yan et al. Highly coordinated gene regulation in mouse skeletal muscle regeneration. JBC 278(7):8826-8836 (2003).
22. G. Warren et al., Mechanisms of skeletal muscle injury and repair revealed by gene expression studies in mouse models. J physiol. 15;582: 825-841. (2007).
23. D. Hardy et al, Comparative study of injury models for studying muscle regeneration in mice. PLoS One (2016).
24. P. Hojman et al. Molecular mechanisms linking exercise to cancer prevention and treatment. Cell Metabolism 27:10-21 (2018).
25. Ballard-Barbash et al., Physical activity, biomarkers and disease outcomes in cancer survivors: a systematic review. J Natl Cancer Inst. 104(11):815-840. (2012).
26. Koelwyn et al, Exercise-dependent regulation of the tumor microenvironment. Nature Reviews: Cancer 17:620-˘632 (2017).
27. E. Ferraro et al, Exercise-induced skeletal muscle remodeling and metabolic adaptation: redox signaling and role of autophagy. Antioxid redox signal. 21(1):154-176. (2014).
28. B. Egan, J. Zierath, Exercise metabolism and the molecular regulation of skeletal muscle adaptation. Cell metabolism 17:162-184. (2013).